Engineered Protein Nanoparticles as Therapeutics for Gliomas

by

Ava Mauser

A dissertation submitted in partial fulfillment
of the requirements for the degree of
Doctor of Philosophy
(Biomedical Engineering)
in the University of Michigan
2024

Doctoral Committee:

Professor Joerg Lahann, Chair
Professor Maria Castro
Professor James Moon
Assistant Professor Connie Wu

Ava K. Mauser

mausera@umich.edu

ORCID iD: 0009-0006-4361-4004

Dedication

For Maui and Papa

For keeping me strong in times of uncertainty

Acknowledgements

While I believe many of my characteristics are intrinsic, I cannot ignore my parents' impact on my value for education. I remember being a child crying not wanting to go to school. My mother said I would end up on a box on Central – a street in downtown Albuquerque, New Mexico. I answered back, "I like boxes". While that stubbornness rings true to who I've always been, I knew deep down, I did not want to live in a box. I was taught that someone can take everything from you, but they cannot take away what you know. Outside of my parents establishing an educational foundation for me, I am thankful for a vibrant, stable childhood. Mommy – thank you for making me laugh and reminding me not to take life so seriously. Your charisma and ability to light up a room are inspiring to me. Daddy – thank you for being a role model; without you, I don't know if I would be an engineer or a scientist. I always tell myself what you would tell me growing up: "try your best, as that is all you can do".

You are lucky if you have grandparents in your life, but if you have grandparents who are like a second set of parents, you are blessed. Maui and Papa, thank you for your unwavering support and unconditional love. There was never hesitation in helping me, even when I did not ask. That sense of stability was instrumental to my success; I could not imagine how much more challenging it would have been without feeling grounded. Maui, you always listened to me, remembered my research progress, and encouraged me every step of the way. You made me feel seen and heard in times I felt invisible. Papa, thank you for believing in me when I want to reach for the stars, but keeping me grounded. I appreciate every care package I received – even if I did get a little tired of Taco Bell flavored sunflower seeds and biscochito dust.

To my sister, best friend, and confidant, Olivia: I have a hard time putting into writing how appreciative to have you. You inspire me to be more thankful, patient, and positive. There is no one in this world who understands me like you do and while we know this world is unpredictable, we will always have each other. Outside of being a sister, I want to thank you for becoming a mother as I simultaneously became an aunt. Alexandria, you are the sunshine wrapped in skin that

I did not know I needed. You made the last years of my PhD more fun as I witnessed you growing up. While you are too young to read, know that I love you and know that "Ah-tee" is always here for you.

To the rest of my family, thank you for your words of support and cheering me on. To my Grandma Mauser and Aunt Margaret – I hope you look down and I have made you proud. Aunt Margaret, you were the epitome of intellectual curiosity. Whenever I had the chance, I spoke about your accomplishments. Grandma Mauser, while you could not witness me embarking on my graduate school journey, I am grateful for the impact you've had on me. I admired your calm presence and witty personality. Both my grandma and my aunt passed from cancer, which made my research compelling. I found comfort knowing I was contributing to the field in their memory.

Sergio, thank you for your love and patience. Over the past year, you have kept me accountable with my personal goals, challenged my perspectives, and have taught me to regulate stress better. This has led to substantial personal growth, and I thank you for pushing me to be a better version of myself each day.

To my friends, thank you for your emotional support, the laughs, and adventures over the years. Noah, Jeff, Carolina, Tanner – thank you for being my close friends in the BME department. Nahal and Laura, thank you for being some of my best friends in and out of the Lahann Lab. Mische, we can't seem to get away from each other. Despite so many possibilities for graduate school, we both ended up at Michigan. Even more impressive, our offices ended up being two doors down from each other. It was always so much fun to reminisce on our times in New Mexico and at UNM. When in doubt, we could always laugh about the Golden Formula. Melanie, thank you for consistently showing up for me. You have been one of my most supportive friends and I couldn't ask for anything more. Well, maybe do not let me run another 5K with you in the heat of Austin, TX. That would be my only request.

To my fuzz, Zephyr, thank you for the cuddles, and companionship.

To my coach, Sarah, thank you for helping me reach my fitness goals since 2019. Working with you has enabled me to feel in control of *something* in the chaos of a PhD program.

To Keli Hand, thank you for the professional advice you have given me over the years. I have admired your success as a woman in engineering and I am thankful for the guidance. I took every piece of advice to heart, whether that was how to navigate difficult conversations, or what outfit to wear for an interview.

Undoubtedly, the work presented in this thesis would not exist without the mentorship from my advisor, Professor Lahann. When I was looking for a lab, I was disappointed when other labs rejected my interest in shadowing their lab because my experience did not align with their research. However, this did not concern Professor Lahann. He did not ask about what I knew and how that could benefit the lab, but what I wanted to learn. He knew that one’s tenacity and curiosity were qualities that were far more valuable than teachable skills. Professor Lahann, thank you for challenging me, encouraging me, and believing in me (usually more than I have in myself). I am proud to have a mentor who not only fostered my independence as a scientist, but a mentor who deeply cared about the wellbeing of his students and graciously helped us whenever he could. I have grown tremendously throughout my PhD, and I attribute that to you and the Lahann Lab.

I would like to thank the Lahann Lab members – past and present. Thank you to Dr. Yeongun Ko, Dr. Dylan Neale, Dr. Ayse Muniz, Dr. Jason Gregory, Dr. Daniel Quevedo, Dr. Nahal Habibi, Dr. Stephanie Christau, Dr. Judith Witte, and Dr. Laura Saunders for your mentorship at the beginning of my PhD. I would like to especially thank Nahal for taking me under her wing. While Nahal taught me many laboratory techniques, what set her apart from other mentors was her ability to empathize and her inability to be judgmental. When I was nervous about a new technique, she would offer to watch me or call me to walk me through it. The feeling of learning without judgement fostered my curiosity and confidence as a scientist. Outside of the laboratory, Nahal has become one of my dear friends. I am thankful for all the fries and ice cream dates, the collection parties, and our heart-to-heart conversations. Laura – I am selfishly thankful you changed labs. It was a relief to meet someone whom I could relate to on many levels: personal, academic, and scientific. I am grateful for your constant support throughout my PhD, even after you graduated. You have reminded me that there is light at the end of the tunnel. To Dr. Jeff Raymond, thank you for your commitment to my success - professionally and academically. Thank you to the current members of the lab including, Dr. Michael Triebwasser, Dr. Seongjun Moon, Yao Yao, Anthony Berardi, Chris Kim, John Kim, Albert Chang, Fjorela Xhyliu, Arit Patra, Julio Zelaya, Josh Flint, and Yuxuan Deng. I will cherish our memories as Team Feesh, floating down the Huron River in animal-themed floaties, and going to “northern” Michigan for a lab retreat and forever calling bagels, “circular bread”. I am thankful for our scientific discussions and collaborations. Thank you to the undergraduate students I’ve been fortunate to mentor throughout the years including Yazmin Hernandez, William Brown, Lauren Molloy, and Sophia Lee. While lab-related skills are important, I hope that above all, I taught you to believe in yourself and do not underestimate yourselves. Thank you for contributing to my growth as a scientist and mentor, and to the research presented in this thesis. I'd also like to thank Isabel Waibel for choosing me to mentor you for your master's thesis. Thank you for making the lab so much fun, your organizational skills, and the work you put into the project. You have inspired me in many ways.

Thank you to my collaborators I have been fortunate to work with over the years. Thank you to Professor Maria Castro for being one of my earliest mentors during my PhD. Thank you to the members of the Castro Lab I worked closely with in effort to understand the therapeutic effectiveness of my work. Thank you to Dr. Kaushik Banerjee, Dr. Anzar Mujeeb, Dr. Felipe Núñez, Ayman Taher, and especially, Padma Kadiyala. Padma, thank you for always helping me understand the biology side of our collaborations, your insightful perspectives, and your friendship. Thank you to Dr. Colin Greineder for bringing enthusiasm into projects, teaching me how to perform experiments, and never shying away from failed experiments. You always had a Plan B, which taught me that disproving a hypothesis is as useful as proving one.

To my committee members (Professor Joerg Lahann, Professor Maria Castro, Professor Connie Wu, Professor James Moon), thank you for the feedback and support, particularly in the last year of my PhD.

Thank you to all the administrative staff and core staff who helped my research run smoothly. Thank you to Maria Steele for reminding me to register for classes, ensuring I stayed on top of my requirements, and being exceptionally helpful throughout my PhD. Thank you to the Biointerfaces staff including Karl Olsen, Sarah Spanninga, MaryBeth Westin, Lisa Moran, and Nadine Wong for assisting me either scientifically, or administratively. Thank you to the MC^2 Core especially Bobby Kerns and Haiping Sun for spending time to help me improve my SEM imaging skills.

Lastly, I would also like to thank my funding sources including the National Science Foundation Graduate Research Fellowship Program, the Rackham Merit Fellowship, and the Tau Beta Pi Fellowship. These funding sources gave me freedom in my PhD, and above all, made me feel like I belonged as a PhD student.

To those I have not personally named – thank you. This was not an easy journey, but it was a fulfilling one. Without the support, none of this would be possible.

Table of Contents

List of Tables

List of Figures

Abstract

Gliomas are the most common malignant type of central nervous system tumor for which treatment options are usually limited to maximal safe surgical resection, radiotherapy, and chemotherapy. Protein-based nanoparticles are promising therapeutic candidates as they leverage the advantages of nanoparticles-mediated delivery while exploiting protein's selectivity, low immunogenicity, versatility, and biodegradability. Recently, therapeutic efficacy was achieved in a glioma model using synthetic protein nanoparticles (SPNPs), which were produced through electrohydrodynamic (EHD) (co) jetting. This thesis sought to expand the utility of these SPNPs for glioma therapy.

Nanoparticle-mediated delivery of small molecules is often explored for glioma therapy since the majority of small molecules are excluded from the brain, however using SPNPs has yet to be described. In the first part of this thesis, the hydrophobic small molecule, paclitaxel, was solubilized into albumin through high pressure homogenization then subjected to EHD jetting to form paclitaxel SPNPs. The paclitaxel SPNPs showed favorable morphology, release kinetics, stability, and retained paclitaxel's toxicity in vitro. For the first time, a hydrophobic small molecule was loaded into an EHD-produced SPNPs, which sets foundation for hydrophobic small molecule-loaded SPNPs.

Next, bicompartmental SPNPs were fabricated to contain two therapeutics of differing size, solubility, and function: STAT3 siRNA and paclitaxel. Nanoparticle combination therapy is the cornerstone of advanced therapy as it allows two or more therapeutics to be delivered while exploiting the advantages of combination therapy. These STAT3i/paclitaxel bicompartmental SPNPs released siRNA and paclitaxel over time, exhibited stability, and showed anti-glioma activity in glioblastoma IDH wild-type (grade 4) glioma cell cultures.

Finally, an SPNP containing siRNA against an autophagy related gene, ATG7, was fabricated to re-sensitize mutant IDH astrocytoma (grade 2) to radiotherapy. When combined with radiotherapy, long term survival was achieved in a mutant IDH astrocytoma (grade 2) model. Long

term survivors were rechallenged with a second tumor and achieved 100% survival, despite not receiving additional treatment suggesting immunological memory.

While the work described in this thesis only represents a fraction of the capabilities possible with EHD-jetted SPNPs for glioma therapy, it lays the groundwork for future SPNP exploration, whether in glioma or with other loaded molecules.

Chapter 1 Introduction

This chapter contains portions of text originally published as:
“Protein Nanoparticles: Uniting the Power of Proteins with Engineering Design Approaches.”
N Habibi*, A Mauser*, Yeongun Ko*, and Joerg Lahann. *Shared co-first authorship.
Advanced Science (2022)

1.1 Gliomas

1.1.1 Classification of gliomas informs diagnosis and treatment

Gliomas represent the most common malignant primary brain tumor with 20,000 people being diagnosed annually in the United States.[1] The diagnosis and treatment ultimately depend on the classification of the glioma, which began in 1926 with the publication of the book, *A Classification of the Tumours of Glioma Group on Histogenetic Basis with a Correlated Study of Prognosis,* by Bailey and Cushing.[2] Since then, the classification of central nervous system (CNS) tumors has been reported by the World Health Organization (WHO) with the first edition being published in 1979 followed by second, third, fourth and fifth edition in 1993, 2000, 2007, and 2016, respectively.[3] In 2021, the WHO published the 5th edition of the Classification of Tumors of the CNS adopting molecular alterations for the first time. This builds upon established approaches such as histology and immunohistochemistry to provide an integrated diagnosis (histological diagnosis, CNS WHO grade, molecular information).[3] As a result, there have been several changes when compared to the prior edition in 2016 such as different nomenclature and grading, differentiation between pediatric and adult gliomas, the introduction of 22 new tumor types, and the revision of 13 tumors. This allows clinicians to accurately diagnose patients and provide appropriate treatment. With the inclusion of molecular diagnosis, it enables clinical trials to be more well-defined with only homogeneous patient populations being enrolled in clinical trials.[1] Stratifying studies in this manner can lead to better designed clinical trials and expedite the therapy development.[1] In the 2021 edition, glial tumors are separated into six categories: pediatric-type diffuse low grade gliomas, pediatric-type diffuse high-grade gliomas, adult-type diffuse glioma, circumscribed astrocytic glioma, glioneuronal and neuronal tumors, ependymomas. Adult type diffuse gliomas are further categorized as: (1) astrocytoma, IDH mutant (WHO grades 2-4), (2) oligodendroglioma, IDH mutant and 1/19q deleted (WHO grades 2 and 3), and (3) glioblastoma, IDH wild type (WHO grade 4).[1,3] In this thesis, only astrocytoma IDH mutant grade 2 and glioblastoma IDH wild-type grade 4 will be described in more detail since other types were not investigated for therapeutic efficacy.

1.1.1.1 Astrocytoma IDH mutant grade 2

Astrocytoma IDH mutant gliomas are molecularly defined by their mutation in isocitrate dehydrogenase 1/2 (IDH1/2) leading to the conversion of alpha-ketoglutarate to D-2-hydroyglutarate (2-HG) within the Krebs Cycle. Accumulation of 2-HG causes downstream epigenetic changes and is thought to promote tumorigenesis.[4] Many are accompanied by further genetic alterations in tumor protein 53 (TP53) and loss of α-thalassemia/mental retardation, X-linked (ATRX) expression usually leading to a diagnosis of IDH mutant astrocytoma. The grading from 2-4 of these tumors is assigned by the observed histopathology with high grades showing necrosis or neovascularization. Exceptions to this are if there is cyclin dependent kinase inhibitor 2A/B (CDKN2A/B) homozygous deletion, regardless of histopathology, it is assigned to grade 4.[5]

Astrocytoma IDH mutant grade 2 is typically found in patients between 30-35 years old and is relatively rare with 1 out of 200,000 people being diagnosed each year.[6] Treatment usually begins with maximal safe resection and could require postoperative treatment (radiotherapy and chemotherapy).[1] Radiotherapy combined with procarbazine, lomustine, vincristine (PCV) has demonstrated the best survival outcomes (13.3 years versus 7.8 years with radiotherapy alone) and is considered the standard of care for postoperative treatment.[6–8] Because of the lower incidence rate and higher median survival of these gliomas, less attention is given to addressing the limited therapeutic options.[9] Furthermore, the difficulty in culturing IDH mutant cells creates challenges in developing therapies at the preclinical stage.[7] The current status of therapeutic approaches include IDH inhibitors, DNA methyltransferase inhibitors, poly (ADP-ribose) polymerase (PARP) inhibitors and DNA repair enzymes, and immunotherapies.[10]

1.1.1.2 Glioblastoma IDH wild-type grade 4

Glioblastoma IDH wild-type grade 4 accounts for 48.6% of all malignant primary CNS tumors with 13,000 cases diagnosed each year in the United States and a 5-year survival rate less than 5%.[1,11,12] These diffuse astrocytic gliomas require one of the following genetic lesions: gain in chromosome 7 (including epidermal growth factor receptor amplification), loss of chromosome 10, telomerase reverse transcriptase (TERT) promoter mutations.[1] For treatment, maximal surgical resection is typically conducted followed by radiotherapy with concomitant and adjuvant temozolomide (TMZ) (Stupp Protocol).[13] To predict whether a patient will respond to TMZ, O^6-methylguanine-DNAmethyltransferase (MGMT) promoter methylation status can be determined. Patients with methylated MGMT promoter have better median survival of 23.4 months and respond to TMZ whereas patients with unmethylated MGMT promoter have a median survival of 12.6 months and typically do not respond to TMZ.[1] Unfortunately, most patients will experience tumor recurrence from which there is only a 6.2-month survival time after the initial onset.[12] These patients may receive additional surgical resection and chemotherapy (retreatment with TMZ or treatment with lomustine or bevacizumab). New therapies are needed given that the Stupp protocol has been in practice since 2005 and modifications to dosing has moderately improved survival from 14 months to 18 months.[12] Regardless of the classification, the therapeutic approval for gliomas has been disappointing. This can be attributed to several challenges, which will be discussed in the following section.

1.1.2 Pitfalls and challenges with treating gliomas

No curative options are available for astrocytoma IDH mutant WHO grade 2 and glioblastoma wild-type grade 4. The lack of translation of preclinical therapies to clinical oncology is attributed to several factors such as ineffective transport to the brain, poor stability, poor solubility, non-ideal pharmacokinetics and pharmacodynamics, cytotoxicity, and resistance.[14]

The delivery of therapeutics to the brain has largely been hampered by the blood-brain barrier (BBB) – a physical and physiological barrier that separates the circulating blood from brain tissue. While the BBB is important for maintaining the homeostasis of the CNS, its high selectivity through an intricate network of endothelial cells and tight junctions wrapped around capillaries makes delivering noninvasive therapeutics for glioma extremely challenging.[15] The most common type of therapeutic class are small molecules, but over 98% are impenetrable to the BBB.[16]

Macromolecules have a less promising fate with the majority being excluded from the brain due to their size. As gliomas grow, they can form their own vasculature thus compromising the BBB and leading to the formation of the blood-tumor barrier (BTB).[17] Though more penetrable than the BBB, the BTB is highly heterogeneous and can vary with tumor type, size, location.[18] In lower grades, the BTB resembles more similarities to the BBB than the BTB in glioblastoma, IDH wild-type, for example.[18]

Another consideration for systemic therapeutic development in gliomas is the toxicity profile. Cytotoxic drugs are typically administered at the maximum tolerated dose to achieve dosages within the therapeutic window, but can cause systemic toxicity due to their non-selectivity and limit the ability for patients to complete treatment.[19] For example, in glioblastoma IDH wild-type (WHO grade 4), only 44-50% of patients complete the full standard of care and a fourth who start treatment can finish the six cycles of TMZ.[20] Balancing the toxicity and the therapeutic effect is challenging and has warranted efforts in therapeutic drug monitoring.[21] Cytotoxic agents also pose a concern for the rapid onset of resistance. However, combination therapy has made headway in mitigating or slowing down resistance by targeting more than one pathway.[9]

Stability and solubility of anti-tumor agents can impact efficacy and delivery. For example, paclitaxel, a cytotoxic hydrophobic small molecule, must be solubilized in harsh solvents prior to administration. The solvent-based system causes hypersensitivity reactions, toxicity, non-linear pharmacokinetics, and requires special medical tubing for administration.[22,23] Stability of the therapeutic in vivo is crucial in mediating a therapeutic response. Prodrugs (like TMZ) are inactive forms of therapeutic agents, but upon administration, they are transformed into active metabolites.[24] This improves the stability and selectivity, but only addresses one aspect of the challenges.[25] Another aspect of stability is the half-life of the molecule when administered. It is not uncommon for therapeutics to be administered frequently to achieve therapeutic levels, but this is met with lower patient compliance and toxicity.[26,27]

The obstacles mentioned above only represent a few of the challenges that have limited the translation of therapeutics to the clinic. While there are some strategies to overcome these issues (i.e. prodrugs for stability), developing anti-tumor agents for systemic delivery to glioma will require a solution that addresses more than one of the challenges. One method is through nanoparticle-mediated delivery.

1.1.3 Nanoparticles to overcome current limitations

Nanoparticles (NPs) are attractive drug delivery platforms as they enable sustained release, longer circulation times, spatiotemporal release, active targeting, stability, and facilitate tuning of their pharmacokinetic parameters. These properties are a result of engineered properties such as the size, shape, charge, composition, surface conjugation or coating, and encapsulated cargo as shown below in **Figure 1-1**.

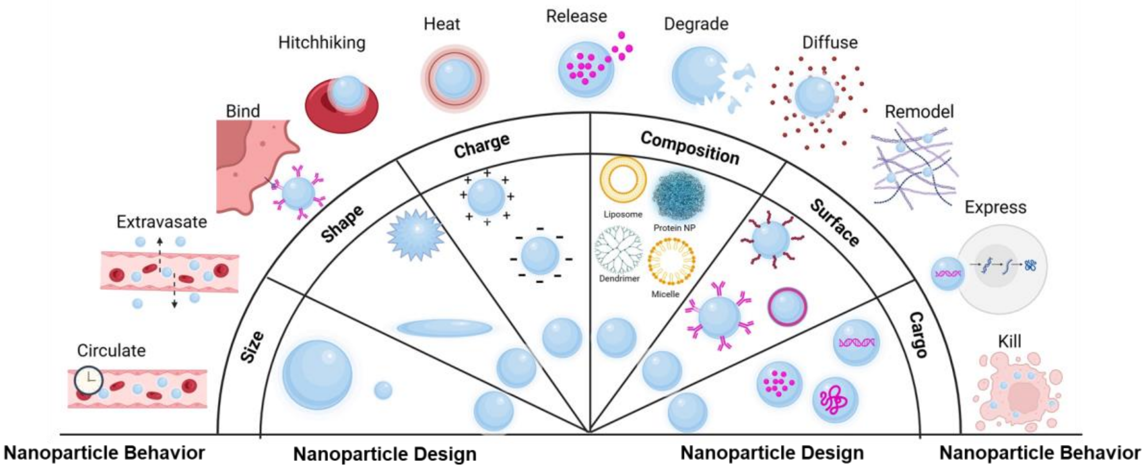

Figure 1-1. Nanoparticle design (size, shape, charge, composition, surface, cargo) impacts behavior (circulation, extravasation, binding, hitchhiking, heat, release, degradation, diffusion, remodeling, expression, and cytotoxicity). This Figure was reproduced with modification with permission from Hauert S. et al.[28] (Copyright Elsevier Publishers). Made with Biorender.com.

However, despite decades of research efforts to leverage these favorable properties of NPs, they have ultimately fallen short, especially in the context of gliomas. In the last decade, literature showed only 0.8% (median) of administered NPs reach the solid brain tumor.[29] The few FDA approved nano-formulations (i.e. Doxil and Abraxane) are effective in decreasing the toxicological profile of drugs in patients but do not significantly improve the therapeutic index.[29] In addition, these nanotherapeutics are not approved for glioma treatment due to the inability to penetrate the BBB and poor in vivo stability. To improve the delivery efficiency, a few strategies have been employed including creating different entry pathways to improve penetration depth, investigating materials with stealth properties, and developing multi-functional NPs. Of note is the rise of protein-based nanoparticles. Such carriers are idea because of their favorable properties: biodegradable, low immunogenicity, serum stability, metabolizable, favorable in vivo clearance profiles, and high modularity for drug attachment and various surface modifications.[30–32] In the next section, protein nanoparticles will be discussed further in terms of the motivation, fabrication methods, and their relevance as a therapeutic.

1.2 Protein Nanoparticles

1.2.1 Motivation

Proteins are central to biological function.[33,34] They are macromolecular molecules involved in a myriad of biological functions ranging from DNA repair, catalysis of metabolic reactions or cell signaling. To fully appreciate the specificity and efficiency with which proteins operate, their hierarchal structure and their interactions in biological environments must be considered. The primary structure, i.e., the sequence with which the 20 natural amino acids are lined up via peptide bonds, encodes a unique bar code that characteristically identifies each protein.[35] The secondary structure relates to conformational motifs such as alpha helices, beta sheets and conformational turns of the amino acid chains. A tertiary structure of the protein emerges from longer-range intramolecular interactions involving disulfide bridges, hydrogen bonding, or van der Waals, hydrophobic, and electrostatic interactions, whereas its quaternary structure further considers intermolecular interactions. To emphasize how impactful even minute changes in a protein's composition can be, consider sickle cell anemia.[36] Hemoglobin, the protein contained in red blood cells, has a quaternary structure that includes two alpha and two beta chains. A single base substitution of the more apolar valine instead of glutamic acid promotes hydrophobic interactions with an adjacent beta chain and ultimately alters the shape of the cell.[36] This change in structure increases the rigidity of the membrane and blocks effective transport through capillaries of the body.

In the last 20 years, the number of known protein structures have increased by 10 times with over 170,000 structures available in 2021 according to the Protein Data Bank.[37] The increased rate with which these proteins are discovered resulted in an improved mechanistic understanding of how proteins interact with each other, and their biological environments. A particular hotspot of contemporary research is the development of protein therapeutics.[33,34] As therapeutic agents, proteins leverage several properties such as specificity, environmental tolerance, recombinant production,[38] and, at least in the case of human proteins, may benefit from faster regulatory approval processes.[33] Not only protein conjugates, monoclonal antibodies, or enzymes, but also protein nanoparticles (PNPs) feature these characteristics.[39] PNPs can exhibit characteristics from both proteins like inherent function, specificity, high degree of modification flexibility while leveraging the advantages of nanoparticles: controlled release, improved bioavailability, and stability.

While PNPs have not been as extensively researched compared to other nanoparticle platforms, the idea of using proteins as cargo carriers is not new. The epitome of an ideal nanoparticle is a natural virus; viruses are structurally ordered, possess precise surface topologies, and can release cargo through controlled mechanisms all of which was established through evolution.[40,41] Consequently, this has enabled viruses to overcome biological barriers, achieve high levels of specificity for targeted host cells, and even evade immunological responses. Using viruses as inspiration for drug delivery vehicles, engineered viral vectors like lentiviruses, adenoviruses and adeno-associated viruses have found applications in gene therapy ranging from cancer to infectious and inflammatory diseases.[42] Furthermore, drawing on inspiration from both viral vectors and nanoparticles, virus-like particles (VLPs) have emerged as another type of protein nanoparticle. They are devoid of all genetic material, and are self-assembled through viral proteins and represent a safer version of the viral vectors.[43] Outside of viral vectors and VLPs, protein nanoparticles can take a third, more modular form: engineered protein nanoparticles. Engineered PNPs have advantages over viral vectors such as lower immunological responses and may address concerns of production when compared to VLPs. These engineered PNPs can be produced from a various sources of proteins (from plant to serum) and has been exploited in various applications ranging from biotechnology to food industries.[44–51]

The ability to produce these PNPs for the range of applications is because of the advantages including versatility, conjugation capabilities, biodegradability, availability and affordability and relatively low immunogenicity.

(i) Versatility: The range of available proteins that can be used for PNPs is vast, providing unprecedented versatility of PNPs, yet, the design space goes beyond natural proteins, as recombinant protein technologies have been effectively used. The design space for proteins is almost unlimited. For a 200-residue protein, 20^{200} possible amino-acid sequences exist, yet only a small subset has been sampled by evolutionary processes.[52]

(ii) Conjugation capabilities: The type of amino acids and their side chain within the primary structure of proteins offer a variety of binding sites that can be exploited for subsequent conjugation or surface modification of PNPs.[53,54] Proteins have been used for covalent incorporation of dyes, hydrophobic drugs, or other active ingredients.[45,55–57] Apart from chemically conjugating to functional groups, the ligand-binding properties of proteins can utilized for surface modification. For example, it was shown that both BSA PNPs bound to immobilized anti-BSA polyclonal antibodies and PNPs made from monoclonal antibodies against hepatitis B virus S antigen demonstrated specific binding to the corresponding antigen.[58] The distinct binding sites of proteins are also widely exploited in antibody purification strategies.[59] Specifically, PNPs were incorporated into affinity precipitation techniques, that combine the high selectivity of an affinity ligand with advantages of precipitation technologies.[59,60]

(iii) Biodegradability: Compared to conventional synthetic nanoparticles, like polymer-based nanoparticles, another crucial property defining PNPs is the fact that their constituents can be cleaved by proteolytic enzymes. For example, Langer et al. studied the enzymatic degradation of human serum albumin (HSA) nanoparticles.[61] Both, intestinal and gastric enzymes effectively degraded HSA PNPs that were crosslinked with glutaraldehyde.[61] The degradation kinetics were shown to be dependent on the degree of crosslinking with highly crosslinked PNPs requiring longer time for degradation. In addition to intestinal and gastric enzymes, the intracellular enzyme cathepsin B was also able to degrade crosslinked HSA PNPs, suggesting the degradability of PNPs after cell uptake.[61]

(iv) Availability and affordability: PNPs based on soy proteins, for example, are abundant, low-cost, and renewable, with increasing industrial interest in food applications.[62–65] Soy PNPs further contain protected polyunsaturated fatty acids. Similarly, rice bran oil-based soy PNPs are used in soy yogurts to promote antiradical scavenging.[66] In another food-related application, PNPs are used as emulsifiers to stabilize food dispersions.[67] As an example, cereal protein-based nanoparticles, mainly made from wheat gliadin and maize zein proteins, have gained broader attention as stabilizers of air-water or oil-water interfaces.[67]

(v) Immunogenicity: Proteins of human origin, such as HSA or lipoproteins are particularly well-suited for applications where low immunogenicity is required.[68] The immunogenicity of biopharmaceutical protein formulations is an important area of research and relies on combinations of multiple methods such as in silico modeling, cell culture tests, and animal studies.[69] In addition to size, composition, and dose, critical attributes that impact the immunogenicity of a protein include its primary amino acid sequence, chemical degradability, and its propensity for misfolding.[70,71] However, in general, there is a need for better predictive tools that can account for the heterogeneity of patients and treatments to advance the understanding between PNP properties and potential immunogenicity.[69,70]

1.2.2 Fabrication Methods

The high degree of flexibility of engineering PNPs is underscored by the range of possible proteins that can be used as well as the technologies in place to produce them. In this thesis, two methods are used: Nanoparticle albumin bound (Nab) Technology and Electrohydrodynamic (co) jetting. As such, these two methods will be described thoroughly. However, other methods such as emulsification, desolvation, self-assembly, nanospray drying will be described briefly.

1.2.2.1 Nanoparticle albumin bound (Nab) Technology

The Nab process produces albumin nanoparticles capable of encapsulating hydrophobic drugs through a combination of high shear, cavitation, and pressure. High pressure homogenizers force water insoluble or partially soluble drugs into the albumin solution. Although other proteins have been considered, albumin is the ideal candidate due to its 35 cysteine residues -34 are occupied through disulfide linkages and only one Cys residue features a free sulfhydryl group (Cys34).[72] When the crude mixture (albumin, hydrophobic drug, and solvent) is introduced to high shear conditions, the disulfide bridges are disrupted, and under further involvement of Cys34 are reshuffled into new disulfide bonds. If needed, chemical modification can be employed to introduce additional Cys residues.

The nab technology has been successfully applied to a range of small-molecule drugs. Among the most successful are taxanes, such as paclitaxel and docetaxel. Taxanes represent a particularly important class of antineoplastic drugs which work by stabilizing microtubules and preventing proliferation. Traditional methods for delivering these agents require solubilization in surfactants to improve their bioavailability and solubility, but also introduce adverse side effects and cumbersome treatment regimens. For the solvent-based delivery of paclitaxel for example, mixtures of Cremophor EL (CrEL) and ethanol must be prepared. This procedure is associated with a range of detrimental effects, such as the fact that CrEL can cause leaching of plasticizers from medical-grade polyvinyl chloride tubing sets and elevates hepatic toxicities.[23] Further, CrEL is known to cause hypersensitivity reactions.[73,74] Outside of toxicities and administration issues, the conventional CrEL delivery displays non-linear pharmacokinetics in the case of paclitaxel which has been attributed to the formation of CrEL micelles, which entrap paclitaxel and reduce the amount of free drug available.[75]

In 2005, American Bioscience Inc. developed nanoparticle albumin bound (Nab) paclitaxel, one of the very first nanomedicines that has subsequently been approved by the FDA and commercialized under the tradename Abraxane for the treatment of metastatic breast cancer. These PNPs are formed by high shear in a high-pressure homogenizer optimized to form ~130 nm sized paclitaxel loaded albumin nanoparticles.

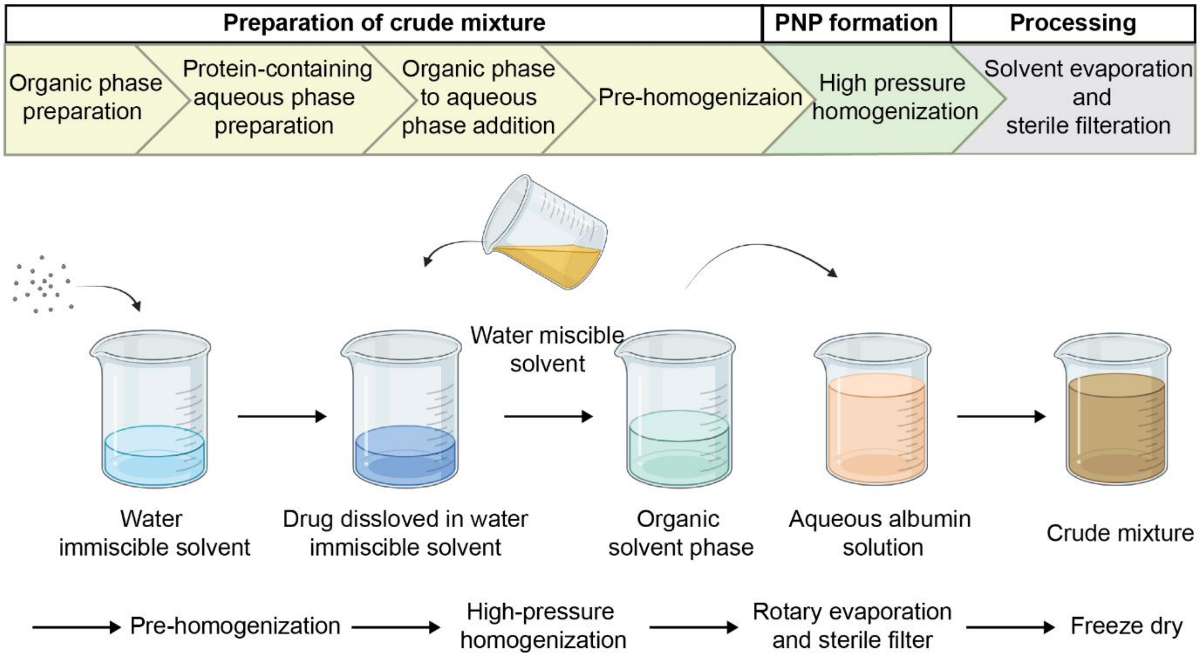

Figure 1-2. Workflow illustration of nanoparticle albumin bound (Nab) technology. Reproduced with permission. [32]

Figure 1-2 depicts the main steps of the Nab technology. The albumin PNPs are produced by first dissolving the paclitaxel in a water immiscible organic solvent (<5% solubility in water) to obtain an "oily phase".[76] A water miscible organic solvent (>10% solubility in water) is added to create the organic phase mixture.[76] This organic phase mixture is reconstituted into an emulsion comprised of an aqueous protein phase and an organic phase[76] Unlike in direct emulsification, the use of external surfactants is not necessary during nab technology. This crude mixture is first subjected to an initial, pre-homogenization then added to a high-pressure homogenizer where it experiences high local shear, cavitation, and local heating thereby forming new intermolecular crosslinks within the protein.[76] The remaining solvent is removed and the <200 nm PNPs are isolated by filtration.

Exploiting albumin’s ability to naturally sequester hydrophobic molecules enables Nab-paclitaxel formulations to simultaneously overcome several drawbacks associated with the traditional methods.[45] Unsurprisingly, Abraxane was also FDA approved for first line treatment of advanced non-small cell lung cancer and late-stage pancreatic cancer in 2012 and 2013, respectively. More recently (2019), Abraxane in combination with Tecentriq (a PD-L1 inhibitor) was approved for advanced triple negative breast cancer expressing PD-L1. In a recent meta-analysis of clinical trials into metastatic breast cancer, Nab paclitaxel was significantly better than conventional approaches in overall response rate, disease control rate, progression-free survival, and overall survival with the adverse events and dose discontinuation rate being comparable between both methods.[77] Abraxane is continuously expanded to other cancers, particularly as a combination therapy, to augment current treatments or as a maintenance treatment.[78–80] According to clinicaltrials.gov, 302 clinical trials have been completed with using the search key of Nab paclitaxel or Abraxane. There are 135 active clinical trials with Nab paclitaxel and 266 studies that are being recruited.

Although other instruments can induce high shear and cavitation, high pressure homogenization remains the method of choice. High pressure homogenizers (HPHs) work by passing the initial material through one small orifice (one stage) or two small orifices (two stage) under high pressure (typically 10-500 MPa) and thereby facilitating size reduction through a combination of shear, cavitation and turbulence.[81] Both the pressure and number of cycles in HPHs have been studied as important parameters affecting particle size.[81] In addition to the homogenization parameters, other parameters including the choice of organic solvent to solubilize the therapeutic agent, the ratio of drug solution to aqueous HSA solution, and concentration of the drug have shown to influence the size and its distribution.[82] Furedi et al. found when optimizing a voriconazole-loaded albumin nanoparticle, increasing the cycles to 6 or above resulted a stable polydispersity index.[82]

Since the development of Abraxane, others have prepared PNPs though high-pressure homogenization encapsulate therapeutics to reduce toxicity associated with traditional delivery, improve bioavailability, and/or alter the pharmacokinetics. While many are interested in delivering active agents as shown in **Table 1-1**, stimuli responsive drugs like photosensitizers for photodynamic therapy can also be incorporated.

Table 1-1. Studies of Nab-technology produced nanomedicines.

Application	Protein	Drug/loaded entity	Cycles	Pressure (MPa)	Solvent	Size (nm)	Refs.
Anti-fungal treatment	Albumin	Voriconazole	6	~179	Chloroform	35-85	82
Idiopathic pulmonary fibrosis	Albumin	Tacrolimus	9	138	Chloroform and ethanol	182.1±28.5	83
Pancreatic cancer	Albumin	Gemcitabine	9	138	Chloroform	150±27	84
Colon cancer, pancreatic carcinoma	Albumin	Curcumin	9	138	Chloroform	130-150	85
Non-small cell lung cancer	Bovine serum albumin	Curcumin	9	138	9:1 Chloroform: Ethanol	128.3 ± 3.0	86
		Curcumin and doxorubicin				134.0 ± 14.7	
		Doxorubicin				131.80 ± 8.4	

Specifically, Temoporfin (mTHPC), a photosensitizer, was incorporated into the Nab system to mitigate prolonged infusion rates and adverse side effects with the commercially available Foscan, which is formulated with ethanol and propylene glycol.[87]

In summary, Nab technology is a fabrication method for albumin nanoparticles encapsulating hydrophobic drugs through a combination of high shear, cavitation, and pressure. Nab technology is the first commercialized nanomedicine (Abraxane) after FDA approvement in 2005. One of advantages of Nab technology is a delivery of hydrophobic drugs without incorporating harmful solubilizers such as CrEL. Nab technology overlaps with some aspects of the emulsification procedure, as it can be thought of as a contemporary emulsification approach, with the difference that the Nab technology does not require external crosslinking to ensure stability, the use of surfactants is not necessary, and there are more degrees of control within the process.[88] Potential drawbacks of this technique include limitations on the stabilizing agents if they do not naturally contain or cannot be chemically modified to have sulfhydryl and/or disulfide groups. However, it cannot be overlooked that this method has enjoyed broad translational successes.

1.2.2.2 Electrohydrodynamic (co) jetting

Electrohydrodynamic (co) jetting is a variation of electrospraying. During atomization via electrosprays, electrical potential differences of several kilovolts are employed to disperse a fine mist of nanodroplets.[89,90] The solution at the tip of the capillary experiences the electric field causing positive ions to accumulate at the liquid surface. Electric shear stresses distort the meniscus to establish a Taylor cone.[90–92] With increasing the voltage, the repulsive electrostatic forces overcome the surface tension, and the jet breaks up into small droplets.[89,90,92] The highly charged nanodroplets travel towards the grounded collection plate. During this process, the solvent is rapidly evaporated and the remaining non-volatile compounds are solidified into micro- or nanoparticles.[90,92]

EHD co-jetting, has been used to prepare more complex particles including multicompartmental micro- and nanoparticles with various applications in drug delivery.[93,94,103–106,95–102] EHD co-jetting utilizes two or more needles as capillaries in a side-by-side configuration. The input solutions are pumped into the needles at a flow rate forming laminar flow to ensure a stable interface between the jetting solutions. Once a droplet forms out of the needle, an electric field is applied to the system that distorts the meniscus into a Taylor cone and forms an electrified polymer jet. This jet breaks up into a spray of fine, charged droplets that undergo rapid solvent evaporation and subsequent solidification of nonvolatile components. Due to rapid solvent evaporation, the initial flow-determined geometry of the input solutions is preserved in the fabricated nanoparticles giving access to particle architectures that would be otherwise impossible or hard to achieve.

The size of the nanoparticles is tunable by changing the EHD jetting parameters that are either jetting solutions-related (surface tension, dielectric constant, viscosity, polymer concentration, and molecular weight), process-related (fluid flow rates, the distance between the needle and a counter electrode, the electric voltage, and the capillaries diameter) or environment-related (temperature, pressure, and humidity).[107]

This technology has been extended to an adaptable synthetic PNPs fabrication method based on reactive electrojetting and has shown to retain the native structure of the protein.[108–113] The jetting solutions include a dilute solution of proteins and reactive macromers, which will react together during and after the electrospraying process to stabilize the fabricated PNPs.[112] Proteins (transferrin, insulin, hemoglobin, lysozyme, albumin) with various crosslinking strategies were investigated to evaluate the feasibility of the EHD jetting system to produce stable PNPs.[112] More recently, a systematic study of PNPs was performed to further understand how formulations can impact the morphology of PNPs.[114]PNPs were formed from proteins (hemoglobin, transferrin, mucin, insulin, albumin) and compared with blends with albumin. As shown in **Figure 1-3**A, the

PNPs were stabilized with the polyethylene glycol (PEG)-based macromer, O,O′-bis[2-(N-succinimidyl-succinylamino)ethyl]polyethylene glycol (PEG-NHS).[114] The EHD jetted PNPs were imaged (**Figure 1-3**B-I) and analyzed. The sizes of single-protein PNPs revealed a size trend of transferrin>albumin>mucin~hemoglobin>insulin, with insulin having the smallest size.[114] The polydispersity was similar between groups ranging from 0.11 to 0.19 as well as circularity (0.82 to 0.85).[114] Blends of the proteins (insulin, hemoglobin, transferrin, mucin) with albumin (**Figure 1-3**F-I) showed the following size trend from largest to smallest: mucin/albumin, insulin/albumin, transferrin/albumin, hemoglobin/albumin. The dry-state PNP sizes (singular proteins and blends) ranged from 51 nm to 81 nm with only ~30 nm difference in average size. However, once the PNPs were collected and in solution, the range was 215 nm. Therefore, the EHD jetting formulation of these proteins had little influence of the as-jetted, or dry state of these PNPs, but more pronounced differences were observed once in solution. This highlights the importance of analyzing protein formulations, particularly their behavior in solutions.

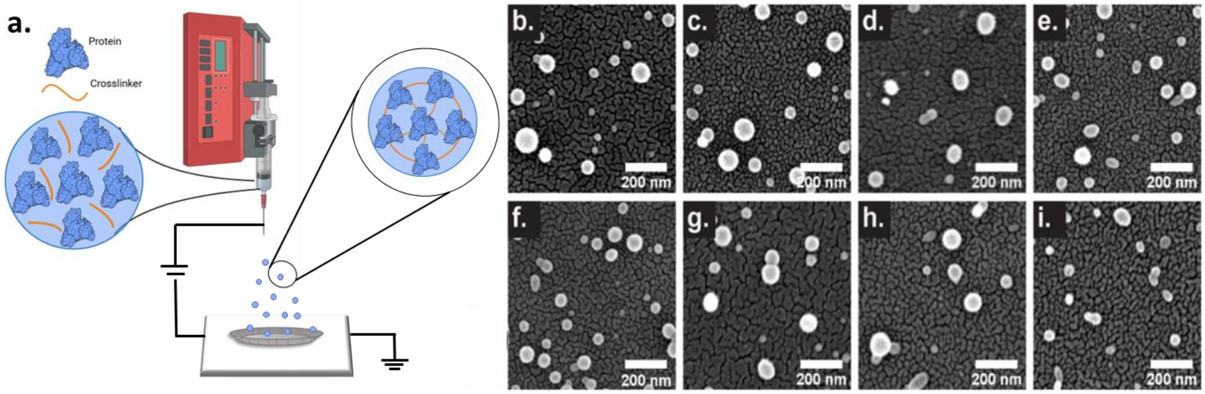

Figure 1-3. A. EHD jetting of protein and macromer form crosslinked protein nanoparticles. B-I. SEM images of single protein and blended PNPs. B. Hemoglobin/albumin PNP. C. Transferrin/albumin PNP. D. Mucin/albumin PNP. E. Insulin/albumin PNP. F. Hemoglobin PNP. G. Transferrin PNP. H. Mucin PNP. I. Insulin PNP. Scale bar = 200 nm. Reproduced with modification.[114]

One potential consideration related to the appropriate applications of electrospraying is the limited throughput of the system. The reliance on parallel capillaries to produce a multifluidic interface contributes to the low particle fabrication yield of this technique; therefore, a needleless EHD co-jetting setup was designed to scale this process.[115] In this platform a stable extended fluid interface was achieved by using a designed plate, where two different fluids were pumped to flow on each side of the plate and combine at the edge (the outlet of a microchannel). By applying a high electric field, multiple distinct Taylor cones were formed spontaneously along the fluid interface at the device outlet, resulting in about 5-fold higher production rate of bicompartmental PNPs.[115]

Electrospraying is a modular atomization technique capable of producing micro- and nanoparticles for applications spanning from food to drug delivery. This technique has several merits including the retainment of biological activity and structure of proteins after fabrication, the tunability of process parameters, capability to load a myriad of therapeutic agents, and the ability to produce compartmentalized nanoparticles leading to more tunable features. However, low throughput is an underlying demerit encountered in electrospraying. Efforts are currently being made to scale the process by adopting a needless electrospraying technique.

1.2.2.3 Other PNP Fabrication Methods

Outside of Nab Technology and EHD (co) jetting, other fabrication methods exist including emulsification, desolvation, nanospray drying, and self-assembly. Because these methods are outside the scope of this thesis, they will only be summarized. More detailed information about these methods can be found elsewhere. [30,116]

To produce PNPs via emulsification, water in oil (W/O) methods are exclusively used. Briefly, the immiscible solution is exposed to low-speed homogenization and added dropwise to an oil phase. Because the continuous phase (oil) is thermodynamically unstable, it requires additional molecules to reduce the surface energy of the interface. Surface reducing agents such as surfactants (or emulsifiers) are critical to lower the interfacial energy between the phases, which are susceptible to coalescence. The surfactant acts as a barrier and the formation of nanoparticles occurs. Thereafter, chemical crosslinking or heat denaturation is employed to maintain the PNP structure. Beyond water-in-oil emulsification, there has not been substantial progress with producing PNPs. This can be attributed to a few reasons. The first is that proteins themselves act as emulsifiers because of their amphiphilic nature. They are such effective stabilizers, PNPs themselves are routinely used in applications like food to stabilize the water and oil interface in Pickering emulsions where droplets are susceptible to coalescence.[117–119] Therefore, the role of proteins in emulsification is better suited as a component of the process than the desired product. Secondly, the other PNP fabrication methods are better suited for nanomedicine applications as they have a higher degree of flexibility.

Desolvation is one of the more frequently used fabrication methods to produce PNPs.[30,120] Nanoparticle fabrication relies on precipitation in the presence of a desolvating agents, i.e., a poor solvent, to reduce the protein's water-solubility to induce aggregation.[30] Exposure to a desolvating agent induces conformational changes in the protein and decreases its overall solubility.[30] Once a threshold is reached, the protein undergoes phase segregation and precipitates in the form of PNPs.[30,120,121] However, PNPs still can lack permanent stability and can rapidly undergo redissolution, requiring the need for crosslinking.[120] Owing to its simplicity, scalability, and low fabrication costs, desolvation methods are frequently employed for PNP production.[122] Despite this, it requires the use of organic solvents and/or crosslinking strategies that alter the protein's native structure and therefore can lead to a loss of function and increased immunogenicity.[122,123]

Spray drying is a well-established process commonly used in the pharmaceutical, chemical, and food industries to produce dry powder from a liquid phase in a one-step continuous process.[124] This technique is comprised of a four-stage setup: (i) atomization of the input solution into a spray, (ii) spray-air (hot drying gas) contact, (iii) drying of the spray, and (iv) separation of the dried final product from the drying gas.[124,125] The particle properties can be tuned by manipulation of the process parameters and are impacted by the particular spray dryer configuration. Overall, various industries employ nanospray drying as it is a relatively streamlined, hands-off method to produce solid protein-nanoparticles from an initial aqueous formulation input. This technique relies on the spray dryer, which has witnessed a few generations of improvement to obtain smaller, monodisperse particle populations and higher throughput. Aside from this technique requiring less user involvement than others, it has also shown that the design space for improvements to the spray dryer instrumentation continues to be improved upon, suggesting potential growth of this method. Since there are limited studies using this method to fabricate PNPs along with recent improvements to the instrumentation, it is difficult to assess how it will fare when compared to the other methods. Its success will likely depend on whether this technique can produce particles with characteristics competitive with the other methods to warrant its use. For example, most nanomedicines are smaller than 460 nm, so if size cannot be changed, it may render this technique less useful for PNP fabrication.

Lastly, PNPs can be spontaneously fabricated via self-assembly of natural, modified, or de novo proteins. The underlying principle is based on complex protein-protein interactions which can be distinguished from other fabrication methods. Resulting PNPs are highly conserved protein clusters, behaving site-specific, orientational dependent, ordered, and monodisperse. However, the system strongly relies on computational assistance for atomic-scale accuracy. [52,126,127] One of concerns would be immunogenicity of self-assembled PNPs since the building block proteins are mostly mutated or de novo designed except for natural PNPs. Also, stability of self-assembled PNPs in blood stream where complicated intermolecular interactions may interfere with the self-assembly remains an unanswered question. Despite of these concerns, the atomic-scale accuracy and unlimited protein design space make this approach unique and promising for nanoparticle-based delivery system.

1.2.2.4 Summary and comparison of PNP fabrication methods

The main PNP production methods are Nab Technology, EHD (co) jetting, emulsification, desolvation, nanospray drying, and self-assembly. Each of these have its own merits and demerits as shown in **Table 1-2**. While emulsification is commonly used in the development of polymeric nanoparticles, it appears to be limited for PNP applications due to the competitive nature between protein and external surfactants acting as the emulsifier. Nanospray drying is constricted by the configuration and design of the device to produce PNPs at a sufficiently small size for therapeutic applications. Desolvation is a popular PNP fabrication technique but raises concerns for maintaining the native structure and function of the protein leading to immunogenicity and toxicities. Self-assembly, nab technology and EHD (co) jetting are likely to be the leading methods of PNP production. Nab technology and self-assembly leverage the protein’s inherent structure to form PNPs, which gives it an advantage over other methods. EHD (co) jetting provides a large design space to produce defined PNPs and preserve the protein’s structure.

Table 1-2. Comparison of protein-based nanoparticle synthesis methods.

Technique	Merits	Demerits	Critical parameters affecting nanoparticle size	Refs.

Emulsification	• Only requires typical laboratory equipment	• Relatively large nanoparticles • Low loading • Release of drug is difficult to control • Removal of surfactant and oil	• Concentration • Emulsification time • Emulsifier • Ratio of aqueous to non-aqueous solutions • pH of aqueous solutions	[128,129]
Nab-technology	• No external crosslinking methods needed • Entrapment of hydrophobic drugs	• Relies on presence of sulfhydryl and/or disulfide groups for crosslinking	• Choice of organic solvent • Concentration of drug • Ratio of drug to protein solutions • Concentration of protein • Number of cycles of the HPH • Pressure of HPH	[81,130]
Desolvation	• High yield • Easy to manufacture • Low cost • Narrow dispersity of PNPs	• Possible protein denaturation leading to loss of function	• Desolvating agent amount • pH of protein solution • Desolvating agent dielectric constant • Desolvating agent addition mode	[122,123,131–133]
EHD	• Narrow dispersity of PNPs • Retainment of secondary structure • Multicompartment PNPs • Ability to entrap both hydrophobic and hydrophilic drugs • PNPs in dry state (avoiding degradation or undesired payload release)	• Low throughput • Molecular weight dependent • Lack of spatial control of payload	• Protein concentration • Solvent dielectric constant • Macromer to protein ratio • Crosslinker properties	[111–113,115]
Self-assembly	• Monodisperse particles • Unlimited geometry of PNP • Unlimited monomeric peptide design space	• Hinges upon computational calculations • Low yield • Unavailable for existing native proteins	• Protein concentration • Monomeric peptide design	[52,126,141,142,127,134–140]

1.2.3 Protein nanoparticles in glioma nanomedicine

The application of nanoparticles in the field of medicine, or more specifically, the use of nanotechnology to diagnose, prevent and treat diseases, is referred to as nanomedicine. Nanomedicine largely seeks to improve patient outcomes by addressing limitations associated with current drugs formulations, especially poor bioavailability. Other potential advantages exist that are responsible for the traction it has received; nanoparticles can alter solubility, stability, and bioavailability of various types of therapeutics including hydrophobic or hydrophilic small molecules, peptides, and nucleic acids.[34,143–147] Additionally, blood circulation half-life and tissue targeting can be augmented by decorating nanoparticles with stealth moieties or targeting ligands.[148] The release of encapsulated drugs can be precisely tuned to maintain the drug concentration within its therapeutic window over a prolonged period of time.[149] Despite the impressive progress made in the field of nanomedicine with clear evidence of early successes,[150] broad clinical translation of novel nanoparticle platforms is still limited due to a series of bottlenecks.[151] Nanoparticles suffer from rapid clearance from circulation, accumulation in the liver, inefficient permeation across the endothelium into target tissues and overall inefficient delivery to target cells.[152] One promising approach is the use of proteins as structural components in nanoparticle-based drug delivery systems.[151] Protein-based nanomedicine is founded on the premise to explore the endogenous properties of proteins to design carrier systems with improved drug delivery profiles. The advantages of PNPs can be delineated by dissecting the individual components of PNP: nanoparticles and proteins. In **Figure 1-4**, the benefits of nanoparticles and proteins for drug delivery are listed. The intersection between these are the benefits of PNPs in nanomedicine. The use of PNPs for glioma nanomedicine has been explored especially with albumin and transferrin.

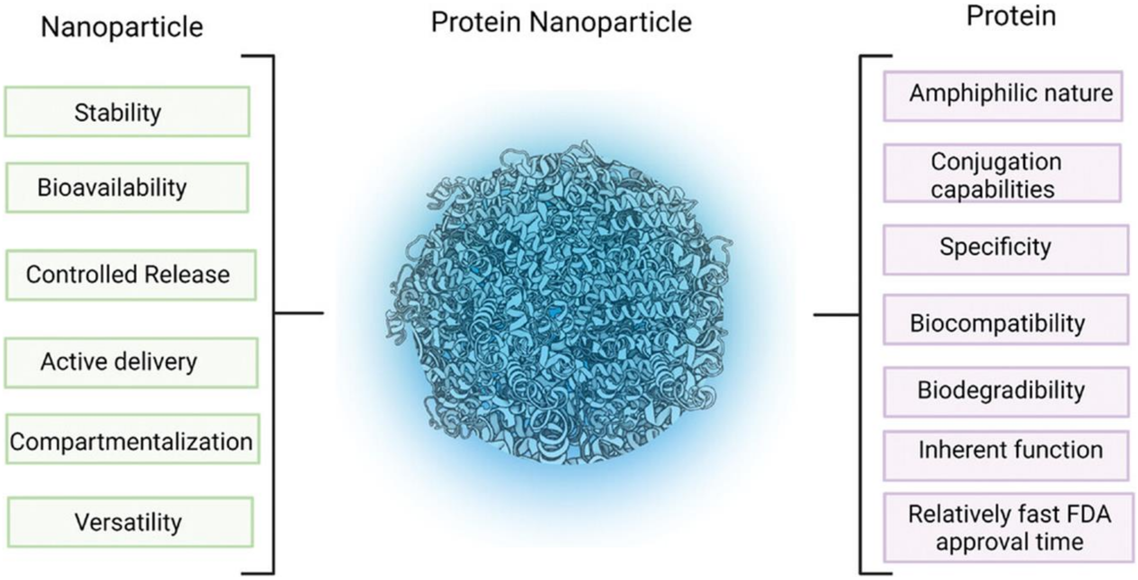

Figure 1-4. Protein nanoparticles combine the benefits of nanoparticles (stability, bioavailability, controlled release, active delivery, compartmentalization, versatility) with those of proteins (amphiphilicity, conjugation capabilities, specificity, biocompatibility, biodegradability, inherent function, and relatively fast FDA approval time).[32]

1.2.3.1 Transferrin Nanoparticles

Transferrin is responsible for the transportation of iron throughout the body.[153] When iron binds to the transferrin, it undergoes a conformational change that allows it to specifically recognize transferrin receptors highly expressed in immature erythroid cells, placental tissue, and rapidly dividing cells.[154] It then becomes internalized through the transferrin-mediated transcytosis pathway and the bound iron is released due to a change in endosomal pH.[155] This transcytosis pathway has been of interest to facilitate transport of therapeutics across biological barriers like the blood brain barrier and to achieve targeting to cells, especially malignant cells for cancer applications.[156–158] In gliomas, transferrin receptor 2 expression is correlated with more aggressive phenotypes and has thus been exploited for glioma targeting.[159] Functionalized nanoparticles with antibodies or the protein represent the majority of reports exploiting transferrin-mediated targeting, with the minority being completely constructed of transferrin.[160–165] While there are promising reports of transferrin being used as a carrier and targeting material, there are concerns with the preservation of targeting capabilities once in vivo.[166,167] Specifically, it has been reported that the formation of biomolecular coronas around transferrin-functionalized nanoparticles can render the targeting properties inactive.[168]

1.2.3.2 Albumin Nanoparticles

Arguably the most important protein to be used as a protein carrier with intrinsic function is albumin. HSA, the most abundant plasma protein, is responsible for the circulation of hydrophobic nutrients and hormones throughout the body and represents the gold standard in protein for nanomedicine technology.[169] Its popularity as a carrier can be attributed to several characteristics. The first is stability; HSA is stable at a pH range between 4 and 9 and at temperatures as high as 60 °C for up to 10 hours.[170] Second, albumin has a few transport benefits; (i) it can bind to cell-surface receptors such as glycoprotein 60 and mediate endothelium transcytosis,[171] (ii) it may cross mucosal barriers through receptor mediated transcytosis by engaging with receptors such as the neonatal Fc receptor,[172] and (iii) transportation and accumulation to tumors and inflamed tissues are preferential.[121,173] As an example of leveraging targeting, albumin nanoparticles targeted glioblastoma tumors through the overexpression of albumin-binding proteins on the tumor vessel endothelium: secreted protein acidic and rich in cysteine (SPARC) and glycoprotein 60.[111] Like transferrin PNPs, it is more commonly employed to conjugate the nanoparticles with the protein as opposed to completely constructing the particle from the protein.[111,174–178] This is probably for two reasons. First, there is more familiarity with other polymeric nanoparticles amongst researchers in the nanotechnology field. Secondly, the retainment of the protein's function could be compromised by the fabrication method, which limits the methods available to researchers.

1.3 Objectives

The main objective of this thesis is to expand the use of Synthetic Protein Nanoparticles (SPNPs) produced via EHD (co)-jetting to encapsulate different therapeutics for the treatment of glioma. Prior to this thesis, the exploitation of SPNPs for glioma therapy was limited to the publication by Gregory et al.[111] While these results are impactful, it only scratches the surface of the possible SPNPs that could be used for glioma treatment for two reasons. Firstly, this is only one type of glioma. As discussed earlier in **Chapter 1**, there are categories of gliomas which may find SPNP therapy beneficial. Secondly, a siRNA against STAT3i was used, which only represents one class of therapeutics (siRNAs) against one target (i.e. STAT3) out of many possible targets. In this thesis, I describe the exploration of other therapeutic moieties to be loaded into the SPNPs for glioma, which are outlined in the following aims.

Aim 1: Develop the framework for hydrophobic small molecule loaded SPNPs using paclitaxel and assess the efficacy in glioblastoma. Hydrophobic small molecules represent an important class of therapeutics in oncology. However, the delivery of these to the brain for glioma treatment is virtually impossible with the presence of the blood-brain barrier, which excludes most small molecules. The use of nanoparticles to encapsulate such molecules has been investigated extensively; however, not in SPNPs. EHD jetting to incorporate hydrophobic small molecules is challenging as it must balance the solubilization of the molecule, have a high enough loading, must not denature the protein, and must also be "jettable". **Chapter 2** describes how SPNPs can be fabricated to encapsulate paclitaxel, a hydrophobic small molecule. We demonstrate that high pressure homogenizing the paclitaxel with the albumin prior to EHD imparts ideal SPNP characteristics and can elicit a cytotoxic effect in glioma cells. Therefore, this work lays the foundation for SPNPs to deliver hydrophobic small molecules in glioma therapy.

Aim 2: Engineer dual-loaded, multi-functional SPNPs for the delivery of paclitaxel and STAT3 siRNA in glioblastoma. Monotherapies have presented challenges of acquired resistance[179,180]. Therefore, NP combination therapy has emerged in effort to overcome resistance, promote synergism to improve the therapeutic index, unify two drugs' pharmacokinetics and reduce toxicity while maintaining the benefits from NPs[181,182]. Bi-compartmental NPs can leverage existing advantages of NP delivery while enabling fine tuning of the individual compartments. Furthermore, by segregating the compartments, drug interactions are minimized, and differing solubilities (i.e. hydrophobic versus hydrophilic drugs) of drugs is not a concern. This work takes advantage of the EHD co-jetting system to produce bi-compartmental SPNPs to encapsulate STAT3 siRNA and paclitaxel for high grade glioma.

Aim 3: Expand upon siRNA delivery with synthetic protein nanoparticles to evaluate the therapeutic efficacy in grade II mutant IDH1 astrocytoma to restore sensitivity to ionizing radiation. Grade II mutant IDH1 astrocytoma is resistant to ionizing radiation (IR) because of epigenetic reprogramming of the transcriptome caused by the mutation in IDH1. It has recently been shown that autophagy pathways are upregulated and when inhibiting it, radiosensitivity is restored. In **Chapter 4**, we use siRNA against ATG7 – an autophagy related gene – loaded into SPNPs to inhibit autophagy and restore sensitivity to ionizing radiation. This work broadens the applicability of siRNA delivery in glioma by using a different target (ATG7) and a different glioma (grade II mutant IDH1 astrocytoma).

Outside of these aims, this thesis also reflects on the published work I have contributed to regarding glioma therapy via SPNPs (**Chapter 5**). Because these are published, a focus on the PNP production and characterization is provided with some in vitro or in vivo results. In the last chapter, **Chapter 6**, I discuss future directions and conclusions. Overall, this thesis seeks to broaden the application of SPNPs in glioma therapy, but there exists much work to be conducted to fully investigate its full potential.

Chapter 2

Controlled Delivery of Paclitaxel via Stable Synthetic Protein Nanoparticles

This chapter contains portions of text originally submitted as:

"Controlled Delivery of Paclitaxel via Stable Synthetic Protein Nanoparticles."

Ava Mauser, Isabel Waibel, Kaushik Banerjee, Jingyao Gan, Anzar A. Mujeeb, Sophia Lee, William Brown, Jason Gregory, Jeffery Raymond, Matthias Franzeb, Anna Schwendeman, Maria Castro*, Joerg Lahann* (In preparation)

2.1 Abstract

Despite decades of intense research, glioma remains a disease for which no adequate clinical treatment exists. Given the ongoing therapeutic failures of conventional treatment approaches, nanomedicine may offer alternative options because it can increase the bioavailability of drugs and alter their pharmacokinetics. Here, we report a new type of synthetic protein nanoparticles (SPNPs) that allow for effective loading and controlled release of the potent cancer drug, paclitaxel (PTX) - a drug that so far has been unsuccessful for glioma treatment due to hydrophobicity, low solubility, and associated delivery challenges. SPNPs were prepared by electrohydrodynamic (EHD) jetting of dilute solutions of PTX-loaded albumin made by high-pressure homogenization. After EHD jetting, PTX SPNPs possessed diameters of 165 ± 44 nm and a zeta potential of -19 ± 8 mV. For a SPNP formulation with a total PTX loading of 9.4%, the loading efficiency was 94%, and controlled release of PTX was observed over two weeks (6% burst release). PTX SPNPs were more potent (78% lethality) than free PTX (45% lethality using 0.2% DMSO). Using flexibly engineered SPNPs, this work outlines an efficient strategy for the delivery of hydrophobic drugs that are otherwise notoriously hard-to-deliver and generally require the use of harmful co-solvents.

2.2 Introduction

IDH wild-type glioblastoma (grade 4) is the most common and aggressive form of primary brain cancer with a median survival of 15 months and has witnessed few therapeutic advancements in the last couple of decades.[183] Challenges that hamper GBM therapeutic efficacy include: (i) tumor heterogeneity, (ii) treatment resistance, (iii) immunosuppressive tumor microenvironment (TME), and (iv) the blood-brain barrier (BBB).[183,184] Paclitaxel (PTX) is a promising drug candidate that has had limited clinical success for GBM; despite its widespread use for the treatment of breast, lung, ovarian, and Kaposi’s sarcoma.[185] Its antitumoral effect is attributed to microtubule stabilization, causing mitotic arrest and inhibiting cell proliferation.[186] Despite the unquestionable potency of PTX, traditional pharmaceutical formulations require solubilization using co-solvents and/or surfactants to improve their bioavailability. Solvent-based delivery of paclitaxel is commonly achieved by solubilization in a mixture of Cremophor EL (CrEL) and ethanol, which are known to cause hypersensitivity reactions[73,74] and hepatic toxicity.[23] Beyond toxicity concerns, CrEL delivery of paclitaxel has non-linear pharmacokinetics due to the intermittent formation of micelles, which entrap paclitaxel and further reduce the amount of free drug available.[75] Therefore, alternative delivery strategies have been explored through the use of nanoparticles such as liposomes, micelles, polymeric nanoparticles, and albumin-bound paclitaxel (e.g., Abraxane).[187] Abraxane is formed through high-pressure homogenization, which uses high shear, cavitation, and pressure (nanoparticle albumin bound (nab) technology). This approach produces physical drug-protein aggregates, where paclitaxel is sequestered within hydrophobic pockets of albumin. However, the resulting aggregates are metastable and rapidly dissociate after administration.[188] Despite significant stability concerns, Abraxane has witnessed clinical success as it is the first and only FDA-approved protein nanotherapeutic on the market for cancer, including breast cancer, non-small cell lung cancer, and adenocarcinoma of the pancreas.[189] However, diminishing low drug concentrations in brain tumors have so far dwarfed all therapeutic efforts that use Abraxane, or any other PTX-based therapeutic, for the treatment of glioma.[190] The only demonstration found of Abraxane efficacy, in the context of glioma treatment, was achieved by opening the BBB through low-intensity pulsed ultrasound (LIPU) with microbubble injection.[190] While this is now being explored in a clinical trial (NCT04528680), this method requires invasive interventions by implanting a device post-surgical resection to emit ultrasound. Therefore, improving the transport of PTX therapeutics to the brain without invasive measures would have major clinical ramifications.

Nanoparticles offer several advantages, such as controlled release, active targeting, and stability, among others. Of the materials available to construct nanoparticles, proteins represent an ideal carrier material due to their versatility, conjugation capabilities, biodegradability, availability and affordability, and relatively low immunogenicity.[32] Recently, chemically stabilized protein nanoparticles have demonstrated effective transport into intracranial brain tumors in mice, resulting in high *in vivo* efficacy after delivering siRNA and small molecules through fabrication via electrohydrodynamic (EHD) jetting.[111,174] Although these results demonstrate the potential for EHD jetting to produce diverse protein nanomedicines, the current formulations are not optimal to deliver hydrophobic small molecules (such as PTX); largely because the solvent system used to solubilize these drugs are incompatible with the protein nanoparticle requirements. The development of novel processes to prepare nanoparticles equipped with high payloads of hydrophobic drugs is thus critically needed considering that more than 66% of drugs with high potential to treat brain cancer are small molecules,[183] whereas approximately 98% of these drugs cannot access the brain.[16]

Here, we report a versatile platform for the manufacturing of protein nanoparticles containing hydrophobic small-molecule drugs based on EHD jetting of aqueous solvent systems.[191] Our work establishes for the first time that EHD jetting of solutions comprised of protein-bound PTX can result in well-defined and stable protein nanoparticles (**Figure 2-1**) with sustained release profiles of PTX from the nanoparticles and *in vitro* therapeutic effects. This opens the possibility of translating PTX SPNPs to preclinical models of glioma as a prelude to subsequent clinical adoption.

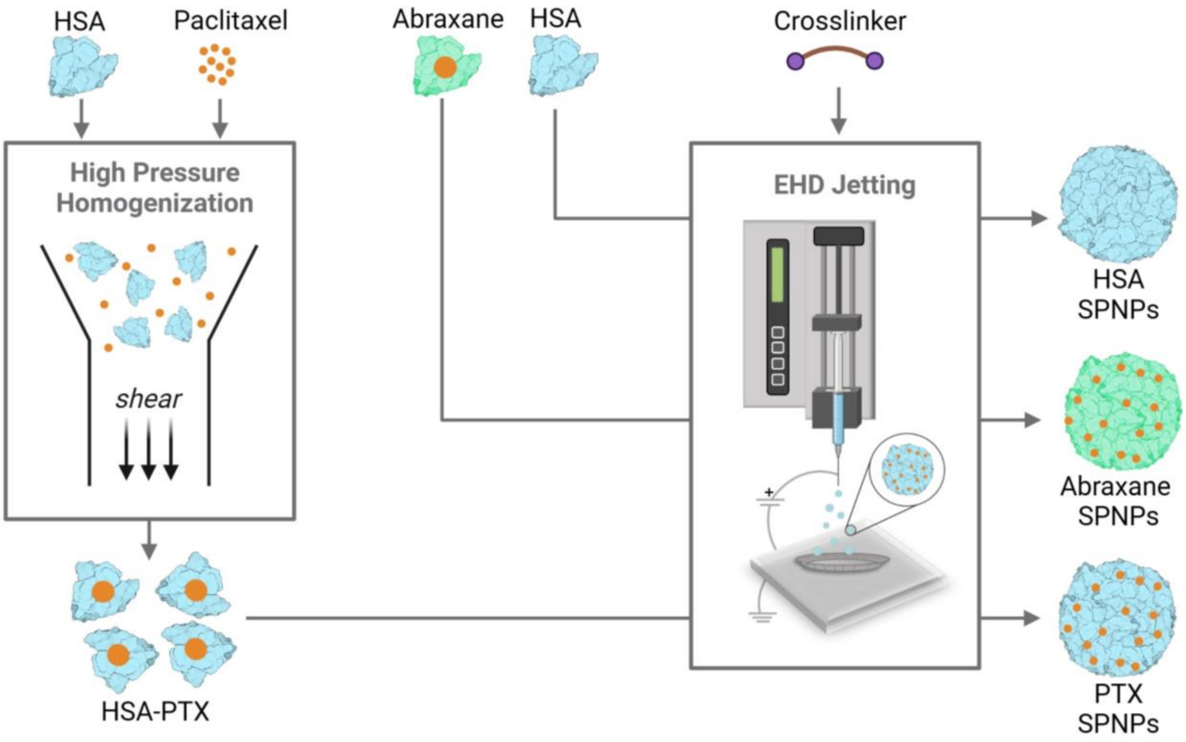

Figure 2-1. Overview of the preparation of synthetic protein nanoparticles (SPNPs): HSA SPNP (control), PTX SPNP, and Abraxane SPNP. PTX SPNPs were synthesized in a two-step process. First, high-pressure homogenization of human serum albumin and paclitaxel results in protein-bound paclitaxel (HSA-PTX) jetting solutions with well-defined drug content and drug-to-protein ratios. Subsequently, the jetting solutions were processed via EHD jetting to form PTX-loaded nanoparticles (PTX SPNP). For comparison, commercially obtained Abraxane was also processed via EHD jetting, but used a commercial PTX/albumin formulation as jetting solution. "Empty" nanoparticles without PTX (i.e., HSA SPNP) were also prepared by EHD jetting and were included as a control. In all instances of EHD jetting, the same bifunctional chemical crosslinker was used. Created with BioRender.com.

2.3 Materials and Methods

2.3.1 Materials

Acetic acid (A6283), human serum albumin (A1653), ethylene glycol (102466), O,O′-Bis[2-(N-Succinimidyl-succinylamino)ethyl]polyethylene glycol (#713783), Tween20 (P2287), chloroform (C2432), formic acid (A117), HPLC-grade methanol (34860), Hellmanex III (Z805939) were purchased from Sigma Aldrich. Albumin from bovine serum albumin, Alexa Fluor™ 647 conjugate (A34785), LC-MS grade water (51140), ProLong™ Gold antifade reagent (P10144), and LC-MS grade acetonitrile (A955), were purchased from ThermoFisher Scientific. Ultrapure distilled water (10977) distilled water (15230-162), and Dulbecco's Phosphate Buffered Saline (14190-144) were purchased from Gibco. Abraxane (E1068) was purchased from Selleckchem.

Pierce™ 660 nm protein assay reagent (22660), pre-diluted protein assay standards of bovine serum albumin set (23208), Pierce™ BCA protein assay kit (23225), and dialysis devices (Slide-A-Lyzer® MINI Dialysis Devices, 0.5 mL) were purchased from Thermo Scientific. Paclitaxel (P-9600) was purchased from LC Laboratories. FITC-Paclitaxel (#R-OR-040) was purchased from Ruixibio. CellTiter-Glo 2.0 (#G9242) was purchased from Promega.

2.3.2 Glioma cell lines and culture condition

Genetically engineered mouse glioma models: OL61 (shp53/NRAS/EGFRvIII) and NPD-AC2 (shp53/NRAS/PDGFβ) were developed by the sleeping beauty transposon system as described before.[192–194] OL61 cells were grown in Dulbecco's modified eagle medium (DMEM) (Gibco, 12430-054) supplemented with 10% fetal bovine serum (Biowest, S1520-500), 200mM L-Glutamine (1X) (Gibco, 11360-070), 100ug/mL Normocin (INVIVOGEN, ant-nr-2) and 100 units/mL antibiotic-antimycotic (Anti-Anti, Gibco, 15240-062). NPD cells were grown in Dulbecco's modified eagle medium nutrient mixture F-12 with L-Glutamine (DMEM/F-12 (Ham) (1:1) (1X); Gibco, 11330-032) supplemented with 2%B-27 (Gibco, 12587-010), 1% N-2 (Gibco, 17502-048), 100ug/mL Normocin (INVIVOGEN, ant-nr-2) and 100 units/mL antibiotic-antimycotic (Anti-Anti, Gibco, 15240-062). In addition, hFGF (Peprotech, 100-18B-1MG) and hEGF (Peprotech, AF-100-15-1MG) were supplemented twice weekly at 20 ng/ml.[195,196]

2.3.3 Fabrication of HSA-PTX

HSA-PTX was produced using high-pressure homogenization.[76] Paclitaxel (30 mg) was dissolved in 550 µL of chloroform at 37 ˚C. Meanwhile, chloroform (5 mL) was added to 37.5 mL of distilled water and vortexed. The mixture was allowed to settle to produce two phases: chloroform, and water saturated with chloroform. The saturated top phase was removed and 29.4 mL of it was added to 294 mg of HSA. Once the HSA was solubilized, the dissolved paclitaxel solution was added. The crude mixture was then tip-sonicated at an amplitude of 50 for 1 minute continuously at room temperature to pre-homogenize the mixture. The pre-homogenized solution was split between two 20 mL syringes for high pressure homogenization with the Avestin® EmulsiFlex-B15. The mixture was homogenized for 7 cycles at 24,000 psi. The resulting homogenized sample was then frozen at -20 °C, lyophilized over 72 hours, and weighed. Aliquots were prepared by resuspending the homogenized HSA/PTX in ultrapure water at a concentration of 39.33 mg/mL.

To produce FITC-labeled HSA-PTX, FITC-PTX was used instead of the PTX. The amount of FITC-PTX was scaled to have the same contribution of PTX in the crude mixture.

2.3.4 Fabrication of SPNPs

Electrohydrodynamic jetting was used to produce nanoparticles as previously described.[111,114,174,197] The distance from the tip of the needle and the collection plate was maintained at 9 cm, with a positive voltage lead attached to the tip of the needle, and a grounding lead connected to the stainless-steel platform beneath the aluminum collection plate. To produce HSA SPNPs, the jetting formulation consisted of 2.5% (wt/v) HSA, which was solubilized in a co-solvent system of 1:4 ethylene glycol to ultrapure water. Next, a bi-functional crosslinker, [O,O'-Bis[2-(N-Succinimidyl-succinylamino)-ethyl]polyethylene glycol], was added at 10% ($wt/wt_{protein}$). The PTX SPNPs and Abraxane SPNPs were formulated similarly, but instead of pure HSA, HSA-PTX and commercially available Abraxane were used, respectively. The PTX SPNPs without high-pressure homogenization consisted of 2.5% (wt/v) HSA, 10% PTX, and a co-solvent system of 20% (v/v) methanol and 80% (v/v) water. The crosslinker was added at 10% (wt/wt) relative to the HSA like the other formulations. The jetting solutions were filled into a 1 mL syringe equipped with a 25-gauge stainless steel needle and was pumped at a rate of 0.1 mL/hour onto an aluminum collection plate. The voltage (5-8 kV) was applied to form a stable Taylor Cone. The collection plate was changed every 30 minutes, then placed into an incubator at 37 °C for 7 days to crosslink.

2.3.5 Collection and processing of SPNPs

After crosslinking for 7 days at 37 ˚C, SPNPs were collected following protocols previously described.[114,174] Briefly, 3-5 mL of collection buffer (0.05% v/v Tween20 in DPBS) was added to the crosslinked SPNPs and physically agitated with a plastic razor blade in order to release the nanoparticles from each aluminum collection plate. The solution with released nanoparticles was then transferred to a 50 mL falcon tube, tip sonicated in an ice bath for 30 seconds at an amplitude of 5 (1 second on, 3 seconds off), then filtered through a 40 µm cell strainer. The filtered particles were then centrifuged at 3200 rcf for 5 minutes at 4 ˚C. The pellet was discarded, and the supernatant was further processed; it was split into 2 mL Eppendorf tubes then centrifuged at 22300 rcf for 1 h at 4 ˚C. The supernatant was discarded, and the pellets were combined. The combined pellet was washed with ultrapure water for characterization studies. For cell studies, the pellet was resuspended in DPBS.

2.3.6 Scanning Electron Microscopy (SEM) and analysis

Scanning electron microscopy (SEM) was performed to characterize nanoparticles in their dry state. For EHD jetted samples, silicon wafers were placed on top of the aluminum collection plate during jetting, then adhered onto an SEM stub equipped with double sided copper tape. All samples were gold sputter coated (50 seconds), then imaged using the FEI Nova 200 SEM/FIB. The following parameters were used for all imaging: voltage of 17 kV, current of 0.14 nA, and a dwell time of 10 µs. SEM images were analyzed with ImageJ using previously described protocols.[114] Two hundred unique nanoparticles were characterized for each nanoparticle type to obtain an average diameter, circularity, and PDI.

2.3.7 Dynamic Light Scattering (DLS) and Electrophoretic Light Scattering (ELS)

Hydrated nanoparticles were characterized using the Zetasizer Nano ZS (Malvern Panalytical) for size and zeta potential measurements. Nanoparticles were diluted to a concentration of 0.0375 mg/mL in ultrapure water.

2.3.8 Nanoparticle Tracking Analysis

Concentration and size distribution of hydrated SPNPs were measured using the Nanosight Nanoparticle Tracking Analysis (NTA) device. Samples were prepared by diluting the SPNPs with ultrapure distilled water by a factor of 800 to a final volume of 1 mL. The sample was loaded into a 1 mL disposable syringe and placed within the syringe pump of the NTA. The measurement was performed a total of 5 times with a sCMOS camera, a camera level of 9, a 488 nm laser, a syringe pump speed of 20 AU, a temperature of 24 ºC, and a capture duration of 60 s. After capture, the videos were analyzed by the built-in NanoSight Software NTA 3.1 Build 3.4.4. with a detection threshold of 7. All videos passed the software's quality check.

2.3.9 Protein Concentration

Protein concentration was determined using the Pierce™ 660 nm protein assay reagent with pre-diluted protein assay standards (Bovine Serum Albumin) set and the Pierce™ BCA protein assay kit following the manufacturer's protocol.

2.3.10 Circular Dichroism (CD) Spectroscopy

Circular dichroism (CD) spectroscopy was used to understand how the nanoparticle fabrication method affected the secondary structure of the proteins over time. Measurements were taken in a 1 mm Jasco quartz cuvette via the Jasco J-815 spectrometer in a range of 260 nm to 190 nm with a data pitch of 0.2 nm, digital integration time of 1 second, bandwidth of 1.0 nm, scan speed of 100 nm/min, and total of 3 accumulations per measurement. Between each CD measurement, the cuvette was washed in Hellmanex III cuvette cleaning solution at (2% v/v in DI water) for 5 minutes at 80 ˚C then washed 10 times with deionized water and finally washed with ethanol to expedite the drying time. Each sample was diluted in ultrapure water to 37.5 ug/mL. Dichroweb was used to quantify the fraction of each secondary structure using the CDSSTR method with reference set 7.[198–200]

2.3.11 Ultra-Performance Liquid Chromatography – Mass Spectroscopy (UPLC-MS)

Paclitaxel was weighed and dissolved in 50% (v/v) methanol and 50% (v/v) ultrapure water to produce a series of standard solutions (500, 250, 125, 62.5, 31.25 ng/mL). The paclitaxel from *in vitro* release experiments and from loading experiments were performed using a ACQUITY UPLC H-Class PLUS equipped with a quaternary solvent manager, an FTN-H sample manager, a heated column compartment, a TUV detector and an ESI mass detector (Qda). The chromatographic detection was performed using an ACQUITY UPLC BEH C18 column (2.1x 50 mm, 1.7 µm, Waters) by isocratic elution with the mobile phase comprised of 0.1% formic acid in water: acetonitrile (60:40%, v/v) at a flow rate of 0.8 mL/h. An injection volume of 10 µL and a detection wavelength of 227 nm was used. The column and samples were maintained at a temperature of 25 ˚C and 4 ˚C, respectively. The run time was 5 minutes, and the retention time was 2.4 minutes. Mass spectral data were obtained in positive electrospray mode (ESI+) in MRM mode for paclitaxel at m/z of 876.44.

2.3.12 In vitro release

PTX SPNPs with and without high pressure homogenization were collected, processed, and characterized as described above. The PTX SPNPs (1000 ug/mL, 1 mL) were placed inside a 15 mL 10 kDa MWCO dialysis membrane (Slide-a-Lyzer) with the release medium of distilled water with 2% (v/v) methanol and 0.1% (v/v) acetic acid relative to the methanol. The device was allowed to shake continuously at 37 °C over 17 days. At predetermined time points, 2.5 mL of the dialysate was removed and frozen at -20 °C and replaced with 2.5 mL of release medium. The frozen samples were lyophilized overnight, resuspended in 1 mL of 50% v/v methanol and 50% v/v ultrapure water then analyzed via UPLC-MS.

2.3.13 Loading efficiency

Centrifugal spin filtration and UPLC-MS detection were used to determine the loading efficiency of the HSA-PTX. Lyophilized HSA-PTX was resuspended in ultrapure water at a concentration of 3.28 mg/mLin a 1:5 methanol:water (v/v) solution. Spin filters (100 kDa and 10 kDa) were prepared according to the manufacturer's instructions. The suspension was split between two prepared 100 kDa spin filters (300 µL each) and spun down at 5000 rcf for 1 minute. The filtrate was removed, and the filter was replenished with additional suspension solvent (1:5 methanol:water, (v/v)) at 5000 rcf and 10,000 rcf for the second, and third time, respectively, for 1 minute each spin. For the 4-10 subsequent washes, the speed remained constant at 15,000 rcf for 1 minute. After processing with the 100 kDa filter to separate any unbound HSA and PTX, the dialysate from the first filtration was subjected to an additional filtration step. The filtrate (HSA and PTX) was added to 10 kDa spin filters and washed with the methanol/water mixture for 10 times at 15,000 rcf for 1 minute each wash. The filtrate from the second filtration step was analyzed via UPLC-MS to determine unbound or unloaded PTX in the HSA-PTX. The following equation was used to calculate the loading efficiency.

$$Loading\ Efficiency\ (\%) = \frac{PTX\ in\ crude\ mixture - unloaded\ PTX}{PTX\ in\ crude\ mixture} * 100\%$$

To determine the loading of PTX SPNPs, the paclitaxel used was tagged with FITC. The high-pressure homogenization and electrohydrodynamic jetting procedures were conducted as described in previous sections. The collection and processing of the SPNPs were also performed as previously described. Standards were produced by dissolving a known weight of FITC-PTX in 9:1 ultrapure distilled water:methanol (v/v) from a range of 9.5 ug/mL to 650 ug/mL. The standards contained the same amount of HSA that was in the SPNP composition. The SPNPs were resuspended in a water/methanol solvent system of that of the standards. Spectral readings of absorbance were read from 400 nm to 700 nm overnight. Absorbance values were recorded at 490 nm (λ_{max}). The NTA device was used as previously described to determine the size distribution of the FITC labeled PTX SPNPs in suspension. The following equation was used to calculate the loading efficiency.

$$Loading\ (\%) = \frac{m_{FITC-PTX,measured}}{V_{sample,SPNPs} * \rho_{SPNPs,hydrated} * \frac{m_{FITC-PTX,theoretical}}{m_{SPNPs,theoretical}}} * 100\%$$

Where $m_{FITC-PTX,measured}$ represents the mass of FITC labeled PTX in the sample based on the absorbance measurements. $V_{sample,SPNPs}$ denotes the accumulated volume of all FITC labeled PTX SPNPs in the sample and is calculated using NTA size distribution. $\rho_{SPNPs,hydrated}$ represents the density of the hydrated SPNPs and was calculated through multiplying the density of the dry particles by the swelling ratio. $\frac{m_{FITC-PTX,theoretical}}{m_{SPNPs,theoretical}}$ represents the theoretical mass fraction of FITC-PTX with respect to the total mass of FITC labeled PTX SPNPs and was determined from the composition of the homogenized FITC-PTX-HSA solution**.**

2.3.14 OL61 and NPD cell survival assay

Mouse OL61 (shp53/NRAS/EGFRvIII) and NPD-AC2 (shp53/NRAS/PDGFß) cells were plated at a density of 1000 cells per well in a 96-well cell culture plate 24 h before treatment. Cells were then incubated with either Abraxane or with PTX-HSA for 72 h in triplicate wells per condition to determine the half maximal inhibitory concentration (IC_{50}). After the IC_{50} doses were established, we proceeded to treat both cell types either HSA SPNPs, HSA-PTX, PTX (0.2µM) or PTX SPNPs at their respective IC_{50} dosed for 72 h in triplicate wells per condition. Cell viability was determined with CellTiter-Glo 2.0 (Promega, G9242) Luminescent Cell Viability Assay following the manufacturer's protocol. The resulting luminescence was read with the Enspire Multimodal Plate Reader (PerkinElmer, Model 2300-0000). Data were represented graphically using the GraphPad Prism software (version 8), and statistical significance was determined by one-way ANOVA followed by Tukey's test for multiple comparisons.

2.3.15 Statistical Analysis

Statistical analysis was performed using Prism 9.4.1 (GraphPad Software). Samples were first tested for normality prior to performing the statistical analysis method. A statistical threshold of

$p=0.05$ was used where p-values less than 0.05 were considered statistically significant. No experimental values were excluded from the analysis.

2.4 Results and Discussion

2.4.1 Production of PTX SPNPs, HSA SPNPs, and Abraxane SPNPs

As shown in **Figure 2-1**, HSA SPNPs were prepared via EHD jetting of an aqueous HSA solution (2.5% wt/v). Here, a bifunctional PEG oligomer was added at 10% wt/wt relative to albumin to facilitate covalent reactions between amine groups of the albumin and the NHS ester groups, resulting in stable amide bonds. Abraxane SPNPs were produced similarly, but the albumin component was replaced with commercially purchased Abraxane (2.5% wt/v). For the preparation of PTX SPNPs, we used an aqueous jetting solution that was prepared using a lab-scale high-pressure homogenizer (Avestin® EmulsiFlex-B15). Briefly, a pre-homogenized crude mixture of paclitaxel (1 mg/mL) in a saturated chloroform-water mixture was high pressure homogenized at 24,000 psi for 7 cycles, followed by freeze drying.[76] Afterwards, the HSA-PTX mixture could readily be suspended in ultrapure water. The final jetting solution contained a freshly thawed aliquot of HSA-PTX, ethylene glycol (20 v-%), and the bifunctional PEG oligomer. The concentrations for all components were matched to the jetting solution used to prepare the HSA SPNPs. In addition, great care was taken to ensure that all EHD jetting parameters were identical for all groups (**Table 2-1**).

Table 2-1. Jetting and solution parameters to produce SPNPs.

Parameter	Value
Flow Rate (mL/hour)	0.1
Applied voltage (kV)	5-8
Distance from needle tip to grounded plate (cm)	9
Needle gauge	25
HSA concentration (wt/v)%	2.5
Ultrapure water: ethylene glycol (v/v)	4:1
Bifunctional PEG oligomer (wt/wt_{HSA})%	10

In brief, the various jetting solutions were mixed, and the jetting solution was loaded into a syringe equipped with a stainless-steel needle and pumped at a rate of 0.1 mL/hour. A positive voltage source was attached to the needle and was grounded to a stainless-steel plate. The voltage was adjusted until a stable Taylor Cone was formed, which occurred between 5-8 kV. The charged droplets traveled toward the grounded plate; whereby rapid solvent evaporation produced solid nanoparticles on the grounded collection surface. The solid SPNPs were then stored at 37 ºC for 7 days prior to further analysis.

2.4.2 Characterization of PTX SPNPs, HSA SPNPs and Abraxane SPNPs

To assess initial parameters such as size and shape, the as-jetted SPNPs were characterized by scanning electron microscopy (SEM, **Figure 2-2A-C**).

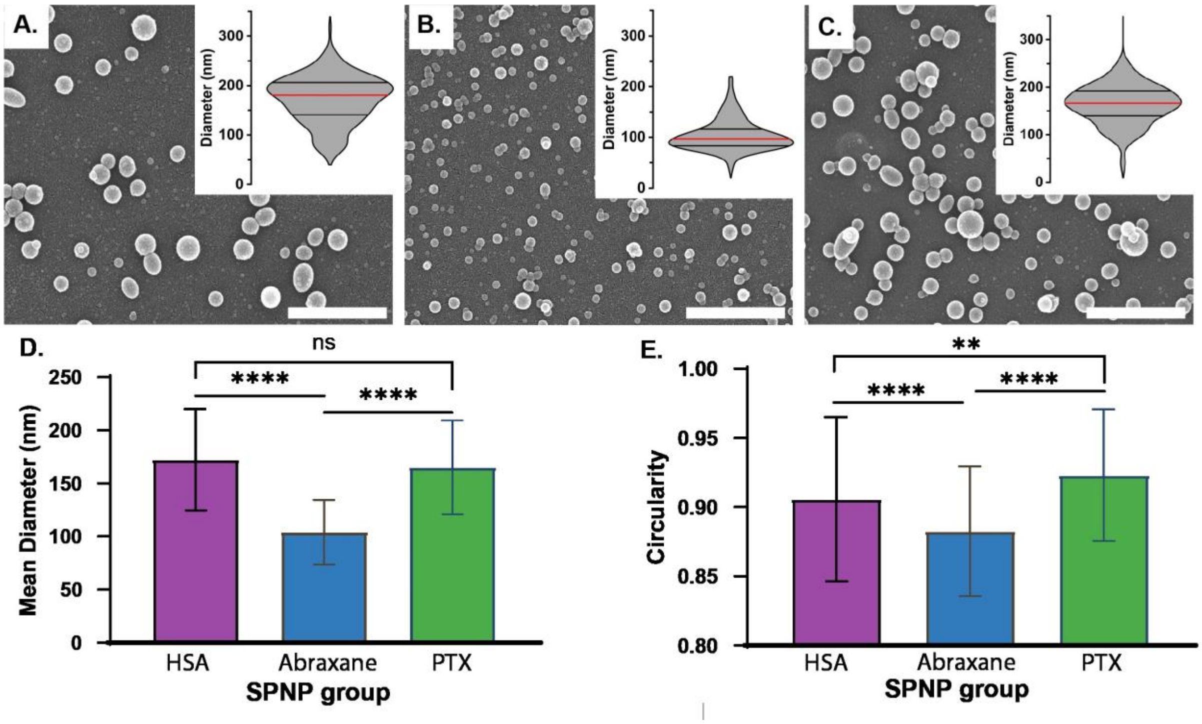

Figure 2-2. Characterization of as-prepared SPNPs. SEM micrograph images of A. HSA SPNPs, B. Abraxane SPNPs, C. PTX SPNPs (scale bar = 1 μm). The corresponding distributions are shown as insets. Violin plot: red = median, black = interquartile range. D. Mean diameter. E. Circularity of HSA SPNPs (purple, left), Abraxane SPNPs (blue, middle), and PTX SPNPs (green, right). Ns = not significant, * $p<0.05$, ** $p<0.005$, **** $p<0.0001$; unpaired t test; $n = 200$.

HSA SPNPs and PTX SPNPs had a mean diameter of 173 ± 48 nm and 165 ± 44 nm, respectively. The fact that their mean diameters were not statistically different suggests that the jetting solutions must behave very similarly (**Figure 2-2D**). In contrast, the average diameter of the Abraxane SPNPs was significantly smaller at 104 ± 30 nm ($p<0.0001$). While this may point toward differences in the aggregation behavior of the HSA constituents, no significant differences were observed between the commercially purchased Abraxane formulation and the HSA-PTX formulations produced in our laboratory, based on dynamic light scattering of their aqueous solutions (DLS, **Supplemental Information**). The fact that EHD jetting of pressure-homogenized HSA-PTX solutions gave rise to similar particle sizes and polydispersity than jetting of drug-free HSA solutions suggests that the payload plays only a subordinary role and the observed difference may rather be related to electrohydrodynamics. The violin plots of each group – shown as an inset of the SEM – indicate very narrow size distributions for all three formulations with PDI values <0.21. We suspect that the lower mean diameter of the Abraxane SPNPs compared to PTX SPNPs is due to residual salt, stemming from the commercially purchased Abraxane. In fact, it is well known that jetting solutions with higher salt concentrations tend to produce nanoparticles with smaller sizes because residual salts increase the conductivity and therefore decrease the critical droplet size during jetting.[201] Compared to free HSA, high-pressure homogenization does not alter the sizes and size distributions of the resultant SPNPs after EHD jetting. The size variations are further corroborated by the morphological features of the different SPNP groups. HSA SPNPs (**Figure 2-2A**) and PTX SPNPs (**Figure 2-2C**) were similar in shape, whereas the Abraxane SPNPs appeared to be more disk-like (**Figure 2-2B**). The circularity of HSA SPNPs, PTX SPNPs, and Abraxane SPNPs were 0.91, 0.92, and 0.88, respectively (**Figure 2-2D**). A similar trend in the circularity was observed between the SPNPs; the circularity between the Abraxane SPNPs was more significantly different compared to the PTX SPNPs (p<0.0001) and HSA SPNPs (p<0.0001) than when the HSA SPNPs and PTX SPNPs were compared with each other (p<0.005).

After EHD jetting and crosslinking, all SPNPs were collected and processed under identical conditions. Briefly, the SPNPs were removed from the collection plate using a dilute surfactant aqueous solution and physical agitation. The collected SPNPs were purified by filtration and serial centrifugation to obtain the final SPNPs. The resulting SPNPs were characterized in water to analyze their hydrodynamic radii, zeta potential, and secondary structure, which was compared to an aqueous solution of HSA (**Figure 2-3**). Unsurprisingly, the hydrodynamic diameters measured for the three SPNP formulations were similar for all groups (**Figure 2-3**A).

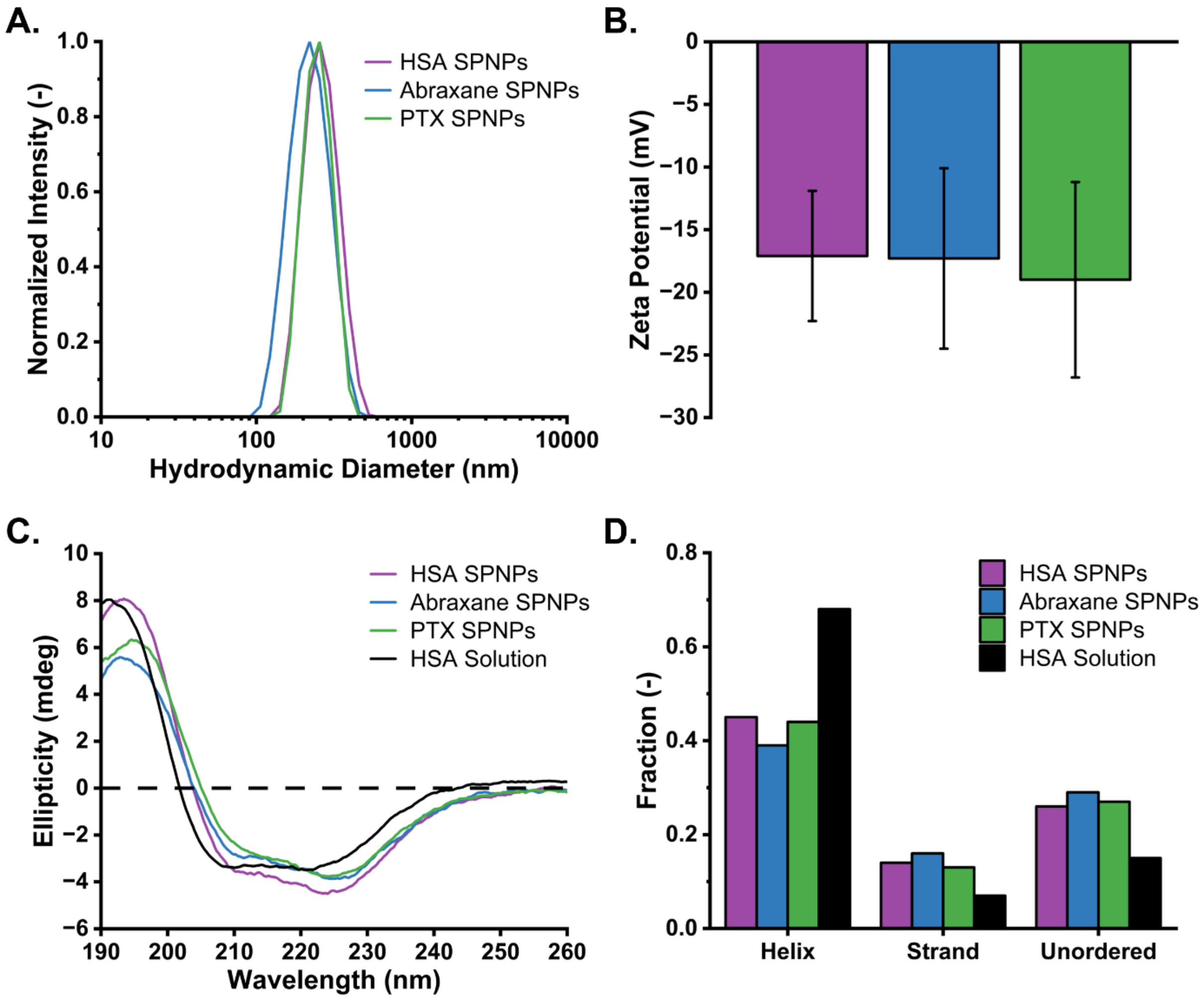

Figure 2-3. Characterization of HSA SPNPs, Abraxane SPNPs, and PTX SPNPs suspended in water. A. Intensity-based DLS. B. Zeta potential. C. CD spectra D. Fractions of helix, strand, and unordered secondary structures based on the respective CD spectra.

The fact that the groups exhibit similar sizes and distributions points towards a high degree of consistency among the various processing conditions. The zeta potentials (**Figure 2-3**B) were negative for all particle groups (HSA SPNPs = -17 ± 5 mV, Abraxane SPNPs = -17 ± 7 mV, and PTX SPNPs = -19 ± 8 mV) and statistically indistinguishable ($p>0.05$). In addition, circular dichroism (CD) spectroscopy was used to assess HSA's secondary structure within the various SPNP formulations. **Figure 2-3**C shows individual CD spectra and compares them to an HSA solution control. While the spectra of all three SPNP formulations are comparable, they are different from the solution of free HSA. We attribute the changes in the CD spectra to the chemical reactions of lysine residues of HSA with the bifunctional PEG crosslinker that are required to stabilize the SPNPs. This is corroborated in **Figure 2-3**D, where the CD spectra were analyzed via Dichroweb to extract the fractions of helix, strand, and unordered. Here, the helix content is decreased and unordered content is increased. The fractions of helix, strand, and unordered for the various SPNPs are similar.

2.4.3 Storage Stability and Reproducibility of PTX SPNPs

An important aspect of nanoparticle-based delivery systems is long-term stability and reproducibility. First, the stability of PTX SPNPs was assessed by storing the various SPNP formulations in ultrapure water at 4 ºC for two weeks (**Figure 2-4**).

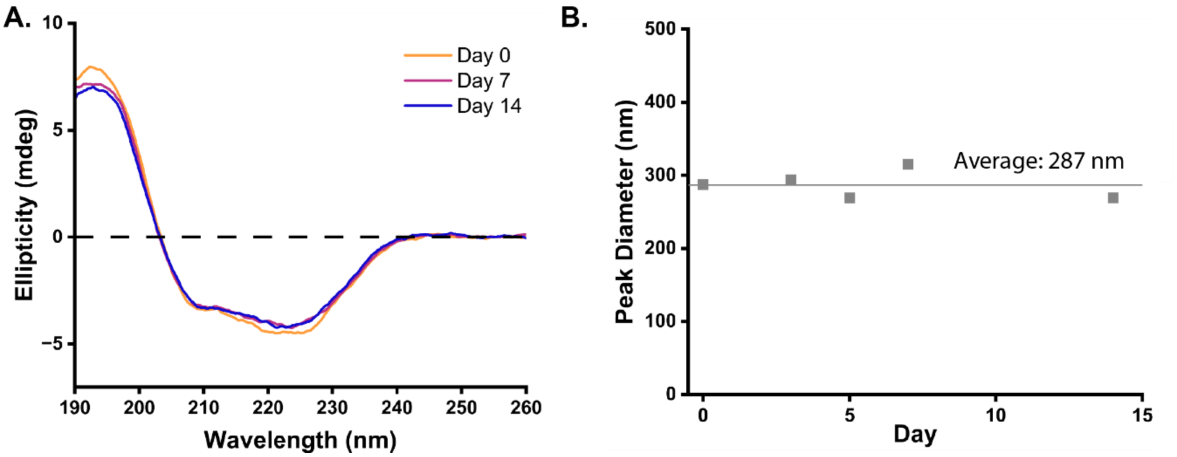

Figure 2-4. Storage stability of PTX SPNPs in ultrapure water over 14 days. A. CD spectra. B. Hydrodynamic diameter. The average diameter over this period remained at 287 nm.

In that time course, the secondary structure of the protein was monitored using CD spectroscopy. From day 0 to day 14, there were no apparent differences in the CD spectra, indicating that the conformation of the protein in the PTX SPNP formulations remained unaltered. In addition, the size of the PTX SPNPs was monitored via DLS, indicating an average diameter of 287 nm. Not only was the average diameter of the PTX SPNPs stable over time, but it was also reproducible as shown by the low run-to-run variability of three batches in **Figure 2-5**.

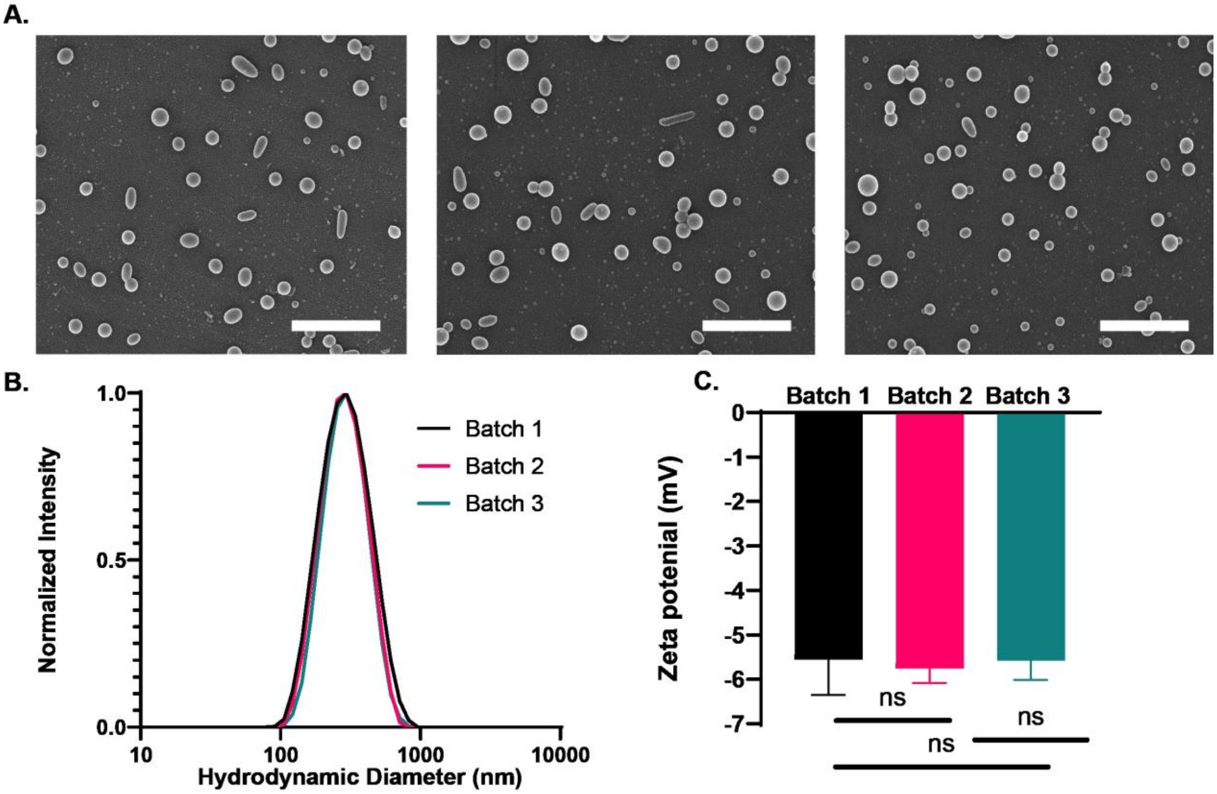

Figure 2-5. Reproducibility of PTX SPNPs from three batches. A. SEM micrographs of as-jetted, dry PTX SPNPs (scale bar = 1 µm). The left, middle, and right images are from batch 1,2 and 3, respectively. B. Intensity DLS of collected and processed SPNPs in DPBS. C. Zeta potential of collected and processed SPNPs in DPBS.

Each batch was highly circular (circularity >0.91) as indicated by the SEM micrographs (**Figure 2-5A**). The DLS size distribution was also consistent with spectra overlap between the batches (**Figure 2-5B**) and the zeta potential of the batches did not significantly differ from each other (**Figure 2-5C**).

2.4.4 Loading and in vitro release of PTX SPNPs

We next determined the amount of drug loading of paclitaxel in PTX SPNP (**Supplemental Information**) using a fluorescent PTX derivative (FITC-PTX). FITC-PTX was used to determine absorbance spectra and standard curves at a wavelength of 490 nm. Using the equations outlined in the method section, the loading efficiency of PTX in PTX SPNPs was 94% and the total loading of paclitaxel was 9.4%. The use of the FITC-labeled paclitaxel within the SPNPs did not change the size or the morphology of the SPNPs (**Supplemental Information**) Thereafter, we performed a release study to understand the paclitaxel release kinetics from the PTX SPNPs.

In vitro release of PTX from PTX SPNPs was conducted using the dialysis method, whereby PTX SPNPs were placed inside a 10 kDa MWCO membrane dialysis device and allowed to agitate at 37 ºC over 2 weeks in media. The media consisted of distilled water supplemented with 2% (v/v) methanol and 0.1% (v/v) acetic acid relative to methanol. Distilled water was used to avoid artefacts in the UPLC-MS detection. Because paclitaxel has poor water solubility, the media was supplemented with 2% (v/v) methanol. This concentration of methanol was sufficient to dissolve three times the amount of PTX loaded within the PTX SPNPs sample. Therefore, the release was not limited by PTX solubility. To avoid transesterification in methanol,[202] which would affect the peak size in UPLC-MS and thus interfere with the quantification of paclitaxel, the media was further supplemented with acetic acid.[202]

We also compared the PTX SPNPs to nanoparticles that were prepared by EHD jetting of the jetting solutions that were not subjected to prior high-pressure homogenization. In this case, these non-homogenized PTX SPNPs (nh-PTX SPNPs) were prepared using identical concentrations of HSA, PTX and crosslinker; however, we used a mixture of 80% (v/v) ultrapure water and 20% (v/v) methanol to ensure solubilization of the PTX. Otherwise, all operational parameters (voltage, distance, flow rate, needle gauge) were identical to those described in **Table 2-1**. This control group (nh-PTX SPNPs) was fully characterized as summarized in **Supplemental Information**. We note that the average diameter of these particles was 156 ± 74 nm with a larger PDI of 0.32, indicating a higher degree of variability. We used DLS as described above to confirm that the PTX-loaded SPNPs without high-pressure homogenization were stable in the release medium. For both groups, dialysate samples were removed at predetermined time points for subsequent UPLC-MS analysis and PTX quantification (**Figure 2-6**).

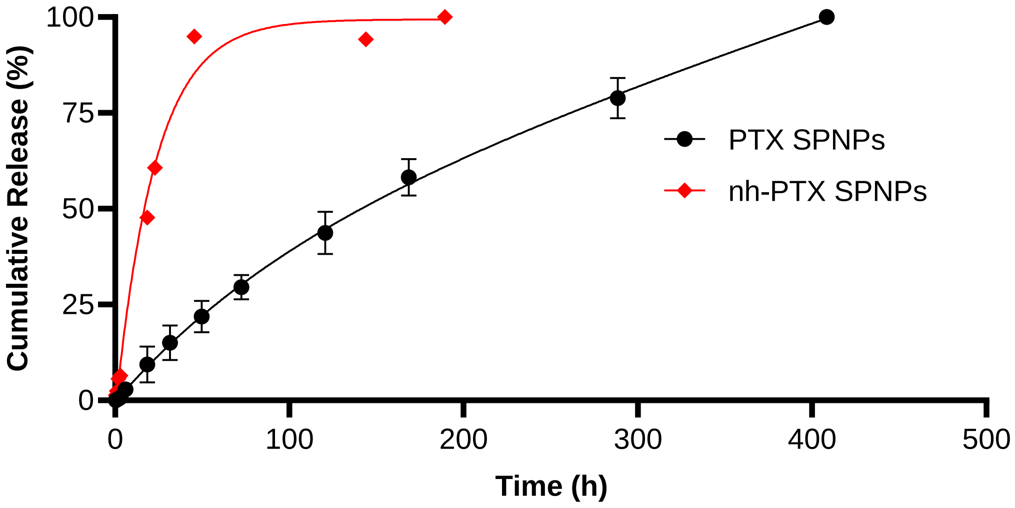

Figure 2-6. Release profile of PTX SPNPs and nh-PTX SPNPs. The release was conducted at 37 °C in distilled water supplemented with 2% (v/v) methanol and 0.1 % (v/v¬¬methanol) of acetic acid. The release profiles are expressed as % cumulative release relative to the total mass released over the duration of the release. The PTX release from PTX SPNPs followed a double exponential decay shown by the solid black line, whereas the drug release from nh-PTX SPNPs followed a single exponential decay (red solid line). Bars represent mean ± SD (n=3 replicates).

The cumulative PTX release from PTX SPNPs followed a negative amplitude double exponential decay with a half-life ($t_{1/2}$) of 122 h. We observed an initial release regime with a time constant of $\tau_1 = 9.7\ h$, constituting 6% of the total released mass of PTX (α_1 =0.06). The second release regime is characterized by a much longer time constant of $\tau_2 = 302\ h$, constituting 94% (α_1 =0.94) of the total release. The initial fast release can be attributed to the removal of surface bound PTX, while the second regime is likely associated with the slow release of PTX from the crosslinked HSA matrix of the SPNPs. In contrast, the release profile of the control particles featured a single release regime with a short time constant $\tau_1 = 22\ h$ and a half-life of 16.8 h, consistent with a much faster release following a single negative amplitude exponential decay. For comparison, the half-life of the PTX SPNPs was 122 h, more than 7 times longer than that of the control particles. Taken together, high-pressure homogenization prior to EHD jetting has a profound impact on the release kinetics and is a prerequisite for the controlled release of PTX from SPNPs.

2.4.5 PTX SPNPs Elicit a Cytotoxic Effect

After characterizing the structure of these PTX SPNPs and validating the use of high-pressure homogenization in the formation of these PTX SPNPs, we next sought to understand their behavior *in vitro* using two glioma cell cultures. Microtubules play an important role in cellular dynamics, specifically during mitosis. During mitosis, tubulin depolymerization separates chromosomes, which is essential for glioma cell survival and proliferation.[203,204] Microtubule inhibitors like PTX elicit a strong antitumoral effect by stabilizing microtubules, causing mitotic arrest and cell death.[205] Therefore, to assess the activity of PTX SPNPs *in vitro*, we measured their cytotoxicity in two glioma cell cultures: OL61wtIDH1-EGFRvIII and NPD-AC2wtIDH1-PDGFβ. These genetically engineered glioma cells harbor characteristic genetic alterations encountered in human disease, i,e., EGFRvIII and PDGFbeta overexpression. We first sought to establish a dose-response from Abraxane and HSA-PTX formulations to obtain their respective IC_{50} values (**Supplemental Information)**

Our results showed that treatment with these solutions markedly inhibited cell proliferation in both glioma cell lines. We determined their IC_{50} values to be 0.42 µM in OL61wtIDH1-EGFRvIII cells and 0.19 µM in NPD-AC2wtIDH1-PDGFβ cells. The observed potency was comparable to Abraxane, which had slightly higher IC_{50} values of 1.84 µM and 1.45 µM in the OL61wtIDH1-EGFRvIII and NPD-AC2wtIDH1-PDGFβ cells. We next tested the hypothesis that the collected SPNP formulations will have enhanced potency. We thus repeated the cell viability assays with both OL61wtIDH1-EGFRvIII and NPD-AC2wtIDH1-PDGFβ cell cultures using nanoparticle doses informed by the IC_{50} values. Three doses of PTX SPNPs were prepared that corresponded to 0.1-fold (0.1x), 1-fold (1x), and 10-fold (10x) of the IC_{50} value observed for HSA-PTX solutions (“x” denotes the IC_{50} value). These doses were prepared by calculating the amount of SPNPs needed to reach that IC_{50} based on a PTX loading of 9.4%. We compared these groups to the high-pressure HSA-PTX formulations with identical doses and included saline and free PTX (0.2µM) as additional controls. Our results confirmed that PTX SPNPs are more potent (32% viability) than HSA-PTX or PTX (55% viability) ($p = 0.0145$) (**Figure 2-7**). In contrast, empty nanoparticles had no overt toxicity in either cell line; even at doses equivalent to 10-fold the IC_{50} values. For both cell cultures, the PTX SPNPs were more effective than the HSA-PTX formulation. This could be attributed to the difference in stability, because the PTX SPNPs were stabilized via crosslinking as part of the particle fabrication process. HSA-PTX formulations are known to dissociate into albumin-paclitaxel subunits upon administration.[188]

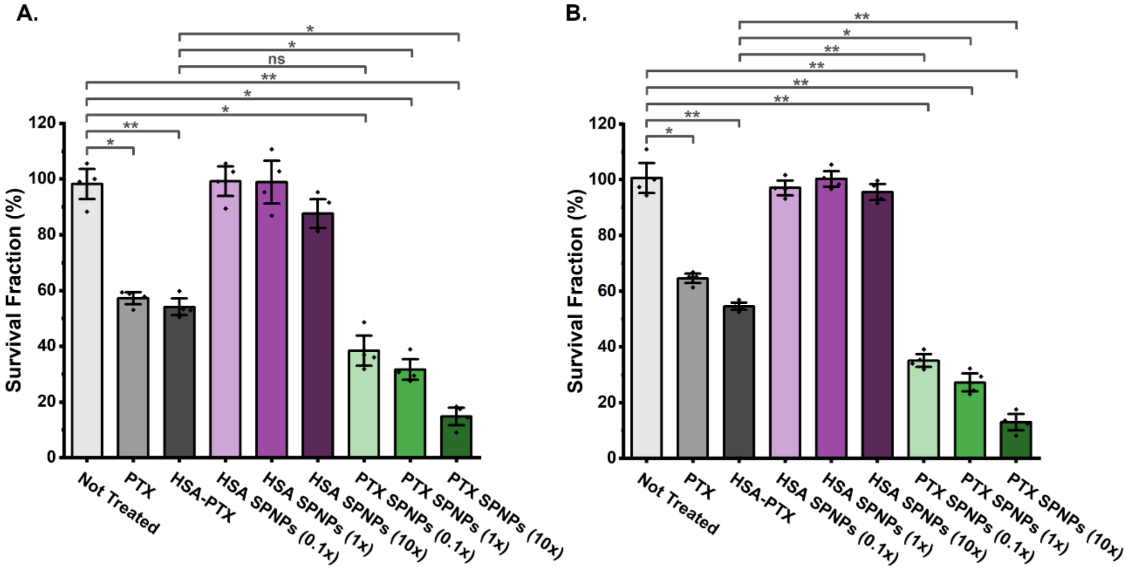

Figure 2-7. PTX SPNPs display high efficacy in murine glioma cells. OL61 (shp53/NRAS/EGFRvIII) A. and NPD-AC2 (shp53/NRAS/PDGFβ) B. mouse glioma cells were treated with either PTX, HSA-PTX, or with PTX SPNP at their respective IC50 doses on the corresponding mouse glioma cells. ns = non-significant, $^*p < 0.05$ $^{**}p < 0.01$; unpaired t test. Bars represent mean ± SD (n = 4 biological replicates).

These results indicate the PTX SPNPs retain PTX's cytotoxicity once contained in a SPNP. It is hypothesized that the mechanism of action follows that of free paclitaxel, albeit its delivery mode differs as shown in **Figure 2-8**.

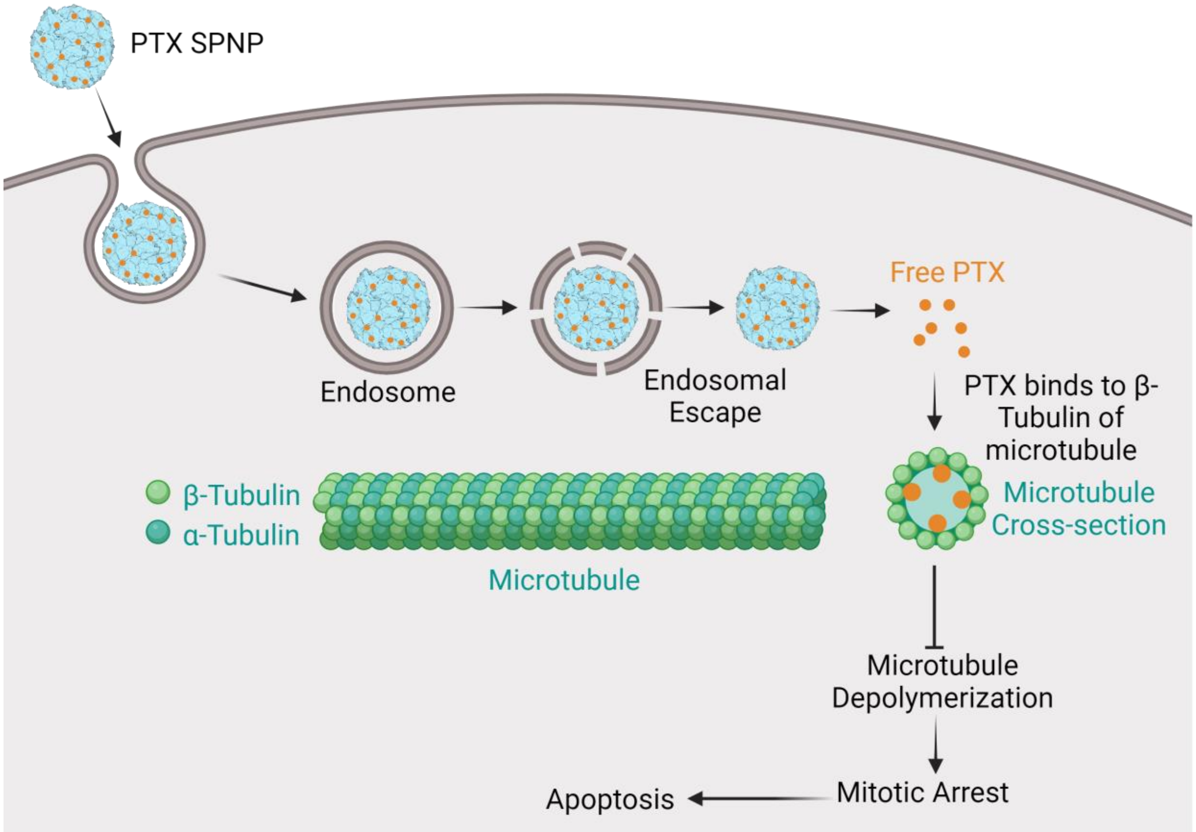

Figure 2-8. Proposed mechanism of PTX SPNPs in HGG cell cultures. Endocytosis of the PTX SPNP occurs followed by endosomal escape. The PTX SPNP is either degraded or PTX is released from the SPNP as “free PTX”. The PTX binds to the β-Tubulin of the polymerized microtubule. As a result, the microtubule is stabilized and cannot undergo microtubule depolymerization. This causes mitotic arrest and apoptosis. Therefore, cell proliferation is inhibited, leading to the cytotoxic effects of PTX SPNPs. Created with Biorender.com.

Endocytosis of the PTX SPNP followed by endosomal escape is the proposed uptake mechanism. Either through PTX release or degradation of the PTX SPNP through proteases, the free PTX binds to β-tubulin of the microtubules. PTX stabilizes the microtubules and prevents microtubule depolymerization. As a result, the microtubules cannot attach to the chromosomes, which initiates the spindle assemble checkpoint, leading to mitotic arrest and thus, apoptosis.[206] It has been reported that the concentration of paclitaxel can impact cellular fate,[207–210] but the results are conflicting. Therefore, further work would need to be conducted with these PTX SPNPs in high grade glioma cell cultures to elucidate which part of the cell cycle is impacted to cause cell death as others have reported.[211]

2.5 Conclusions

Here, we report the production and characterization of stable SPNPs for controlled release of the hydrophobic antineoplastic agent, paclitaxel. These PTX SPNPs were prepared via electrohydrodynamic jetting of HSA-PTX formulations with PTX loadings as high as 9.4%. Through control experiments, we confirmed the controlled release of PTX with minimal burst (6%) and established that high-pressure homogenization prior to electrojetting is a prerequisite for the controlled release of PTX. The differences in nanoparticle formulations resulted in significant improvement in their therapeutic activity against glioma cells. More generally, the work constitutes a novel framework to produce precisely engineered protein nanoparticles for the controlled release of hydrophobic drugs via electrohydrodynamic jetting. In the context of this thesis, this work establishes the framework for loading hydrophobic small molecules into albumin SPNPs.

2.6 Supplementary Information

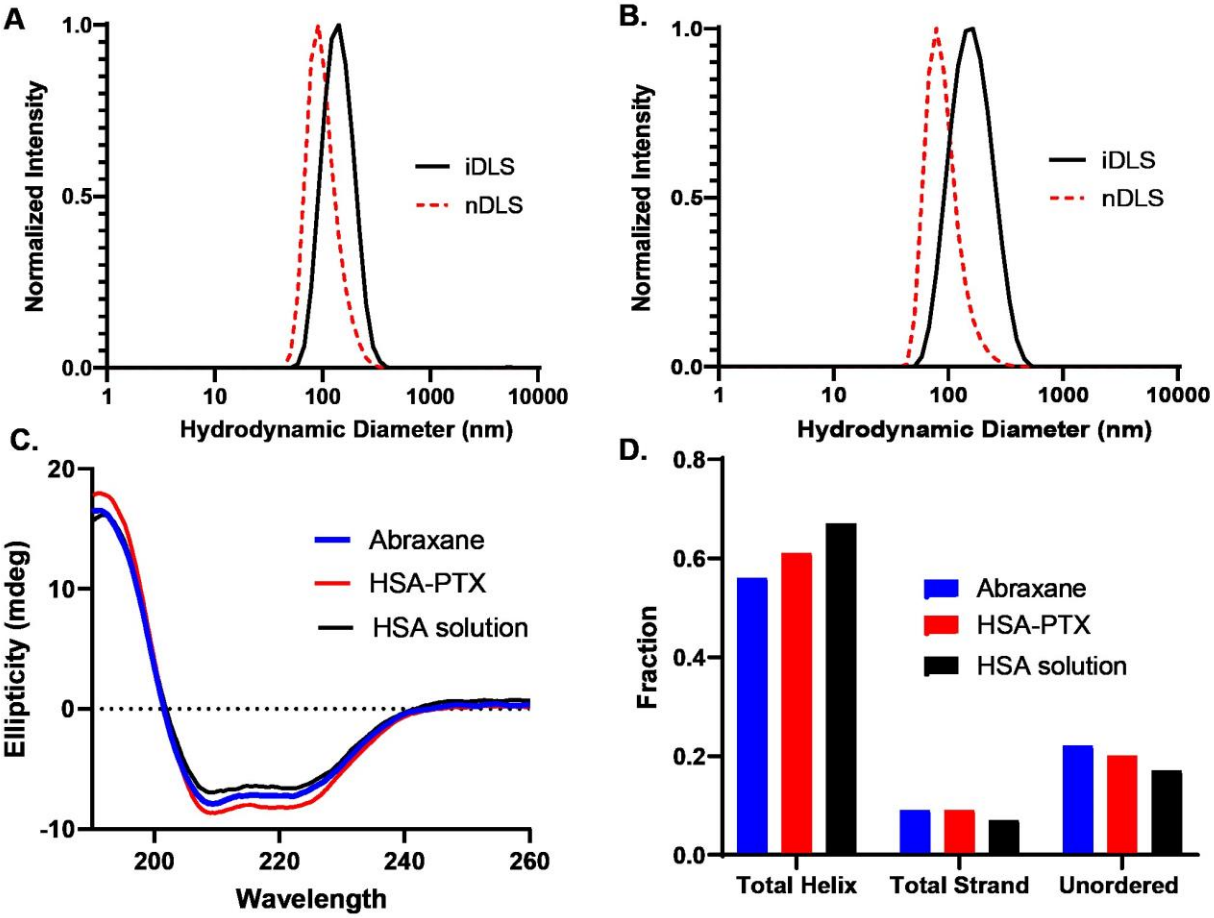

Figure 2-9. Characterization comparison of Abraxane and HSA-PTX. A. Intensity DLS (iDLS), and numbers DLS (nDLS) of Abraxane. B. IDLS and nDLS of HSA-PTX. C. CD spectra of Abraxane, HSA-PTX, and native HSA in solution. D. CD spectra secondary structure analysis through Dichroweb for fractions of total helix total strand, and unordered.

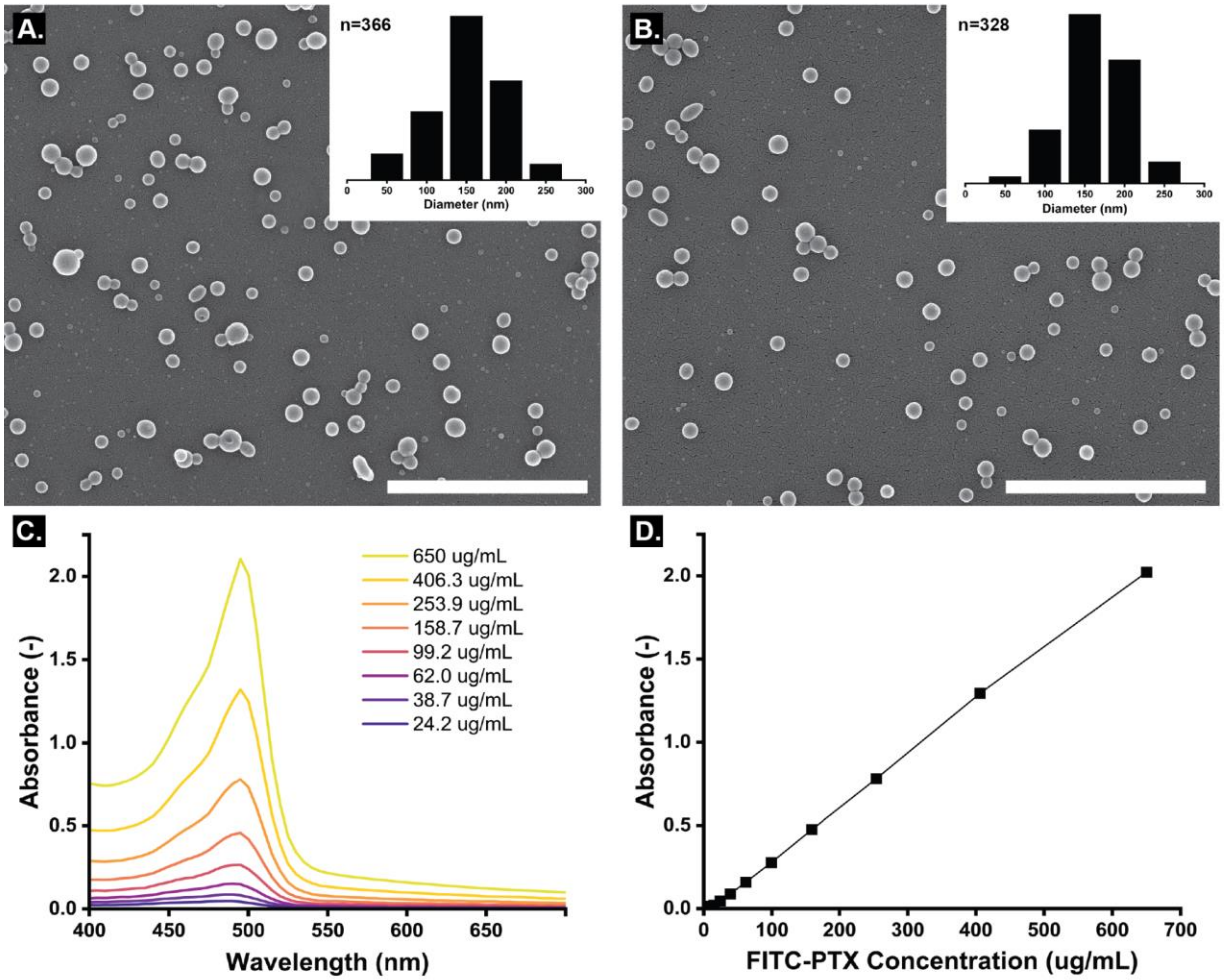

Figure 2-10. Characterization of PTX-FITC SPNPs. SEM micrograph images of A. FITC-PTX SPNPs. B. PTX SPNPs. (Scale bar = 2 µm). The corresponding size distribution is shown as an inset (n represents the number of particles considered for the ImageJ analysis). C. Absorbance spectra of non-jetted FITC-PTX at different concentrations. D Linear FITC-PTX standard curve calculated with absorbance values at 490 nm.

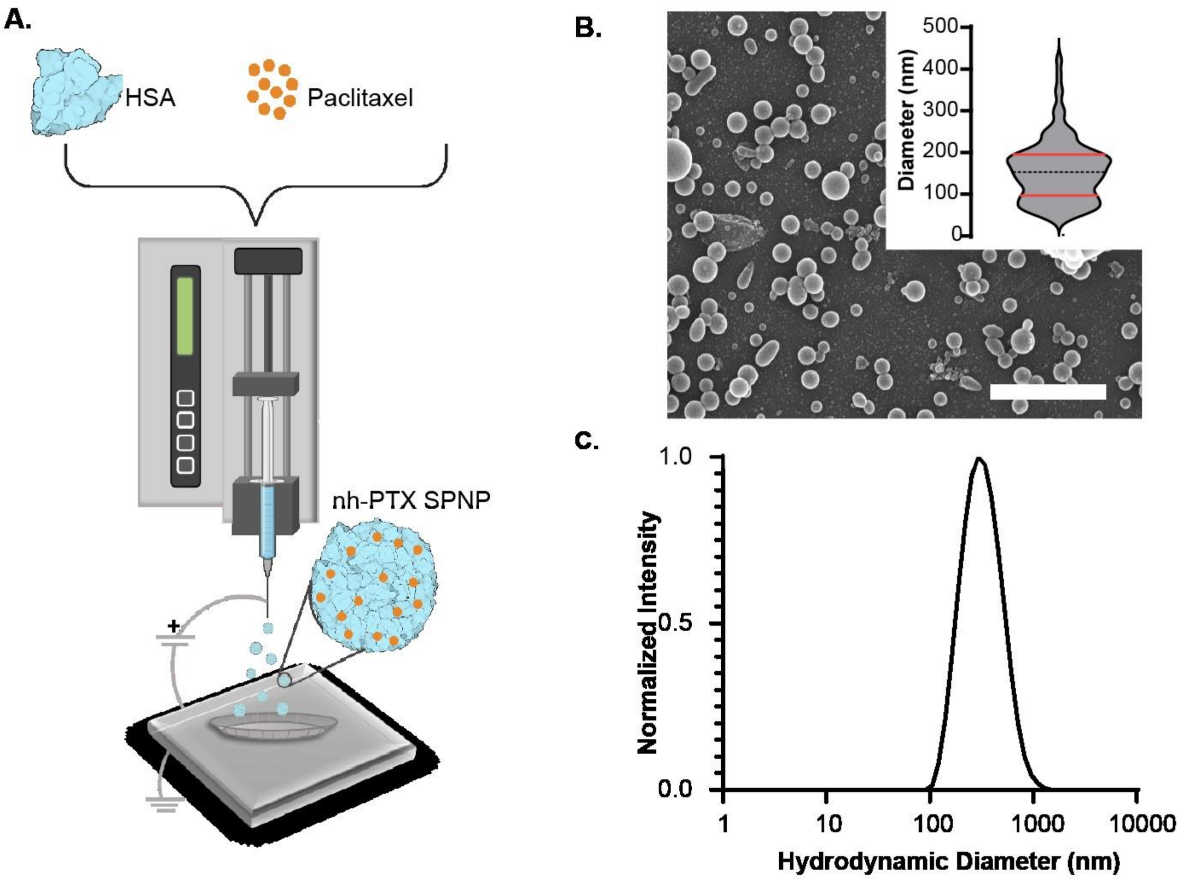

Figure 2-11. Characterization of non-homogenized PTX SPNPs (nh-PTX SPNPs). A. Fabrication of nh-PTX SPNPs through EHD jetting using a mixture of HSA and PTX without high pressure homogenization. B. SEM micrograph depicting the electrosprayed SPNPs (scale bar = 1 µm). The violin plot inset shows the diameter distribution of the SPNPs (n=200). C. DLS spectra.

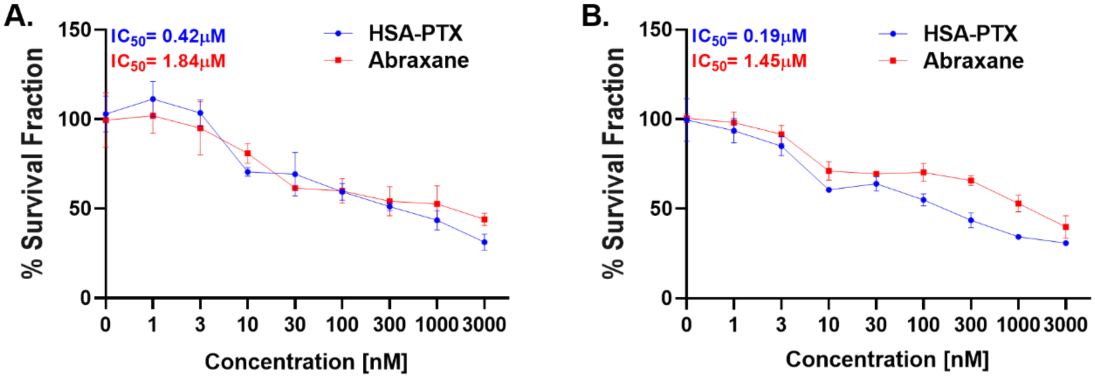

Figure 2-12. Dose-response curves of HSA-PTX and Abraxane on mouse glioma cells. OL61 (shp53/NRAS/EGFRvIII) (A) and NPD-AC2 (shp53/NRAS/PDGFβ) (B) murine glioma cells were incubated for 72 h with nab-Paclitaxel and Abraxane at the indicated doses. Cell viability was assessed using Promega Cell Titer Glo Assay. GraphPad Prism was used to determine IC_{50} values of the compound's cytotoxicity, shown in µM. Data are shown as means ± SD. *n* =4 biological replicates. Statistical analysis was done through non-linear regression analysis and non-parametric t-tests. ***p<0.001 level of significance.

Chapter 3

Dual Delivery of STAT3 siRNA and Paclitaxel via Bi-compartmental Synthetic Protein Nanoparticles for High Grade Glioma

This chapter contains portions of text from the following article:
“Dual Delivery of STAT3 siRNA and Paclitaxel via Bicompartmental Synthetic Protein Nanoparticle for High Grade Glioma”
Ava Mauser, Kaushik Banerjee, Anzar A. Mujeeb, Sophia Lee, Jingyao Gan, Isabel Waibel, Albert Chang, Nahal Habibi, Anthony Berardi, Anna Schwendeman, Maria Castro*, Joerg Lahann* (In preparation)

3.1 Abstract

Nanoparticle combination therapy seeks to unite the benefits of combination therapy with the delivery advantages of nanoparticles. This strategy could be particularly important in gliomas, whereby their heterogeneity limits monotherapy. Here, we developed bicompartmental synthetic protein nanoparticles (biSPNPs) through electrohydrodynamic co-jetting to encapsulate siRNA against STAT3 (STAT3i) and paclitaxel (PTX). We show that two drugs of differing characteristics can be loaded into a single nanoparticle separated into two compartments, which expands the use of electrohydrodynamic jetting to deliver more than one drug relevant for glioma therapy. The STAT3i/PTX biSPNPs were 159 ± 42 nm in their dry-state size, swelled to 237 nm in the hydrated state and were negatively charged at -18.7± 1.6 mV. In vitro release studies showed PTX and siRNA release with different kinetics. The SPNPs size was relatively stable over two weeks with a non-significant change in size ($p>0.05$). In human and mouse high grade glioma (HGG) cells, the biSPNPs with IR showed the greatest cytotoxicity, compared to control groups.

Lastly, we show that the STAT3i/PTX biSPNPs cause the release of damage associate molecular patterns (DAMPs), which support immunogenic mediated cell death.

3.2 Introduction

Nanoparticle therapy has gained traction as a promising therapeutic delivery modality in glioma due to their ability to facilitate sustained release and active targeting, improve bioavailability, and overcome biological barriers. Arguably, the most important benefit of nanoparticle therapeutic strategies in treating gliomas is ability for nanoparticles to penetrate the blood-brain barrier to delivery therapeutics that would otherwise be rendered useless because of the insufficient delivery.[16] While the delivery of such therapies through nanoparticles is promising, there still exists the concern of acquired resistance, which is the onset of resistance to the drug by the overexposure of it. In doing so, this strengthens other cellular pathways to offset the effect of the delivered therapy which allows the tumor to grow. In glioma, tumor recurrence is virtually inevitable and multifaceted.[212] Therefore, nanoparticle combination therapy has emerged to overcome resistance, promote synergism to improve the therapeutic index, unify two drugs' pharmacokinetics and reduce toxicity while maintaining the benefits from nanoparticles[181,182]. Nanoparticles can achieve combination therapy in the following ways: (1) dual loaded where the drugs are combined in a single nanoparticle, (2) co-delivery where two drugs are delivered in two separate nanoparticles, and (3) multicompartmental where drugs are delivered in a single nanoparticle but are separated into compartments. Co-delivery can unify the pharmacokinetics (PK) of the two drugs, however, it might be difficult to achieve in all combinations due to the drugs differing characteristics (i.e., solubility).[182] Further, there may also be drug-drug interactions that affect the drug's efficacy, safety stability, and release.[182] While dual loaded nanoparticles can minimize the interactions and addresses issues of solubility, it is difficult to achieve synchronizing PK, biodistribution, and therapeutic effect at the target site.[181] By segregating the compartments to produce bi-compartmental nanoparticles, drug interactions are minimized, and differing solubilities (i.e., hydrophobic versus hydrophilic drugs) of drugs is not a concern.[213] Multi-compartmental configurations could also facilitate the precise release of the therapeutics at their synergistic ratio. It is unlikely that if there is a synergistic ratio between two drugs, that all other ratios would have the same level of synergy. It is possible that at different ratios, that the combinations is only additive, or even antagonistic. Therefore, the multi-compartmental configuration allows more design space to achieve desired release kinetics at such synergistic ratios. When comparing multi-compartmental to a co-delivery system, one may question the loading differences. As an example, if a bi-compartmental nanoparticle was to deliver the same dose as a co-delivery system, it would need to double the loading of each drug into each compartment or dose twice as many nanoparticles. The latter is favorable because doubling drug loading in one compartment is not as straightforward.

Here, we present the development, characterization, and therapeutic efficacy of bi-compartmental synthetic protein nanoparticles (biSPNPs) loaded with Signal Transducer and Activator of Transcription 3 (STAT3) siRNA and paclitaxel. STAT3 is an intracellular signaling protein that has been associated with immunological function, cell proliferation, and tumorigenesis.[214–216] In glioma, higher expression of STAT3 is observed in more aggressive gliomas, leading to a worse prognosis.[215] Therefore, STAT3 has served as a target for therapeutic intervention glioma.[216,217] Prior work[218] demonstrated that SPNPs loaded with siRNA against STAT3 can knockdown the expression of STAT3, effectively reach the tumor microenvironment, and provide a strong therapeutic response. In addition to STAT3 siRNA, the biSPNPs were loaded with paclitaxel, a water insoluble small molecule that prevents cellular proliferation.[219] Systemic delivery of paclitaxel requires solubilization in harsh solvents that cause toxicity,[23] and inadvertently form micelles, which reduce the amount of available paclitaxel and lead to non-linear pharmacokinetics.[75] Further, small molecules are routinely excluded from the brain,[16] which necessitates alternative delivery strategies. In **Chapter 2**, paclitaxel SPNPs were produced for glioma therapy and showed greater toxicity in glioma cells when compared to free paclitaxel. Combining these molecules into a single biSPNP demonstrates the ability to co-load two starkly different molecules into a single nanoparticle through the EHD co-jetting technology. Furthermore, we showed the biSPNPs ability to kill adult high-grade glioma (HGG) cells in vitro and the release of damage associated molecular patterns (DAMPs), which elicit effective anti-high grade glioma immunity.

3.3 Materials and Methods

3.3.1 Materials

STAT3 siRNA was purchased from Cell Signaling Technology (6582S and 6353S). Branched polyethyleneimine (PEI, 181978), NHS-PEG-NHS (713783), human serum albumin (A1653), ethylene glycol (102466), chloroform (C2432), acetic acid (A6283), Tween20 (P2287), and methanol (34860) were purchased from Sigma Aldrich. Albumin from Bovine Serum (BSA) Alexa Fluor™ 647 conjugate (A34785), UltraPure™ DNase/RNase-Free Distilled Water (10977015), Cy3-siRNA (AM4621), Pierce^{TM} 660nm Protein Assay (22660), Pierce™ BCA Protein Assay (23225), DMEM (12430054), L-Glutamine (25030-081), trypsin-EDTA (25300054), Penstrep (15140122), Liptofectamine™ 2000 (11668027), ATP determination kit (A22066), and Cy™3-labeled Negative Control (AM4621) were purchased from ThermoFisher Scientific. IRGD peptide (HY-P0122) was acquired from MedChemExpress. DPBS (14-190-250) and DI water (15-230-204) were purchased from Fisher Scientific. Paclitaxel (P-9600) was purchased from LC Laboratories. Float-A-Lyzer G2 Dialysis Device (G235036) was purchased from Repligen. Fetal bovine serum (FBS, S11150) was purchased from Atlanta Biologicals. WP1066 (S2796) was purchased from Selleckchem. CellTiter-Glo 2.0 Luminescent Cell Viability Assay (G9242) was purchased from Promega.

3.3.2 Fabrication of STAT3i/PTX biSPNP and Empty biSPNP

BiSPNPs were fabricated through electrohydrodynamic co-jetting as previously described. Two jetting solutions for each compartment of the STAT3i/PTX biSPNP were prepared: (1) STAT3i and (2) PTX. For the STAT3i compartment, PEI (60 kDa, 5% w/v, 50 µL) and siRNA (1 nmol/100 µL, 150 µL) were allowed to complex for 30 minutes at room temperature. In the meantime, solubilized HSA (39.33 mg/mL, 1.5 mL) was combined with Alexa Fluor 647 BSA conjugate (5 mg/mL, 59 µL) followed by iRGD (100 ug/mL, 4.8 µL) and ethylene glycol (472 µL). After 30 minutes of complexation, the PEI/siRNA complex was added to the bulk formulation and mixed immediately after the addition. Finally, the bifunctional crosslinker (47.6 mg/mL, 124 µL) was added. The PTX compartment was formulated in a similar manner with the exception of STAT3 siRNA and the addition of PTX. Instead of adding PTX directly into the jetting formulation, the PTX was high pressure homogenized with HSA to obtain HSA-PTX. This HSA-PTX was produced following a previously described method in **Chapter 2.** Briefly, 294 mg of HSA was dissolved in saturated chloroform/DI water mixture (29.4 mL). PTX (30 mg) was dissolved in chloroform (550 µL) then added to the HSA/chloroform/DI water mixture. This crude mixture was tip-sonicated at an amplitude of 50 for 60 seconds continuously. This pre-homogenized mixture was high pressure homogenized using the Avestin® EmulsiFlex-B15 for 7 cycles at 24,000 psi.

This process formed HSA-PTX, which was frozen overnight at -20 ˚C then freeze dried for 2 days. The HSA-PTX was weighed and resuspended in ultrapure water to obtain a concentration of 39.33 mg/mL aliquots, each at 1.5 mL. These aliquots were frozen at -20 ˚C until used for EHD co-jetting. After thawing an aliquot of HSA-PTX, Alexa Fluor 647 BSA Conjugate (5 mg/mL, 59 µL) and iRGD (100 µg/mL, 4.8 µL) were added. Next, 472 µL of ethylene glycol was added and mixed. Finally, the bifunctional crosslinker (47.6 mg/mL, 124 µL) was pipetted into the solution.

The Empty biSPNPs were produced as control biSPNPs without the STAT3 siRNA and the PTX. In the case of the empty STAT3 siRNA compartment's formulation, the bPEI, iRGD, Alexa Fluor 647 BSA conjugate, ethylene glycol and crosslinker concentration and volumes remained the same; However, additional water in place of the siRNA was added to keep the total volume consistent and keep the water volume at 80% (v/v/). For the empty PTX compartment's formulation, HSA (39.33 mg/mL, 1.5 mL) was used instead of HSA-PTX. The Alexa Fluor 647 BSA conjugate, ethylene glycol, and the crosslinker volumes and concentrations remained the same.

The final formulation per compartment consisted of 2.5% (w/v) HSA in a co-solvent system of 80% (v/v) ultrapure water and 20% (v/v) ethylene glycol, and 10% (w/w) crosslinker relative to HSA. Both compartment solutions were loaded into a 1 mL syringe with a 25-gauge stainless steel blunt needle bent to facilitate the union of two needles. The syringes were attached to a 3D printed EHD co-jetting holder and the needles were held together with plastic tubing. These were loaded into a syringe pump set to a pump rate of 0.1 mL/hour. A positive voltage lead was attached to the joined needles via an alligator clip and was grounded 9 cm below the tip of the needle to a stainless-steel plate. The voltage was adjusted until a stable Taylor Cone was present.

3.3.3 Cellular uptake of iRGD SPNPs in GL26-WT cells

IRGD SPNPs were produced by varying the amount of iRGD. This follows the same formulation as previously stated, but with different amounts of iRGD. Alexa Fluor 647 BSA conjugate was incorporated at 0.5% wt/wt relative to the HSA to fluorescently label the SPNPs. GL26-WT cells were cultured in DMEM supplemented with fetal bovine serum (10% v/v), L-glutamine (1% v/v) and Penstrep (1% v/v). Cells were seeded in a 96-well plate at a density of 30,000 cells per well with a total volume of 100 µL per well. After 24 hours of cell seeding, the media was removed, washed with PBS, then SPNPs were added at a concentration of 15 µg per well and a total volume of 100 µL. The treatment was allowed to incubate with the cells for the treatment time (either 15 minutes or 1 hour). At the predetermined time point (15 minutes or 1 hour), the nanoparticle-containing media was removed, washed twice with DPBS (100 µL each wash), and trypsin was added (200 µL per well). Once detached, the cells were removed and placed into flow cytometry tubes containing 500 µL of FACS buffer (DPBS with 2% v/v fetal bovine serum, by volume) on ice. The tubes were centrifuged at 500 rcf for 5 minutes. The supernatant was discarded, and the cells were resuspended in fresh FACS buffer, vortexed, and washed once more. Next, DAPI FACS mixture was prepared (1:1000 dilution of DAPI (1 mg /mL) in FACS). To the groups needing DAPI staining, 100 µL of the DAPI dilution was added. Finally, flow cytometry was performed using the Coulter Cytoflex. Cells were gated using 10,000 cells gating criteria. First, cells were gated according to the size and complexity (removing debris). Thereafter, doublets were removed, gating only on the single cell populations. Next, live cells were gated from using the DAPI staining. Lastly, uptake was determined by gating the live cells that were positive for Alexa Fluor 647, the dye used to label the SPNPs. Each time point had three biological replicates. Flow cytometry data was analyzed using FlowJo Software.

3.3.4 Scanning Electron Microscopy (SEM) and SEM analysis of biSPNPs

Dry-state, or as-jetted biSPNPs were characterized by Scanning Electron Microscopy (SEM) with a FEI Nova 200 SEM/FIB. To prepare samples for SEM, silicon wafers were placed on top of the collection plate during EHD jetting, gold sputter coated with a SPI-Module Carbon/Sputter Coater] for 40 seconds then placed on an SEM stub covered in double-sided copper tape. The SEM stub was loaded the SEM and imaged with the following operational parameters: voltage of 17 kV, current of 0.14 nA, and a dwell time of 10 µs. The SEM images were analyzed through ImageJ according to a protocol previously described by our group.[114] All SEM analyses were performed with n=200 individual biSPNPs.

3.3.5 Structured Illumination Microscopy (SIM)

SIM was performed with a Nikon N-SIM +A1R microscope (Nikon) and a 100X objective (Nikon). Excitation was performed at 488 nm and 647 nm sequentially with collection occurring at a Hamamatsu Orca-Flash 4.0 detector with bandpass filters of 525/50 and 700/75 nm for each channel. Z-stack images were obtained with a step size of 100 nm. Image processing and analysis occurred in ImageJ (NIH). The images were processed in the following way: (1) channels were imported separately; (2) background correction was obtained through histogram inspection and contrast adjustment; (3) 2D images were produced through flattening with no further adjustment; (4) 3D images were rendered from the Z-stack and the particle was rotated to present the seam between feature halves; (5) a gamma adjustment of 2.0 was used to minimize the appearance of low intensity distortion in the 3D image; (6) the 3D image was then rendered as a 2D image for presentation.

3.3.6 Collection of biSPNP

The STAT3i/PTX biSPNPs were removed from collection plates through physical scraping while using a 0.05% (v/v) Tween20 in DPBS solution on ice. Approximately 3-4 mL of collection buffer was added to a plate and scraped for about 1 minute. The released STAT3i/PTX biSPNPs from this plate were then transferred to a second plate to repeat the scraping process for 1 minute. This was then transferred to the next pan until 6 pans were scraped. After the sixth plate, the released biSPNPs were collected into a 50 mL falcon tube on ice. The six pans were scraped for a second round with fresh collection buffer then was combined with the previous collection into the 50 mL falcon tube. If more than six pans needed to be collected, this procedure was repeated in sets of six or less.

3.3.7 Size Exclusion of biSPNP

Next, the 50 mL Falcon tube(s) containing the released biSPNPs were tip-sonicated with an amplitude of 5 for 30 seconds (1 second on, 3 seconds off) in an ice bath. This sonicated suspension was filtered through a 40 µm cell strainer into a new 50 mL Falcon tube, centrifuged at 3200 rcf for 5 minutes, and the supernatant was distributed amongst 2 mL Eppendorf tubes. The Eppendorf tubes were subjected to high-speed centrifugation (22300 rcf) for one hour at 4 ˚C. The supernatant was discarded, and the pellets were combined using 1 mL of DPBS, tip sonicated at the settings previously described, and centrifuged again at 22300 rcf for 1 hour at 4 ˚C to wash the biSPNPs. The supernatant was discarded, and the pellet was once more resuspended in 1 mL of DPBS, and tip sonicated. The biSPNPs were stored at 4 ˚C.

3.3.8 Characterization of hydrated STAT3i/PTX biSPNP

Post size-exclusion, hydrated biSPNPs were characterized according to their size, polydispersity, zeta potential, and concentration. The hydrated size and polydispersity indices were measured via

Dynamic Light Scattering (DLS) with the Zetasizer Nano ZS (Malvern Panalytical). The samples were either diluted in DPBS or ultrapure water and measured in a disposable low volume cuvette. The zeta potential measurements were also conducted using the Zetasizer Nano ZS (Malvern Panalytical) in ultrapure water or DPBS with a ZETA disposable folding capillary cuvette. Protein concentration was determined through the Pierce™ BCA Protein Assay or through Pierce™ 660nm Protein Assay according to the manufacturer's instructions. Nanoparticle concentration was characterized with NTA system by ZetaView (Particle Metrix GmbH). Nanoparticle stock was diluted (1000-10000x) for the optimal concentration (average particles 75-300 per frame). The detection parameters were set at the sensitivity of 75 and shutter at 100, to detect particles with a minimum brightness of 25, minimum area of 9, a maximum area of 1000, a maximum brightness of 255, a tracking radius of 25, and minimum trace length of 15 for 3 cycles. Data was analyzed using the Particle Metrix Software.

3.3.9 BiSPNP stability studies

The storage stability of STAT3i/PTX biSPNPs was assessed by measuring the hydrodynamic size via DLS over time at 4 ˚C in either DPBS. A stock of biSPNPs (2.2 mg/mL) was kept at 4 ˚C and at the time of measurement, the stock was briefly vortexed, and ten microliters of the stock was diluted into 390 microliters of DPBS. Samples were measured via DLS for 3 automatic measurements. The average of three measurements were taken and represents the reported spectra and values. The three measurement peak values were extracted from the Zetasizer and used as replicate values. The error bar is plotted as the standard deviation of the three automatic measurements.

3.3.10 In vitro release of PTX and siRNA from biSPNPs

To study the dual release of PTX and siRNA from biSPNP, a Cy3-siRNA/PTX biSPNP was produced. Instead of using the STAT3 siRNA, a Cy3-siRNA was incorporated into the jetting formulation. The other components remained unchanged, and the collection, processing, and characterization followed the methods as decided above. Cy3-siRNA/PTX biSPNPs (2655 ug/mL, 960 µL) suspended in ultrapure water were placed inside a Float-A-Lyzer G2 Dialysis Device (MWCO of 300 kDa, 1 mL). This dialysis device was subsequently placed inside a 50 mL Falcon tube containing 15 mL of release medium (distilled water supplemented with 2% (v/v) methanol and 0.1% (v/v) acetic acid relative to methanol). The Falcon tube containing the dialysis device was kept at 37 ˚C for over two weeks while shaking. At each time point, the dialysis device was removed and placed into a new Falcon tube containing 15 mL of release medium at 37 ˚C. Once the dialysis device was removed from the Falcon tube at the time point, it was frozen at 20 ˚C, then freeze dried. The samples were resolubilized in 500 µL of 50%(v/v) ultrapure water and 50% (v/v) methanol. Because the dialysis membrane was large and could allow the passage of free protein and siRNA, the samples were processed to isolate the PTX. The samples loaded in 3 kDa Amicon centrifugal filters and were centrifuged at 14,000 rcf for 1 hour at 4 ˚C. The filtered samples were transferred into HPLC vials then analyzed through UPLC-MS.

To study the in vitro release of siRNA, a second release study was performed. Cy3-siRNA/PTX biSPNPs (1 mL, 5000 ug/mL (by P660), 1.33 x 10^{12} biSPNPs/mL (zetaview)) were rotated at 37 ˚C in the release media (water with 2% v/v methanol and 0.1% v/v acetic acid, relative to the methanol) At the predetermined time point, the sample was centrifuged at 22300 rcf for 1 hour at 4 ˚C. The supernatant was removed carefully without disturbing the pellet. That supernatant was the release sample for that timepoint. The pellet was resuspended through sonication in 1 mL of fresh release media. The resuspended biSPNPs were allowed to continue to release at 37 ˚C until the next time point was ready for retrieval. DLS measurements were taken on day 5 and 14 of the biSPNPs immediately before centrifugation to understand the size. Three instrumental replicates were used to obtain averages of spectra and resulting peak diameters. In addition, Cy3siRNA/PTX biSPNPs that were stored at 4 ˚C were measured on day 5 and 14 as controls. The detection of Cy3-siRNA was conducted by measuring the fluorescence of the samples and comparing it to a standard curve of Cy3-siRNA. The Cy3-siRNA standard curve was generated by serial diluting free Cy3-siRNA in the release media and measuring the fluorescence. The same settings were used for detecting the release sample's fluorescence. The in vitro release curve was produced by summing the release time point's fluorescence with the prior time point's fluorescence then dividing that by the total fluorescence observed for the release experiment. That was then multiplied by 100% to obtain the cumulative release.

3.3.11 Steady-State Fluorescence Spectroscopy

Steady-state emission spectra of release samples were recorded on a Horiba FluoroMax Plus spectrofluorometer equipped with a 150 W xenon arc lamp, Czerny-Turner monochromators, an R928P photomultiplier tube capable of detection from 185-850 nm, and reference photodiode for monitoring lamp output. Excitation and emission slit widths were set to 4 nm. All samples were measured in the release media. Fluorescence values were extracted at λ_{max}= 566 nm. Three instrumental measurements were taken and the standard deviation is reported as an error.

3.3.12 Ultra-Performance Liquid Chromatography – Mass Spectroscopy (UPLC-MS)

UPLC-MS was used for the detection and quantification of released PTX from the biSPNPs. To create a standard curve, PTX was precisely weighed then dissolved in a 50% (v/v) methanol in water solution to produce the following standard solutions: 50000, 25000, 3125, 1562.5, 781.3, 390.6, 195.3, 97.7, 48.8, 24.4, 12.2, 6.1 and 0 ng/mL. The PTX from the release and standards was quantified using the Waters Acquity UPLC system (Waters Corp., Milford, MA, USA) equipped with a quaternary solvent manager, a sample manager, a heated column compartment, an ESI mass detector (QDa), and a cooling autosampler. The chromatographic separation of paclitaxel was performed with an ACQUITY UPLC BEH C18 column (2.1 mm×50 mm, 1.7 µm, Waters, Milford, MA, USA). Mobile phase A (0.1% formic acid in water) and mobile phase B (0.1% formic acid in acetonitrile) were operated with an isocratic elution (60:40 v/v) at a flow rate of 0.8 mL/min. An injection volume of 10 µL and a detection wavelength of 227 nm were used. Each sample and standard were analyzed three times. The column and samples were maintained at a temperature of 25 ˚C and 4 ˚C, respectively. The total run time was 5 minutes. Mass spectral data were obtained in positive electrospray mode (ESI+) in MRM mode for paclitaxel at m/z of 876.44.

3.3.13 STAT3i/PTX biSPNP Dose Preparations

After the fabrication, collection, processing, and characterization of the biSPNPs, doses for in vitro and in vivo studies could be prepared. For in vitro studies, the IC50 of the PTX in the cell line of interest was obtained. The amount of STAT3i/PTX biSPNPs needed was determined by back calculating how many STAT3i/PTX biSPNPs were needed to reach that IC50 of PTX from knowing the loading of the PTX. The empty biSPNP dose was the same as the STAT3i/PTX biSPNP. For in vivo studies, the biSPNP concentration was diluted to 1400 ug/mL in DPBS. Each injection dose was 200 µL of the 1400 µg/mL for a total of 280 µg of biSPNP per mouse.

3.3.14 In vitro cytotoxicity

Mouse GL26-WT and patient-derived glioblastoma cells HF2303, were plated at a density of 1000 cells per well in a 96-well plate 24 hours prior to treatment. Cells were then incubated with either saline, free-paclitaxel (Selleckchem, S1150), free-STAT3 siRNA, Lipofectamine^{TM} 2000, WP1066, empty-BiSPNPs, and loaded-BiSPNPs (STAT3i/PTX) alone or in combination with radiation at their respective IC_{50} doses for 72 hours in triplicate wells per condition. Mouse and patient-derived glioma cells were pretreated with 2h prior to irradiation with 3 Gy and 14 Gy of radiation, respectively. Cell viability was determined with CellTiter-Glo 2.0 Luminescent Cell Viability Assay following manufacturer's protocol. Resulting luminescence was read with the Enspire Multimodal Plate Reader (PerkinElmer). Data were represented graphically using the GraphPad Prism 9.0 software, and statistical significance was determined by one-way ANOVA followed by Tukey's test for multiple comparisons.

3.3.15 Determination of released DAMPs and Type I Interferon level in conditioned media

To analyze the levels of DAMPs, type I interferons, and inflammatory cytokines in the tumor-conditioned media and on tumor cells, mouse and patient-derived glioma cells were seeded at a density of 1 x 10^6 cells into a 6-well plate. The cells were then allowed to settle overnight before treatment. On the next day, cells were treated with either saline, free-paclitaxel, free-STAT3 siRNA [STAT3i], Lipofectamine^{TM} 2000, WP1066, empty-BiSPNPs and loaded-BiSPNPs (STAT3i/PTX) for 2 hours in triplicate wells prior to receiving 3Gy for mouse cells and 14Gy for patient-derived cells of irradiation. Release of DAMPs was assessed 72 hours post-irradiation. For assessing the level of calreticulin, cells were harvested, dispersed with accutase, and stained with anti-calreticulin antibody (1:200) in PBS supplemented with 2% FCS (flow buffer) for 30 min at 4 °C. Cells were rinsed twice using flow buffer. The samples were then analyzed using a BD FACS ARIA SORP using 647 lasers. Data were analyzed with FlowJo version 10 software. Concentrations of HMGB1, IL33, IL6, IL1α, TNF-α, IFNγ, IL1β, IFN-β, CCL2, CCL5, CXCL10 in the culture supernatants were measured by quantitative ELISA, either following the manufacturer's protocol (R&D) or through Immunology Core at the Rogel Cancer Center, Michigan Medical School. ATP levels in the cell cultures' supernatants were determined by ATP determination kit following the manufacturer's instructions.

3.3.16 Statistical Analysis

Normality tests were performed to determine whether parametric or nonparametric tests would be used for statistical analysis. The number of groups compared dictated which test to use. P values less than 0.05 were deemed statistically different. Error bars are plotted as the average ± standard deviation, unless otherwise stated. All statistics were performed with Prism 9.4.1 (GraphPad Software).

3.4 Results and Discussion

3.4.1 Fabrication and characterization of STAT3i/PTX biSPNP

STAT3i/PTX bicompartmental synthetic protein nanoparticle (STAT3i/PTX biSPNPs) were produced through electrohydrodynamic co-jetting. First, two separate solutions were prepared that represented each compartment: the paclitaxel and the STAT3 siRNA as shown in **Figure 3-1**A.

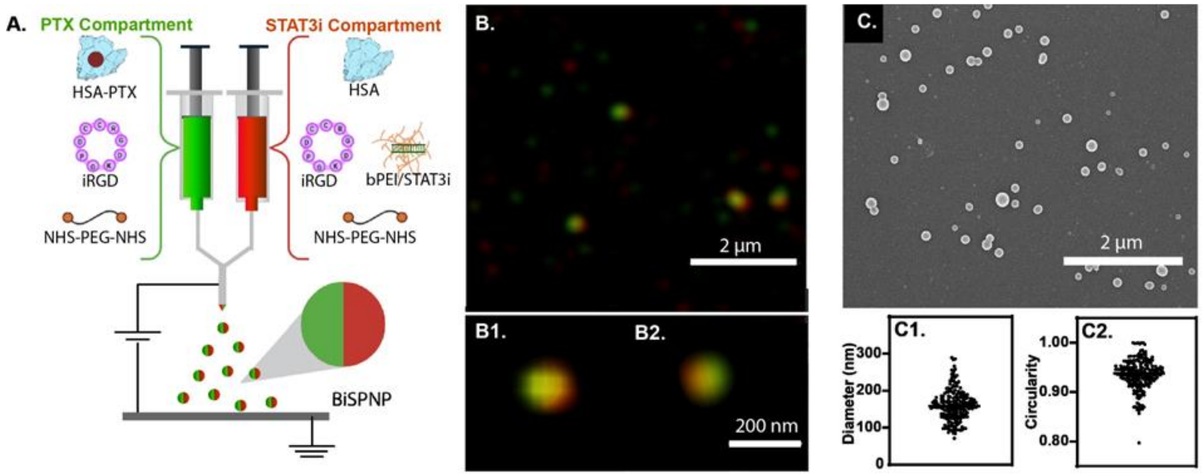

Figure 3-1. Electrohydrodynamic co-jetting to fabricate STAT3i/PTX biSPNPs. The left compartment contains paclitaxel (PTX) in the form of HSA-PTX whereby the paclitaxel is sequestered within the hydrophobic domains of the albumin. It also contains the tumor peptide, iRGD, and the bifunctional crosslinker, NHS-PEG-NHS. The second compartment, located on the right, represents the STAT3 siRNA compartment. It features the complexed branched PEI with STAT3i siRNA (bPEI/STAT3i), albumin, iRGD, and the NHS-PEG-NHS. Through EHD co-jetting, biSPNPs are formed with distinct PTX and STAT3 siRNA hemispheres. B. Structured illumination Microscopy of the STAT3i/PTX biSPNPs, each with a different fluorescent dye to show the two hemispheres. Scale bar is 2 microns for the top image and 200 nanometers for the bottom images (B1 and B2). C. Scanning Electron Microscopy (SEM) of the STAT3i/PTX biSPNPs. The diameter and the circularity of n=200 analyzed STAT3Ti/PTX biSPNPs are shown in C1 and C2, respectively.

The paclitaxel (PTX) compartment consisted of HSA-PTX, iRGD, and the bifunctional crosslinker. The HSA-PTX was produced by high pressure homogenization as described in **Chapter 2**. The paclitaxel was used in this form as it was shown to possess better morphological features after EHD jetting, high loading, and desirable release kinetics. The second compartment, STAT3 siRNA (or STAT3i), as shown as the right compartment in **Figure 3-1** had been previously described by Gregory et al.[218] It consisted of HSA, STAT3 siRNA complexed with branched PEI (bPEI/STAT3i), iRGD, and the bifunctional crosslinker. The formulations were in a co-solvent system of 80%(v/v) water and 20%(v/v) ethylene glycol, which were pumped together in a side-by-side configuration. A positive voltage (8-10 kV) was applied to the joined needles from both compartments to initiate the EHD co-jetting to produce biSPNPs. Each compartment used iRGD as the tumor penetrating peptide because of its in vivo targeting capabilities shown when incorporated in SPNPs.[111] In addition, in vitro uptake studies showed the highest uptake in glioma cells was observed at this concentration (**Supplemental Information**).

To confirm the bicompartmental configuration of the SPNPs, Structured Illumination Microscopy (SIM) was performed on EHD co-jetted biSPNPs (**Figure 3-1**B). The PTX and the STAT3i compartments each contained an Alexa Fluor dye to visualize the individual compartments. The green compartment in **Figure 1B** represents the PTX compartment, which contained an Alexa fluor 488. Contrastly, the red compartment corresponds to the STAT3i compartment, which contained Alexa Fluor 647. These results indicate that during EHD co-jetting, the compartments are maintained in the formation of biSPNPs.

To obtain more information regarding the morphological features of the STAT3i/PTX biSPNPs, Scanning Electron Microscopy (SEM) was performed and is shown in **Figure 3-1C**, which shows the STAT3i/PTX biSPNPs in their as-jetted dry state, prior to any processing. SEM micrographs were used with ImageJ analysis to determine the diameter and circularity of 200 analyzed biSPNPs according to previously reported methods.[114] The average dry-state diameter was 159 ± 42 nm, the average circularity was 0.94 ± 0.03, and the PDI was 0.197. After incubating the SPNPs at 37 ˚C, the SPNPs were collected with a 0.05% (v/v) Tween20 in DPBS. The SPNPs were then subjected to serial centrifugation to obtain the desired size of the SPNPs. First, the collected SPNPs were tip sonicated on ice then filtered through a 40-micron filter. The filtered SPNPs were spun at 3200 rcf for 5 minutes. The pellet contained larger SPNPs and aggregates, which were discarded. The supernatant was further processed by centrifuging at 21300 rcf for 1 hour at 4 ˚C. The pellets from the resulting centrifugation were combined, then washed with fresh DPBS to remove residual Tween20 from the collection step. Thereafter, the final SPNPs were resuspended in fresh DPBS, and tip sonicated on ice. These SPNPs were characterized using Dynamic Light Scattering (DLS) and Electrophoretic Light Scattering (ELS).

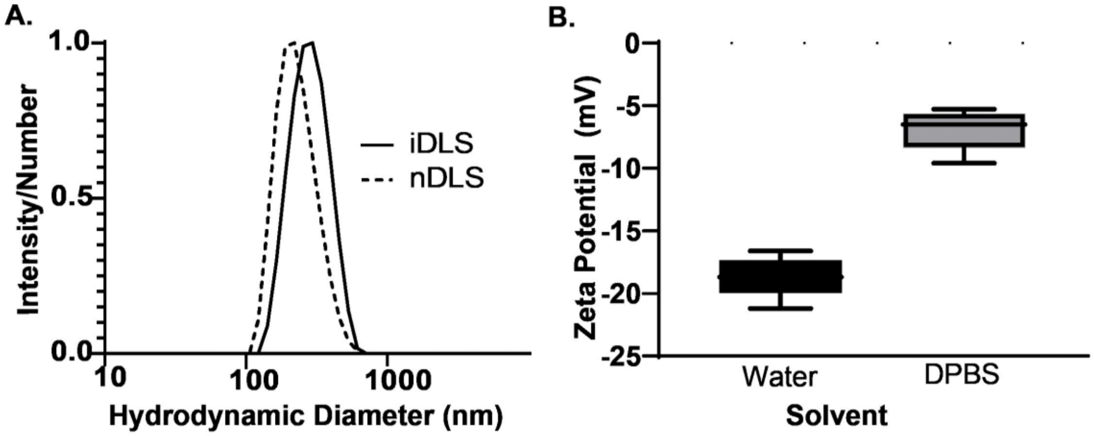

Figure 3-2. A. The hydrodynamic diameter in DPBS after collection and processing. Intensity DLS (iDLS) is shown in the solid line and the number DLS (nDLS) is shown as the dotted line. B. The zeta potential in water (-18.7 ± 1.6 mV, n=6 instrument replicates) and DPBS (-6.9 ±1.5 mV, n=6 instrument replicates).

Figure 3-2A shows the hydrodynamic size of the STAT3i/PTX biSPNPs in PBS as the number-spectra (dashed line, peak diameter = 237 nm) and the intensity-spectra (solid line, peak diameter = 292 nm). The z-average was 285 nm with a PDI of 0.244. The surface charge in water via ELS was -18.7 ± 1.6 mV and in DPBS was -6.9 ± 1.5 mV. This negative zeta potential is expected due to the SPNP being produced from HSA protein.

3.4.2 In vitro release of PTX and siRNA from biSPNPs

In vitro release studies were performed to understand the release of PTX and siRNA from the biSPNPs. BiSPNPs were formulated using a negative control siRNA that was tagged with Cy3 (Cy3-siRNA) and PTX to form Cy3siRNA/PTX biSPNPs. The formulation was the same as the STAT3i/PTX biSPNPs except the type of siRNA used. This was chosen for ease of detection which was previously reported.[218] After collecting and processing the biSPNPs, they were placed inside a prepared 300 kDa dialysis device following the manufacturer's instructions. The dialysis device was then placed inside a 50 mL tube containing 15 mL of dialysis media. The dialysis was allowed to agitate over time at 37 ˚C. At predetermined time points, the dialysis device was removed and placed inside a fresh 50 mL tube containing pre-warmed dialysis media (15 mL). The samples were subsequently frozen at -20 ˚C then freeze dried. The samples were resuspended 0.5 mL of a 1:1 mixture of methanol and ultrapure water, by volume. Fluorescence readings were performed on the samples, but no detectable Cy3siRNA was recorded. It was hypothesized that there were not enough nanoparticles in the release study to obtain detectable release. Therefore, the sample within the dialysis membrane was removed and measured for Cy3 fluorescence. There were sufficiently high fluorescent counts indicating that there would be detectable fluorescence if Cy3siRNA was released. It was then questioned whether the released Cy3siRNA could not bypass the membrane despite it being sufficiently larger than the size of siRNA. The retrieved dialysis sample was then spun down at 21130 rcf for 1 hour at 4 ˚C to separate nanoparticles from any released Cy3siRNA. The supernatant was measured, but only 1.9% of the total fluorescence came from this sample after one month of release. It was possible that siRNA was stuck on the membrane and could not be detected. While the siRNA could not be detected for release, the release samples were processed to measure the PTX. The release samples were filtered through a 3 kDa centrifugal filter at 14,000 rcf for 1 hour at 4 ˚C. The filtrate was analyzed via UPLC-MS to obtain the following release profile.

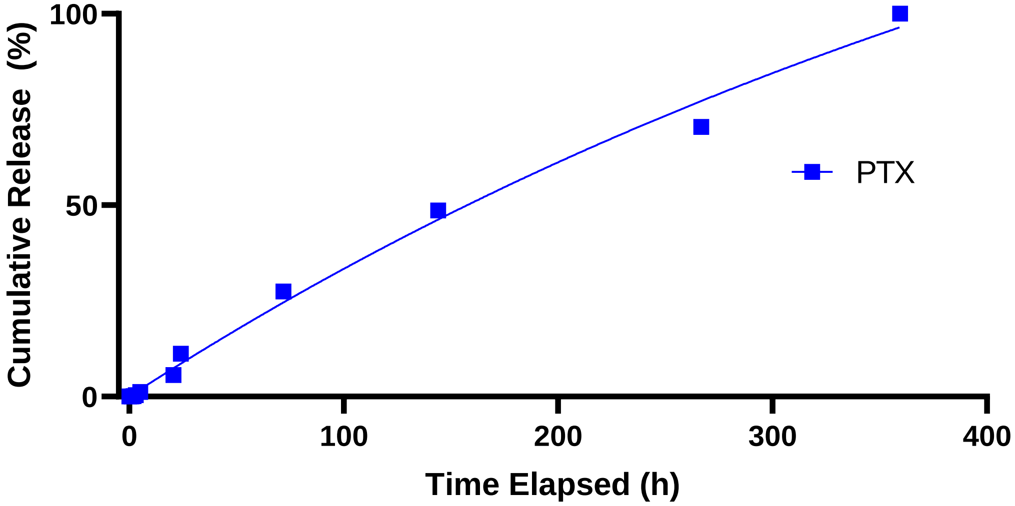

Figure 3-3. In vitro release profile showing the release of PTX from Cy3siRNA/PTX biSPNPs. Cy3siRNA/PTX biSPNPs were placed inside a 300 kDa dialysis device. The device was placed inside 15 mL of release media (water with 2%(v/v) methanol and 0.1%(v/v) acetic acid, relative to methanol) inside a 50 mL tube and allowed to agitate at 37 ˚C. At predetermined timepoints, the dialysis device was removed from the 50 mL tube and placed inside a new 50 mL tube containing 15 mL of fresh pre-warmed release media. The release samples were frozen, freeze dried, then resuspended in 0.5 mL of 1:1 (v/v) co-solvent mixture of methanol and ultrapure water. The samples were then filtered through a 3 kDa centrifuge filter by centrifuging at 14,000 rcf for 1 hour at 4 ˚C. The filtered samples were analyzed via UPLC-MS (n=3). The release curve is plotted as the percent of cumulative release. The values were normalized using the last time point value.

To address the concern of siRNA sticking to the dialysis membrane, another in vitro release study was conducted, but using a different method. To avoid using a dialysis membrane, the release study was performed using the centrifugation method. Briefly, Cy3siRNA/PTX biSPNPs were resuspended in 1 mL of release buffer and allowed to rotate at 37 ˚C. At predetermined timepoints, the sample was spun down, the supernatant was removed which represented the release sample for that time point. The pellet was resuspended in the release buffer and allowed to continue releasing 37 ˚C under rotation until the next release sample was retrieved. Throughout the release (Day 5, 9 and 14), Cy3siRNA/PTX biSPNP were measured for their size through DLS (**Supplemental Information)**. The release samples were analyzed through fluorescence to obtain the following release curve as the cumulative release percentage normalized using value from the last time point.

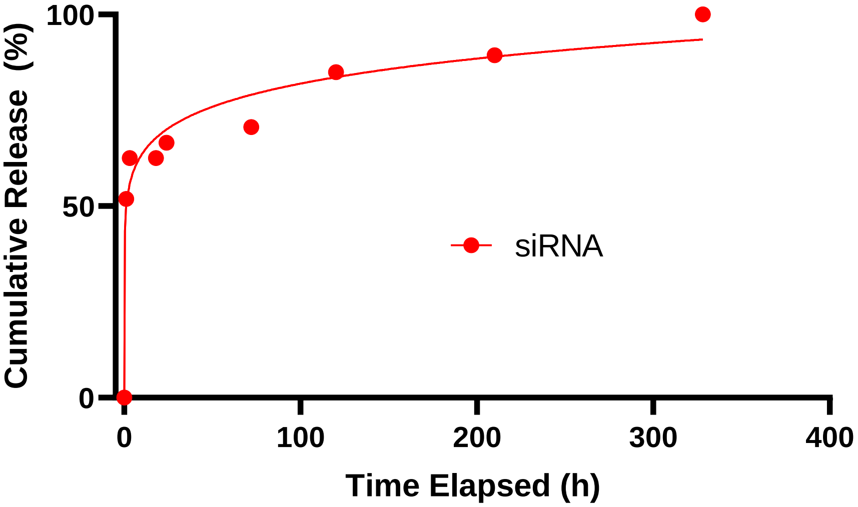

Figure 3-4. Cumulative release percentage of Cy3siRNA from Cy3siRNA/PTX biSPNPs. Cy3siRNA/PTX biSPNPs were incubated at 37 ˚C in 1 mL of release media (water supplemented with 2% (v/v) methanol and 0.1% (v/v) acetic acid, relative to methanol). At predetermined time points, the biSPNPs were centrifuged at 21130 rcf for 1 hour at 4 ˚C. The supernatant was removed, which was the release sample for that time point. The biSPNPs were resuspended and allowed to continue releasing until the next time points. The release samples were detected using a fluorometer for three instrumental replicates. The graph depicts the cumulative release percent, which was normalized according to the total amount released (or the last cumulative time point).

The release exhibits a burst release with most of the fluorescence being detected within the first few hours of the release. The fitted line follows a logarithmic curve with an R-squared of 0.98. It should be emphasized that these release curves are plotted as the cumulative release, which was then normalized to the last value. Therefore, all the release curves show a cumulative release at 100%, but this does not mean that 100% of the loaded molecule was released. The amount of siRNA released here would be calculated as the cumulative fluorescence from the release divided by the fluorescence measured in the biSPNPs prior to the release study. This value was then multiplied by 100%. This was calculated to be 61.5%, so 61.5% of the Cy3siRNA detected in the biSPNPs was measured in the release samples. While this represents the fluorescence detected through this method, it is important to understand what is releasing since this method did not a method to verify the compound. Therefore, DLS was used to understand the size and whether the centrifugation was sufficient to pellet the nanoparticles. All samples were measured three times then averaged as shown in the **Supplemental Information.** The contents of the release samples show sizes that are indicative of nanoparticle sizes (around 100-200 nm). This put into question whether siRNA was really released, or if the fluorescence was just detecting nanoparticles that could not be spun down and contained the siRNA, which was subsequently measured. Therefore, additional processing was performed. The release samples were spun down at 21130 rcf for 3 hours at 4 ˚C. The top 0.5 mL (of a total of 1 mL) of the samples was carefully removed and analyzed for their size. According to **Supplemental Figure 3-17**, the spin down did not effectively remove the distributions that could be nanoparticles. Therefore, these samples were filtered through a 220 nm syringe filter and measured again. The resulting DLS sizes are shown in **Supplemental Figure 3-18**. The sizes decreased but were still on the scale of nanoparticle sizes. Despite these results, the fluorescence was measured again and graphed with the original siRNA release.

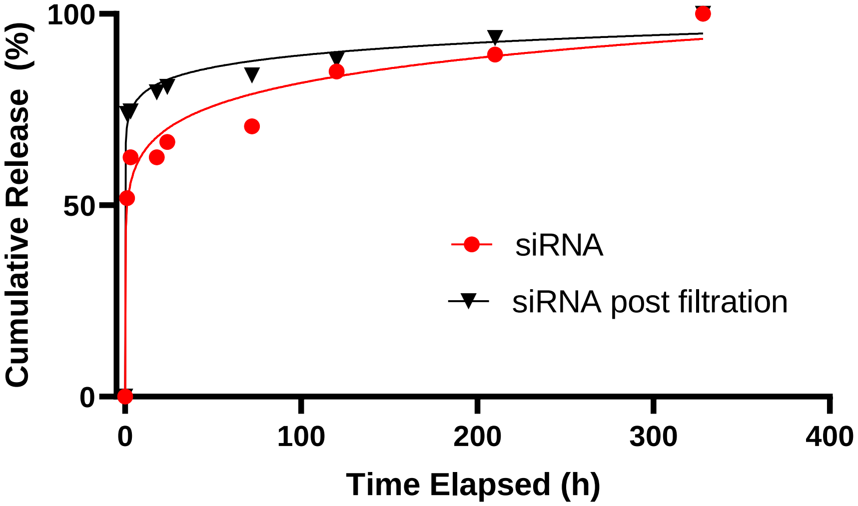

Figure 3-5. In vitro release of Cy3siRNA from Cy3siRNA/PTX biSPNPs comparing before and after filtration. The black line (siRNA post filtration) shows the release curve of siRNA after processing and filtering the release samples shown in red. The plot is graphed as the percent of cumulative release relative to the last time point's release value.

As described earlier, the percent released was 61.5%, which was representative of 61.5% of the total fluorescence was detected in the release samples. However, the DLS data showed nano-sized particles. This put into question what was releasing during this study, but if 61.5% of the fluorescence was detected from the release study, and if it was biSPNPs that did not get spun down, one would expect that 61.5% of the biSPNPs would also be in the release samples. This was clearly not the case because after a three-hour spin down, there were no visible pellets of biSPNPs and after one hour spin downs for the release study, the pellet was large and visible. To further understand the calculation of percent Cy3siRNA released according to fluorescence was calculated after the processing of the release samples. This calculation resulted in a total of 11% of the total fluorescence being detected. Through these steps, most of the fluorescence was removed from the samples. An explanation for what is occurring could be that the release samples contain polyplexes. In the formulation of the siRNA compartment, branched PEI and siRNA are complexed together. It's been shown that polyplexes can be on the nano-scale.[220] It is unlikely that the siRNA is freely diffusing out of the biSPNP, but is rather maintained in its polyplex form as indicated by the DLS. To elucidate the release mechanism of siRNA from these biSPNPs, further studies can be conducted using methods previously reported.[221,222] While certainly interesting, it should be emphasized that these in vitro release studies are limited as they cannot recapitulate the complex biological environment that the nanoparticles experience.

3.4.3 Storage Stability of STAT3i/PTX biSPNPs

The size stability of the STAT3i/PTX biSPNPs was studied through DLS over two weeks (**Figure 3-6**). A stock solution of biSPNPs was stored at 4 ˚C and at time points, the stock solution was briefly vortexed. Vertexing was conducted to obtain a true sample population of the mixture as opposed to just the top, which may exclude larger particles that could settle at the bottom of the tube. Ten microliters of the stock biSPNPs were removed, diluted in DPBS, then measured through DLS. **Figure 3-6**A of the number-DLS shows good overlap for the first three days (Day 0, 1 and 2). The intensity-DLS is shown in the **Supplemental Information**. At a week (Day 7), the distribution is shifted to the right, indicating a larger size. After two weeks (Day 14), the distribution overlaps well with the day 7 spectra, but slightly larger. **Figure 3-6**B depicts the average peak diameter of both intensity and number DLS from three measurements. Again, the overall trend is upwards towards a higher peak diameter. However, using statistical analysis (Brown-Forsythe and Welch ANOVA tests) there was not a significant difference between sizes in both groups (number-based DLS sizes and intensity-based DLS sizes) ($p>0.05$). Additional statistical analyses (Mann-Whitney) were performed to compare day 0 to all time points. It was found again that there were no statistical differences between any of the days and the first day ($p>0.05$).

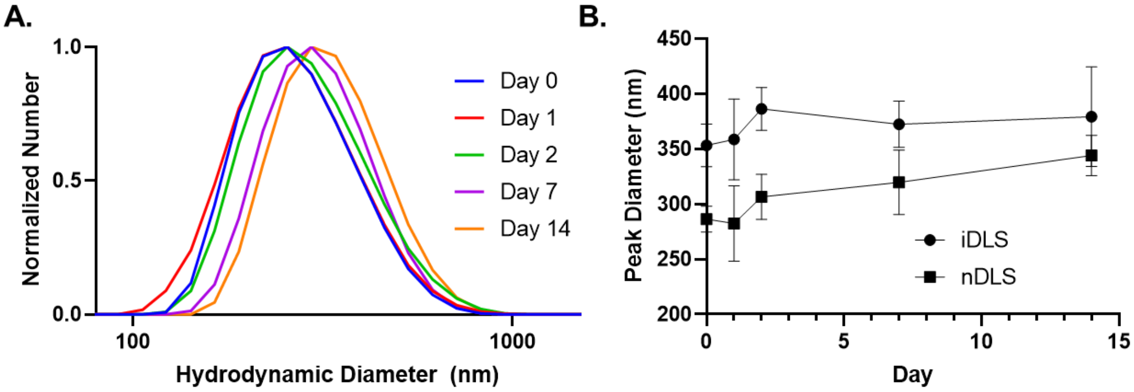

Figure 3-6. Storage stability of STAT3i/PTX biSPNPs at 4 ˚C. A. Normalized number-based DLS showing the hydrodynamic diameter distribution of the biSPNPs over two weeks. B. Plot of the peak diameter of the biSPNPs over time. Both the number- and intensity- DLS is shown. The data is plotted as the average of three measurements with the error bar showing the standard deviation.

3.4.4 Characterization comparison of biSPNPs

The primary therapeutic biSPNP used in this chapter is mouse specific STAT3 siRNA/ PTX biSPNPs, which were termed as STAT3i/PTX biSPNP. In this section, they will be referred to as mSTAT3i/PTX biSPNPs. Other biSPNPs were made as controls, or for specific experiments. Empty biSPNPs were produced as negative control for the loaded biSPNPs, which did not contain any STAT3 siRNA or PTX. BiSPNPs with human specific STAT3i were produced to form hSTAT3i/PTX biSPNPs for testing the biSPNPs in human glioma cells. Lastly, Cy3siRNA/PTX biSPNPs were fabricated for in vitro release experiments to detect the siRNA through fluorescence readings. Establishing morphology and charge equivalence between the groups is crucial. If the sizes were different between the control and the loaded biSPNP, for example, it would not be clear whether the therapeutic impact was compounded by the physical characteristics and not the payload alone. **Figure 3-7**A-C shows the SEM images for the mSTAT3i/PTX biSPNP (**Figure 3-7A**), hSTAT3i/PTX biSPNP (**Figure 3-7B**), empty biSPNP (**Figure 3-7C**), and Cy3siRNA/PTX biSPNP (**Figure 3-7**D). To the right of each micrograph shows the size distribution of the SPNPs analyzed from SEM images. Each analysis was performed with n=200 SPNPs. The average size for the mSTAT3i/PTX, hSTAT3i/PTX, empty biSPNP, and Cy3siRNA/PTX biSPNPs were 159 ± 42 nm, 170 ± 32 nm, 170 ± 24 nm, and 176 ± 46 nm, respectively.

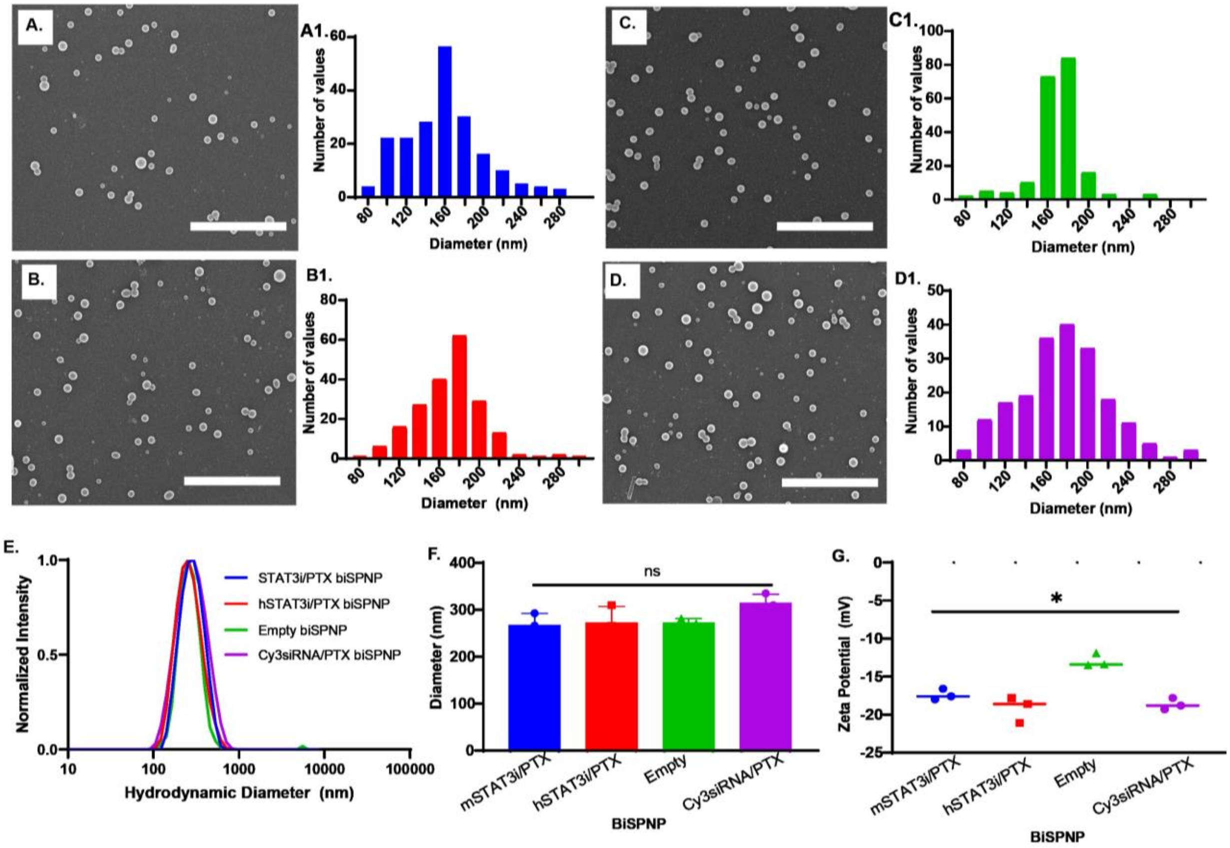

Figure 3-7. Comparison of the mouse STAT3i/PTX biSPNPs (mSTAT3i/PTX biSPNPs), human STAT3i/PTX biSPNPs (hSTAT3i/PTX), and empty biSPNPs. A. SEM micrograph of mSTAT3i/PTX biSPNPs (scale bar = 2 micron) and the corresponding diameter distribution of 200 analyzed biSPNPs (A1). B. SEM micrograph of hSTAT3i/PTX biSPNPs (scale bar = 2 micron) and the corresponding diameter distribution of 200 analyzed biSPNPs (B1). C. SEM micrograph of Empty biSPNPs (scale bar = 2 micron) and the corresponding diameter distribution of 200 analyzed biSPNPs (C1). D. SEM micrograph of Cy3siRNA/PTX biSPNP (scale bar = 2 micron) and the corresponding diameter distribution of 200 analyzed biSPNPS (D1). E. The hydrodynamic diameter of all groups measured via DLS. F. The peak diameter from the DLS spectra in E are not statistically different (p>0.05, Kruskal-Wallis test). G. The zeta potential of all biSPNP groups in water is significantly different (*p<0.05, Kruskal-Wallis test).

After the collection and processing procedure, the SPNPs were analyzed in their hydrodynamic state. From **Figure 3-7E**, the DLS shows good spectral overlap between the groups. Despite each of the SPNPs having a slightly different distribution of size from **Figure 3-7A1-D1**, the processing of the SPNPs ensures that the SPNPs are comparable sizes. The average diameter of the SPNPs is plotted in **Figure 3-7F**, which shows that the sizes are not significantly different (p>0.05, Kruskal-Wallis test). The zeta potential for all groups is negative and were significantly different from each other (p<0.05, Kruskal-Wallis test). The empty biSPNPs are slightly less negative (-12.9 ± 0.9 mV) than the other groups (mSTAT3i/PTX biSPNP = -17.4 ± 0.7 mV, hSTAT3i/PTX biSPNP =

-19.2 ±1.7 mV, Cy3siRNA/PTX biSPNP = -18.6 ± 0.8 mV). Note that the mSTAT3i/PTX biSPNPs zeta potential reported here (-17.4 ± 0.7 mV) is slightly different from what was reported in the first results section (-18.7 ± 1.6 mV) because six replicates were used whereas in this section, three replicates were used. When comparing the groups without the empty biSPNPs, they were not significantly different from each other (p=0.23, Kruskal-Wallis test). This could be attributed to the formulation differences. In the empty biSPNPs, a siRNA was not included, but PEI was. Since PEI is positively charged and is typically complexed with the negatively charged siRNA, this could skew the zeta potential towards a more positively charged biSPNP.

3.4.5 Targeting STAT3 together with paclitaxel (PTX) to inhibit tubulin depolymerization sensitizes mouse-HGG and human patient-derived HGG cells to radiotherapy and induces immunogenic cell death

In this study we sought to determine whether treatment with bi-compartmentalize synthetic protein nanoparticles (biSPNPs) containing siRNA against STAT3 (STAT3i) and PTX would sensitize both murine-HGG and human patient-derived HGG cells to radiotherapy and induce immunogenic cell death (ICD). We performed cell viability assay with neural progenitor cells (NPCs) derived murine-HGG (i.e., GL-26) and human patient-derived HGG (i.e., HF2303) cells by treating them with the IC_{50} values of biSPNP and IR. Data analysis demonstrated that biSPNP (STAT3i/PTX) markedly enhanced radiosensitivity and inhibits the cellular proliferation in both mouse-HGG (**Figure 3-8**B) and patient-derived glioma cells (**Figure 3-8**C). Treatment with biSPNP (STAT3i/PTX) + IR showed a consistent decrease in survival of mouse-HGG (i.e., GL-26) cells tested, ranging between 85% for the biSPNP (STAT3i/PTX) + IR treated group ($p \leq 0.0001$) in comparison to 70.82% for the biSPNP (STAT3i/PTX) treated group after 72h of treatment (**Figure 3-8**B). Similarly, biSPNP (STAT3i/PTX) in combination with IR showed a marked decrease in survival of patient-derived glioma cells tested ranging from 88.15% for the biSPNP (STAT3i/PTX) + IR treated group ($p \leq 0.0001$) in comparison to 75.01% for the biSPNP (STAT3i/PTX) treated group after 72h of treatment (**Figure 3-8**C).

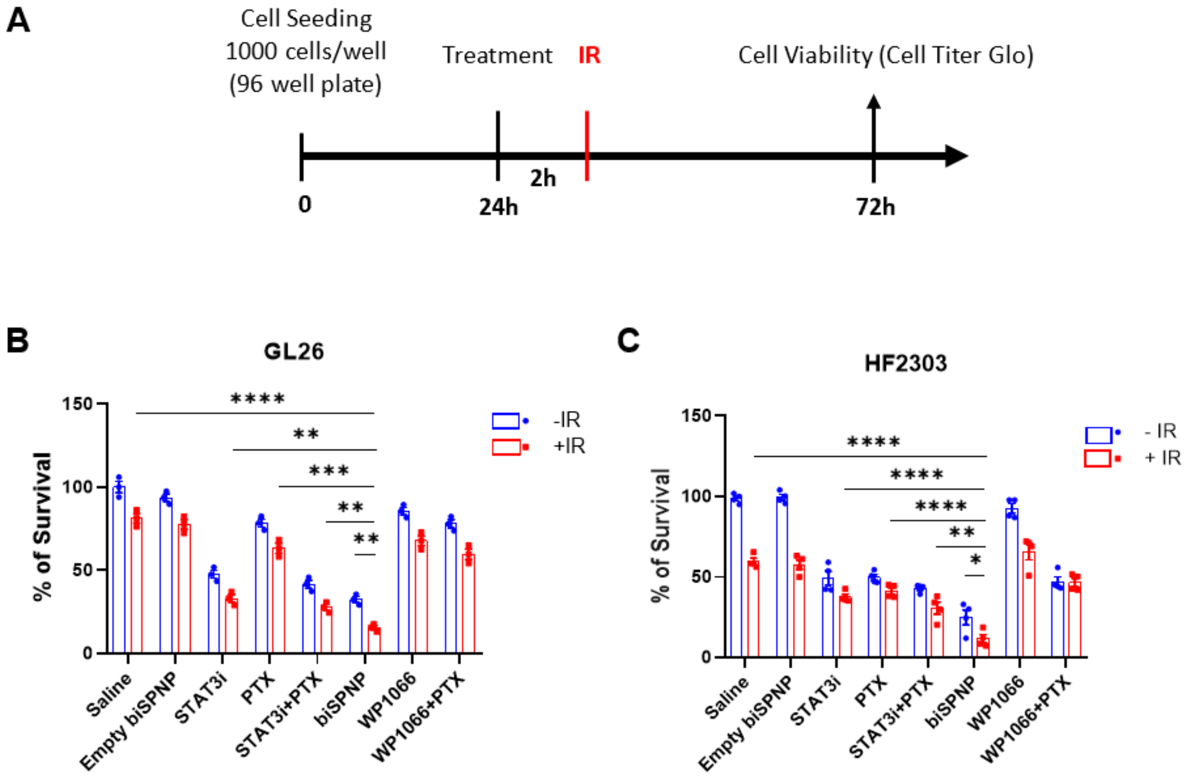

Figure 3-8. In *vitro* inhibition of STAT3 and depolymerization of tubulin through biSPNP (STAT3i/PTX) increases radiosensitivity in murine GL26 HGG and human patient-derived cells. (A) (A) Schematic shows the timeline of the in vitro application of biSPNP (STAT3i/PTX) and/or radiation in mouse-HGG (GL-26) and patient-derived HGG cells (HF2303). (B) GL-26 and (C) HF2303 cells were treated with either biSPNP (STAT3i/PTX), empty-BiSPNP, free-STAT3 siRNA (STAT3i), free-PTX, WP1066 (a novel STAT3 inhibitor) or in combination with radiation (3Gy) at their respective IC50 doses for 72 h. Cells were pretreated with the respective compounds 2h prior to irradiation with 3Gy of radiation. Bar plot shows the % of viable mouse GL-26 or human HF2303 cells after treatment either with saline, biSPNP, Empty-biSPNP, free-STAT3 siRNA, free-PTX, WP1066 or in combination with IR (3 Gy). All the statistical analysis was done through unpaired t test. Bars represent mean ± SEM (n = 3 biological replicates). ns= not significant, *p<0.05 **p< 0.01, ***p< 0.0001, ****p< 0.0001.

Previously, systemic delivery of STAT3i SPNPs has been shown to enhance antitumor responses against glioma *in vivo* by targeting STAT3 dependent immune pathways.[218] Also, paclitaxel (PTX) has been reported to effectively induce GBM cell death in several *in vitro* studies.[223] Therefore, we assessed whether anti-tumor responses caused by biSPNP (STAT3i/PTX) alone or in combination with IR were due to the induction of immunogenic cell death (ICD) in mouse-HGG and patient-derived glioma cells. We measured the levels of Calreticulin (CRT), ATP, HMGB1, IL1α, IL6, IL33 and TNFα, common damage associated molecular pattern (DAMPs) molecules associated with ICD and expressed/released by dying tumor cells. We first quantified the level of CRT expression on the surface of mouse-HGG cells in response to biSPNP (STAT3i/PTX) or in combination with IR. Mouse-HGG i.e., GL-26 cells treated with biSPNP (STAT3i/PTX) + IR displayed a 3.40-fold ($p \leq 0.0001$) increase in CRT expression relative to 2.73-fold ($p \leq 0.0001$) increase in biSPNP (STAT3i/PTX) treated group compared to saline treated controls after 72h of treatment (**Figure 3-9**B-C).

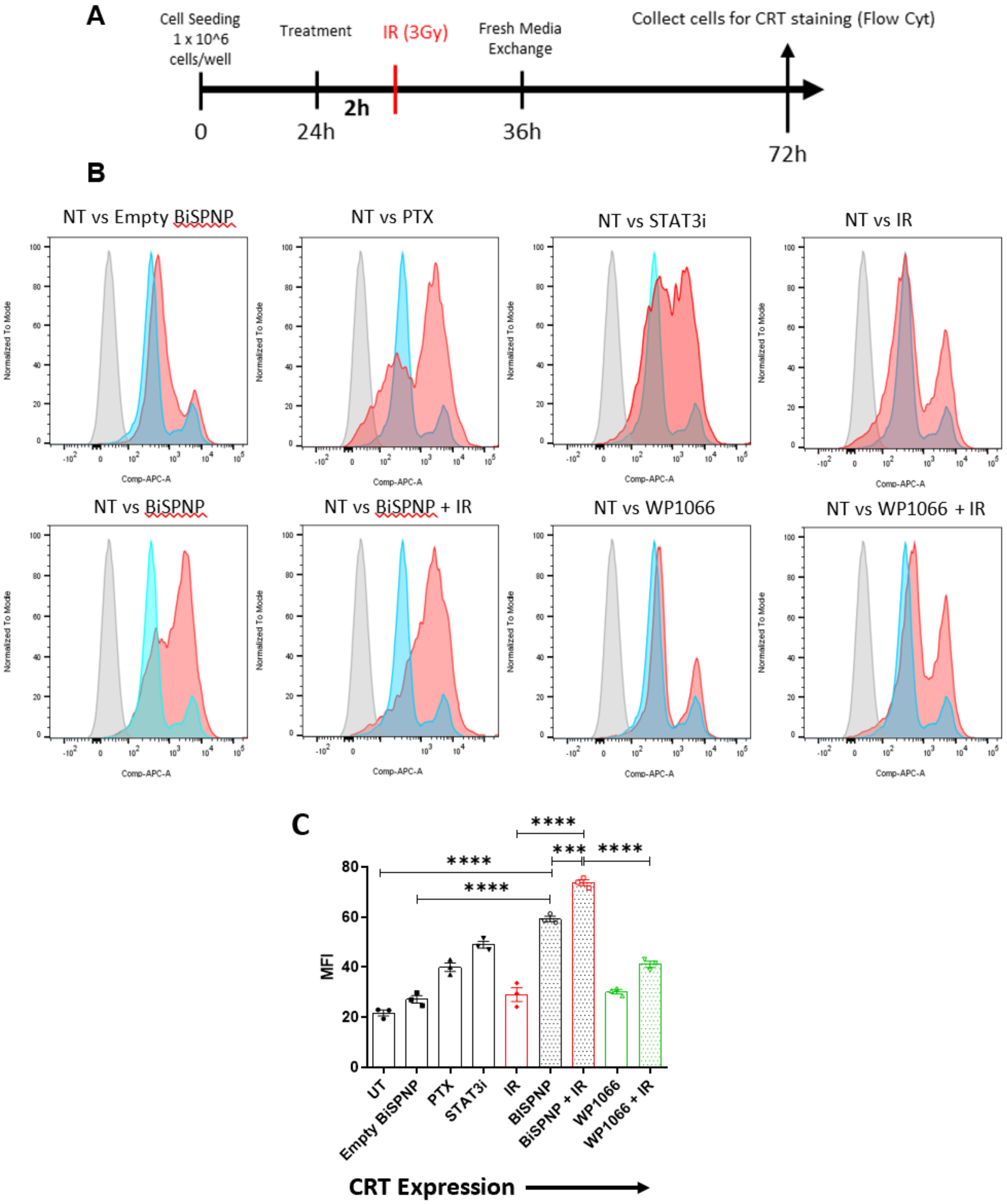

Figure 3-9. BiSPNP (STAT3i/PTX) enhances the surface Calreticulin expression on GL26 cells. (A) Timeline of treatment to assess Calreticulin expression as ICD marker following biSPNP (STAT3i/PTX) treatment. (B-C) Surface

expression of Calreticulin on GL26 cells were determined following biSPNP treatment (at IC50 values) alone or in combination with 3Gy of IR. Representative histograms and bar diagrams display calreticulin's expression levels following different therapeutic treatments (In histograms: blue = non-treated and red =treated) compared to non-treated, non-irradiated controls (grey). Cells were also treated with combined (STAT3i+PTX), free-PTX, free-STAT3i, empty-biSPNPs and WP1066 at their respective IC50 values within the same experimental condition and analyzed after 72h. MFI= mean fluorescence intensity. ns= non-significant, *p< 0.05, **p<0.01, ***p<0.001, ****p<0.0001; unpaired t-test. Bars represent mean ± SEM (n= 3 biological replicates).

We also tested the release of HMGB1 in the supernatant of both mouse and patient derived HGG cells in response to biSPNP (STAT3i/PTX) or biSPNP (STAT3i/PTX) + IR treatments. We observed a 5.83-fold ($p \leq 0.001$) increase levels of HMGB1 release in GL-26 cells when treated with biSPNP (STAT3i/PTX) compared to saline treated control (**Figure 3-10**B). We observed an additional 1.67-fold ($p \leq 0.01$) increase in extracellular HMGB1 release in the supernatant of GL-26 cells treated with biSPNP (STAT3i/PTX) + IR (**Figure 3-10**B) relative to saline treated control.

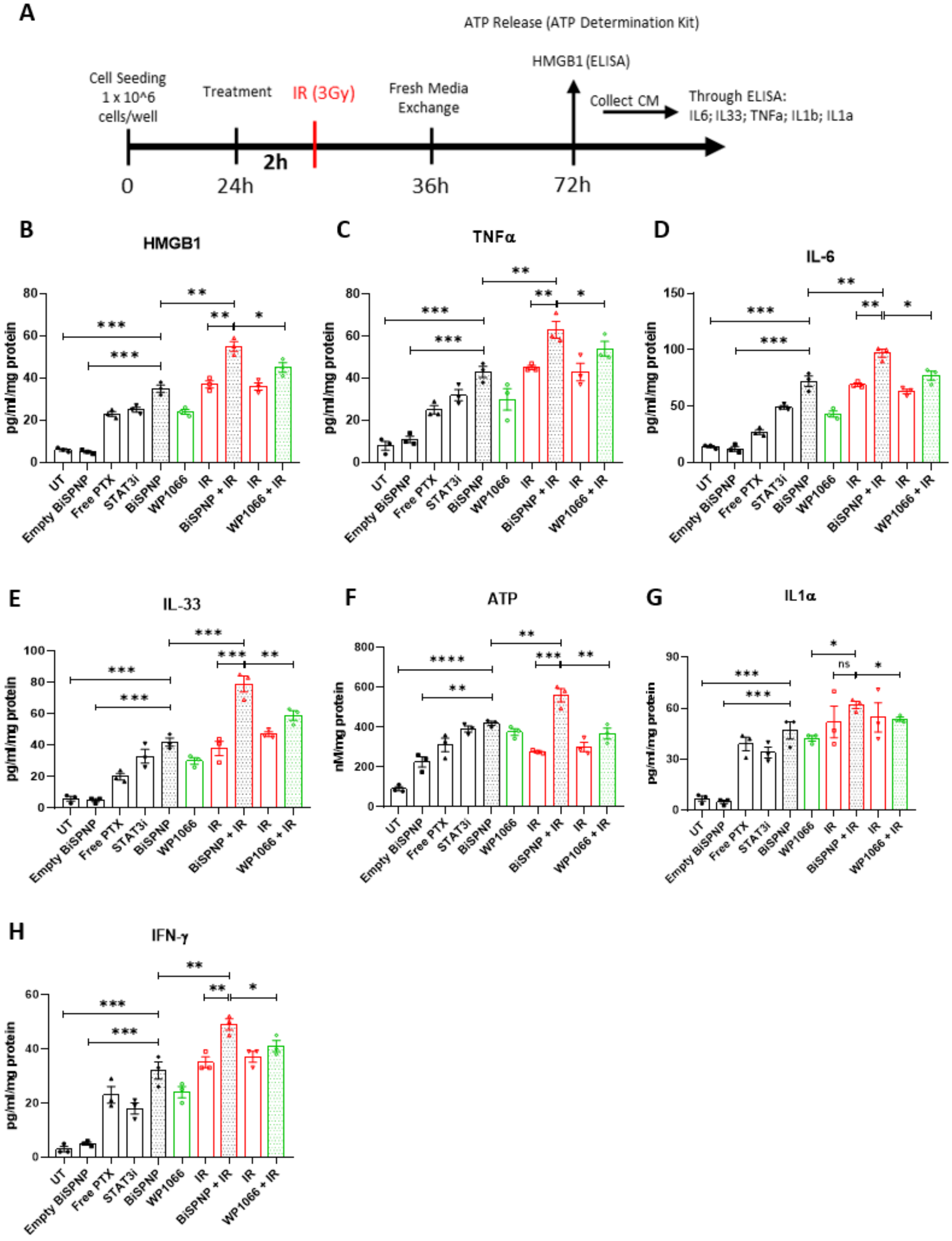

Figure 3-10. BiSPNP (STAT3i/PTX) in combination with radiation enhances the immunogenic cell death (ICD) markers in murine GL26 HGG cells. (A) Timeline of treatment to assess ICD following BiSPNP (STAT3i/PTX) and other therapeutic treatments. (B-H) Quantitative ELISA shows the levels of DAMPs as ICD markers i.e., HMGB1, TNFα, IL6, IL33, ATP, IL1α, and IFNγ in the mouse HGG GL26 cells after treatment either with biSPNP, empty-biSPNP, free-PTX, free-STAT3 siRNA, WP1066 or in combination with IR (3Gy) at their respective IC50 doses and analyzed after 72h. All the statistical analysis were done through unpaired t test. Bars represent mean ± SEM (n = 3 biological replicates) ns= non-significant, *p<0.05, **p<0.01, ***p<0.001, ****p<0.0001.

A similar response was elicited in human patient derived HGG cells treated with biSPNP (STAT3i/PTX) alone or in combination with IR (**Figure 3-11B**). There is a 2.68-fold ($p \leq 0.001$) increase levels of HMGB1 release in HF2303 cells when treated with biSPNP (STAT3i/PTX) (**Figure 3-11B**) and an additional 1.37-fold ($p \leq 0.05$) increase in extracellular HMGB1 release in the culture supernatant when treated with biSPNP (STAT3i/PTX) + IR (**Figure 3-10B**) compared to saline treated control (**Figure 3-11B**). We observed comparable results for additional DAMPs such as ATP, TNFα, IL6, IL33 and IL1α in GL-26 mouse-HGG (**Figure 3-10C-H**) and human patient derived HGG (**Figure 3-11C-G**) relative to their respective saline treated control when treated with BiSPNP (STAT3i/PTX) alone or in combination with radiation. Taken together, these results demonstrated that biSPNPs (STAT3i/ PTX) in combination with IR enhances the radio-sensitivity and induces ICD in both human and mouse high-grade glioma cells.

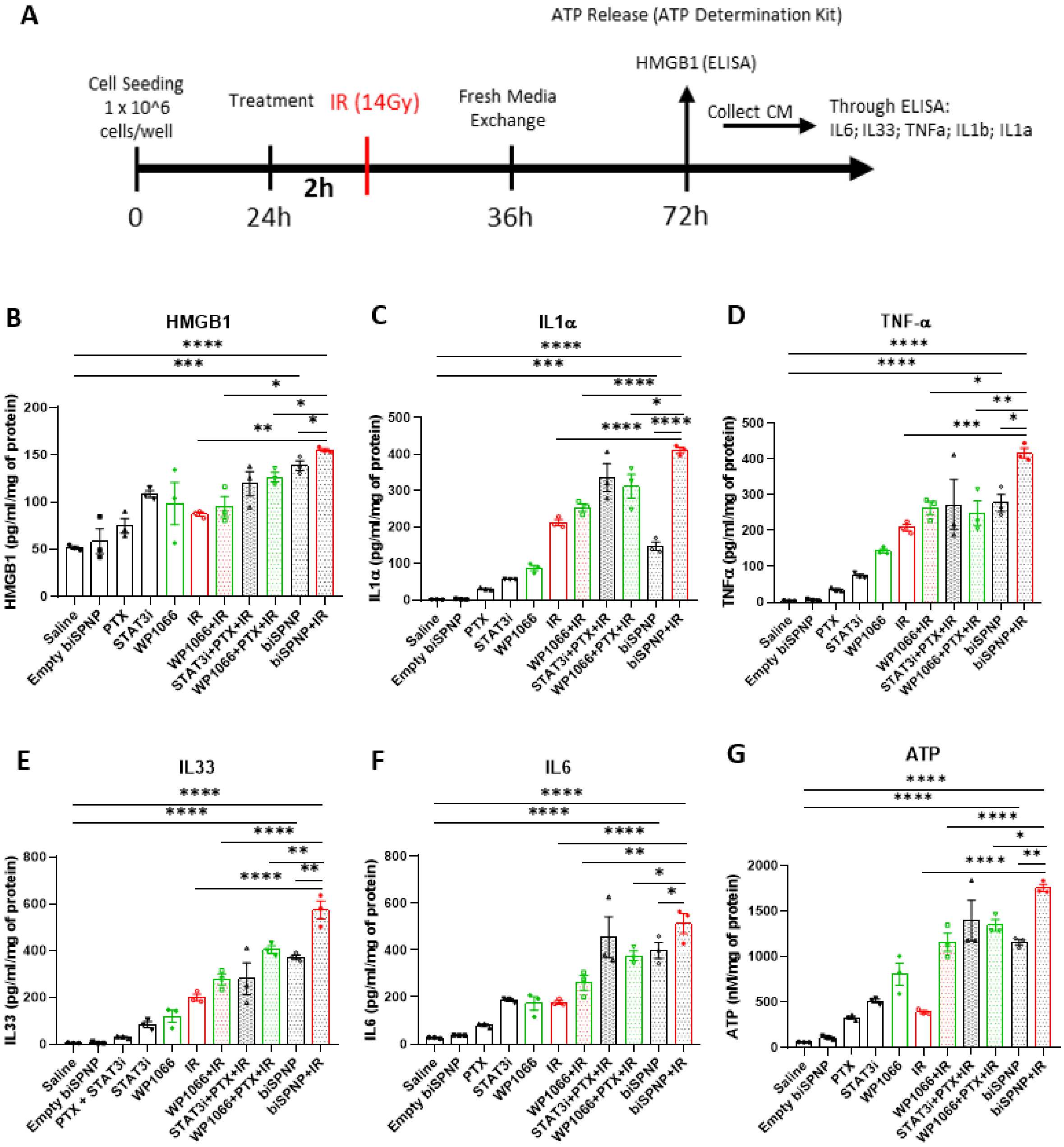

Figure 3-11. biSPNP (STAT3i/PTX) in combination with radiation enhances the immunogenic cell death (ICD) markers in human patient derived HGG cells. (A) Timeline of treatment to assess ICD following biSPNP (STAT3i/PTX) and other therapeutic treatments. (B-G) Quantitative ELISA shows the levels of DAMPs as ICD markers i.e., HMGB1, IL1α, TNFα, IL33, IL6, and ATP in the patient-derived HGG, HF2303 cells after treatment either with biSPNP, empty-biSPNP, free-PTX, free-STAT3 siRNA, WP1066 or in combination with IR (14Gy) at their respective IC50 doses and analyzed after 72h. All the statistical analyses were done through unpaired t test. Bars represent mean ± SEM (n = 3 biological replicates) ns= non-significant, $*p<0.05$, $**p<0.01$, $***p<0.001$, $****p<0.0001$.

3.4.6 Treatment with Paclitaxel and STAT3 siRNA with irradiation exhibit increased release of Type I interferons from mouse-HGG and human patient derived HGG cells.

Type-1 interferons (IFNs) would play a pivotal role in anti-glioma immunosurveillance through promotion of type-1 adaptive immunity and suppression of immunoregulatory cells.[224] Within the immunosuppressive tumor microenvironment (TME), interferons stimulate tumor-infiltrating lymphocytes to promote immune clearance and essentially reshape a "cold" TME into an immune-activating "hot" TME.[225] There to assess whether anti-tumor immune responses caused by biSPNP alone in conjunction with IR were due to the induction of type-I adaptive immunity in mouse and patient derived HGG cells. We measured the levels of IFNβ, IL1β, CCL2, CCL5 and CXCL10 as common type-I IFNs associated with type-I adaptive immunity, released by the dying tumor cells. We measured the release of IFNβ in the culture supernatant of both mouse and patient derived HGG cells in response to biSPNP (STAT3i/PTX) or biSPNP (STAT3i/PTX) + IR treatments. We observed a 5.58-fold ($p \leq 0.001$) increase in levels of IFNβ release in GL-26 cells when treated with biSPNP (STAT3i/PTX) compared to saline treated control (**Figure 3-12**B). We observed an additional 1.4-fold ($p \leq 0.01$) increase in extracellular IFNβ release in the supernatant of GL-26 cells treated with biSPNP (STAT3i/PTX) + IR (**Figure 3-12**B) relative to saline treated control.

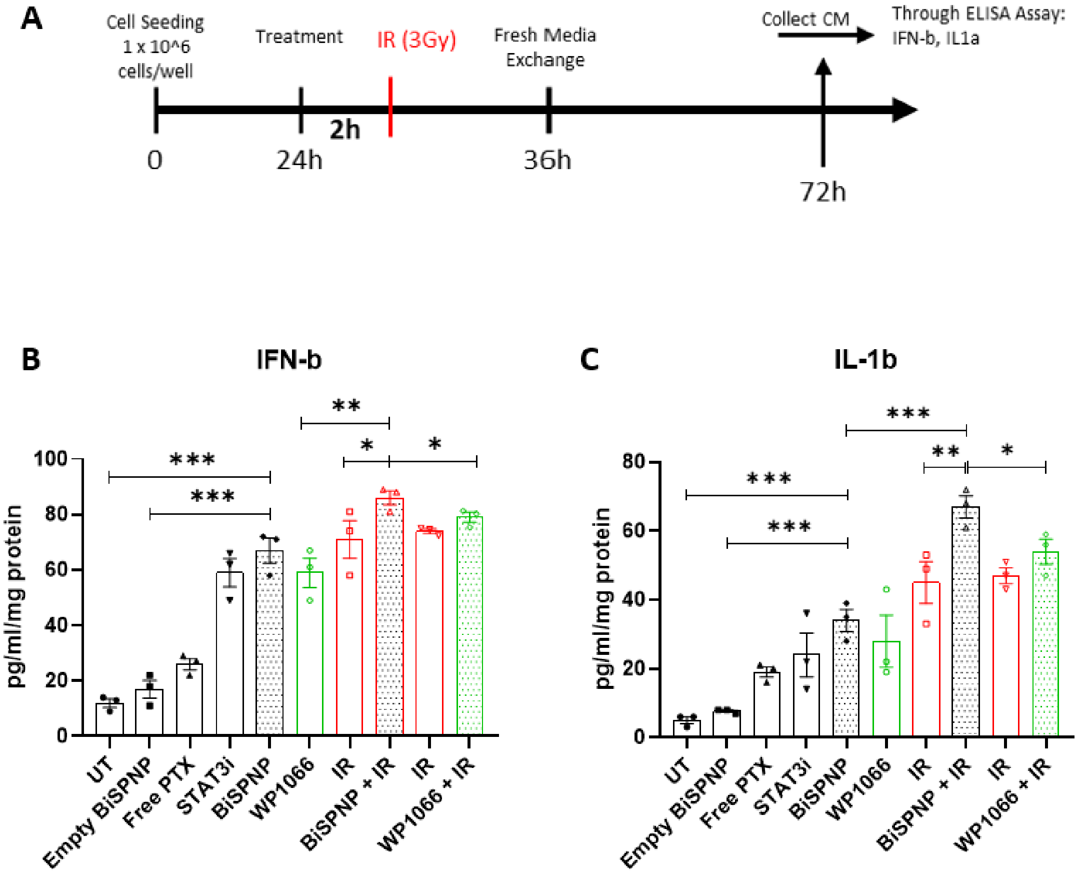

Figure 3-12. In Vitro inhibition of STAT3 and depolymerization of tubulin through BiSPNP (STAT3i/PTX) increases the release of Type I IFNs in murine GL26 HGG cells. (A) Timeline of treatment to assess Type I IFNs following BiSPNP (STAT3i/PTX) and other therapeutic treatments. (B-C) Quantitative ELISA shows the levels of Type I IFNs as pro-immunogenic markers i.e., IL1α and IFNβ in the mouse HGG GL26 cells after treatment either with BiSPNP, empty-BiSPNP, free-PTX, free-STAT3 siRNA, WP1066 or in combination with IR (3Gy) at their respective IC50 doses and analyzed after 72h. All the statistical analysis was done through unpaired t test. Bars represent mean ± SEM (n = 3 biological replicates) ns= non-significant, $^*p<0.05$, $^{**}p<0.01$, $^{***}p<0.001$, $^{****}p<0.0001$.

A similar response was elicited in human patient derived HGG cells treated with biSPNP (STAT3i/PTX) alone or in combination with IR (**Figure 3-13**B). There is a 283.5-fold ($p \leq 0.0001$) increase levels of IFNβ release in HF2303 cells when treated with biSPNP (STAT3i/PTX) (**Figure 3-13**B) and an additional 1.66-fold ($p \leq 0.001$) increase in extracellular IFNβ release in the culture supernatant when treated with biSPNP (STAT3i/PTX) + IR (**Figure 3-13**B) compared to saline treated control (**Figure 3-13**B). We observed comparable results for additional type-I IFNs such as IL1β in GL-26 mouse-HGG (**Figure 3-12**C) and CCL5, CCL2, and CXCL10 in human patient derived HGG (**Figure 3-13**C-E) relative to their respective saline treated control when treated with BiSPNP (STAT3i/PTX) alone or in combination with radiation. Taken together, these results demonstrated that biSPNPs (STAT3i/ PTX) in combination with IR enhance the release of type-I

IFNs and reshape an immunosuppressive TME into an immune-activating TME in both human and mouse high-grade glioma cells.

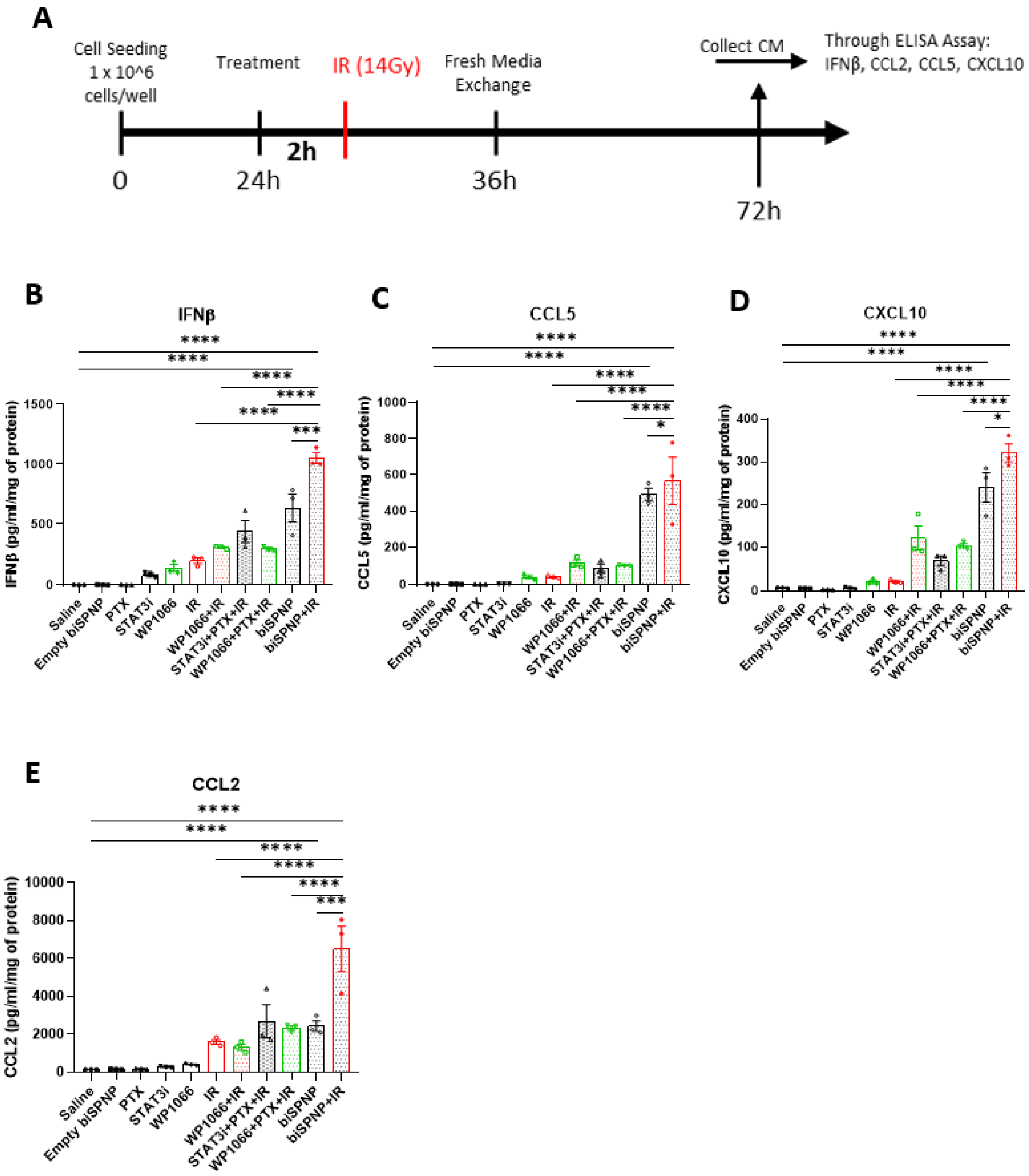

Figure 3-13. In Vitro inhibition of STAT3 and depolymerization of tubulin through BiSPNP (STAT3i/PTX) increases the release of Type I IFNs in patient derived HGG cells. (A) Timeline of treatment to assess Type I IFNs following biSPNP (STAT3i/PTX) and other therapeutic treatments. (B-E) Quantitative ELISA shows the levels of Type I IFNs as pro-immunogenic markers i.e., IFNβ, CCL5, CXCL10 and CCL2 in the patient derived HGG, HF2303 cells after treatment either with biSPNP, empty-biSPNP, free-PTX, free-STAT3 siRNA, WP1066 or in combination with IR (14Gy) at their respective IC50 doses and analyzed after 72h. All the statistical analyses were done through unpaired t test. Bars represent mean ± SEM (n = 3 biological replicates) ns= non-significant, *$p<0.05$, **$p<0.01$, ***$p<0.001$, ****$p<0.0001$.

3.5 Conclusions

In this work, we developed bi-compartmental synthetic protein nanoparticles (biSPNPs) fabricated through electrohydrodynamic co-jetting to encapsulate two therapeutics relevant for glioma: STAT3 inhibitor (STAT siRNA) and the antineoplastic agent, paclitaxel (PTX). This builds upon single-compartment SPNPs that were loaded with PTX (**Chapter 2**) and STAT3 siRNA.[218] Combination therapy is becoming increasingly popular over monotherapies to address the concern of resistance. Additionally, in instances where the effect of the two drugs together elicits a stronger therapeutic effect than the individual drugs, this can decrease the dose needed leading to a reduction in toxicity. Using nanoparticles as the delivery strategy protects the cargo and leverages the benefits of nanoparticle mediated delivery: controlled release, protection, targeting, longer half-lives, and the ability to overcome biological barriers. Not only was the development of these SPNPs feasible, but they showed to be cytotoxic in glioma cell cultures. Currently, work is underway to assess the efficacy of the STAT3i/PTX biSPNPs in high grade glioma mouse models. We hypothesize that these biSPNPs will provide a better survival outcome in glioma-bearing mice, and elicit a powerful immune response, as indicated by the preliminary in vitro results.

3.6 Supplementary Information

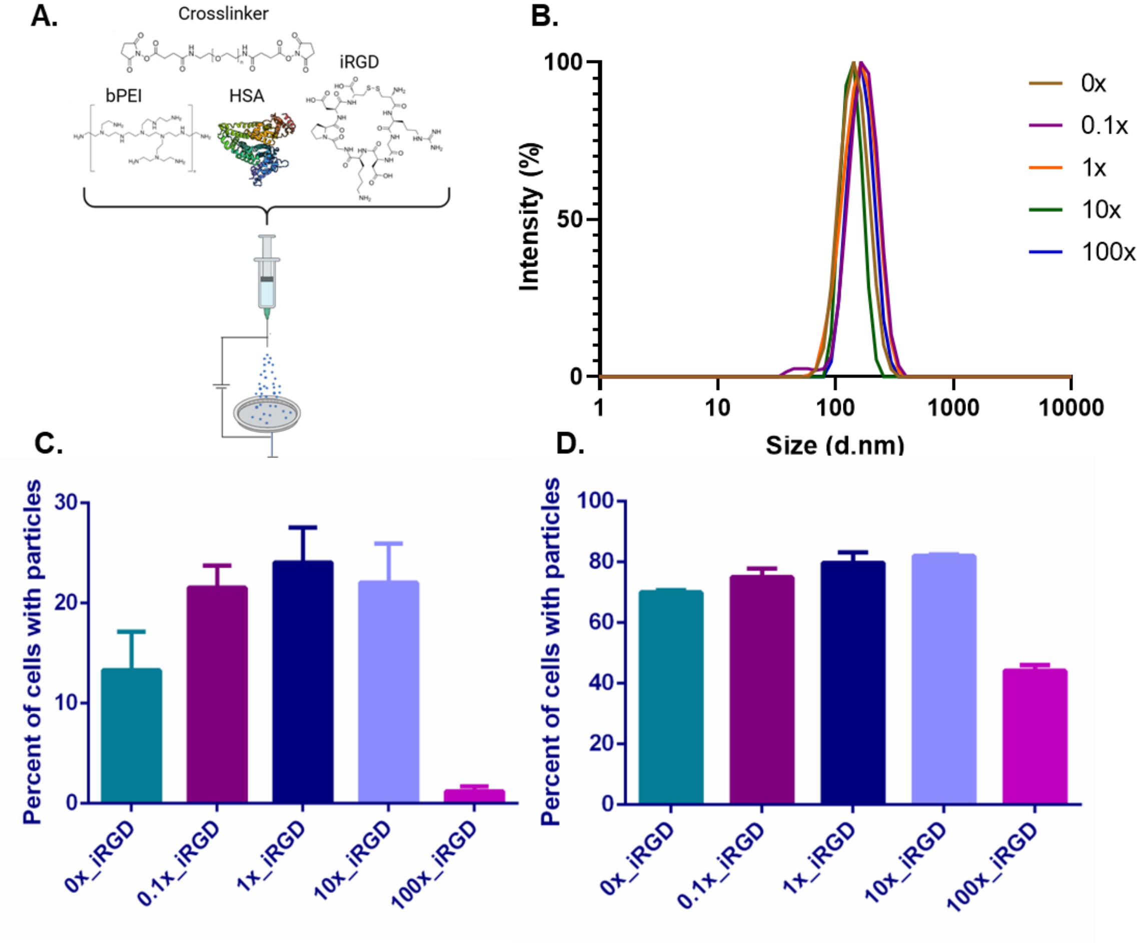

Figure 3-14. Synthetic protein nanoparticles encapsulated with varying amounts of iRGD impact uptake. A. Electrohydrodynamic jetting to produce iRGD SPNPs. HSA, iRGD, branched polyethyleneimine (bPEI), and crosslinker (NHS-PEG-NHS, 2kDa) are incorporated into the jetting solution to produce iRGD SPNPs. B. Dynamic Light Scattering showing the size distribution of each of the nanoparticle groups. The concentration 0x represents no iRGD. The 1x concentration is that listed in the methods. The other concentrations were based on the 1x concentration (i.e. 10 x is 10 times more than the 1x concentration). C. Cellular uptake (shown as percent of cells with SPNPs) of iRGD SPNPs in GL26-WT cells in 15 minutes. D. Cellular uptake (shown as percent of cells with SPNPs) of iRGD SPNPs after one hour of treatment in GL26-WT cells. Three biological replicates were used. The bar graphs show the mean with the error plotted as the standard deviation.

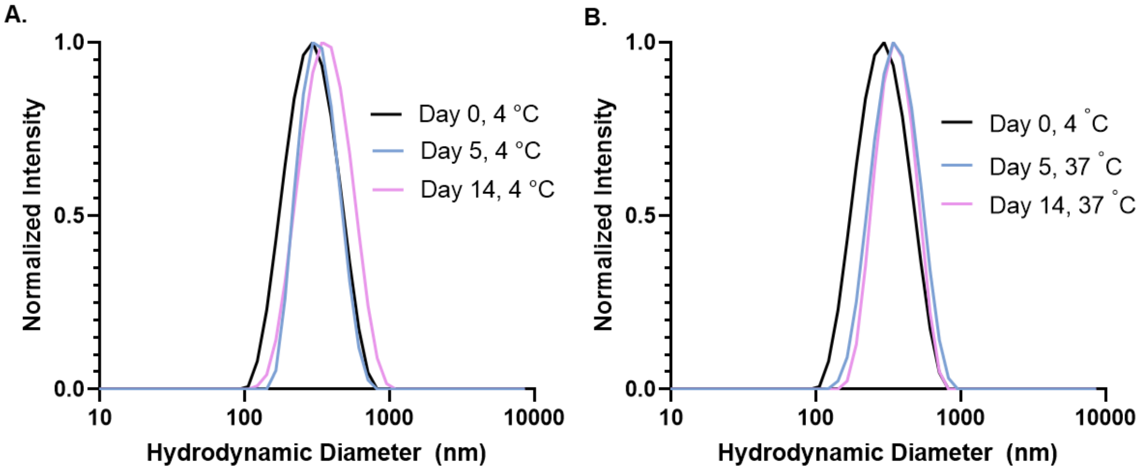

C.

Day	Temperature (˚C)	Intensity (nm)	Numbers (nm)	PDI
0	4	310	219	0.366
5	4	337	283	0.303
5	37	373	294	0.354
14	4	384	287	0.298
14	37	369	311	0.288

Figure 3-15. Size of Cy3siRNA/PTX biSPNPs at 37 ˚C during the release study compared with Cy3siRNA/PTX bSPNPs stored at 4 ˚C. A. Cy3siRNA/PTX biSPNPs stored at 4 C measured on Day 0, 5 and 14. B. Cy3siRNA/PTX biSPNPs during the release on Day 5 and 14 compared with the biSPNPs on Day 0. C. Summary table of the sample's conditions, their DLS intensity size, DLS numbers size, and PDI.

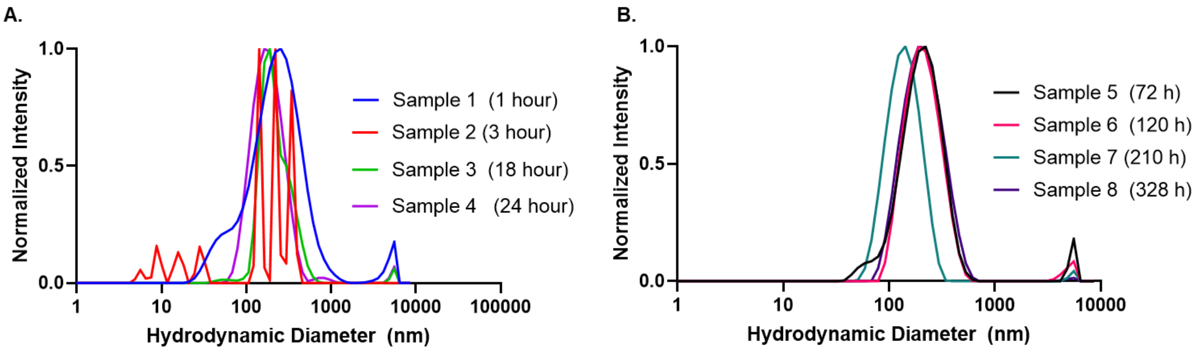

Figure 3-16. DLS spectra of the release samples from the centrifugation release method. A. Samples 1 through 4 (first 24-hour time points) B. Samples 5 through 8 (from 72 hours to 328 hours).

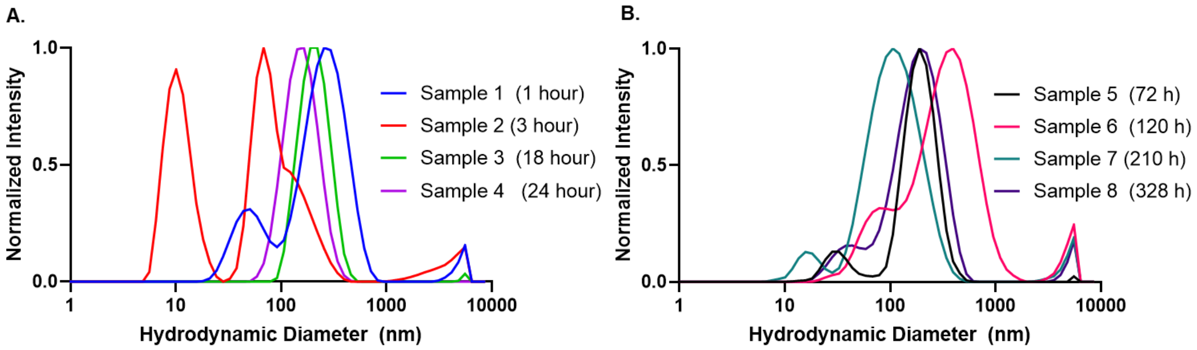

Figure 3-17. DLS of release samples after 3-hour centrifugation at 21130 rcf for 3 hours at 4 ˚C. The top 0.5 mL of sample was removed and measured through DLS, which is shown. A. First four samples. B. Last four samples.

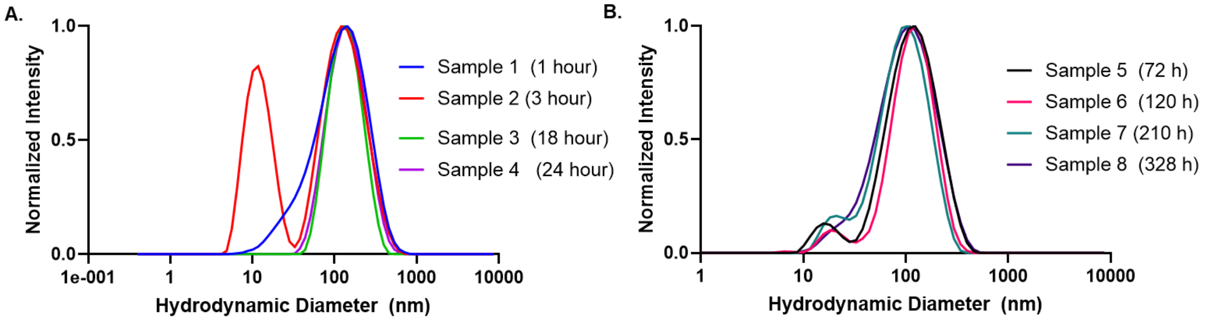

Figure 3-18. DLS of the release samples after the high-speed centrifugation (21130 rcf, 3 hours, 4 ˚C) followed by 220 nm syringe filtration.

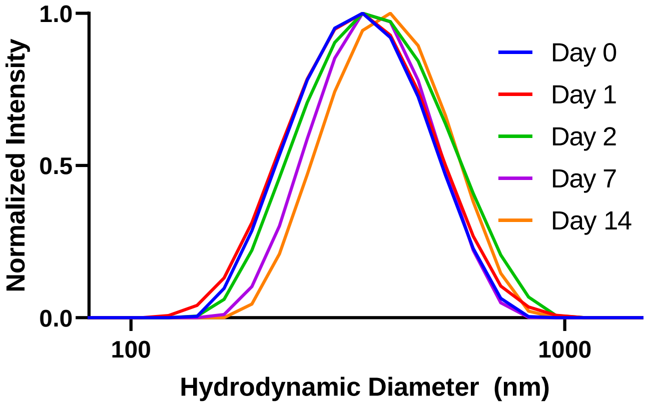

Figure 3-19. Hydrodynamic diameter of STAT3i/PTX biSPNPs over time at 4 ˚C reported as normalized intensity.

Chapter 4

Autophagy Inhibition via SiRNA-Loaded Synthetic Protein Nanoparticles Restores Sensitivity to Ionizing Radiation in Diffuse Astrocytoma

The material in this chapter has been adapted from the following article:
Felipe J Núñez*, Kaushik Banerjee*, Anzar A. Mujeeb*, Ava Mauser*, Claire E. Tronrud, Ayman Taher, Padma Kadiyala, Stephen V. Carney, Maria B. Garcia-Fabiani, Andrea Comba, Mahmoud S. Alghamri, Syed M. Faisal, Zeribe Nwosu, Hanna Hong, Tingting Qin, Maureen A. Sartor, Mats Ljungman, Shi-Yuan Cheng, Henry D. Appleman, Pedro R Lowenstein, Joerg Lahann, Costas Lyssiotis, Maria G. Castro. "Metabolic reprogramming in mutant IDH1 glioma alters oxidative phosphorylation and induces autophagy with therapeutic implications." *In Preparation* (*Equal contributions)

4.1 Abstract

Diffuse astrocytoma is a lower-grade glioma characterized by its genetic alterations, namely the mutation in isocitrate dehydrogenase and the inactivation of ATRX and TP53. These genetic lesions ultimately cause epigenetic reprogramming of the transcriptome and lead to ionizing radiation (IR) resistance. Recent analyses revealed mitochondrial metabolism downregulation and upregulation in autophagy. Inhibition of autophagy *in vitro* has demonstrated restoration of radiosensitivity, but eliciting a similar therapeutic response *in vivo* represents its own set of challenges, particularly delivery. Here, we produced a synthetic protein nanoparticle (SPNP) containing siRNA against an autophagy related gene, ATG7, to inhibit autophagy and restore IR sensitivity. The SPNPs also included the tumor penetrating peptide, iRGD, to facilitate transportation of the SPNPs into the tumor microenvironment. Delivery of these SPNPs *in vivo* improved the median survival and led to an anti-glioma immunological memory in mIDH1 glioma

bearing mice. This work provides a promising therapeutic strategy for the treatment of diffuse astrocytoma.

4.2 Introduction

Low grade gliomas are slow growing, indolent tumors that account for approximately 5% of primary brain tumors and are found in patients in their 30's and 40's. [226] Despite a better short-term prognosis than higher grade gliomas, they inevitably progress to higher grades. [226] Lower grade gliomas harboring mutations in isocitrate dehydrogenase 1 or 2 (IDH1/2) have better prognosis (~6.6 years) compared to their wild type counterparts (~1.6 years) but have been shown to be drivers in gliomagenesis.[196,226] Maximal surgical resection is often the first line of treatment as it delays malignant transformation and extends survival.[227] However, because of the infiltrative nature of gliomas, recurrence is virtually unavoidable.[227] Ionizing radiation represents another standard therapeutic intervention,[228] but IDH1 mutated gliomas with ATRX and TP53 inactivation - classified as diffuse astrocytomas - are resistant to irradiation (IR). This resistance is a direct result of the implications of the IDH1 mutation.[196] IDH1 catalyzes the conversion of isocitrate to α-ketoglutarate (α-KG), but mutation of an active site residue R132, generally to histidine, imparts aberrant catalytic activity.[229] IDH1-R132H (mIDH1) converts α-KG to 2-hydroxyglutarate (2-HG), an oncometabolite. 2-HG inhibits histone and DNA demethylases, thus transforming the methylome, altering gene expression, and impacting glioma progression [230]. Unfortunately, inhibition of 2-HG showed no effect on tumor growth although levels of 2-HG decreased.[226] Treatment with temozolomide, a DNA alkylating agent used as a common chemotherapy in glioma treatment, causes further mutations in 60% of cases which is met with progressively worse malignancies.[226] More recently, there were promising results in the RTOG9802 trial. It showed prolonged overall survival in patients when treatment with IR in combination with procarbazine, lomustine and vincristine (PCV) when compared to groups with only IR therapy.[231] Despite this benefit, a retrospective study showed one year of PCV treatment was associated with significant toxicities and only 50% of the patient population continued treatment after 6 months.[232] While the exploration of additional chemotherapies can be used for treatment, this only serves as a temporary treatment approach. The importance of connecting the evolving understanding of the biological landscape of gliomas to inform treatment is crucial.

Another therapeutic strategy is to re-sensitize IDH mutant astrocytoma to IR by interfering with pathways that confer IR resistance. In diffuse astrocytoma, mitochondrial dysfunction has been demonstrated and in response, autophagy is upregulated. Autophagy is a conserved process that recycles intracellular components including damaged organelles, protein aggregates and cellular waste, maintaining energetic homeostasis and protecting cells against stress.[233] It is activated in response to cellular stressors such as increases in reactive oxygen species, depletion of nutrients, and DNA damage.[234] Autophagy can then induce DNA damage response activation (to facilitate cell protection and survival), thus causing resistance to IR in tumor cells.[235] Preliminary results conducted *in vitro* demonstrated that autophagy inhibition re-sensitizes tumor cells to IR. In addition, a genetically engineered autophagy deficient mouse mIDH1 glioma model was developed, and a survival analysis revealed that mIDH1 glioma-bearing mice with autophagy inhibition had a significantly lower median survival (MS) when compared with the control. Taken together, inhibition of autophagy to restore sensitivity to IR could be a promising therapeutic approach. However, systemic delivery of these inhibitors is challenging as it must be protected from degradation and cross the blood-brain barrier to elicit a therapeutic effect. To overcome these challenges, as well as imparting beneficial therapeutic delivery characteristics like active targeting and controlled release, nanoparticles are commonly investigated.

Here, we constructed a synthetic protein nanoparticle (NP) loaded with the tumor penetrating peptide, iRGD, and an siRNA against the autophagy related gene 7 (ATG7) to cross the blood-brain barrier and deliver the therapeutic cargo directly to the tumor microenvironment. These ATG7i-NPs led to prolonged survival, anti-tumor immunity, and immunological memory in a mIDH1 glioma mouse model when combined with IR. Therefore, the use of nanoparticle-mediated autophagy inhibition in combination with ionizing radiation (IR) is an attractive therapeutic strategy for mIDH1 glioma patients.

4.3 Materials and Methods

4.3.1 Genetically engineered mutant IDH1 glioma model

All animal studies were conducted according to guidelines approved by the Institutional Animal Care and Use Committee at the University of Michigan. All animals were housed in an AAALAC accredited animal facility; and they were monitored daily. Studies did not discriminate sex, and both male and females were used. The strains of mice used in the study were C57BL/6 (The

Jackson Laboratories, 000664). The wt-IDH1 and mIDH1 glioma models used in this study were generated previously for our group.[196] using SB Transposon System. The plasmid used to generate those models are: (i) SB transposase and luciferase (pT2C-LucPGK-SB100X, henceforth referred to as SB/Luc), (ii) a short hairpin against p53 (pT2-shp53-GFP4, henceforth referred to as shp53), (iii) a constitutively active mutant of NRAS, NRAS-G12V (pT2CAG-NRASV12, henceforth referred to as NRAS), (iv) a short hairpin against ATRX (pT2-shATRX53-GFP4, henceforth referred to as shATRX), and (v) mutant IDH1^{R132H} (pKT-IDH1(R132H)-IRES-Katushka, henceforth referred to as mIDH1). Neonatal P01 wild-type C57BL/6 mice were used in all experiments. The genotype of SB- generated mice involved these combinations: (i) shp53, NRAS, and shATRX (wt-IDH1), (ii) shp53, NRAS, shATRX, and IDH1^{R132H} (mIDH1). Mice were injected according to a previously described protocol.[192] Plasmids were mixed in mass ratios of 1:2:2; 1:2:2:2, or 1:2:2:2:2 (20 μg plasmid in a total of 40 μL plasmid mixture) with in vivo-jetPEI (Polyplus Transfection, 201-50G) (2.8 μL per 40 μL plasmid mixture) and dextrose (5% total) and maintained at room temperature for at least 15 min prior to injection. The lateral ventricle (1.5 mm AP, 0.7 mm lateral, and 1.5 mm deep from lambda) of neonatal mice (P01) was injected with 0.75 μL plasmid mixture (0.5 μL/min) that included: (1) SB/Luc, (2) NRAS, (3) shp53, (4) with or without shATRX, and (5) with or without IDH1^{R132H}. To monitor plasmid uptake in neonatal pups, 30 μL of luciferin (30 mg/mL) was injected subcutaneously into each pup 24-48 hours after plasmid injection. In vivo bioluminescence was measured on an IVIS Spectrum (Perkin Elmer, 124262) imaging system. For the IVIS spectrum, the following settings were used: automatic exposure, large binning, and aperture f = 1. Pups without luminescence were euthanized according to an approved protocol: Committee on Use and Care of Animals (UCUCA) PRO00007617. For *in vivo* imaging of tumor formation and progression in adult mice, 100 μL of luciferin solution was injected intra-peritoneally (ip) and mice were then anesthetized with oxygen/isoflurane (1.5-2.5% isoflurane). To score luminescence, Living Image Software Version 4.3.1 (Caliper Life Sciences) was used. A region of interest (ROI) was defined as a circle over the head, and luminescence intensity was measured using the calibrated unit's photons/s/cm2/sr. Multiple images were taken over a 25-minute period following injection, and maximal intensity was reported. For survival studies, animals were monitored daily for signs of morbidity, including ataxia, impaired mobility, hunched posture, seizures, and scruffy fur. Animals displaying symptoms of morbidity were transcardially perfused using Tyrode's solution, followed by fixation with 4% paraformaldehyde (PFA) in phosphate buffered saline (PBS).

4.3.2 Primary glioma neurosphere cultures (NS)

Mouse glioma neurosphere (NS) cultures were generated as previously described.[195,196] Briefly, brain mice tumors were harvested at the time of euthanasia by transcardial perfusion with Tyrode's solution only. The tumor mass was dissociated using non-enzymatic cell dissociation buffer, filtered through a 70 µm strainer and maintained in neural stem cell medium DMEM/F12 with L-Glutamine (Gibco, 11320-033), B-27 supplement without Vitamin A (1X) (Gibco, 12587-010), N-2 supplement (1X) (Gibco, 17502-048), Penicillin-Streptomycin (100X) (10,000 IU Penicillin) (10,000 µg/mL Streptomycin) (Corning, Cellgro, 30-001-CI), and Normocin (1X) (invivogen, ant-nr-1) at 37 °C, 5% CO_2. Human-EGF (Shenandoah Biotech, 100-26) and Human-FGF (Shenandoah Biotech, 100-146) were added twice weekly at 1 µL (20 ng/µL each stock, 1000x formulation) per 1 mL medium.

4.3.3 Generation of human glioma neurospheres from patient tumor biopsies

SF10602 cells were generated in Dr. Joseph Costello's laboratory at UCSF from resected biopsies from patients harboring mIDH1 tumors with TP53 and ATRX mutation.[236] SF10602 were cultured and maintained in serum free glioma neural stem (GNS) cell medium comprises of Neurocult NS-A (Stem Cell Technologies) supplemented with 2 mM L-glutamine (Gibco, 11320-033), N-2 (Gibco, 17502-048), B-27 (without vitamin A, Gibco, 12587-010), Normocin (100 µg/ml) (InvivoGen, ant-nr-1), 0.1mg/mL sodium pyruvate (Gibco, 11360-070) and Antibiotic-Antimycotic (1X) (Gibco, 15240-062) at 37 ºC, 5% CO_2. Human EGF (animal-free; PeproTech, AF-100-15), Human FGF (animal-free; PeproTech, 100-18B) and PDGF-α (animal-free; PeproTech, 100-13A) were added twice weekly using 1µL of 20 ng/µL stock solution for each growth factor, equivalent to 100X formulation per 1mL medium.

4.3.4 Confocal microscopy and image analysis

Cells were placed into the incubator chamber of the microscope at 37 °C with a 5% CO_2 atmosphere. Microscopy confocal images were acquired using a single photon laser scanning inverted confocal microscope LSM 880 AxioObserver (Carl Zeiss, Jena, Germany). Two laser lines were used for simultaneous excitation with a Plan-apochromat 63x/1.4 numerical aperture

(NA) oil DIC M27 objective. Cells transfected with mCherry-GFP-LC3 were excited at 488 nm and 561 nm, and cells stained with MitoTracker™ green dye at 405 nm and 488 nm wavelength, respectively. Line-sequential scan mode and 1.4 scan zoom were used. The system was driven by ZEN Black software. Multichannel immunofluorescence images were processed and analyzed using Fiji (NIH). Autophagosome (green) and autolysosome (red) were manually identified and quantified using the plugging Cell Counter.

4.3.5 Implantable syngeneic murine glioma models

Female C57BL/6 mice, aged 6-8 weeks old, were used for implantation models. Intracranial tumors were established by stereotactic injection of 5 x 10^4 wt-IDH1 or mIDH1 mouse tumor NS into the right striatum using a 22-gauge Hamilton syringe (1 μL per minute) with the following coordinates: +1.00 mm anterior, 2.5 mm lateral, and 3 mm deep. The presence of tumors was verified 5 days post-implantation (DPI) by bioluminescence imaging.

4.3.6 Generation of iRGD Nanoparticles (NPs) with siRNA against ATG7

The preparation of the SPNP formulations followed previously reported methods but with modifications.[111] In the basic formulation, two solutions were prepared separately then combined. Human serum albumin (7.5% w/v, Sigma, # A1653) was solubilized in a solvent system comprised of ultrapure deionized water (80% v/v; ThermoFisher Scientific #10977) and ethylene glycol (20% v/v; Sigma, #102466). The peptide, iRGD (MedChemExpress, #HY-P0122) was then added along with BSA Alexa Fluor 647 conjugate (0.25% w/w relative to the albumin; Thermofisher Scientific, #A34785) to produce fluorescently labeled SPNPs. Then, the ATG7 siRNA (Origene, #SR427399) was resuspended according to the manufacturer's protocol, and complexed for 30 minutes at room temperature under rotation with 60 kDa branched polyethyleneimine (5% w/v; Sigma, #181978) before also being added to the serum albumin solution. Next, a bi-functional macromer, O,O'-Bis[2-N-Succinimidyl-succinylamino)ethyl]polyethylene glycol (Sigma, #713783), was added at 10% w/w relative to the human serum albumin solution. Once mixed, the two solutions were mixed to form the final formulation. For empty SPNP groups, all the components that were added in the iRGD ATG7 siRNA SPNPs were included except for the ATG7 siRNA. These formulations were subjected to electrohydrodynamic jetting to produce SPNPs. The parameters used were the same as previously described. Briefly, the final formulation was loaded into 1 mL syringes equipped with a 1.5" 25-gauge stainless steel blunt needle. It was pumped at a rate of 0.2 mL/hour to form droplets at the base of the needle. A voltage source was connected to the needle and grounded at the collection plate, located 6 inches from the base of the pump. The voltage was adjusted typically to a range between 8 kV and 15 kV to achieve a stable Taylor cone whereby rapid evaporation of the solvent occurred, creating solid nanoparticles on the collection plate. The collection plate was replaced with a clean plate every 30 minutes until the solution within the syringe emptied. The collection plates were enclosed and incubated for 7 days at 37 ˚C to form stable crosslinks. After the one-week period of incubation, the SPNPs on collection plates were removed. Three to four milliliters of 0.01% (v/v) Tween 20 (Sigma, #P2287) in DPBS (Gibco, 14190-144) was added to each pan and physically agitated with plastic razor blades to release the SPNPs off the plate. The SPNP suspension was collected into a falcon tube. Each pan was agitated with fresh 0.01% Tween 20 in DPBS three times. The collected SPNPs was tip sonicated at an amplitude of 7 for 30 seconds (1 second on and 3 seconds off) in an ice bath to break up aggregates, strained through a 40 µm filter into a new falcon tube then centrifuged at 3220 rcf for 5 minutes. The supernatant was removed and distributed into 2 mL Eppendorf tubes and centrifuged for 1 hour at 4 ˚C at 21,500 rcf. The supernatant was discarded, and the resulting pellets were combined into a single 2 mL tube. The particles were washed two times with fresh DBPS without Tween 20.

4.3.7 NP size, surface charge, and concentration characterization

Scanning electron Microscopy (SEM): SEM samples were prepared by placing a silicon wafer on top of the collection plate during the jetting process. The samples were then placed on a copper tape covered SEM stub, then gold coated for 40 seconds and visualized through the FEI NOVA 200 SEM/FIB instrument. The dry state SPNP quantification of morphology parameters were conducted through ImageJ analysis as described previously.[114] The hydrodynamic diameter and zeta potential was determined through Dynamic Light Scattering (DLS) on the Malvern Zetasizer. Samples were prepared by diluting the stock sample in DBPS and measured in folded capillary zeta cells. An average of at least three measurements was used to characterize each sample. Bicinchoninic acid assay (BCA assay; Thermoscientific, #23225) was used to quantify SPNP concentration. A standard curve was prepared for every SPNP concentration quantification measurement.

4.3.8 In vivo assay with radiation and autophagy deficient models

To evaluate the effect of the combination of radiation (IR) treatment and autophagy inhibition, we tested the effect of IR (20 Gy) and the administration of iRGD nanoparticles loaded with a siRNA against *Atg7* (siRNA-Atg7-NP) *in vivo*. Twenty mice were implanted with mIDH1-OVA mouse tumor NS as stated above, and 7 days post implantation, mice were divided in the following 4 groups (n=5 animals): Control (no treatment); siRNA-Atg7-NP only; IR only; and IR + siRNA-Atg7-NP. Animals were treated with 2 Gy IR, for five consecutive days, for two weeks. siRNA-Atg7-NP (2.0 x 10^{11} particles) were administered in 6 injections, intravenously (tail vein injection), every other day over 5 days, for two weeks (3 injections/week). Animals were euthanized at day 21 post implantation or when they became symptomatic due to tumor burden. The tumor and the spleen were collected to analyze the development of anti-tumor immune response. Tissue processing was performed as detailed previously.[237] Cell suspensions from tissues were resuspended in PBS containing 2% fetal bovine serum (FCS) (flow buffer) for antibody staining for flow cytometry. All flow data were acquired on a FACSAria flow cytometer (BD Biosciences) and analyzed using Flow Jo version 10 (Treestar). Before antibody staining, non-specific antibody binding was prevented using CD16/CD32 and all samples were stained with LIVE/DEAD Fixable Aqua Dead Cell Stain Kit (Thermo Fisher) to assess viability. To analyze the presence of anti-tumor specific T cells, cell suspensions were stained with anti-mouse CD45, CD3, CD8, and SIINFEKL-H2Kb-tetramer-PE in flow buffer for 30 min on ice. Cells were then washed two times with flow buffer prior to data acquisition. To assess T cell activation status, Grazyme B (GrzB) and IFNγ intracellular staining were performed. To accomplish this, cell suspensions from tissue were cultures with 100 mM of SIINFEKL for 24 hours in 10% fetal bovine serum (FBS)-media with 55 µM 2-mercaptoethanol. Brefeldin and monensin (BD Biosciences) were added for the last 6 hr of the culture. Cells were first stained with CD45, CD3 and CD8 antibodies, followed by intracellular stains for GrzB and IFNg (BD Biosciences). Intracellular stains were performed using the BD intracellular staining kit according to the kit instructions.

4.3.9 Immunohistochemistry (HIC) of paraffin-embedded brains

Following perfusion, mouse brains were fixed in 4% PFA (paraformaldehyde) for an additional 48 hours at 4 °C, then transferred to 70% ethanol, and processed and embedded in paraffin at the University of Michigan Microscopy & Image Analysis Core Facility using a Leica ASP 300 paraffin tissue processor/Tissue-Tek paraffin tissue embedding station (Leica). Tissue was sectioned using a rotary microtome (Leica) set to 5 μm in the z-direction. Antigen retrieval and immunohistochemistry (IHC) of paraffin-embedded sections were performed using antibodies and dilutions listed in Table S1. Images were obtained using brightfield/epifluorescence (Zeiss Axioplan2, Carl Zeiss MicroImaging) or laser scanning confocal microscopy (Leica DMIRE2, Leica Microsystems) and analyzed using LSM5 software (Carl Zeiss MicroImaging). Immunostaining was performed using the Discovery XT processor (Ventana Medical Systems). Tissue sections were blocked with blocking solution (1 x PBS with 0.2% Tween-20 with 5% Goat Serum) for 2 hours. Sections were incubated with primary antibody (Cell Signaling (99940S)-Anti-CD3ε (D4V8L); Abcam (ab125212)-Anti-CD68; Millipore (MAB386)-Anti-MBP; Millipore (AB5541)-Anti-GFAP) at 4˚C overnight. Tissue sections were then labeled with Secondary Biotinylated antibody (1:1000)) in PBS with 0.2% Tween-20 for 15 minutes at RT and 4˚C overnight. ABC Avidin-Biotin-COMPLEX Binding was done using VECTASTATIN ABC Reagent (Vectastain Elite ABC kit). Sections were incubated for 1 hour with VECTASTAIN ABC Reagent (in the dark) and then washed with gentle agitation. Colorimetric Detection of Peroxidase was performed using Betazoid DAB Chromogen kit (BioCare BDB2004) according to the manufacturer’s instructions. Hematoxylin Counterstain was done, and coverslips were mounted with a xylene-based mounting medium and let dry on a flat surface at room temperature until ready for imaging.

4.4 Results

4.4.1 Fabrication, characterization, and reproducibility of ATG7i Nanoparticles (NPs)

Nanoparticles (NPs) were produced through electrohydrodynamic jetting (**Figure 4-1A).** The jetting solution comprised of human serum albumin, iRGD, siRNA against ATG7, branched polyethyleneimine, and a bifunctional macromer in a cosolvent system of ultrapure water (80%v/v) and ethylene glycol (20%v/v). This solution was pumped at laminar flow towards the collection plate while a voltage was applied at the tip of the needle and grounded at the collection plate. The induction of the electric field caused the rapid acceleration of solid NPs towards the collection plate while the solvent evaporated on its descent. According to the analysis of the SEM images, the jetted NPs had an average dry-state diameter of 104 ± 42 nm (**Figure 4-1B-C**). After collection and processing, the ATG7i NPs swelled to a diameter of 238 nm according to dynamic light scattering (**Figure 4-1D**). The zeta potential in DPBS was slightly negative at -6.84 ±0.69 mV.

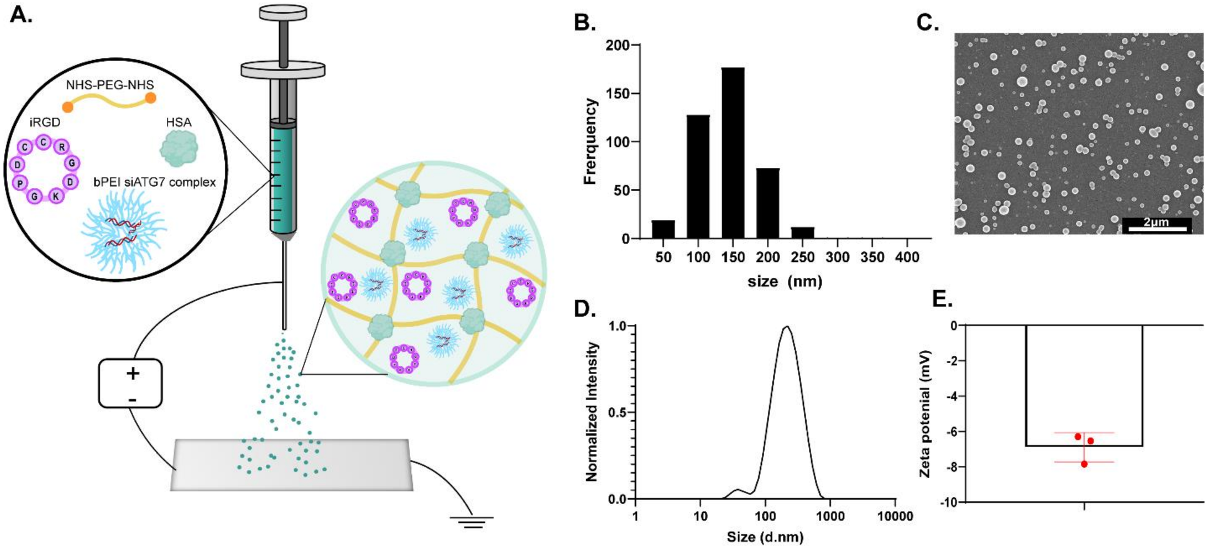

Figure 4-1. A) Electrohydrodynamic jetting to produce ATG7i NPs. All components (lysine-containing iRGD, branched PEI- ATG7 siRNA complex, PEG crosslinker) are added in the initial solution as shown as the blown-up bubble on the left. Throughout jetting, solid SPNPs land on the plate and are crosslinked for 7 days. The right blown up bubble shows a single ATG7i NP whereby the HSA is crosslinked throughout the particle. **B**) Histogram of dry state SPNP diameter (mean diameter: 104 ± 42 nm, circularity = 0.93 ±0.09, PDI = 0.219) analyzed from Scanning Electron Microscopy (SEM) of n>400 individual SPNPs. **C)** SEM micrograph (scale bar = 2 µm). **D)** Intensity-based DLS spectra ($Z_{average}$ =185 nm, peak diameter = 238 nm, PDI = 0.289). **E)** Zeta potential (-6.84 ± 0.69 mV).

The control NPs (Empty NPs) were also produced as shown in **Supplemental Figure 4-6**. These NPs did not contain siRNA and were used as a negative control for the survival studies. The reproducibility of the production of ATG7i NPs was assessed (**Figure 4-2**). Three separate batches were produced via EHD jetting and characterized according to their morphology via SEM, hydrated size via DLS, and surface charge through ELS. The SEM images for the batches are shown in **Figure 4-2A-C** with their corresponding size distributions below. The appearance of the ATG7i NPs were highly circular (>0.90) and have the highest population fraction at 100-150 nm. Runs 1, 2 and 3 had diameters of 104 ±42, 141 ± 44 nm, and 114 ±55 nm, respectively. The polydispersity of the analyzed NPs was between 0.219 and 0.248 (**Figure 4-2D**). After the batches were incubated at 37 ˚C for 7 days, they were collected and processed separately. The DLS spectra show overlapping, indicating collection and processing were consistent (**Figure 4-2E**). Similarly, the zeta potential was slightly negative for each run (**Figure 4-2F**).

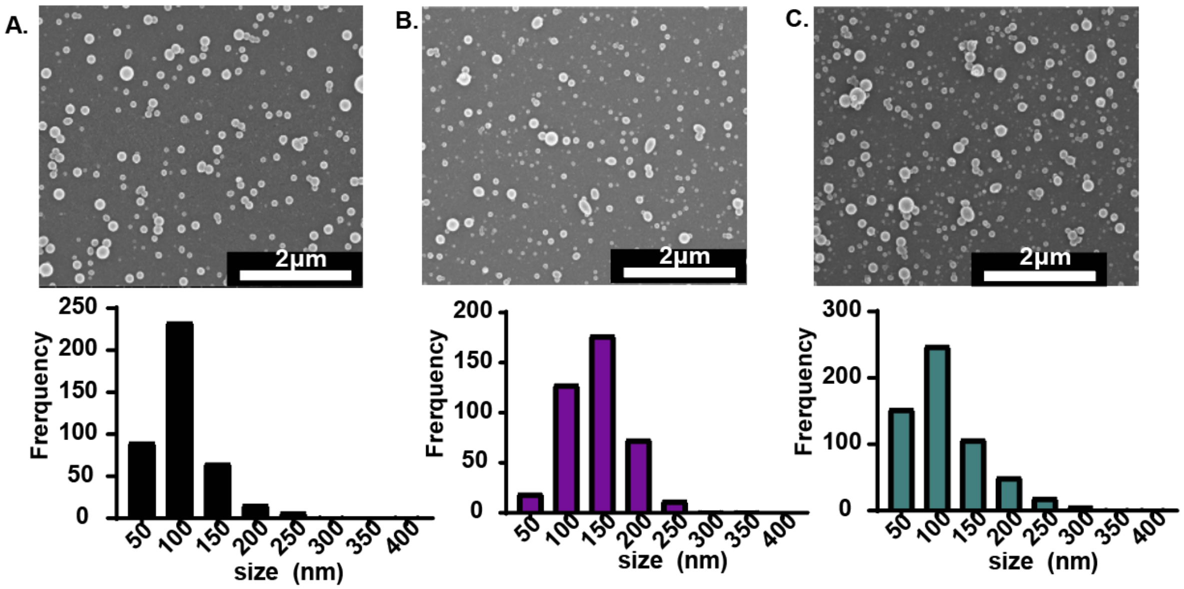

D.

	Diameter (nm)		Circularity		PDI
	Mean	SD	Mean	SD	Mean
Run 1	104	42	0.93	0.088	0.219
Run 2	141	44	0.92	0.060	0.244
Run 3	114	55	0.91	0.125	0.248

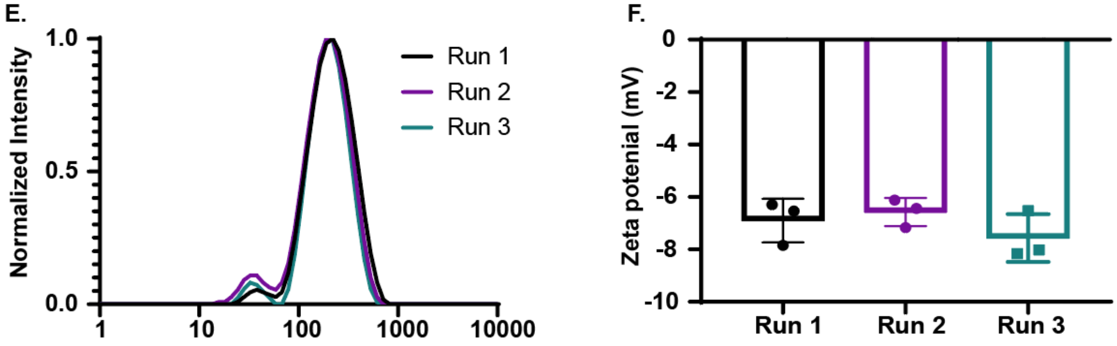

Figure 4-2. Comparison of ATG7i NPs characteristics that were fabricated and collected in three independent sessions. **A-C)** An SEM image (top) and the corresponding histogram (below) of the size distribution in the dry state of run 1 (**A**), run 2 (**B**), and run 2 (**C**). **D)** Summary table of dry-state SPNP characterization (diameter, circularity, and PDI) for run 1, run 2, and run 3.**E**) Intensity DLS spectra post-collection of the three runs. **F)** Zeta potential.

4.4.2 Inhibition of autophagy via ATG7i NPs prolongs the survival of mDIH1 glioma-bearing mice

We then studied the impact of autophagy inhibition in combination with radiation treatment using our cell implantable mouse mIDH1 glioma model.[196] We intracranially implanted mIDH1 glioma NS in mice, and 7 days later the animals were split in five groups: i) saline control, ii) treated with empty NPs, iii) treated with IR, iv) treated with ATG7i NPs, and v) treated with IR + ATG7i NP at indicated doses and schedule in the figure below.

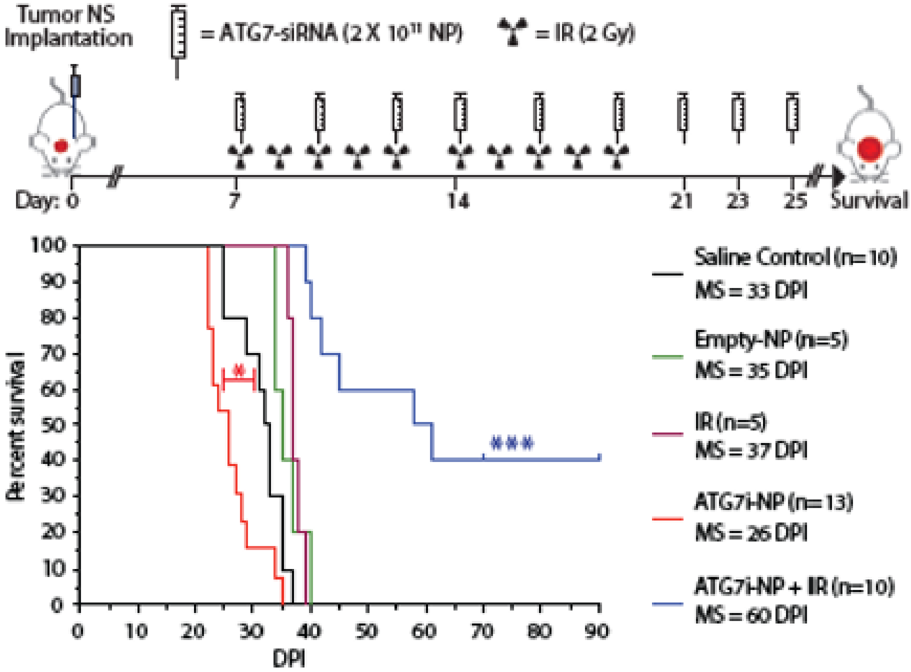

Figure 4-3. ***In vivo* autophagy inhibition radiosensitizes mIDH1 gliomas and enhances survival.** (A) Autophagy inhibition effect using Atg7i-NP on radio-response in mIDH1 glioma model. Adult mice implanted with 50,000 mIDH1-NS (Day 0). At 7 DPI, animals split into groups: (i) untreated saline control; (ii) 9 doses of $2x10^{11}$ empty SPNPs every other day; (iii) 2 Gy/day; (iv) 9 doses of $2x10^{11}$ Atg7i-NP every other day; (v) 9 doses of $2x10^{11}$ Atg7i-NP every other day and 2 Gy/day (days 7-16). Kaplan-Meier survival curves made for each experimental group (****P*<0.001, Mantel-Cox test).

In the genetically engineered mouse mIDH1 glioma model, the autophagy inhibition alone significantly decreased MS ($P < 0.05$) when compared with the control group. However, IR + ATG7i-NP had a notable impact on MS (MS = 60 DPI; $P < 0.001$) when compared with all the experimental groups **(Figure 4-3)**. Intriguingly, we observed that the combined treatment prolonged the survival of mice long-term (> 90 DPI).

Long-term survivors from the IR + ATG7i NP treatment groups were rechallenged with mIDH1 mouse-NS in the contralateral hemisphere (**Figure 4-4**).

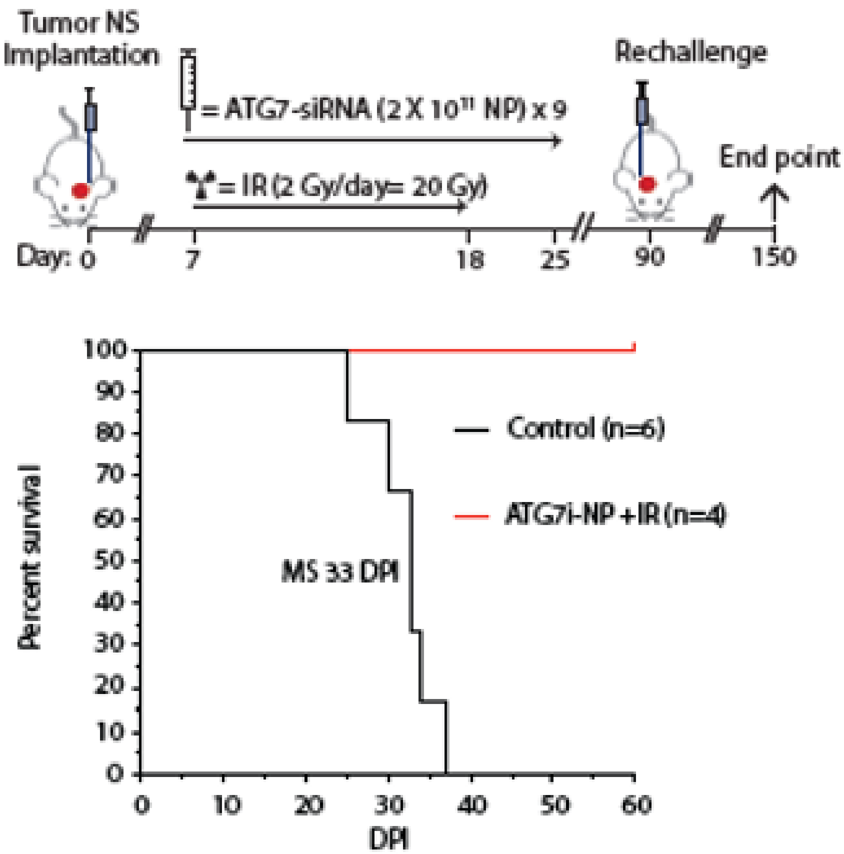

Figure 4-4. Survival of rechallenged mIDH1 bearing mice, which survived after ATG7i NP+IR combined treatment. Tumor neurosphere implantation occurred on Day 0 and treatment was given starting Day 7 with 2x10^{11} NPs for three doses a week for three weeks (total of 9 doses). In addition to the NP treatment, IR was given as 2 Gy/day for a total of 20 Gy for the duration of treatment. Long term survivors were rechallenged at Day 90 with a second tumor. The survival curve shown indicates the survival of the mice after the rechallenge whereby no further treatment was given after the implantation of the second tumor. Control had a median survival of 33 DPI, whereas the ATG7 NP+ IR group remained tumor free until 60 DPI whereby the animals were sacrificed.

These animals remained tumor free without further treatment, whereas control mice implanted with glioma cells succumbed due to tumor burden (MS = 33 DPI; $P \leq 0.0001$) (**Figure 4-4**). The animals were sacrificed at 60 DPI after tumor rechallenge, these mice showed no evidence of microscopic intracranial tumor. These results suggest the development of anti-glioma immunological memory in mIDH1 glioma rechallenged animals previously treated with IR + ATG7i NP. None of these treatments produced hepatic alterations compared with control group as shown by **Supplemental Figure 4-7 and Figure 4-8.**

4.4.3 Immune response from siATG7 SPNP therapy

We next aimed to study the anti–mIDH1 glioma–specific immune response elicited by IR + ATG7i NP therapy, specifically on T-cell proliferation. Mice bearing mIDH1 tumors harboring a surrogate tumor antigen, ovalbumin (OVA), were treated with saline, IR, ATG7i NP, or IR + ATG7i NP (**Figure 4-5A**).

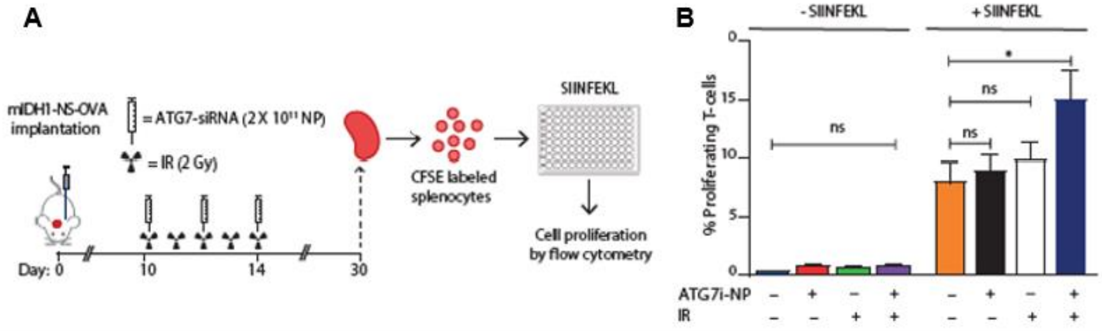

Figure 4-5. Experimental design analyzing ATG7i NP treatment + IR on T cell proliferation. Mice implanted with 50,000 NPAI-OVA-NS. At 10 DPI, mice treated with 2 Gy/day radiation and Atg7i-NP every other day. Splenocytes collected after 30 DPI. SIINFEKL (100 nM) added to splenocytes. **(B)** T cell proliferation measured as CFSE staining reduction in CD45+/CD3+/CD8+ populations. Bars (mean ± SEM) represent proliferating CD8+ T cell percentage within treatment groups (n=5 replicates; one-way ANOVA followed by Tukey's test. **P*<0.01; ns=non-statistically significant).

Mice were euthanized 14 days after the last treatment dose (30 DPI) and the spleen were removed and processed for flow cytometry analysis. Splenocytes were fluorescently labeled with 5- and 6-carboxyfluorescein diacetate succinimidyl ester (CFSE) and stimulated for 4 days with 100 nM SIINFEKL (**Figure 4-5A**), where T-cell proliferation was measured as the reduction of CFSE staining in the CD45+/CD3+/CD8+ population. After SIINFEKL treatment, we observed that T-cell proliferation was significantly increased ($P < 0.05$) in mIDH1 glioma-bearing mice treated with IR + ATG7i NP (**Figure 4-5B** and **Supplemental Figure 4-10**) when compared with the control group. This indicates that the combined treatment was able to induce a systemic anti–mIDH1 glioma–immune response associated with an enhancement in T-cell proliferation.

4.5 Discussion

Autophagy, a self-digestion pathway crucial for the maintenance of homeostasis in cells at basal levels has also been implicated in cancer to be either used as a pro-survival or pro-death mechanism [238,239]. Whether autophagy acts in a pro-survival or pro-death mechanism have been studied, but results have been conflicting suggesting that autophagy regulation is dependent on several variables (stage of tumor development, presence of genetic mutations, tumor microenvironment, and treatment, among others).[238,240,241] Therefore, the context is crucial to understanding whether autophagy inhibition can impart sensitization to therapies. The tumor model used herein play a cytoprotective role whereby inhibition of autophagy can induce sensitivity to IR.[242] While inhibition through siRNA is a promising strategy to knockdown targets implicated in autophagy, delivery of siRNA systemically is virtually impossible. SiRNAs are known to undergo rapid degradation due to the presence of endonucleases in serum.[243] Further, siRNA must reach its target site, which may require long circulation times and the ability to pass barriers. SiRNAs have poor circulation times on the scale of minutes whereby they get transported through the renal system.[243] Developing systems such as nanoparticles offer strategies to effectively deliver siRNA.[244,245] Several types of nanoparticles have been explored to delivery siRNAs, but here, we employed a protein-based nanoparticle otherwise referred to as synthetic protein nanoparticles. This type of particle was chosen primarily because of its therapeutic success shown in a recent publication.[218] While its success was demonstrated in that model with a different target, it was possible that it could not be extended further. However, as shown in this work, this type of nanoparticle could be formulated to contain a different siRNA (ATG7 siRNA versus STAT3 siRNA) to be used for a different target (autophagy versus STAT3 signaling pathway) in a different glioma model (diffuse astrocytoma versus high grade glioblastoma). We showed that the ATG7i-NPs had a therapeutic impact when in combination with IR. This combination led to increased median survival of mIDH1 glioma bearing mice and long-term survivors. The long-term survivors were rechallenged with a second tumor and showed a 100% survival rate despite not receiving further treatment. This indicated that immunological memory was induced as corroborated by the increased tumor specific T-cell proliferation in mIDH1 glioma mice treated with the ATG7i NPs and IR.

In the context of this thesis, these NPs demonstrated the extendibility of EHD jetted protein nanoparticles to encapsulate siRNAs for glioma treatment. Based on this work and that published prior,[111] other siRNAs can be loaded into these NPs, and even for other diseases beyond glioma.

4.6 Supplementary Information

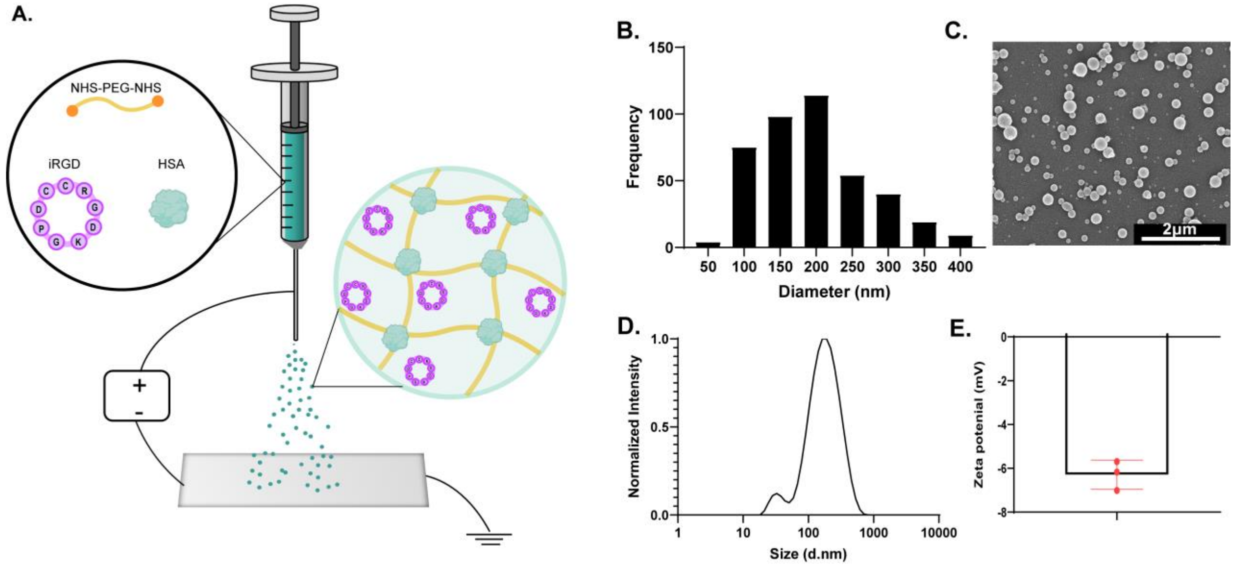

Figure 4-6. Production and characterization of Empty NPs. A. Electrohydrodynamic jetting to produce Empty NPs. HSA, iRGD, and crosslinker are added into the jetting solution with a cosolvent system of 20% v/v ethylene glycol and 80% v/v ultrapure water. Solid empty NPs result on the plate and are crosslinking at 37 ˚C for 7 days. B. Histogram of the dry-state NPs analyzed from the micrograph shown in C (average diameter = 196 ±. 80 nm, circularity = 0.90 ± 0.08, PDI = 0.344; n>400) C. Scanning electron microscopy image of the empty NPs (scale bar = 2 micron) prior to collection. D. Intensity-based DLS spectra (z-average size = 143 nm, peak 1 average = 201 nm, PDI = 0.299). E. Zeta potential in PBS (-6.29 ± 0.67 mV).

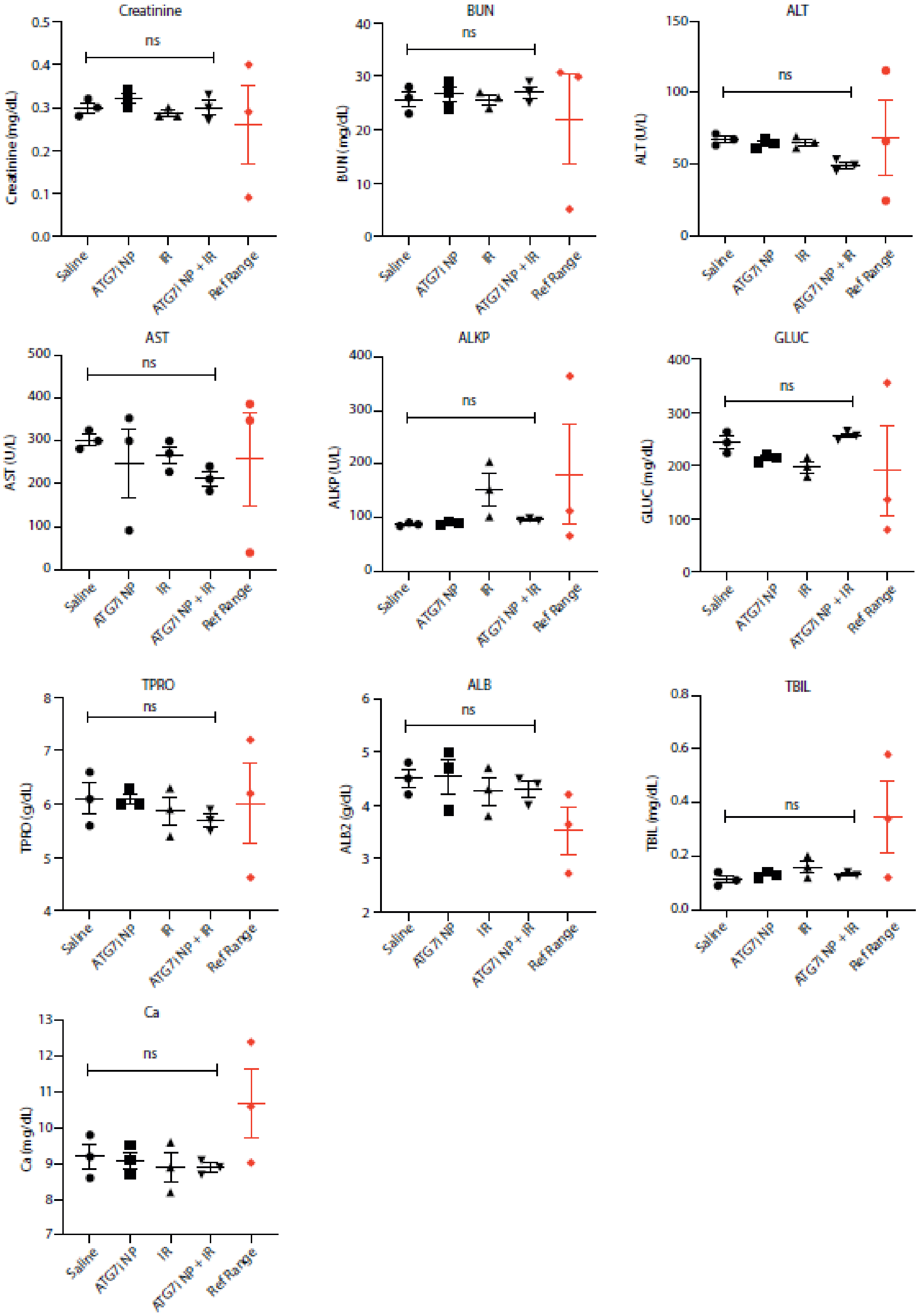

Figure 4-7. Mouse serum biochemical analysis following intravenous ATG7i SPNP in combination with IR treatment. NPAI OVA tumor bearing mice treated with ATG7 inhibitor ATG7i SPNPs in combination with radiation exhibit normal serum biochemical parameters compared with saline treated control. Serum was collected from tumor bearing mice treated with saline, ATG7i SPNPs, IR or ATG7i SPNP + IR at 23 DPI. These markers (creatinine, blood urea nitrogen (BUN), alanine transaminase (ALT), aspartate aminotransferase (AST), alkaline phosphatase (ALKP), glucose (GLUC), total protein (TPRO), albumin (ALB), total bilirubin (TBIL) and calcium (Ca)) were measured in each treatment group and compared to the control. There were not any significant differences. The levels of different

serum biochemical parameters between the treatment groups were compared and were found non-significant, $P > 0.05$ (n = 3 biological replicates).

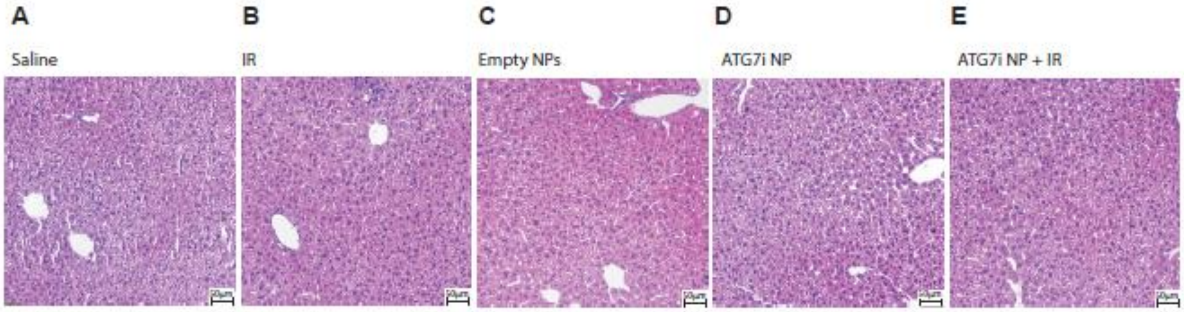

Figure 4-8. Histopathological assessment of livers from tumor bearing mice treated with ATG7i NPs + IR. H&E staining of 5µm paraffin embedded liver sections from Saline [A (20X)], IR [B (20X)], empty NPs [C (20X)], ATG7i NPs [D (20X)] and ATG7i NP + IR [E (20X)] treatment groups. Histology performed on resected livers following complete treatment of NPAI tumor bearing mice. Representative images from an experiment consisting of independent biological replicates are displayed. Black scale bars = 50µm.

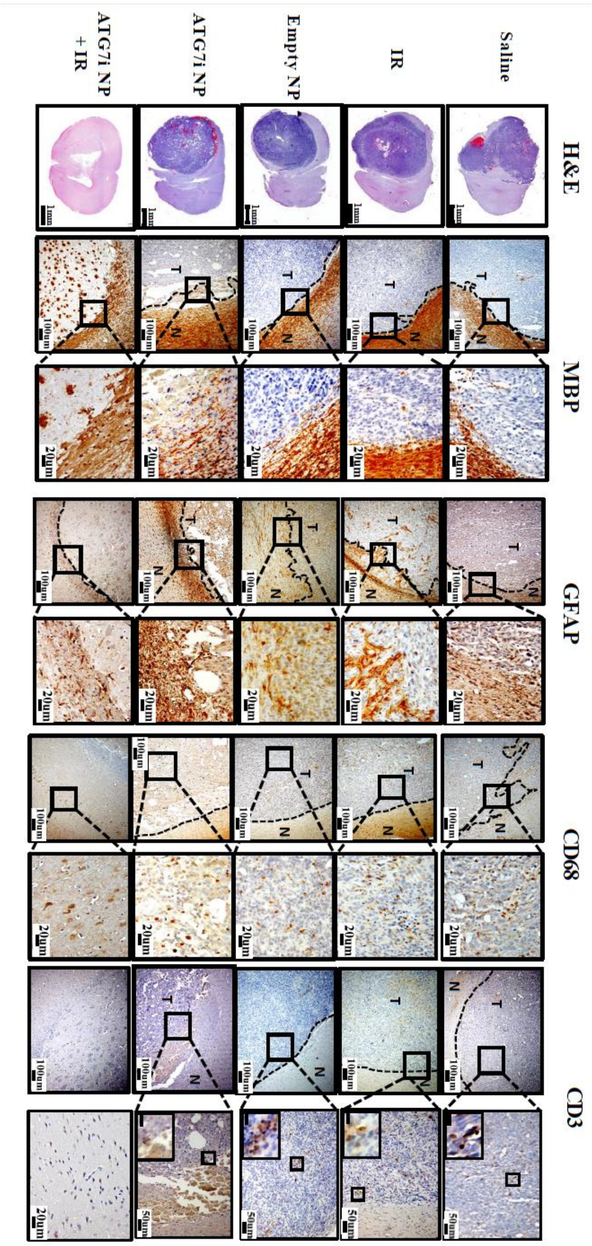

Figure 4-9. H&E staining of 5µm paraffin embedded brain sections from saline, IR, Empty NP, ATG7i-NP and long-term survivors from ATG7i-NP+IR treatment groups (scale bar=1mm). Paraffin embedded 5µm brain sections for each treatment group were stained for myeline basic protein (MBP), glial fibrillary acidic protein (GFAP), CD68, and CD3. Low magnification (10X) panels show normal brain (N) and tumor (T) tissue (black scale bar=100µm). High magnification (40X) panels (black scale bar=20µm) indicate positive staining for areas delineated in low-magnification panels. Representative images from a single experiment consisting of independent biological replicates are displayed.

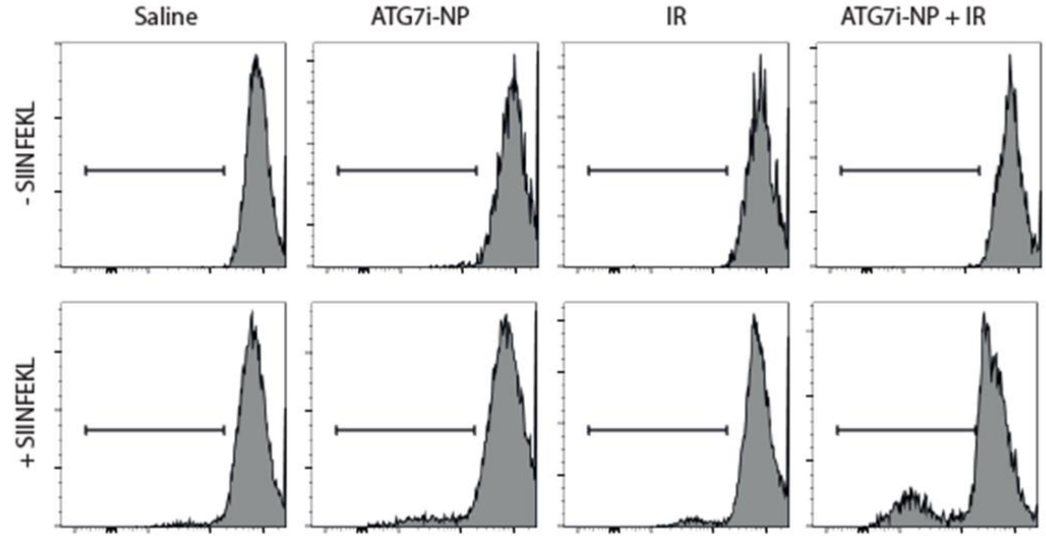

Figure 4-10. T cell proliferation was measured as the reduction of CFSE staining in the CD45+/CD3+/CD8+ population. Upper panel: Representative histograms show CFSE stains of unstimulated splenocytes (inactivated T cells) and Lower panel: Representative histograms show 100nM SIINFEKL-induced T cell proliferation from Saline, ATG7i SPNP, IR and ATG7i SPNP + IR treated groups.

Chapter 5

Broadening the SPNP Platform Toward Other Therapeutics and Proteins

5.1 Introduction

Thus far, this thesis has described three types of protein synthetic protein nanoparticles for the use of glioma treatment. In **Chapter 2**, the production of SPNPs encapsulating a hydrophobic drug (i.e. paclitaxel) was described. In **Chapter 3**, bicompartmental SPNPs were produced to load a hydrophobic drug (paclitaxel) and an siRNA (STAT3 siRNA). **Chapter 4** discussed the expansion of siRNA in SPNPs. Previously, a STAT3 siRNA was delivered using the SPNP technology for the treatment of glioblastoma. Here, it was sought to expand the siRNA delivery to a different target (ATG7) for a different glioma model (diffuse astrocytoma). While these chapters describe the expansion of SPNPs produced via EHD (co) jetting, it only represents a fraction of possibilities and only demonstrates a few examples of what has already been achieved. Published work during my PhD that used SPNPs includes the following papers,[114,174,197,246] but are not here in their entirety for this thesis to reduce redundancy. However, in this chapter, I will provide a summary of two (co)-first author papers with a focus on the SPNP fabrication, characterization, briefly and highlight main in vitro and in vivo results, if applicable. How these works tie into the thesis will also be described, particularly for those works where SPNPs were not produced directly for glioma therapeutic applications.

5.2 Systemic Delivery of AMD3100 SPNPs for Glioma Therapy

Adapted with permission from:

"Systemic Delivery of an Adjuvant CXCR4-CXCL12 Signaling Inhibitor Encapsulated in Synthetic Protein Nanoparticles for Glioma Immunotherapy."

Mahmoud S. Alghamri*, Kaushik Banerjee*, Anzar A. Mujeeb*, Ava Mauser*, Ayman Taher, Rohit Thalla, Brandon L. McClellan, Maria L. Varela, Svetlana M. Stamatovic, Gabriela Martinez-Revollar, Anuska V. Andjelkovic, Jason V. Gregory, Padma Kadiyala, Alexandra Calinescu, Jennifer A. Jiménez, April A. Apfelbaum, Elizabeth R. Lawlor, Stephen Carney, Andrea Comba, Syed Mohd Faisal, Marcus Barissi, Marta B. Edwards, Henry Appelman, Yilun Sun, Jingyao Gan, Rose Ackermann, Anna Schwendeman, Marianela Candolfi, Michael R. Olin, Joerg Lahann**,** Pedro R. Lowenstein , and Maria G. Castro (* equal contribution). ACS Nano (2022)

5.2.1 Introduction

Glioblastoma IDH wild type (WHO CNS grade 4) is an aggressive brain tumor with poor prognosis, characterized by a high level of cellular and molecular heterogeneity, high proliferative capacity, and invasive borders, making GBM challenging to treat.[247] The invasive characteristics of GBM lead to infiltration of tumor cells into the normal brain tissue, making GBM difficult to completely resect and increasing the likelihood of tumor recurrence. This is compounded by the presence of immunosuppressive immune cells which hinder the effectiveness of immunotherapies.[248] Moreover, the presence of the blood–brain barrier (BBB) provides both physical and biochemical barriers to drug delivery into the brain.[17] This limits the brain permeability of many chemotherapeutic drugs, including monoclonal antibodies, antibody–drug conjugates, and hydrophilic molecules that do not readily cross lipid bilayers.[249]

The C-X-C motif chemokine ligand-12/C-X-C motif chemokine receptor-4 (CXCL12/CXCR4) signaling pathway is involved in multiple physiological processes including hematopoiesis,[250] retention of hematopoietic stem cells (HSCs) in bone marrow, and central nervous system (CNS) development.[251,252] Several studies have illustrated the involvement of activated CXCL12/CXCR4 signaling in solid cancers in promoting survival, growth, and metastasis.[253] In GBM, it has been previously demonstrated the CXCL12/CXCR4 signaling pathway is important for sustained invasion,[254] enhanced angiogenesis,[255] and maintenance of glioma stem-cell migration and therapeutic resistance.[256] This pathway is particularly upregulated under hypoxic conditions, a feature that is associated with worse prognosis in GBM.[257] Therefore, blocking this pathway could represent a therapeutic strategy in glioblastoma. One method is using Plexifor (AMD3100), which is a small molecule therapeutic that was initially developed as a blocker of HIV entry. However, its use in glioblastoma has since been explored with it showing tumor recurrence prevention.[255,258] Here, we explore the use of AMD3100 to treat glioblastoma, but packaged within synthetic protein nanoparticles (SPNPs) through electrohydrodynamic (EHD) jetting. It has been shown prior to this that siRNA delivery through SPNPs can successfully deliver therapeutic to the brain.[218] Furthermore, the addition of the tumor penetrating peptide augmented the effect by impacting the biodistribution. In this study, SPNPs were leveraged to deliver a different type of therapeutic – a hydrophilic small molecule (Plexifor (AMD3100) octahydrocholoride) – to produce AMD3100 SPNPs. These SPNPs showed excellent morphological features (high circularity, ~100 nm size), controlled release of AMD3100 from the SPNPs, batch to batch reproducibility, and serum stability. Survival studies revealed a survival benefit when the AMD3100 SPNPs were used with ionizing radiation leading to long-term survivors. Lastly, these survivors showed immunological memory once implanted with a second tumor and given no additional treatment. Taken together, our results demonstrate that the SPNP construct can be expanded to carry a water-soluble small molecule, which highlights the versatility of EHD jetting and SPNPs.

5.2.2 Materials and Methods

5.2.2.1 Materials

DMEM-F12 (11330057), DMEM (12430054), RPMI-1640 (11875119), FBS (10437028), and PBS (14190250) were acquired from GIBCO, Life Technologies. Epidermal growth factor (EGF) and fibroblast growth factor (FGF) were obtained from Peprotech. Supplements N2 (17502048), B27 (17504044), and penicillin–streptomycin (15240062) was bought from GIBCO, Life Technologies. Specific anti-mouse CD8 (100706), anti-mouse CD45 (147716), CD3 (100218), Gr1 (108430), CD11b (101226), Ly6G (127648), Ly6C (128028), CXCR4 (146508), GzmB (372216), and IFN-γ (505826) antibodies for flow cytometry analysis were obtained from Biolegend. SIINFEKL tetramers were obtained from MBL International (TB-5001-1). Viability dye (LIVE/DEAD fixable aqua dead cell stain kit, NC0180395) was purchased from Fisher Scientific. For immunohistochemistry, anti-mouse MBP (MAB386) and GFAP (AB5541) primary antibody were purchased from Millipore Sigma; anti-Nestin antibody (NB100-1604) was purchased from Novus Biologicals; anti-mouse Iba1 (ab178846) and CD68 (ab125212) antibodies were purchased from Abcam; anti-mouse CD8a [(HS-361003(SY)] antibody was purchased from

Cedarlane; anti-mouse CD4 (48274S) antibody was purchased from Cell Signaling. Alexa Fluor 647 anti-calreticulin antibody (ab196159) was purchased from Abcam. AMD3100 was purchased from Selleck Chemical LLC (Cat# S8030).

5.2.2.2 Synthesis of AMD3100 Synthetic Protein Nanoparticles (AMD3100 SPNPs)

AMD3100-SPNPs were fabricated via the electrohydrodynamic jetting process previously established in our group.[114,218] Briefly, human serum albumin was dispersed in a solvent mixture (4:1 v/v) of ultrapure water and ethylene glycol; final concentration of 7.5 w/v%. Bovine serum albumin labeled with Alexa Fluor 647 was added at 0.5 w/w% relative to HSA to generate fluorescently labeled SPNPs. Next, the cyclic nine amino acid transcytotic peptide, iRGD, was added at 355 ng/mg of albumin. Subsequently, 3.75 mg of AMD3100 per mL of jetting solution was incorporated after first dissolving the drug in a small aliquot of ultrapure H_2O. Lastly, a bifunctional OEG (NHS-OEG-NHS, 2 kDa) was added at 10.0 w/w% relative to HAS. This was done to cross-link the SPNPs. To prepare empty SPNPs, we followed the same formulation steps except that ultrapure water was added, in lieu of AMD3100. The complete jetting solutions were pumped through a syringe outfitted with a stainless steel 26-gauge blunt tip stainless needle; the flow rate was kept constant at 0.2 mL h^{-1} while being subjected to a constant voltage (ranging from 7.5 to 10.2 kV) to form a stable Taylor cone at the tip of the needle. Particles were collected in grounded aluminum pans at a needle to collection distance of 15 cm. Particles were then incubated at 37 °C for 7 days to achieve the polymerization process, yielding water-stable protein nanoparticles. SPNPs were then kept in their dry state, at room temperature, and in dark until used for experimentation.

5.2.2.3 Collection and Purification of SPNPs

SPNPs were collected according to a standard protocol developed in our group.[218] In brief, a small volume (5–10 mL) of PBS + 0.5% Tween 20 was added to the aluminum pans containing cross-linked, water-stable AMD3100-SPNPs. Gentle mechanical scraping of the pans using a plastic razor blade was used to transfer the SPNPs from the solid surface into the collection solution. To disperse any aggregates, the NP suspension was briefly sonicated and passed through a 40 µm cell strainer filter. To pellet and remove remaining large protein aggregates, the solution was centrifuged for 4 min at 4000 rpm (3220*g*). The supernatant containing SPNPs was aliquoted into 2 mL Eppendorf tubes and centrifuged at 15,000 rpm (21,500*g*) to pellet the SPNPs. Finally, the pelleted particles were combined into a single concentrated sample. SPNPs were used within 1 week after collection, and they were continually stored at 4 °C in sterile PBS in the interim.

5.2.2.4 Characterization of SPNP Size, Shape, Concentration, and Secondary Structure

SPNPs were extensively characterized as previously described to establish reasonable tolerances against which each batch could be compared. Prior to their use in any experiments, collected particles were similarly measured to ensure they met specifications and to confirm batch-to-batch properties were consistently maintained. Physical characterization comprised the measurement of particle size in both their dry and hydrated state. To determine particle size and shape and to examine their morphology, small silicon wafers were positioned on the grounded aluminum collection surface and were subjected to the same 7-day incubation period required to complete the step-growth polymerization. Samples were gold sputter coated and afterward imaged via SEM using a FEI NOVA 200 SEM/FIB instrument using a current of 0.14 nA and a voltage of 17 kV. SEM images of SPNPs ($n > 300$) were characterized using ImageJ software according to protocols previously developed in our lab.[114] To investigate SPNP properties after hydration, SPNPs were collected and purified as described above. The stock SPNP solution was diluted 100-fold in 0.22 μm filtered 10 mM KNO_3 for subsequent DLS and zeta-potential measurements. To further investigate size and solution concentration, nanoparticle tracking analysis (NTA) was used. DLS, zeta-potential, and NTA analyses were performed using the Malvern Nano ZSP and NanoSight NS300 instruments. The concentration of the AMD3100-SPNP solution was assessed employing the BCA (bicinchoninic acid) assay. To analyze the shape and size of the SPNPs, a SEM PDI is presented. This value does not have a commonly accepted definition, nevertheless we define it as the SDSEM/diameterSEM,AVG. This is done to provide an easy reference number for quantitative comparison between SEM derived data sets. This value can also be compared, qualitatively, to the SDDLS/diameterDLS,AVG for number-average DLS data. While one could square these values for comparison to intensity DLS PDI values, this approach is not recommended due to the nonlinear relationship between number/count-based scores and intensity (direct spectral deconvolution) data. CD spectroscopy measurements were taken of HSA, the prejetting solution, the postjetting solution, and the cross-linked SPNPs. All samples' concentrations were measured via a BCA assay then diluted in ultrapure water to achieve a final concentration of 0.05 mg/mL. Samples were recorded using CD spectrometer (Jasco J-815) in a rectangular quartz cuvette of 1 mm path length. Measurement parameters were set to a wavelength range of 260 to 190 nm, with a step size of 0.2 nm, data integration time of 2 s, slit width of 1.00 nm, and a scanning speed of 100 nm/min. Each spectrum was an average of three measurements and was subsequently baseline corrected using an ultrapure water spectrum before analysis. Dichroweb was used to further analyze the CD spectroscopic data. (53) CDDSTR was chosen as the analysis program with the reference set 7. (54,55) Output data included fractional contributions from helix 1 (α-helix, regular), helix 2 (α-helix, distorted), sheet 1 (β-sheet, regular), sheet 2 (β-sheet, distorted), turns, and unordered. (55)

5.2.2.5 Serum Stability of AMD3100 SPNPs

SPNP samples were distributed into mouse or human serum ($n = 3$) and rotated at 37 °C. SPNPs samples in PBS at 37 °C were included as controls. After 24 h, aliquots of the samples were removed for determination of particle size distribution. Three instrumental determinations were averaged for each sample.

5.2.2.6 In vitro Release of AMD3100 from AMD3100 SPNPs

AMD3100-SPNPs were manufactured and characterized (SEM, DLS, BCA assay) as described before, and resuspended in 1.3 mL of DPBS. The SPNPs were placed on ice and tip sonicated for 30 s, using 1 s on, followed by 2 s off. Samples were then transferred to a dialysis device (Float-a-Lyzer, MWCO 8–10 kDa) prepared following the manufacturer's instructions. The device was placed in 30 mL of DI water and was constantly stirred at 37 °C. The dialysis device was removed at predetermined time points and placed in 30 mL of DI water. After being transferred from the dialysis device, the sample was frozen and freeze-dried over 2 days. After freeze-drying, the SPNP samples were solubilized in 1 mL of 50% (v/v) HPLC grade methanol and 50% (v/v) ultrapure water. They were later evaluated using UPLC-MS.

5.2.2.7 AMD3100 SPNPs in vivo Dose Preparation

AMD3100-SPNPs were collected and purified as previously described prior to diluting the resulting solution to a concentration of 2.7 mg mL^{-1} in sterile PBS. Aliquots of the stock solution were diluted, and standard DLS, zeta-potential, and NanoSight measurements as detailed above were completed to ensure batch-to-batch consistency. Once validated, 100 μL of the stock SPNP solution was allocated per dose per mouse for tail vein injection. Control SPNPs, encapsulating no AMD3100, were collected, purified, characterized, and dosed identically to AMD3100-SPNPs on a particle mass basis.

5.2.2.8 Cell Line and Cell Culture Conditions

Genetically engineered mouse glioma models: RPA (*PDGFRA D842V*/sh*TP53*-GFP/*shATRX*) and OL61 (*shp53/PDGFB/NRAS*), OL61-OVA, were developed by the sleeping beauty model as described before.[192,193] Arf$^{-/-}$ wtIDH1 (*PDGFB/shP53/shATRX/Ink4a/Arf*$^{-/-}$). Tumors were generated by injection of DF-1 (ATCC, CRL-12203) cells transfected with a combination of RCAS plasmids (*RCAS PDGFB-HA*, *RCAS shp53-RFP*) using the FuGENE 6 transfection kit (Roche, 11814443001) according to the manufacturer's protocol and as previously described.[192]

5.2.2.9 Intracranial Glioblastoma Models

Tumor implantation was done as described before. (58) Briefly, mice were anesthetized using ketamine and dexmedetomidine prior to stereotactic implantation with 50,000, 100,000, and 200,000 cells for OL61, Arf–/–, and RPA S8 in the right striatum, respectively. The coordinates for implantation are 0.5 mm anterior and 2.0 mm lateral from the bregma and 3.0 mm ventral from the dura. Neurospheres were injected at a rate of 1 μL/min. Mice were given a combination of buprenorphine (0.1 mg/kg) and carprofen (5 mg/kg) for analgesia.

5.2.2.10 In vivo Radiation

Ten days post-OL61-OVA tumor cell (2 × 104) implantation (bioluminescence signal = 106), mice were subjected to an irradiation (IR) dose of 2 Gy for 5 days a week for 2 weeks for a total of 20 Gy of ionizing radiation. The procedure was performed as described before. (25,32) Briefly, mice were lightly anaesthetized with isoflurane. Mice were then placed under a copper orthovoltage source, with the irradiation beam directed to the brain and body shielded by iron collimators. Irradiation treatment was given to mice at the University of Michigan Radiation Oncology Core.

5.2.2.11 Determination of AMD3100 Brain/Plasma Ratio

Ten days post-tumor implantation (3 × 104 OL61 cells), mice harboring intracranial gliomas were divided into three groups (n = 4 mice/group) and injected with (1) saline, (2) free AMD3100 (delivered i.p.), and (3) AMD3100-SPNP (delivered i.v.). On day 11, mice were anesthetized using ketamine and dexmedetomidine, blood was collected, and brains were harvested after clearing the blood by perfusing with 300 mL of Tyrode solution.

5.2.2.12 Detection of AMD3100 in Plasma

AMD3100 (Selleckchem lot#: S8030) and internal standard (IS, AMD3100-d4, Cayman Cat# 26490) were weighed and dissolved in methanol. A series of AMD3100 standard solutions (200, 160, 120, 80, 40, 20, 10, and 5 ng/mL) were prepared using methanol. Next, 250 ng/mL of AMD3100-d4 was used as IS. Plasma samples (20 µL) were either spiked with 20 µL IS or not spiked, and then they were extracted with 240 µL methanol containing 1% TFA. The mixture was vortexed and centrifuged for 5 min at 12,000 rpm. Supernatants were blown dry with a stream of nitrogen at 45 °C. We reconstituted the residue using 80 µL of 50% methanol in water containing 0.1% formic acid and was then centrifuged for 5 min at 12,000 rpm. We used UPLC-MS to analyze the supernatants. Supernatants for each sample (3 µL volume) were analyzed by UPLC-MS. Analysis was carried out through Xselect HSS T3 column (4.6 mm × 100 mm, 3.5 µm, Waters, Milford, MA, USA). Mobile phase A (0.1% formic acid in water) and mobile phase B (0.1% formic acid in methanol) were operated with an isocratic elution using a flow rate of 1.0 mL/min. The column and sample temperature were 40 and 20 °C, respectively. The injection volume was 3 µL. Analysis of AMD3100 was performed using the Waters Acquity UPLC system (Waters Corp., Milford, MA, USA) consisting of a quaternary solvent manager, sample manager, heated column compartment, ESI mass detector (QDa), and a cooling autosampler.

5.2.2.13 Detection of AMD3100 in Brain

Brain tissue was dispersed into a single cell suspension and passed through a 70 µm cell strainer with 3 mL of PBS. The suspension was frozen using liquid nitrogen and thawed in a 37 °C/water bath three times to generate brain tissue lysate. A series of AMD3100 standard solutions (200, 160, 120, 80, 40, 20, 10, and 5 ng/mL) were prepared using methanol. Next, 250 ng/mL AMD3100-d4 was used as IS. Brain tissue lysates (600 µL) with or without spiking with 20 µL of IS solution, were extracted using 1.2 mL methanol containing 1% TFA. The samples were vortexed and centrifuged for 5 min at 12,000 rpm. Supernatants were subsequently dried using a stream of nitrogen at 45 °C. The residue was reconstituted with 40 µL of 50% methanol in water containing 0.1% formic acid and centrifuged at 12,000 rpm for 5 min. Supernatants (3 µL volume) were analyzed by UPLC-MS. Analysis was carried out using Acquity UPLC BEH C18 column (2.1 mm × 100 mm, 1.7 µm, Waters, Milford, MA, USA). Mobile phase A (0.1% formic acid in water) and mobile phase B (0.1% formic acid in acetonitrile) were operated using a gradient elution at a flow rate of 0.3 mL/min2. The column and sample temperature were 40 and 20 °C, respectively. The injection volume was 3 μL. Analysis of AMD3100 was performed as described above.

5.2.2.14 Statistical Analysis

Sample sizes were selected based on pilot data from experiments done in our laboratories and published results from the literature. Animal experiments were performed after randomization. Data were analyzed by one- or two-way analysis of variance (ANOVA), followed by Tukey's multiple comparisons post-test. Kaplan–Meier survival curves were assessed using the log-rank (Mantel-Cox) test with Prism 8.1 (GraphPad Software). Data were normally distributed, and variance between groups was similar. Values of *p* values less than 0.05 were considered statistically significant. All data were represented as means ± SEM, and the sample size is indicated for all experiments. No experimental values were excluded from the analysis.

5.2.3 Results

5.2.3.1 Fabrication and Characterization of AMD3100 SPNPs

AMD3100 SPNPs were produced by EHD jetting a formulation containing AMD3100. This formulation and order of addition is shown in **Figure 5-1**A. First, human serum albumin was dissolved in a co-solvent system of water (80% v/v) and ethylene glycol (20% v/v). Next, Alexa Fluor 647 BSA conjugate was incorporated at a 0.50 wt% relative to HSA. This was added to fluorescently tag the AMD3100 SPNPs. Next, the tumor penetrating peptide, iRGD, was added followed by AMD3100. Lastly, crosslinker was introduced. This was loaded into a syringe with a needle then EHD jetted (**Figure 5-1**B).

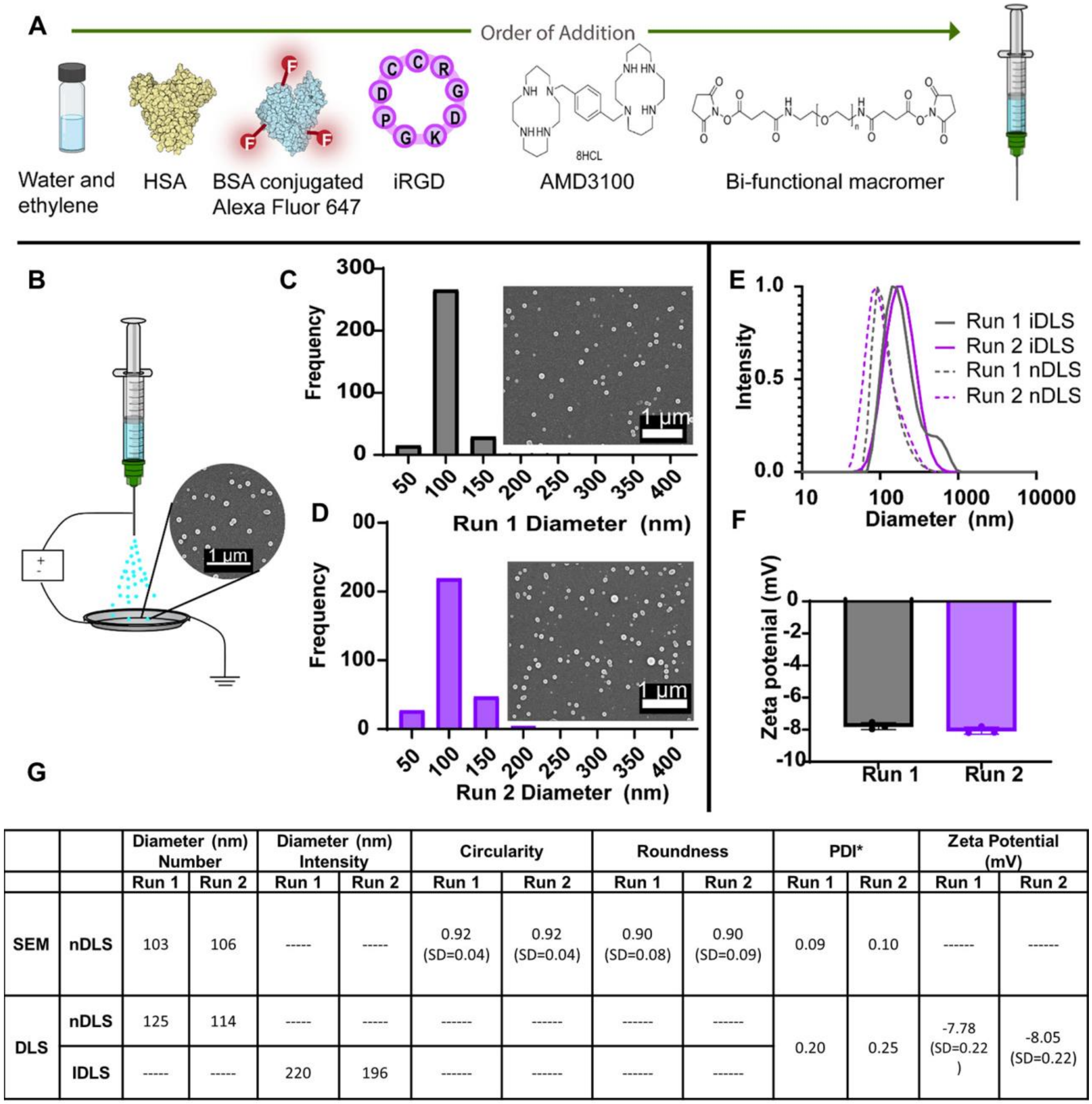

		Diameter (nm) Number		Diameter (nm) Intensity		Circularity		Roundness		PDI*		Zeta Potential (mV)	
		Run 1	Run 2	Run 1	Run 2	Run 1	Run 2	Run 1	Run 2	Run 1	Run 2	Run 1	Run 2
SEM	**nDLS**	103	106	-----	-----	0.92 (SD=0.04)	0.92 (SD=0.04)	0.90 (SD=0.08)	0.90 (SD=0.09)	0.09	0.10	------	------
DLS	**nDLS**	125	114	-----	-----	------	------	------	------	0.20	0.25	-7.78 (SD=0.22)	-8.05 (SD=0.22)
	IDLS	-----	-----	220	196	------	------	------	------				

Figure 5-1. Preparation of electrohydrodynamic (EHD) jetting and characterization of AMD3100-SPNPs. (A) Formulation of AMD3100-SPNPs indicating the order of addition of different components. (B) Schematic of the jetting process for AMD3100-SPNPs depicting a scanning electron microscopy (SEM) image of the SPNPs jetted atop of the collection plate (scale bar = 1 μm). (C) Size distribution of SPNPs of an independent run, run 1, in their dry state characterized via SEM and ImageJ analysis. Average diameter = 103 ± 20 nm (PDI = 0.09). Scale bar = 1 pm. (D) Size distribution of SPNPs of a second independent run, run 2, in their dry state characterized via SEM and ImageJ analysis. Average diameter = 106 ± 25 nm (PDI = 0.10). (E) Numbers-based dynamic light scattering (nDLS) size distribution (dashed) and intensity-based DLS (iDLS) of SPNPs in PBS comparing run 1 and run 2. (F) Zeta-potential of run 1 and run 2. (G) Summary table of SPNP characterization of size, shape, and charge.

Batch to batch variation of jetting AMD3100 SPNPs were assessed and compared (**Figure 5-1**A-G). Results showed that the dry-state SPNPs had an average diameter of about 100 nm in both batch 1 and batch 2 (**Figure 5-1**C-D) These SPNPs were uniquely small after EHD jetting compared to other SPNPs produced. This can be attributed to the AMD3100 purchased, which was 8HCL AMD3100. The hydrochloride salt is the most used salt to make drugs more stable, but salts have a known impact on EHD jetting. Salt increases the conductivity of the solution, thereby resulting in smaller nanoparticles. These AMD3100 SPNPs also had a low PDI of 0.09 and 0.10 as jetted. Furthermore, the SPNPs were highly circular (>0.89). Once the AMD3100 SPNPs were collected and serial centrifuged, the hydrodynamic diameter of both batches was assessed through DLS and were 220 nm and 196 nm in **Figure 5-1**E. The zeta potential for both batches were negative at around -8 mV in DPBS. These results indicate that the AMD3100 SPNPs had low batch to batch variability.

Next, it was of interest to understand whether the EHD jetting and chemical crosslinking had any significant impact on the secondary structure of the albumin in the AMD3100 SPNPs **Figure 5-2**.

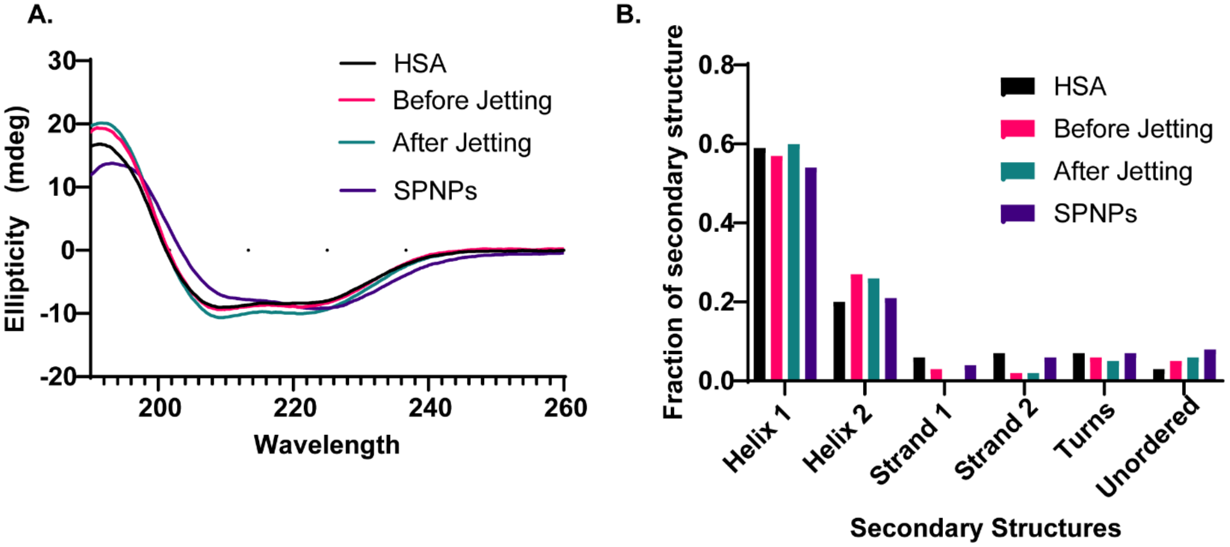

Figure 5-2. Preservation of secondary structures of HSA during AMD3100 SPNP production. (A) CD Spectra and (B) quantification of secondary structures of native HSA, HSA within the jetting solution prior to EHD jetting, HSA within the jetting solution after EHD jetting and HSA as crosslinked AMD3100-SPNPs.

Circular dichroism was performed for four groups. The first group was HSA in solution. This was used as a positive control for native HSA structure. The second group was "Before Jetting", which was the jetting solution prior to being exposed to EHD jetting. The third group was "After Jetting", which was the nanoparticles produced after jetting. These particles were collected immediately without sufficient time to crosslink. The last group was the AMD3100 SPNPs, which were fully crosslinked. The difference between the "After Jetting" and the SPNPs is the extent of crosslinking. According to prior work, the crosslinking at 37 ˚C for 7 days is essential to maximize the yield and produce stable SPNPs in aqueous conditions. Therefore, we were testing the impact of the formulation, jetting (or voltage), and crosslinking on the secondary structure of albumin. The spectra results align well with each other indicating that there was not a significant alteration to the secondary structure of albumin in these groups. **Figure 5-2**B shows the secondary structure fractional analysis of the spectra in **Figure 5-2**A and are categorized as α-helix (regular and distorted), β-sheet (regular and distorted), turns, and unordered. This analysis corroborates the spectra in **Figure 5-2**A.

To assess the stability of the AMD3100 SPNPs in a more physiologically relevant media, the serum stability was tested and compared to a PBS control. The AMD3100 SPNPs size was tested in PBS, mouse serum, and human serum over 24 hours at 37 ˚C (**Figure 5-3**). These results show that the sizes were comparable to each other, and no significant differences were observed. While these results indicate that the SPNPs are stable under these conditions, future work could seek to understand the stability at longer time points.

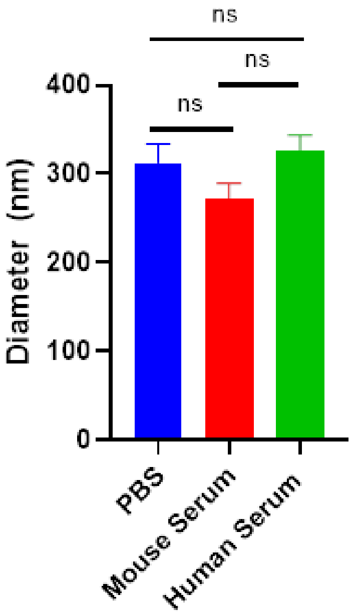

Figure 5-3. AM3100 SPNPs are stable in mouse and human serum. Stability of AMD3100-SPNPs in PBS, mouse serum and human serum at 24h at 37˚ C Size measurements are displayed in intensity based DLS. Ns=not significant, n=3 experimental replicates.

5.2.3.2 In vitro Release of AMD3100 from AMD3100 SPNPs

Another feature of these AMD3100 SPNPs that can characterize them is the release of AMD3100. Therefore, an in vitro release study was conducted to evaluate whether the AMD3100 diffuses out the SPNP if so, what is the release profile. The AMD3100 SPNPs incubated at 37 ˚C for 9 days in a dialysis device. At predetermined time points, the dialysis membrane was removed from the dialysis medium sink and placed into a fresh sink. The release samples were frozen at -20 ˚C then freeze dried. The freeze-dried samples were reconstituted then analyzed via UPLC-MS. The release is shown in **Figure 5-4** and is plotted to show the cumulative release of AMD3100 normalized to the sum of the mass released. An initial burst of 13% occurs in the first 2 hours at a rate of 6.7%/hour. Thereafter, the release was slower at a rate of approximately 2% per hour for the 13 h and 17 h release samples (cumulative release of 22% and 35%, respectively). The next time points demonstrated a slower rate of release of <1% per hour. This suggests that the majority of AMD3100 from the SPNPs is released within the first few hours.

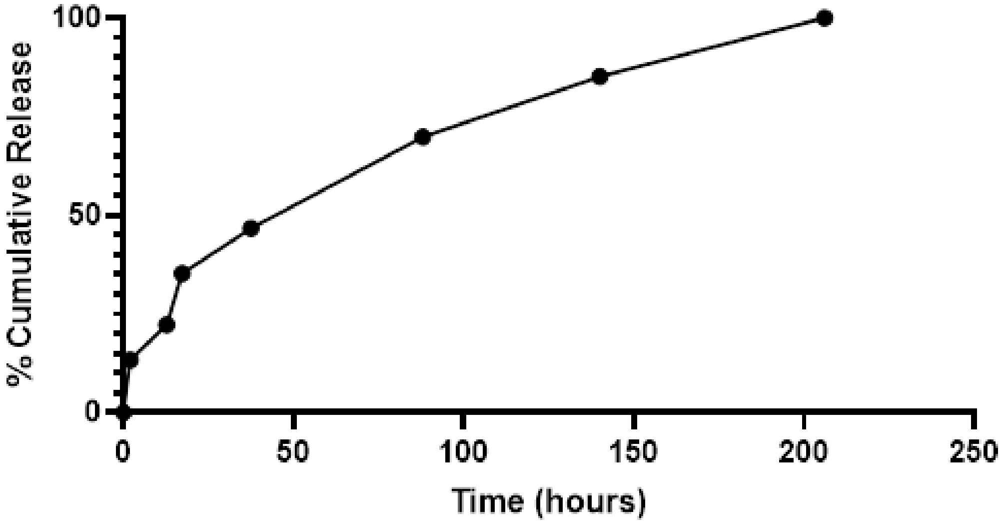

Figure 5-4. In vitro AMD3100 release from AMD3100-SPNPs expressed as % cumulative release relative to the total mass released over 206 hours.

5.2.3.3 AMD3100 SPNPs with Ionizing Radiation Elicit Enhanced Therapeutic Efficacy and anti-GBM immune response

The AMD3100 SPNPs were assessed in vivo for their anti-tumor activity and to assess their immune response. The treatment regimen is shown in **Figure 5-5**A. OL61 tumor cells were implanted on day 0. Beginning on Day 5, treatment began with $2x10^{11}$ AMD3100 SPNPs. Thereafter, 9 more doses were given to each mouse for a total of 10 AMD3100 doses. In addition to the AMD3100 SPNPs, ionizing radiation was used as it represents an important part of the standard of care for GBM. The ionizing radiation was given 10 times over two weeks. After treatment, the survival of the groups was monitored and is shown in **Figure 5-5**B. Outside of the AMD3100 SPNPs (with and without IR), empty SPNPs were tested as a control for the ADM3100 SPNPs. These empty SPNPs were the same as the AMD3100 SPNPs minus the inclusion of the AMD3100. Ionizing radiation, AMD3100 and saline were also tested. The saline control group exhibited a survival of a mere 24 DPI. Empty SPNPs were close to this at a median survival (MS) of 28 DPI. The IR and AMD3100 both improved the MS similarly, but significantly ($p<0.05$). The AMD3100 improved the survival more so compared to the control and AMD3100 alone ($p<0.05$), but the combination of the AMD3100 SPNPs with IR resulted in better survival benefit with 67% of the mice living long term ($p<0.05$). The long-term survivors from the AMD3100 SPNP+IR group were rechallenged with a second tumor and compared to a control. The mice that had previously received treatment with AMD3100 SPNPs and IR were tumor free (**Figure 5-5**C), providing evidence of an underlying immunological memory. Conversely, the control mice did not exhibit a high survival rate. In **Figure 5-5**D, the saline control, IR, AMD3100 SPNPs, and AMD3100 SPNP+IR rechallenged long term survivor are compared. The H&E staining shows the AMD3100 SPNPs provide some tumor burden relief compared to the saline and IR groups, but not to the extent as the AMD3100 SPNP+IR rechallenged long term survivor, where eradication of the tumor can be observed. Immunohistochemistry was used to analyze the whether the integrity of the brain structure was impacted using markers for glial fibrillary acidic protein (GFAP) and myelin basic protein (MBP). In the rechallenged survivor group, there is not any indication of the disturbance of the structure. CD68, a marker for macrophages, was used to assess the level of the immune cellular infiltrates and is shown in the last row of **Figure 5-5**D. An increase of CD68+ cells is observed in groups that received AMD3100 SPNPs or IR. Interestingly, the long-term survivors show a reduced number of CD68+ macrophages.

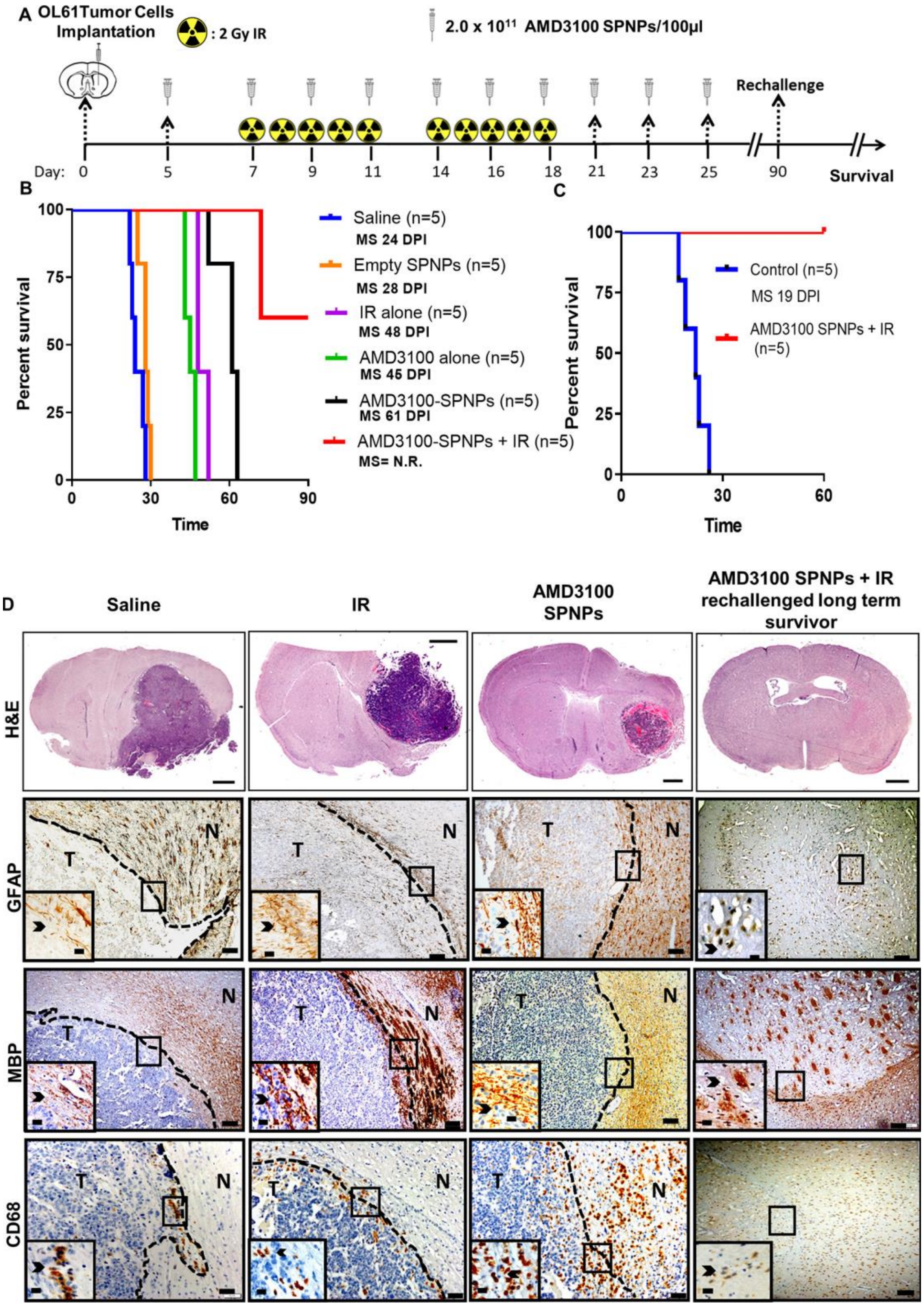

Figure 5-5. Combining AMD3100-SPNPs with IR prolong survival of GBM tumor-bearing mice. (A) Timeline of treatment for the combined AMD3100-SPNPs + IR survival study. (B) Kaplan–Meier survival curve. Significant increase in median survival is observed in all groups receiving AMD3100 alone (i.p.) or IR ($p < 0.01$). Mice ($n = 5$) treated with AMD3100-SPNPs (i.v.) + IR reach long-term survival time point (100 dpi) with no signs of residual tumor. (C) Kaplan–Meier survival plot for rechallenged long-term survivors from AMD3100-SPNPs + IR ($n = 5$) or control (OL61 untreated) ($n = 5$). Data were analyzed using the log-rank (Mantel-Cox) test. Days post implantation =

dpi; NS = not significant; **$p < 0.01$, ***$p < 0.005$. (D) H&E staining of 5 μm paraffin embedded brain sections from saline (24 dpi), IR (48 dpi), AMD3100-SPNPs alone (45 dpi) and long-term survivors from AMD3100-SPNPs + IR treatment groups (60 dpi after rechallenging with OL61 cells) (scale bar = 1 mm). Paraffin-embedded 5 μm brain sections for each treatment groups were stained for CD68, myeline basic protein (MBP), and glial fibrillary acidic protein (GFAP). Low-magnification (10×) panels show normal brain (N) and tumor (T) tissue (black scale bar = 100 μm). Black arrows in the high magnification (40×) panels (black scale bar = 20 μm) indicate positive staining for the areas delineated in the low-magnification panels. Representative images from an experiment consisting of three independent biological replicates are displayed.

5.2.3.4 SPNPs-Mediated AMD3100 Delivery to the Brain in vivo

To assess whether synthetic protein nanoparticle encapsulation improved the access of AMD3100 into the brain, we administered free AMD3100 or AMD3100-SPNPs systemically in brain-tumor-bearing mice and measured the content of the drug in brain and plasma 8 h later using ultraperformance liquid chromatography mass spectroscopy (UPLC-MS).

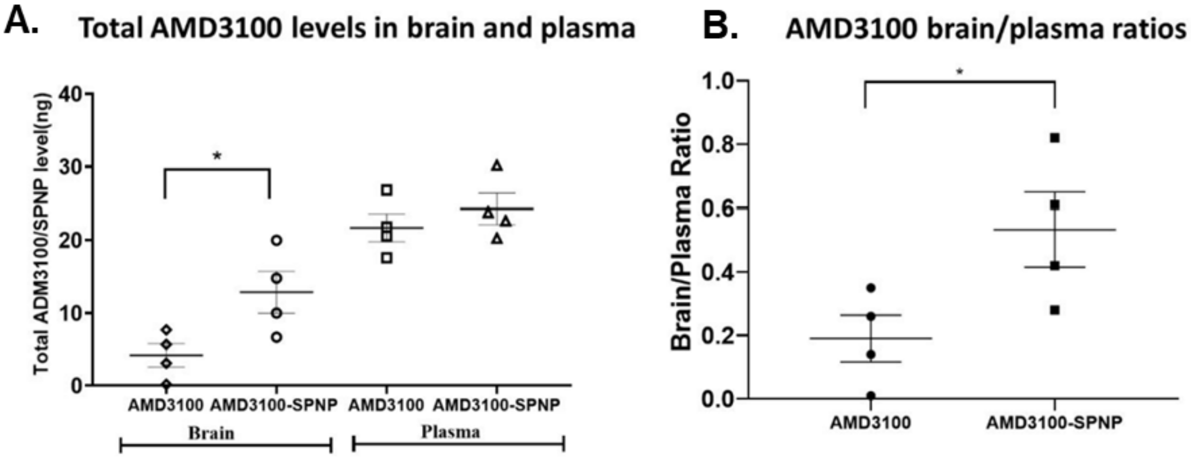
A. Total AMD3100 levels in brain and plasma

B. AMD3100 brain/plasma ratios

Figure 5-6. A. Total levels of AMD3100 in brain tissue and in plasma were 7 measured 8 hours post treatment using Ultra Performance Liquid Chromatography mass 8 spectroscopy (UPLC-MS). B. Brain/Plasma ratios for free AMD3100 (solid circles) and 9 AMD3100-SPNP (solid squares). The data are presented as means ± SEM (n=4/group). * $p<0.05$ (Student's t test).

While the total levels of AMD3100 in plasma were similar in mice treated with free AMD3100 (21.7 ± 1.92 ng) or AMD3100-SPNP (24.2 ± 2.1 ng) (**Figure 5-6**A), the total levels of AMD3100 found in brain tissue were higher when mice received AMD3100-SPNPs (12.875 ng ±2.89) than when they received free AMD3100 (4.175 ng ±1.62) (Figure S12B, $p < 0.05$, Student's t test). In addition, the brain/plasma ratio (B/P) for AMD3100 was found to be ∼3 times higher when AMD3100 was delivered encapsulated in SPNP (0.53 ± 0.11) than when it was delivered as free drug (0.19 ± 0.07) ($p < 0.05$, Student's t test) (**Figure 5-6**B).

5.2.4 Discussion

In conclusion, these results demonstrate that AMD3100 could be packaged within the SPNPs and provide a therapeutic response in GBM models. AMD3100, like paclitaxel, is a small molecule. However, AMD3100 was modified to be water soluble, whereas paclitaxel is considered water insoluble. Water solubility is not only an important consideration in the delivery of free drugs (i.e. without a carrier such as a nanoparticle) systemically but is a consideration when producing SPNPs through EHD jetting. The balance between the solubility of the drug, the limit of denaturation of protein, and the solvent conditions to provide stable jetting, must all be balanced. In this study, AMD3100 was simply added into the formulation without a concern of its solubility, whereas paclitaxel had to be "solubilized" in HSA through high pressure homogenization prior to jetting. In fact, the AMD3100 provided an additional benefit – it decreased the size. This was because the AMD3100 was AMD3100 octahydrochloride. The addition of salt not only improves the solubility of compounds, but it showed to decrease the EHD-jetted size of the SPNPs (higher salt increases the conductivity and thus decreases the size). The release of AMD3100 from the SPNPs was a sustained release, which was very similar to that observed from the paclitaxel SPNPs. The therapeutic efficacy of the AMD3100 SPNPs was also shown by an improvement in the median survival when combined with ionizing radiation, and immunological memory was demonstrated. The mode of delivery also proved to be important with higher brain/blood ratios found in groups treated with AMD3100 SPNPs as opposed to free AMD3100. Outside of the results reported here, we showed that AMD3100 SPNPs block CXCL12/CXCR4 signaling in mouse and human glioblastoma cell cultures, which result in inhibition of glioblastoma proliferation, reduced infiltration of CXCR4+ monocytic myeloid-derived suppressor cells into the tumor microenvironment, restoration of the blood-brain integrity, and the induction of immunogenic cell death. These results are discussed further in the publication, which is cited at the beginning of this section.

5.3 Enzymatic Synthetic Protein Nanoparticles as Colloidal Antioxidants

Adapted with permission from:
"Enzyme-Based Synthetic Protein Nanoparticles as Colloidal Antioxidants"
Ava Mauser, Daniel F. Quevedo, Boya Zhang, Yazmin Hernandez, Anthony Berardi, William Brown, Sophia Lee, Rikako Miki, Jeffery Raymond, Joerg Lahann, Colin F. Greineder
Advanced Therapeutics (2023).
Part of the material in this chapter with modifications is discussed in the following thesis:
Daniel F. Quevedo. Design, Applications, and Processing of Synthetic Protein Nanoparticles. (Doctoral Dissertation) 2020.

5.3.1 Introduction

According to Precedence Research (precedenceresearch.com), the biotherapeutics market represents an integral part of the pharmaceutical industry, with a compounded annual growth rate (CAGR) of 8.6% over 2022-2030. In 2021, they accounted for 28% of FDA approvals in 2021; therapeutic enzymes only made up 4% of the FDA approved drugs and 14% of the biotherapeutics, despite the clear precedent for their therapeutic utility dating back to the mid 1960's.[259,260] Compared to small molecules, which continue to dominate the pharmaceutical industry, therapeutic enzymes offer the following advantages: (1) High-affinity and specificity for substrates, (2) efficient reaction rates, (3) regeneration upon substrate turnover, and (4) they become an obvious choice for the treatment of disorders caused by the absence or deficiency of endogenous enzymes, such as lysosomal storage diseases.[260] However, challenges remain, making it difficult for enzymes to completely realize their full therapeutic potential. The most critical barriers to expanded use include poor circulation half-life (due to endogenous degradation mechanisms), low specificity and the lack of targeting, and an inability to cross certain physiological barriers.[260,261] Enzymes also lack pathways that differentiate between healthy and pathologic substrates, causing off-target effects and thus, may cause toxicity.[260,261] The latter may be mitigated through appropriate targeting strategies. To address these challenges, enzymes have been modified, encapsulated, or immobilized to a scaffold *via* a wide variety of techniques.[262,263] Enzyme fixation, through adsorption or covalent immobilization onto a solid support or packaged into solid matrices,[264,265] is an often-considered strategy for medical applications. While these approaches may improve the thermodynamic stability or the performance of enzymes, they generally limit biomedical application to scenarios in which material can be injected or implanted at the intended therapeutic site. In contrast, enzyme encapsulation in or binding to injectable nanoparticles has the potential to protect them from deactivation, degradation, and immunologic responses.[266] Nanoparticle based therapies simultaneously provide a structure capable of housing additional functionalities, such as affinity ligand targeting, environment- or stimuli-dependent degradation, controlled release, and co-delivery of therapeutics.[267] Utilizing protein as the carrier modality offers several attractive properties including biocompatibility, relatively low immunogenicity, conjugation of targeting or labelling moieties, versatility, and inherent/intrinsic substrate functionality.[32] Several synthetic techniques have been used to encapsulate enzymes in protein nanoparticles, including cross-linked aggregation [268] and coacervation.[123]

As described in **Chapter 1**, protein nanoparticles can be produced from various proteins, including enzymes. Thus far, the SPNPs fabrication via EHD jetting that have been described were made using human serum albumin because they represent a as a modular and robust component.[44,269–271] However, in instances where the type of protein may be better suited for an application (i.e. targeting, or therapeutic effect), then it could be changed. In this work, we present the expansion of our SPNP platform to prepare a novel class of protein particles that are comprised of the therapeutically active enzyme, catalase, with a special focus on the stability.

5.3.2 Materials and Methods

5.3.2.1 Materials

Catalase (#C40), albumin from human serum (#A1653), Tween20 (#P4780), glycine (#G7126), 50% glutaraldehyde solution (#340855), O,O′ -Bis[2-(N-Succinimidyl-succinylamino)ethyl] polyethylene glycol (#713783), Triton X-114 (#X114) and Protease from *Streptomyces griseus* (#P5147) were purchased from Sigma Aldrich. Ultrapure water, Dulbecco's phosphate-buffered saline (DPBS), antibiotic antimycotic (#15240-062), geneticin (#10131-035), and 0.25% Trypsin-EDTA (#25200-056) were purchased from Gibco. Azidobutyric acid NHS ester was purchased from Lumiprobe. NHS ester-PEG$_4$-DBCO was purchased from BroadPharm. Pierce LDH Cytotoxicity Assay Kit (# 88953), Pierce™ BCA Protein Assay Kit (#23225), Sodium Hydroxide (#S318), DAPI (4’,6-Diamidino-2-Phenylindole, Dihydrochloride) (#D1306), and Albumin from Bovine Serum (BSA) Alexa Fluor™ 647 conjugate (#A34785) was purchased from ThermoFisher Scientific. Fetal bovine serum (#35-015-CV) and media base RPMI 1640 (#10-040-CV) were purchased from Corning. Potassium phosphate (# 447670010) was purchased from Acros Organics. Bovine serum albumin (#BP1605-100) was purchased from Fisher bioreagents. EGM-2 BulletKit medium was purchased from Lonza (#CC-3162). Monoclonal anti-ICAM-1 antibodies YN1/1.7.4 (murine ICAM-1 specific), and R6.5 (human ICAM-1 specific) were isolated from the supernatant of cultured hybridoma cells using protein G affinity resin (ThermoScientific). In all cases, antibody purity was confirmed to be >95% via gel electrophoresis and/or size-exclusion HPLC. Isotype control IgGs were purchased from ThermoScientific. Human Umbilical Vein Endothelial Cells (HUVEC) were purchased from Lonza (C2519A) and cultured in EGM-2 BulletKit medium. HUVEC were used at passage 4 for all experiments.

5.3.2.2 Catalase SPNP Preparation, Collection, and Characterization

CAT-SPNPs were prepared via electrohydrodynamic (EHD) jetting, as previously described.[113,114,218,272] The CAT-HSA nanoparticle formulation consisted of 5% (w/v) catalase and 5% (w/v) HSA protein for a total of 10% (w/v) of protein. The proteins were separately dissolved in Ultrapure water (90% v/v) and combined. Then, ethanol (10% v/v) was added to produce the final jetting solution (1 mL final volume). In instances where the SPNPs were fluorescently labeled, BSA Alexa-Fluor 647 Conjugate (0.5% w/w relative to the total protein) was added before the ethanol. This solution was pumped though a 1 mL syringe fitted with a 25-gauge stainless steel needle at a flow rate of 0.1 mL/hr downward toward a grounded aluminum collection plate. A positive voltage supply lead was attached to the needle. The presence of a stable Taylor cone was recorded at voltages between 10 kV and 15 kV. The distance from the needle tip to the collection plate was 9 cm. Collection plates were switched every 30 minutes, then placed in a sealed container with 2.5 mL solution of 20 v/v% glutaraldehyde (GA) in Ultrapure water for 30 minutes to facilitate vapor-phase crosslinking. Crosslinked nanoparticles were collected with 0.01% v/v Tween20 in DPBS, supplemented with 100 mM glycine to quench unreacted aldehyde from GA. Two to three milliliters of collection buffer were added to one plate and scraped with a plastic razor blade. Each plate was scraped three times, each time using fresh collection buffer. The collected nanoparticles were tip sonicated in a 50 mL Falcon tube at an amplitude of 5 for 30 seconds (1 second on, 3 seconds off) in an ice bath. The sonicated suspension was filtered through a 40 µm cell strainer and centrifuged for 1 minute at 3200 rcf. The supernatant was removed and centrifuged at 3200 rcf for 5 minutes. The supernatant was further centrifuged at 22300 rcf for 40 minutes at 4 ˚C to obtain the final nanoparticle population in the pellet. The supernatant was discarded, and the pellets were resuspended in 1 mL of DPBS. The pellets were washed twice with DPBS through centrifugation (22300 rcf, 40 minutes, 4˚C). The washed nanoparticles were suspended in a final volume of 1 mL DPBS, sonicated using the aforementioned settings, then stored at 4 ˚C overnight for experimental use on the following day. Unless otherwise specified, CAT-SPNPs were resuspended in DPBS prior to experimental use or characterization.

Scanning electron microscopy was used to characterize the morphology of nanoparticles in their dry state, prior to collection and hydration. To prepare samples for imaging, silicon wafers were placed atop the collection plate during EHD jetting for 30 minutes. The wafers were then placed on a copper-covered SEM stub, gold sputter coated (40 seconds), then imaged using the FEI Nova 200 SEM/FIB microscope. A voltage of 5 kV, current of 0.40 nA and dwell time of 10 μs were used for all SEM images. Resulting images were analyzed using ImageJ according to previously described methods.[114] Individual nanoparticles (n=313) were analyzed to obtain the calculated morphological properties (circularity, roundness, diameter, PDI). The collected, hydrated nanoparticles were characterized using the Zetasizer Nano ZS (Malvern Panalytical). The size and zeta potential were measured using dynamic light scattering (DLS) and electrophoretic light scattering (ELS), respectively. Nanoparticles were diluted in DPBS and transferred to 10 mm pathlength disposable cuvettes for measurements. All reported DLS and ELS measurements were the averages of a minimum of 3 measurement runs. Protein nanoparticle concentrations were measured using a Pierce BCA assay, using commercial BSA standards for the generation of standard curves. CD spectroscopy was utilized to assess changes to protein secondary structure after jetting throughout this study. For all instances of analysis, the following conditions were held constant: [1] the instrument was a J-815 CD spectrometer (Jasco); [2] the operational range was 260nm to 190nm; [3] a data pitch of 0.2 nm was used; [4] scan rate was 100 nm/min; [5] slit width of 1 nm; [6] reported data is a numerical average of three spectra, accumulated sequentially; [7] all samples were adjusted to 37.5 μg/mL through dilution with Ultrapure water prior to measurement; [8] cuvette cleaning with Hellmanex III cuvette cleaning solution (2% v/v in deionized water) followed by 10 rinses with deionized water and a final drying wash with ethanol. The quantification of secondary structures was conducted using the open-source program, Dichroweb.[198–200,273] The CDSSTR program was used to analyze all secondary structures and the reference set 7 was chosen.[274–277]. Total helix is reported as the sum of the regular helix and distorted helix. After crosslinking, the SPNPs were purified as detailed above and resuspended in

1 mL Ultrapure water prior to dilution. The SPNPs were analyzed over the course of 2 weeks (4 ˚C storage, brought to RT for measurements) and compared to the initial spectra. Samples were independently incubated at 37 ˚C for 0 (control), 5, 10, and 20 minutes of incubation, then brought to RT prior to measurement. A 50:50 (w/w) catalase/HSA solution was also analyzed as a second control over the same range of conditions and time. In addition, SPNPs and native CAT-HSA (control) were diluted such that the final solution was 1:1 ethanol: water (v/v). Measurements were taken at 3 min., 20 min., 30 min., 1 hr., and 24 hr. Both the SPNPs and control were compared relative to their spectra without treatment.

5.3.2.3 Enzymatic Activity Determination

Free (native) catalase and SPNPs were diluted to an effective catalase concentration of 4 µg/mL. Then, the sample was added to a 0.036% w/w hydrogen peroxide in 50 mM potassium phosphate buffer solution. Samples were measured in a 1 mm quartz cuvette where the absorbance was read at 240 nm for two minutes. The activity was calculated as: Activity (U/mL)=s*(2070/(t_2-t_1)), where s is the slope of the linear region, t is time (in seconds). Two measurements per sample were performed.

5.3.2.4 Surface Functionalization of CAT SPNPs

A two-step reaction was performed to conjugate antibodies (YN1, R6.5, rat IgG, and human IgG) to the surface of CAT-SPNPs. First, a 20x molar excess of azidobutyric acid NHS ester relative to the protein concentration of the SPNPs was added to SPNPs in 1 mL of PBS. The reaction mixture was rotated overnight at 4 ˚C. The particles were then washed 3 times to remove unreacted azidobutyric acid NHS ester by centrifuging at 23500 rcf for 1 hour and resuspending the pellet in PBS. After washing, protein concentration was measured. YN1, R6.5, rat IgG, and human IgG antibodies were concentrated to 25 µM and DBCO labeled by incubating each with a 5x molar excess of NHS ester-PEG_4-DBCO (Click Chemistry Tools. https://clickchemistrytools.com) in PBS for 1 hour at room temperature. Unreacted NHS ester-PEG_4-DBCO was removed by repeated washing through a 100 kDa Amicon Ultra Centrifugal filter. The resulting antibody concentration was determined with a ThermoFisher NanoDrop 2000. DBCO-labeled Abs were conjugated to azide-modified nanoparticles via Strain-Promoted Azide-Alkyne Click (SPAAC) reaction at a ratio of 2000 Ab per nanoparticle and rotated overnight at 4 °C. The number of particles per mass of protein was calculated by measuring a known mass of particles by number concentration with

Nanosight, to give a ratio of 7.5×10^{11} particles/mg of protein. After the overnight reaction, the particles were washed 3 times with PBS as previously described.

5.3.2.5 Iodine 125 Labeling of SPNPs

Iodine^{125} Radiolabeling of SPNPs: SPNPs were radiolabeled with ^{125}I using Pierce iodination reagent (ThermoScientific). Free ^{125}I was removed via Zeba desalting columns. In all cases, radiochemical purity was confirmed to be >95% via thin layer chromatography. I^{125}-labeling of SPNPs occurred after azide modification. To remove free iodine post-labeling, desalting columns were used. The desalting columns were prepared by washing them in PBS via centrifugation15 times (100 rcf, 1 minute) prior to use. Approximately 60 mCu of I^{125} was added to a fraction of the SPNPs and briefly vortexed. The I^{125}-SPNPs were subsequently added to the desalting column and spun down for 2 minutes at 1000 rcf. Desalting was considered sufficient if 95% of iodine was contributed from the SPNPs (determined via TLC). Once labeled, this fraction of SPNPs was added to the stock of unlabeled SPNPs. Thereafter, the protein concentration was determined and the half of the SPNPs were antibody modified. After antibody labeling, the concentration was confirmed. Samples were placed inside 5 mL glass flow tubes and counts were measured using PerkinElmer's Wizard^2 2-Detector Gamma Counter. Data was analyzed using Microsoft Excel.

5.3.2.6 Quantitative Binding and Uptake of I^{125}-Labeled SPNPs

REN-ICAM and REN-WT cells were seeded at a density of 100,000 cells/well in a 48-well plate. After 24 hours post seeding, I^{125}-azide-SPNPs and I^{125}-mAb-SPNPs in 200 µL were added to each well at a range of concentrations (0, 0.23, 0.94, 3.75, 15 µg/mL). The plate was subsequently incubated at 37 ˚C for 30 minutes, placed on ice, and the media/treatment was removed to be measured for quantification of unbound SPNPs. The cells were washed twice with media then once with PBS. The media/PBS used for washes were added to a separate set of sample tubes for measurement. Lastly, 200 µL of lysis buffer (50 mL Ultrapure water with 500 µL of TritonX and 0.2 g NaOH) was added to each well and allowed to sit for 5 minutes. The volume of each well was transferred to a separate set of sample tubes. The plate was washed with lysis buffer until there were no more counts from the plate.

5.3.2.7 Cell Culture

Ren–WT (human mesothelioma) cells were cultured in Ren-WT media (RPMI 1640 supplemented with 10% (v/v) fetal bovine serum (FBS) and 1% (v/v) antibiotic antimycotic solution (100X)).

Ren-mICAM cells were cultured in Ren-ICAM media (Ren-WT media with addition of G418 (Geneticin) at a final concentration of 200 μg ml^{-1}).

5.3.3 Results

5.3.3.1 Fabrication and Characterization of Catalase SPNPs

EHD jetting was used to produce all CAT-SPNPs as previously described.[113,114,218,272] First, a jetting solution was prepared by dissolving CAT (5% w/v) and HSA (5% w/v) in a cosolvent system of water (90% v/v) and ethanol (10% v/v). Since ethanol is a known denaturant of protein, its structure under these solvent conditions was assessed over 18 hours but showed no alteration to the protein's secondary structure (**Figure 5-7**).

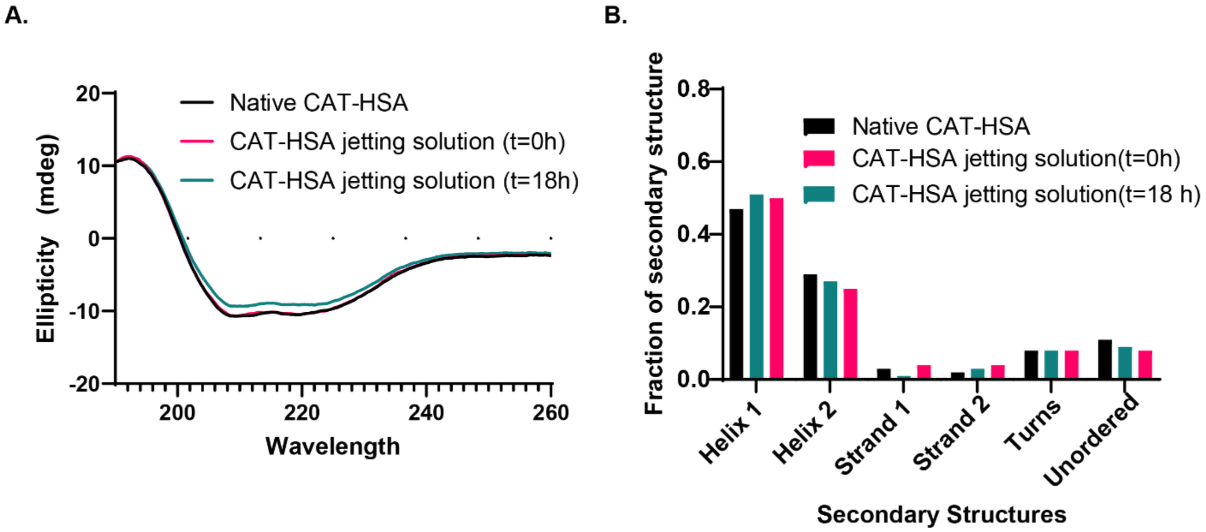

Figure 5-7. Protein conformational stability of the CAT-HSA jetting solution. A. CD spectra of native CAT-HSA in water, CAT-HSA jetting solution (10% v/v ethanol and 90%v/v water) at time zero (t=0h) and after 18 hours (t=18h). B. Secondary structure analysis of native CAT-HSA and the jetting solution at t=0h and 18h.

Next, the jetting solution was loaded into a syringe equipped with a needle and mounted on the syringe pump of the EHD jetting station, where a positive voltage lead was attached to the needle and subsequently grounded at the collection plate. The solution was pumped continuously at a flow rate of 0.1 mL/hour and subjected to a voltage of 10-15 kV. The applied voltage distorts the meniscus to form a Taylor Cone to form an electrical jet. This jet breaks into a charged spray of droplets, where they travel towards the grounded collection plate with high velocities and solvent evaporation. This results in the formation of solid SPNPs at the surface of the collection plate as shown in **Figure 5-8**A. The as-produced (post-jet, pre-collection) CAT-SPNPs were assessed through the SEM (**Figure 5-8**B). Micrographs were obtained of particles that were jetted onto a silicon substrate, crosslinked, and then sputter-coated with gold. The size distribution (n = 313) for the diameters of the particles is presented in **Figure 5-8**B2. The diameters presented as a log-normal distribution: mean of 126 ± 34 nm, minimum of 58.6 nm, maximum of 269 nm, interquartile range (IQR) of 38 nm and median of 125 nm. The geometric results for particle shape were as follows: circularity of 0.92 ± 0.04, roundness of 0.92 ± 0.09, and an aspect ratio of 1.10 ± 0.14. Next, glutaraldehyde (GA) vapor crosslinking was employed to stabilize the EHD jetted SPNPs.[278] Without such stabilization, the SPNPs would dissolve in solution and the structure would be lost. This approach augments past efforts that mostly focused on solution-based bi-functional macromers for stabilizing SPNPs.[114,174,246,279–281] After EHD jetting, solid CAT-SPNPs were treated with a GA solution (20 v/v% in Ultrapure water) for 30 minutes. After crosslinking, collection, and processing, the hydrodynamic diameter of the CAT-SPNPs was assessed through dynamic light scattering (DLS) (**Figure 5-8**C**).** The number average DLS (nDLS) results provided an average diameter of 103 ± 35 nm. The volume average DLS results provided an average diameter of 145 ± 61 nm, while intensity average DLS diameters were 158 ± 55 nm and a PDI of 0.203. The zeta potential was slightly negative at -5.67 mV. Furthermore, the production, collection, and processing of the CAT-SPNPs did not impact the secondary structure (**Figure 5-8**D-E) when compared to the solute mixture (50%(w/w) CAT and 50% (w/w) HSA). Using the diameter obtained from the SEM analysis, a swelling factor of 32% was calculated. While SEM and DLS data should be compared cautiously (individuals data from micrographs of metal coated materials compared to the deconvolution of a population that has a halo of solvent around it from a power spectra), it is useful to assess changes in volume for comparison between different populations in a study.

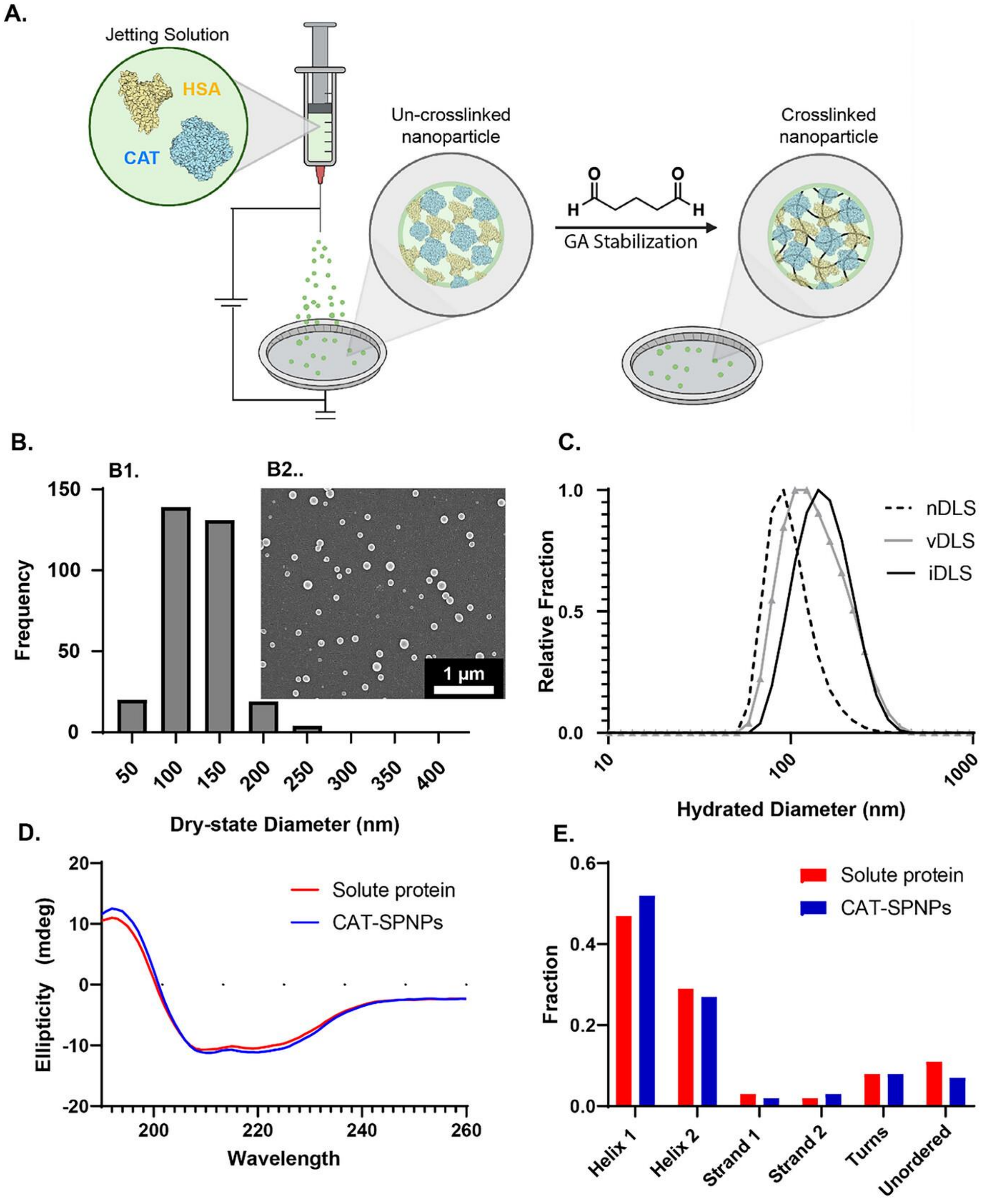

Figure 5-8. Schematic of the preparation of CAT-SPNPs made using EHD jetting. After jetting onto a collection plate, GA stabilization was conducted to form water stable, crosslinked SPNPs. B. Dry-state SPNP size distribution (B1) and SEM micrograph (B2). C. Hydrodynamic diameter of SPNPs post crosslinking, collection, and processing. Intensity-DLS (iDLS) (solid black line), numbers-DLS (nDLS) (dashed black line), and volume-DLS (vDLS) (grey solid line with triangles) are depicted for the same sample. D. CD spectra of CAT-SPNPs. E. CD secondary structure fractional analysis. Created with Biorender.com.

5.3.3.2 Storage Stability of CAT-SPNPs

The stability of the secondary structure of CAT- SPNPs stored at 4 ˚C was recorded over a two-week period as shown in **Figure 5-9**A. With increasing time, the signal intensity decreased, specifically in the alpha helix region (insert of **Figure 5-9**A). From 0 to 3 days, there were marginal changes in the spectra, but noticeable structural alterations occurred during the following days. In **Figure 5-9**A, the analysis of day 0 and day 14 were conducted to observe how the fractions of each secondary structure changed. For this type of deconvolution of CD spectra, the Helix 1 region is typically considered well-ordered, periodically spaced helices and the Helix 2 region is associated with skewed, compressed, or variably spaced helices (typically due to hypercoiling in regions or through helix-external interactions with other moieties in the structure). Here, the Helix 1 portion of the CD signal was significantly altered after a 2-week storage at 4 ℃. The Helix 2 portion of the CD signal also decreased, albeit not as drastically as the Helix 1 signal. The strand 1 signal (associated with β-sheeting) also increased slightly over time. Loss of higher order structure is often associated with increases in turn signals (semi-structured loops and bends) and unorder signals (non-structured). The fraction of turns and unordered signals increased after day 0, although not to the extent one would expect for a fully denatured protein. These findings suggest a 'protective' function of the SPNPs (i.e., increased internal stability).

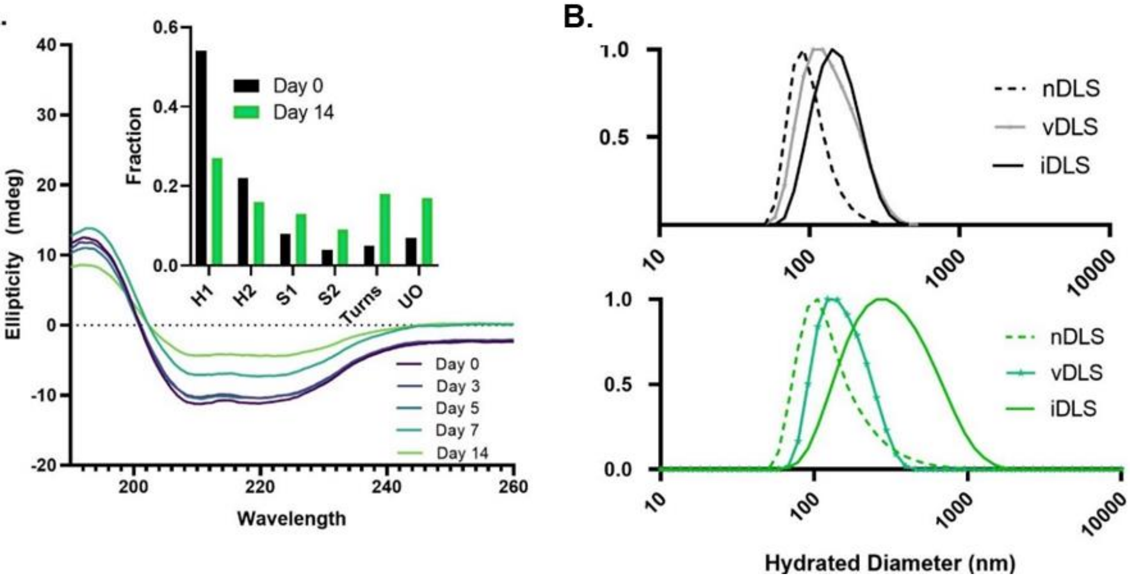

Figure 5-9. Stability of CAT-SPNPs. A. CD spectra and fraction of secondary structures of CAT- SPNPs over 14 days. B. DLS spectra (iDLS, nDLS, vDLS) of CAT- SPNPs on day 0 (top, in black) and day 14 (bottom, in green).

The size of hydrated SPNPs was measured over the course of a 2-week period at 4˚ C. The initial (Day 0, top graph) and final (Day 14, bottom graph) intensity DLS (iDLS), volume DLS (vDLS) and number DLS (nDLS) measurements are shown in **Figure 5-9**B. At Day 0, SPNPs had an intensity diameter of 158 ± 55 nm, while at Day 14 it was 366 ± 235 nm. The nDLS for Day 0 and Day 14 were 103 ± 35 nm and 144 ± 95 nm, respectively. Finally, the vDLS for Day 0 was 146 ± 61 nm and were 512 ± 323 nm for day 14. Diameter values (iDLS, vDLS, nDLS) and their associated standard deviations are shown for each day (0,3,5,7 and 14) in **Table 5-1.** Additionally, the polydispersity index (PDI) and Z_{avg} are reported.

Table 5-1. IDLS, PDI, vDLS, nDLS, and max nDLS of CAT-HSA SPNPs over a 2-week period.

Day	Z_{avg} ± SD (nm)	iDLS ± SD (nm)	vDLS ± SD (nm)	nDLS±SD (nm)	PDI*
0	150 ± 55	158 ± 55	146 ± 61	103 ± 34	0.203
3	157 ± 86	182 ± 86	168 ± 101	90 ± 37	0.218
5	166 ± 101	196 ± 101	182 ± 122	82 ± 36	0.260
7	187 ± 117	210 ± 117	223 ± 144	110 ± 54	0.288
14	290 ± 235	366 ± 235	512 ± 323	144 ± 95	0.439

*PDI reported was obtained from the Zetasizer output.

As shown in **Table 5-1,** the SPNPs appear to become more polydisperse over time. On Day 0, the PDI was 0.203, but by day 14, the PDI increased to 0.439. We note that the SPNPs were sonicated prior to each measurement to avoid settlement or optical cell interactions that could compromise interpretation of the results. Next, the assessment of enzymatic stability of the CAT-SPNPs versus the solute protein (50% catalase, 50% HSA) was performed as shown in the **Figure 5-10**. While the overall trend is a decrease in activity over time, the SPNPs were more successful in retaining the activity compared to the solute protein. After two weeks storage, the native protein dropped to a 54% ± 9% of its initial, day 1 activity. The SPNPs, however, showed a retainment percentage of 74% ± 8%. This strongly suggests that the entrapment of catalase in a nanoparticle form is advantageous in improving the shelf-life of the enzyme.

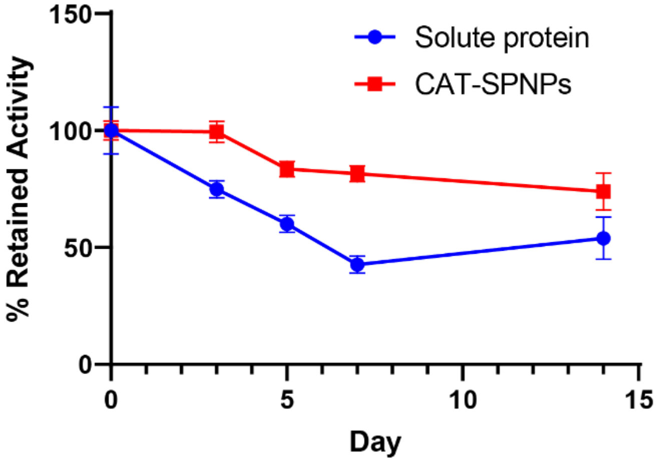

Figure 5-10. Percentage of retained activity of solute protein (CAT/HSA) and CAT-SPNPs over 14 days at 4 ˚C.

5.3.3.3 Heat Stability of CAT-SPNPs

Solute (free) protein (HSA/CAT) and CAT-SPNPs were heated to 40 ˚C for up to 20 minutes to determine if there was an effect on the secondary structure. Heated conditions could be used to understand how physiologically relevant temperatures affect the SPNPs. In **Figure 5-11**, the CD spectroscopy is shown of both free protein and the SPNPs. According to this study, the secondary structures appear to not be affected over the 20-minute period.

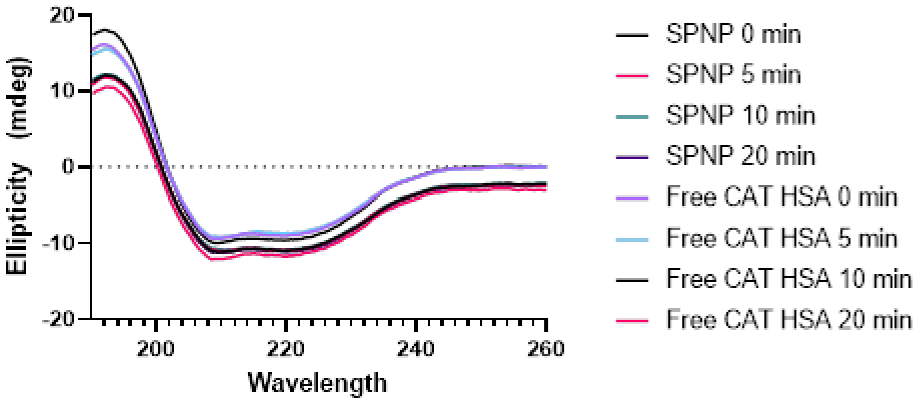

Figure 5-11. CD spectra of free protein (HSA/CAT) and CAT-SPNPs over 20 minutes at 40 ˚C.

The percentage of retained activity of CAT- SPNPs was measured at 0, 5, 10, and 20 minutes at elevated temperature (40 ˚C) and compared to percent of retained activity in free catalase (**Figure 5-12**). Free catalase had a faster loss in the retained activity compared to that of the SPNPs. After twenty minutes, the free catalase had only retained 47% ± 1% of its activity whereas the SPNPs retained 71% ± 5% of their activity.

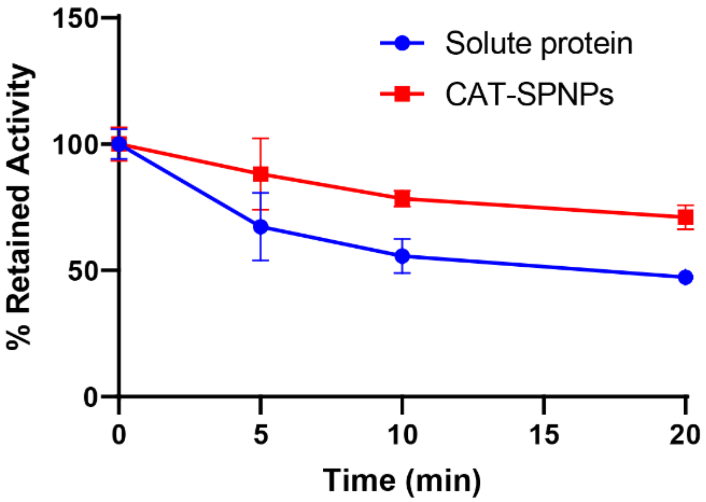

Figure 5-12. Percent of retained activity of solute protein (CAT/HSA) and CAT-SPNPs after 40 ˚C storage for 20 minutes.

5.3.3.4 Solvent Stability of CAT-SPNPs

To study how the secondary structure of the enzyme was altered in a denaturing solvent system, free protein and SPNPs were suspended in a solvent system of 50 v-% ethanol and 50 v-% water. And the change in secondary structure was recorded over a period of 24 hours using CD spectroscopy. The CAT-SPNP stability in this solvent is shown below.

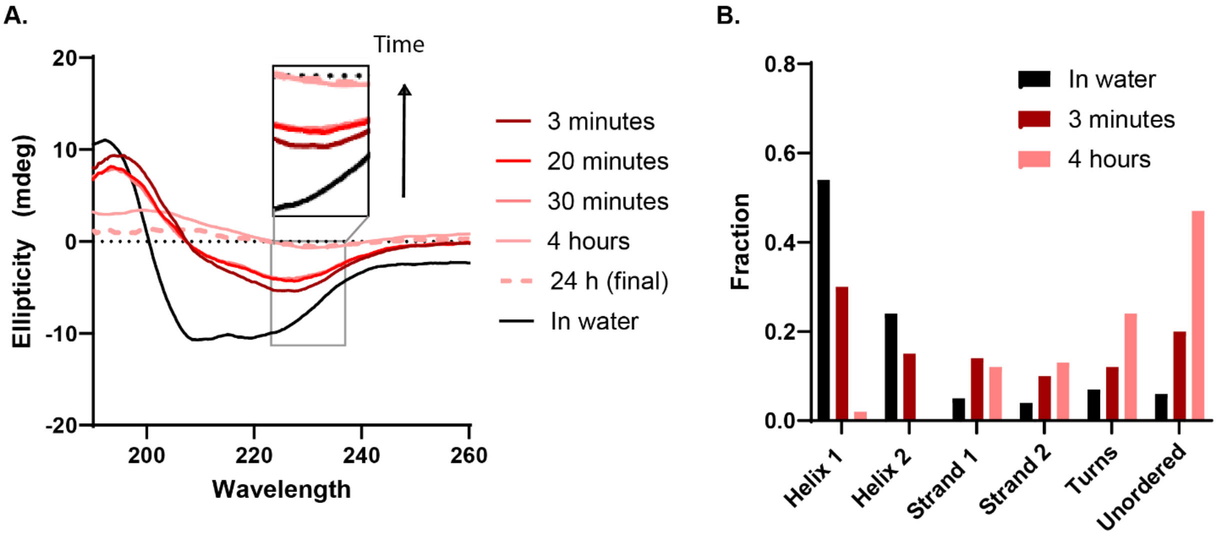

Figure 5-13. Solvent stability of CAT-SPNPs. A. CD spectra of free HSA-CAT in 1:1 by volume ratio of water and ethanol over time. B. Secondary structure analysis of CAT-HSA in water only, 3 minutes of 50% ethanol treatment and 4 hours of ethanol treatment. CAT-HSA in water (without ethanol treatment) is depicted in black.

The free protein was also measured in the same conditions and is shown in **Figure 5-14**. As time increased, the distinctive alpha helix feature decreased as soon as 3 minutes after exposure. This effect continued with time. The quantification of secondary structures is shown for free protein in water, and free protein in the ethanol solvent system at 3 minutes and 4 hours. Both helix 1 (regular helix) and helix 2 (distorted helix) decreased with time. The fraction of turns and unordered increased with time.

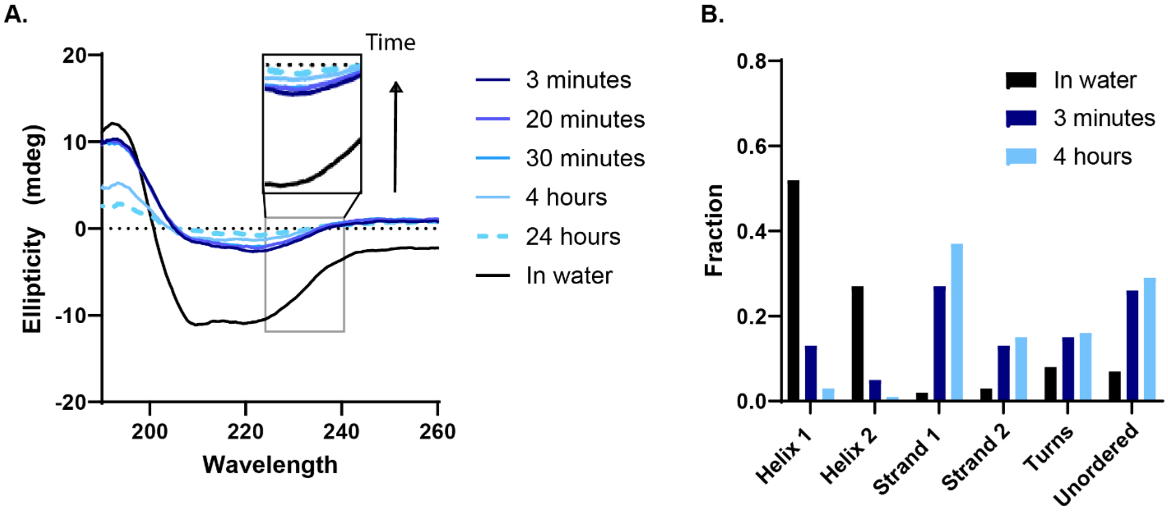

Figure 5-14. A. CD spectra of HSA -CAT SPNPs in 1:1 by volume ratio of water and ethanol over time. B. Secondary structure analysis of CAT-HSA SPNPs in water only, 3 minutes of 50% ethanol treatment and 4 hours of ethanol treatment. CAT-HSA SPNPs in water (without ethanol treatment) are depicted in black.

The helical component decreased by 95% relative percent (compared to 97% in the solution) after 4 hours. However, the increase in the unordered signal for the SPNPs was only 3.1-fold (from 7% to 22% total unordered) compared to the 6.8-fold increase observed in the solution over the same period. Taken together these results indicate that SPNPs provide increased resistance to common denaturants which persisted over 4 hours of exposure. A strategy to further improve the resistance to denaturing solvent systems on the SPNP structure could involve changing the chemical method used to stabilize the SPNPs. In **Figure 5-15** a NHS-PEG-NHS crosslinker was used to crosslink the protein SPNPs as previously reported.[114,218] It is apparent that the ethanol did not have the immediate effect that it did on the VPGA crosslinked SPNPs. Here, the ethanol treatment was conducted for a week, with no obvious changes to the helix and unordered secondary structure. In the VPGA crosslinked SPNPs, there were structural changes as soon as 3 minutes. It should be noted that with the NHS-PEG-NHS crosslinking strategy, there is a difference in the shape of the CD spectra; the alpha helix is less horizontally positioned between 205 nm and 225 nm. This change is not surprising given the bi-functional crosslinker is added to the jetting solution and the SPNP is likely crosslinked throughout rather than mostly just the exterior. Therefore, a tradeoff exists with the choice of crosslinking strategy: a more stable SPNPs (i.e. the NHS-PEG-NHS crosslinker) yields a lesser resemblance to that of its native protein constituents.

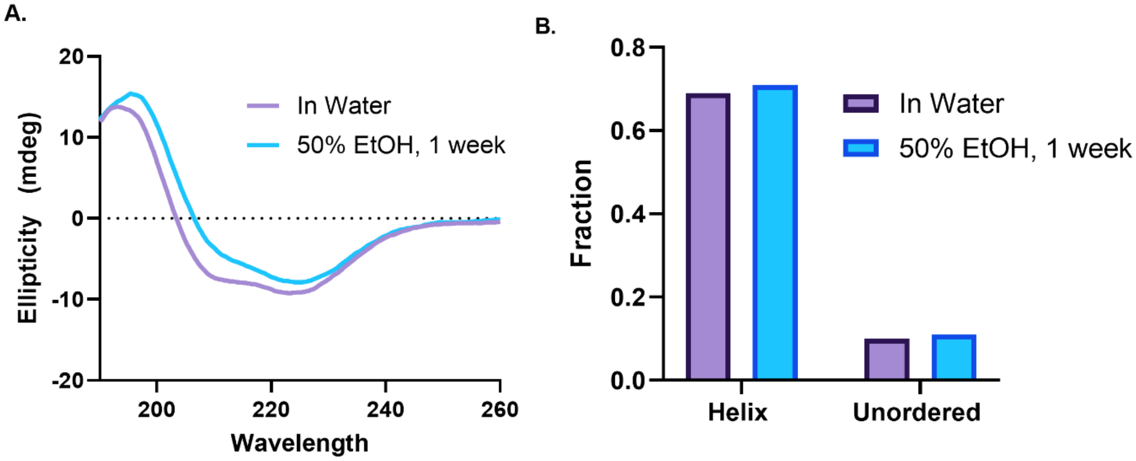

Figure 5-15. Effect of ethanol (50% v/v) on NHS-PEG-NHS crosslinked CAT-SPNPs. A. CD spectra of CAT-SPNPs in the 50% v/v ethanol solvent system versus in water. Fraction of total helix and unorderd of SPNPs in water and ethanol treated for 1 week.

5.3.3.5 Surface Immobilization and Selective Uptake of YN1-Labeled SPNPs

The ability to direct therapeutic enzymes towards specific tissues or cell-types is critical in the mitigation of off-target toxicity. Therefore, antibody labeled SPNPs were produced using a two-step modification procedure (**Figure 5-16A**). We then assessed changes in the viability of targeted CAT-SPNPs in an *in vitro* model. Following EHD jetting and CAT-SPNP collection, lysine residues were reacted with azidobutyric acid NHS ester to introduce azide groups. In parallel, YN1 antibodies were reacted with NHS ester-PEG$_4$-DBCO to introduce DBCO moieties via conjugation to lysine residues. The resulting azide-SPNPs and DBCO-YN1 antibodies were combined to generate YN1-SPNPs via the SPAAC reaction of SPNP-bound azides with antibody-bound DBCOs (**Figure 5-16A**). The YN1-SPNPs were characterized via DLS to assess potential changes in the hydrodynamic diameter compared to unmodified SPNPs (**Figure 5-16B**). Unmodified SPNPs had a mean intensity peak diameter of 256 ± 71 nm and slightly increased to 264 ± 101 nm once azide modified. After the SPAAC reaction, the YN1-SPNP size was measured at 285 ± 85 nm. In terms of the number based DLS, the mean peak diameters for the unmodified SPNPs, azide modified SPNPs, and YN1 SPNPs were 127 ± 34 nm, 132 ± 40 nm, and 142 ± 37 nm, respectively. The PDI after YN1 labeling (PDI = 0.396) was higher than that of the unmodified SPNPs (PDI = 0.292).

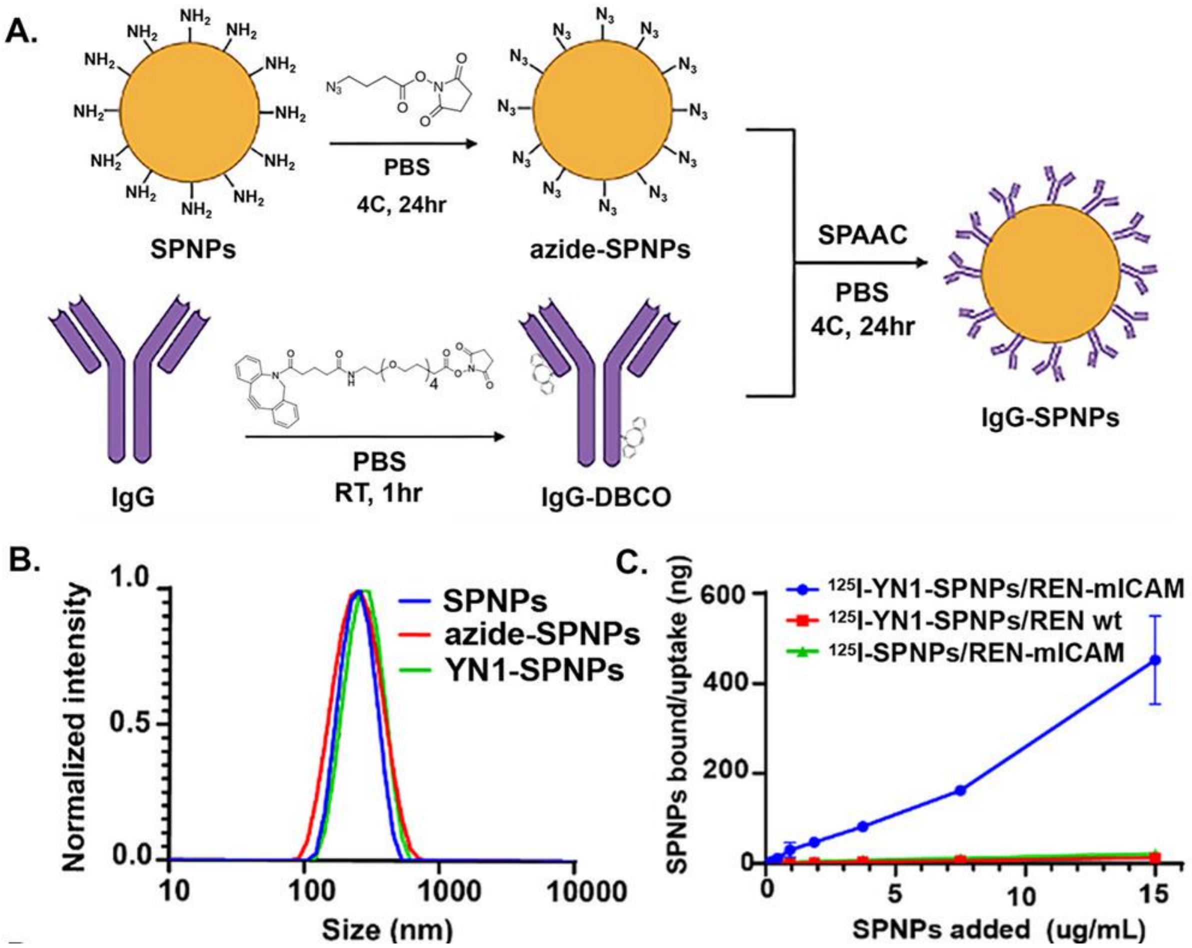

Figure 5-16. Antibody labeled CAT-SPNPs facilitate greater uptake. A. Schematic showing modification of antibodies and SPNPs with DBCO and azide groups, respectively, using NHS ester chemistry. As shown, DBCO-antibodies are conjugated to the surface of azdie-SPNPs via an SPAAC reaction. B. Normalized peak intensity of unmodified SPNPs ("SPNPs"), azide modified SPNPs, and YN1 labeled SPNPs. C Quantitative uptake of I^{125} radiolabeled YN1-SPNPs.

After preparation of the CAT-SPNPs, nanoparticles were subsequently tagged with I-125 through the oxidation of the tyrosine groups of the protein. Thereafter, radiolabeled CAT-SPNPs were further labeled with YN1 antibodies as outlined previously. YN1-labeled SPNPs were tested in REN-WT and REN-ICAM cells. In addition, the control of unlabeled SPNPs were tested in REN-ICAM cells. In the course, a range of concentration of SPNPs (0-15 ug/mL) were added to the cells and were incubated at 37˚ C for 30 minutes. The internalized or bound SPNPs are shown in **Figure 5-16**C. The conjugation of YN1 to the SPNPs resulted in 8.5% of the total added SPNPs to be internalized whereas the unlabeled, or blank SPNPs only resulted in 0.7% to be internalized in REN-ICAM cells. Also preliminary in nature, these data strongly hint towards the possibility that antibody modification of CAT-SPNPs can provide a therapeutic advantage when cell targeting is intended.

5.3.4 Discussion

CAT-SPNPs were produced through EHD jetting to show the versatility of the technique extending towards other proteins outside of HSA. While swapping out the protein is simple, ensuring the function and the stability of the protein is necessary. Here, we showed that the CAT-SPNPs retained their enzymatic activity better than their non-nanoparticle counterparts. In addition, the stability of the CAT-SPNPs was assessed through its storage stability, heat stability, and solvent stability. It was found that the SPNPs as structures were stable in these experiments, except for the solvent stability. We show that this could be mitigated by changing the crosslinking strategy. However, further studies would be needed to validate this crosslinking strategy in terms of enzymatic activity retainment. Specificity of nanoparticle uptake is an important feature to elicit the therapeutic effect on certain cell types. Therefore, we modified the nanoparticles with antibodies and studied the impact on cellular uptake. The results showed a significant increase in the uptake with this modification, which could be used for other types of nanoparticles. In terms of the therapeutic effectiveness, those results can be read elsewhere[197] since it does not directly tie into this thesis. More specifically, antioxidant properties of catalase would likely augment resistance and contribute to a more aggressive phenotype of glioma according to recent literature.[282–284] Because of these findings, decreasing the levels of catalase has been an area of interest to augment oxidative stress and cause glioma cell death.[285] More suitable proteins like transferrin could be used as the SPNP composition, or even blends of proteins.[114] Transferrin receptor (Tf-R) mediated transcytosis has been exploited to facilitate transport across the BBB for decades and has also been used as a target for NP delivery as it is overexpressed in malignant cells and cancer cell lines, particularly gliomas. [156,158,286–289] Therefore, constructing NPs out of transferrin (T-NPs) for targeted glioma treatment is an attractive approach owing to its inherent functionality.[160,290]

Chapter 6

Conclusions and Future Directions

Gliomas account for 80% of all malignant primary brain tumors and usually present with poor prognoses and high mortality rates, particularly for glioblastoma with median survival of 13-16 months.[13,291] The standard of care depends on the classification of the glioma,[3] but generally follows maximal safe surgical resection, radiotherapy and adjuvant chemotherapy.[13,292] Complete surgical resection is virtually impossible with the delicate and intricate nature of the brain. Radiotherapy and chemotherapy with temozolomide typically only improve the median survival by months, yet is the best option for treatment for primary tumors. Unfortunately, these tumors often recur, necessitating additional treatment. Lower grade gliomas have received less attention than IDH wild-type glioblastoma, but the transformation towards more aggressive gliomas has been well described.[226,293] Therefore, treatment options for all types of gliomas are necessary. Little advancements have been made to glioma therapy, which can be attributed to the inter- and intra- heterogeneity of gliomas, the restrictive nature of the blood brain barrier and blood tumor barrier, neovascularization, and inadequate imaging technologies, among others.[294–296] Nanoparticles have gained attention in the glioma therapy space to noninvasively deliver antitumoral agents systemically. In addition, nanoparticles can protect the drug from degradation, allow slow release of the agent within the therapeutic window, extend the half-life, and reduce toxicities.[297] Of the types of nanoparticles, protein nanoparticles represent an important class of nanoparticles owing to the added benefits of protein carriers: versatility, conjugation capabilities, biodegradability, availability and affordability, and relatively low immunogenicity.[32] In the Lahann Lab, we have developed synthetic protein nanoparticles produced through electrohydrodynamic (co) jetting and it was recently shown that these SPNPs have promise in glioma treatment.[218] However, this only represents a fraction of possibilities for treating glioma with SPNPs given there are several classes of gliomas, and a plethora of therapeutics that could leverage nanoparticle-mediated delivery. In this thesis, it was sought to expand SPNP delivery for glioma therapeutic applications. This was accomplished through developing three types of SPNPs, which were described in **Chapters 2-4**.

As discussed in **Chapter 2**, paclitaxel - a potent antineoplastic agent that prevents cellular proliferation - is not approved for glioma treatment. Traditional paclitaxel delivery relies on the solubilization through Cremophor EL, which has been associated with toxicities and altered pharmacokinetic profiles. To mitigate this solubilization method, Abraxane was developed to solubilize paclitaxel within the hydrophobic domains of human serum albumin. While this has eliminated the drawbacks from traditional solvent based delivery and has since been approved for several cancers, it is not approved for glioma due to the inability to pass the blood brain barrier. Therefore, we developed a SPNP loaded with paclitaxel (PTX-SPNPs) that combined Abraxane's solubilization method with EHD jetting. The PTX SPNPs showed desirable morphological features and stability. Combining the solubilization method with EHD jetting proved to be useful in modifying the release kinetics to exhibit a controlled release as opposed to a burst release. The in vitro studies in glioma cells revealed PTX maintained its potency and was more cytotoxic than free, unloaded PTX likely due to differing uptake mechanisms. Considering that the majority of small molecules cannot penetrate the blood brain barrier and small molecules represent a large class of therapeutics, this method can be extended towards other small molecules for glioma delivery. While in vivo effectiveness was not shown here, a survival study is ongoing, which will allow us to assess the therapeutic efficacy in a glioma model.

In **Chapter 3**, STAT3 siRNA and paclitaxel were co-encapsulated into a singular nanoparticle (STAT3i/PTX biSPNPs) into separate compartments through electrohydrodynamic co-jetting. Combination therapy with nanoparticles exploits the benefits of combination therapy and nanoparticle mediated delivery.[298,299] This is of particular interest in gliomas, which have rates of recurrence as high 52%-62% in lower grades and 66.2% in higher grades like glioblastoma.[300,301] By targeting two mechanisms, this has the potential to elicit synergistic effects, which enable lower dosing to obtain a therapeutic response, and can minimize resistance.[302,303] **Chapter 3** underscores the versatility of the EHD jetting technology by encapsulating two different agents of differing characteristics (molecular target, size of molecule, solubility). The biSPNP morphology was comparable to other SPNPs formulations indicating that the bicompartmental configuration does not impact the size or shape of the particles. In vitro studies demonstrated the ability to kill adult high grade glioma cells and caused the release of damage associated molecular patterns to elicit an effective anti-high grade glioma immunity. The in vivo studies are ongoing, which give insight into how these biSPNP fare in a high grade glioma model.

The first demonstration of SPNPs for glioma therapy was by Gregory, J et al.[218] STAT3 siRNA was used, but there exist other targets for which siRNA delivery would be useful. In **Chapter 4**, we used siRNA against ATG7, an autophagy related gene, to inhibit autophagy in diffuse astrocytoma. Diffuse astrocytoma is resistant to ionizing radiation – arguably the most important therapeutic intervention for cancer. Because autophagy is upregulated in diffuse astrocytoma and was shown to confer resistance to ionizing radiation, we developed ATG7 siRNA SPNPs. These SPNPs elicited molecular inhibition of the autophagy signaling pathway, leading to prolonged survival, anti-tumor immunity, and immunological memory in mDIH1 glioma mouse model.

Chapters 2-5 discussed examples of how we can expand EHD jetting to produce SPNPs for glioma applications. We showed that SPNPs can be produced to encapsulate hydrophobic or hydrophilic small molecules, siRNAs, and be dually loaded to deliver two molecules of differing solubilities, size, and function. In addition, instead of encapsulating molecules, the type of protein used to construct the nanoparticle can be altered to exploit its inherent function. While the focus of this thesis was to use these SPNPs for glioma therapy, one could envision this being explored for other types of cancer, slightly modifying the SPNP construct, exploring other therapeutics, and integrating computational platforms to aid in the nanoparticle design. In a subsequent section, a computational program was used to identify synergistic combinations in a glioma defined by its genetic profile. While this work was not completed, it is an exciting area of research. In addition, I explore the EHD jetting processing specifically on how to improve the yield and alter the size. In depth understanding of the EHD processing is necessary to aid in the clinical translation of this work, but also to help inform the design of SPNPs.

6.1 Toward investigating SPNP yield and methods to improve processing

The EHD (co) jetting process has several benefits to produce SPNPs, but a major drawback is the collection and processing time to obtain the SPNPs after jetting, which is apparent when needing large quantities of SPNPs for in vivo studies. This is a multifaceted problem and can be investigated at various angles to arrive at potential solutions. In the following sections, several attempts were made to understand the bottlenecks of the process and how we might be able to improve the process and obtain higher yields. To do that, an understanding of the production, collection, and processing of SPNPs must first be established. SPNPs in question are those that comprise of a 2.5%w/v to 7.5% w/v human serum albumin in a cosolvent system of 80% (v/v) ultrapure water and 20% (v/v) ethylene glycol. The crosslinker used is the bifunctional PEG (O,O′-Bis[2-(N-Succinimidyl-succinylamino)ethyl]polyethylene glycol, 2kDa), which is incorporated at a 10% wt/wt relative to the human serum albumin. The jetting set-up is a single or dual needle (co-jetting) configuration with a flow rate from 0.1 mL/hour to 0.2 mL/hour. The distance from the needle to the aluminum collection plate is about 9 cm. The pans are changed every 20 to 30 minutes then incubated at 37 ˚C for 5-7 days. The collection and processing follow methods mentioned in Chapter 2, 3 and 4. Briefly, the SPNPs are collected using physical scarping with a plastic razor blade in a solution of 0.01-0.05% (v/v) Tween20 in DPBS. Thereafter, the scraped solution is placed inside a 50 mL Falcon tube. The plate is scraped once more, and the solution is added to the same 50 mL Falcon tube. After all plates are scraped twice (or three times), the SPNPs are tip sonicated on ice, filtered through a 40-micron cell filter, then centrifuged at low speed (3200 rcf, 5 minutes). The supernatant is removed and distributed amongst 2 mL Eppendorf tubes, which are then subjected to high-speed centrifugation (21130 rcf, 1 hour, 4 ˚C). After spinning, the supernatant is discarded from the series of tubes. In one of the tubes, DPBS is added, and the pellet is broken up by pipetting up and down. The contents are removed and added to the next tube. Again, the pellet is broken up through pipetting and added to the next tube. This continues until all pellets are combined into a single tube. Next, that tube is spun down again (21130 rcf, 1 hour, 4 ˚C). The supernatant is once again discarded, and the pellet is broken up through tip sonication on ice (5 amplitude, 30 seconds with 1 second on and 2 seconds off). At this point, the SPNPs are characterized.

6.1.1 PNP quantification method

A yield of 1-2% has been noted as typical for SPNP production, where the yield as calculated as the amount of protein detected for the SPNPs divided by the amount of protein put into the jetting solution multiplied by 100%. It must be noted that “low throughput” is a conclusion based on the use of the BCA Assay or P660 Assay for SPNP concentration. These assays are established to determine protein concentration, and not protein nanoparticle concentrations, thus there can be inherent limitations according to the methods used. The BCA assay works by two reactions. In the first reaction, the peptide bonds in the protein reduce Cu^{2+} to Cu^{1+}, which is proportional to the amount of protein present.[304] The second reaction is the chelation of one Cu^{1+} with two bicinchoninic molecules, forming a complex that is absorbed at 562 nm.[304] The P660 assay is based on the binding of a dye-metal complex to protein, which causes an absorption shift at 660 nm. In either case, these assays could be underestimating the amount of protein present because of the inability to penetrate the nanoparticle completely. In a recent study published in 2021, Khramtsov P. et al. compared methods (Bradford Assay, BCA assay, hydrolysis/UV spectroscopy and gravimetric analysis) to detect protein nanoparticles prepared via desolvation.[305] It was found that that dye-binding assays like the BCA assay (and presumably the P660, although not tested directly), led to a 50-60% underestimation of nanoparticle concentration.[305] Furthermore, the type and extent of crosslinking can impact these measurements.[305] It is possible and likely that these assays are also contributing to an underestimation of the protein content in our SPNPs. While that has not been specifically investigated here, it does not tell the full story as the subsequent sections will explain.

6.1.2 Collection surfaces for EHD jetted SPNPs

Throughout the EHD jetting process, the solidified nanoparticles are collected upon disposable aluminum collectors. These pans are used because they offer a relatively stable surface, they are a good size for the spray of nanoparticles, and they are inexpensive. However, under SEM, these pans are extruded surfaces with uneven surfaces. A quick study was conducted to investigate these pans and whether they contribute to the lower yield. Four pans were compared: (1) crosslinked SPNPs with collection, (2) crosslinked SPNPs and not collected, (3) no SPNPs and no collection, and (4) no SPNPs with collection. These groups are shown below in **Table 6-1**. The collected pans used a 0.01% v/v Tween20 in PBS solution (2 mL).

Table 6-1. Collection plates 1-4. Collection plate 1 contains jetted SPNPs that were crosslinked and subsequently collected. Plate 2 also has jetted SPNPs, but they were not collected. Plate 3 does not have SPNPs nor was it collected. Plate 4 does not have SPNPs but was collected. *Collection was with 2 mL of 0.01% (v/v) Tween20 in PBS. Black squares drawn on the plates are the samples that were cut out of the plate and removed for SEM imaging.

Plate	1	2	3	4
NPs jetted and crosslinked	Yes	Yes	No	No
Collected*	Yes	No	No	Yes

The squares drawn on the pans were the sections that were selected for SEM imaging. **Figure 6-1** shows images of the pans without any SPNPs and without collection. This is representative of the integrity of the pans when they are received. In the first image to the left at 120x magnification, there is the appearance of streaks, which can indicate the roughness of the surface. Further, in the 50,000x magnification (rightmost image), there is the identification of a hole in the pan showing that these surfaces are smooth.

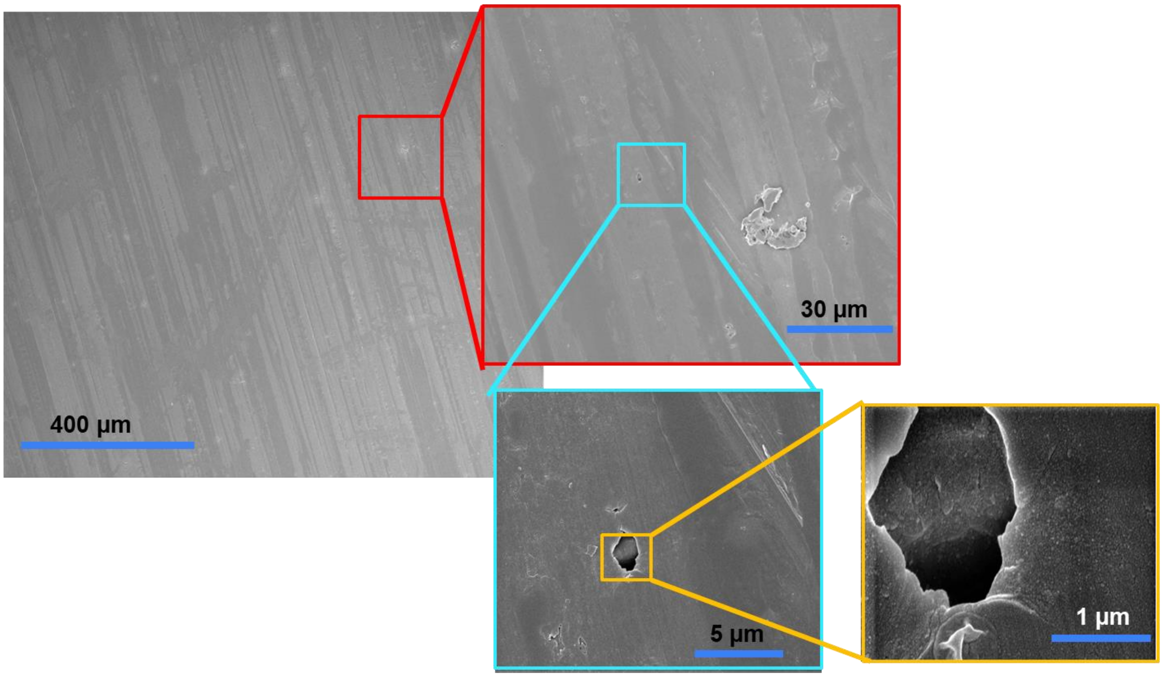

Figure 6-1. Blank pan (pan #3) without any SPNPs and no collection. At 120x magnification, there are streaks. Zooming in by 8000x and 50,0000x magnification, there are features of poor surface integrity with the appearance of holes.

Next, Pan #4 (no SPNPs with collection) was investigated to determine the effect of collecting on the pans. The pan was similar to the blank pan (pan #3), but there was more damage to the plate marked by the presence of more holes or flakes (**Figure 6-1**).

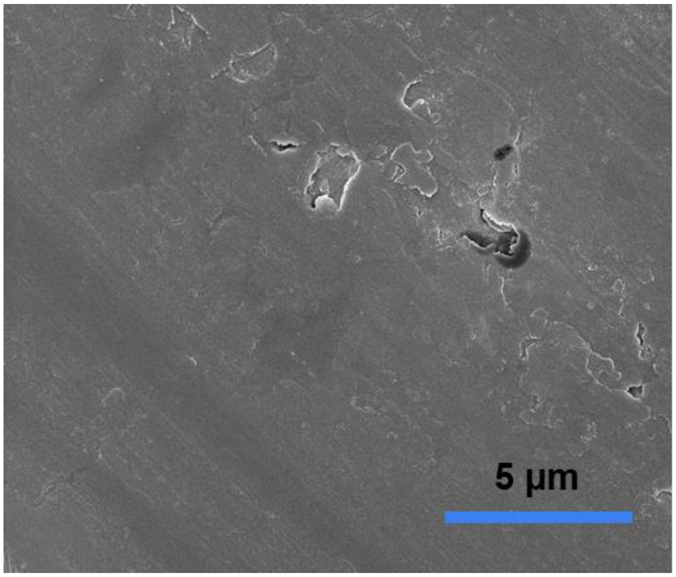

Figure 6-2. Pan #4 (no SPNPs with collection). Surface damage is observed by the presence of flakes or holes in the surface.

This indicates that the physical agitation during collection processes compromises the structure of the pan and can lead to aluminum impurities being contained within the SPNP solution. Next, uncollected SPNPs (plate #2) was imaged to understand the distribution of the SPNPs on the aluminum pan **Figure 6-3.**

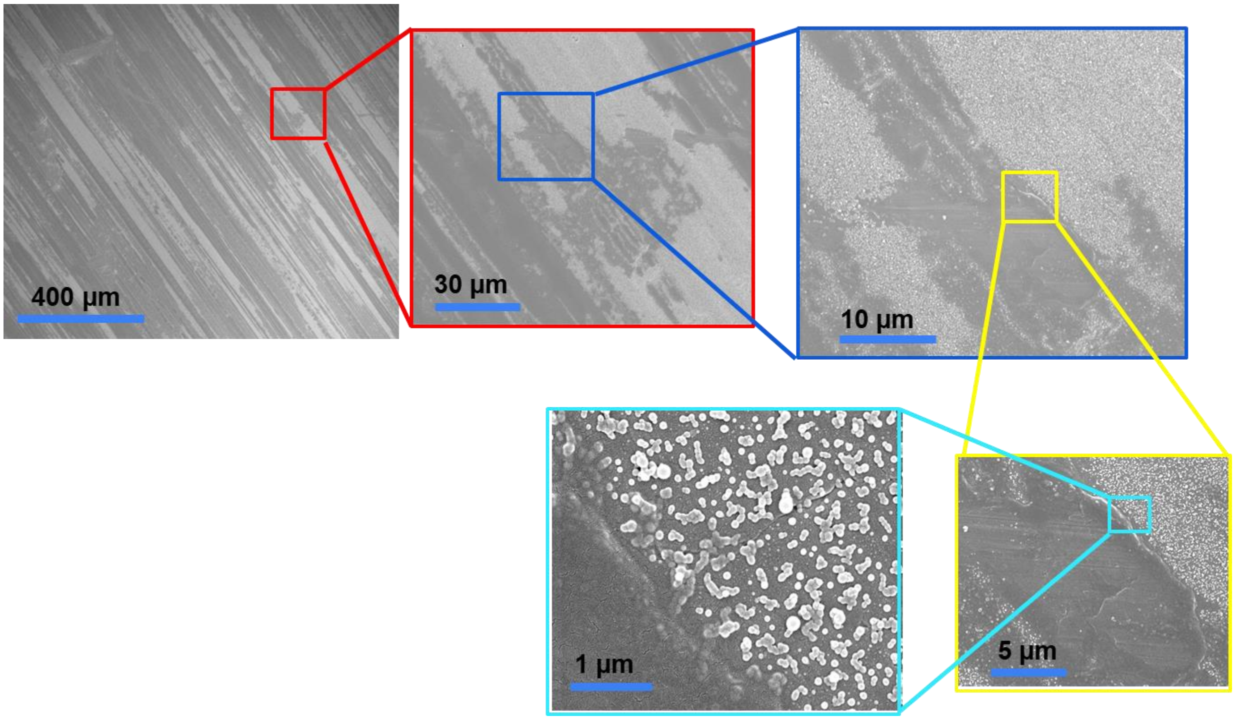

Figure 6-3. Plate #2 (SPNPs, no collection). SPNPs preferentially land in streaks.

After EHD jetting on the pans, the nanoparticles appear to preferentially land in regions of these streaks. It could be that the SPNPs are either on the top of these ridges, or within the valley shown in **Figure 6-4.**

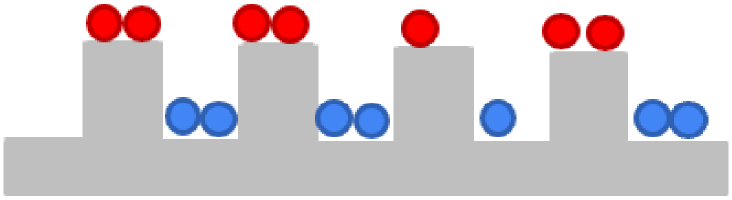

Figure 6-4. Side profile of the collection pan (grey) and the EHD jetted SPNPs preferentially landing on either the ridges (red SPNPs) or the valleys (blue SPNPs).

Next, plate #1 was imaged to see the extent of SPNP removal from the surface following collection. Three rounds of collection were performed, each using 2 mL of collection buffer. The SEM images of plate #1 are shown below in **Figure 6-5**. After collecting the SPNPs, not all the nanoparticles are removed. This can contribute to the lower yield as there are nanoparticles stuck on the plate. If the SPNPs were distributed evenly across the plate, this would suggest there is an issue with rinsing the residual SPNPs, but this is not observed.

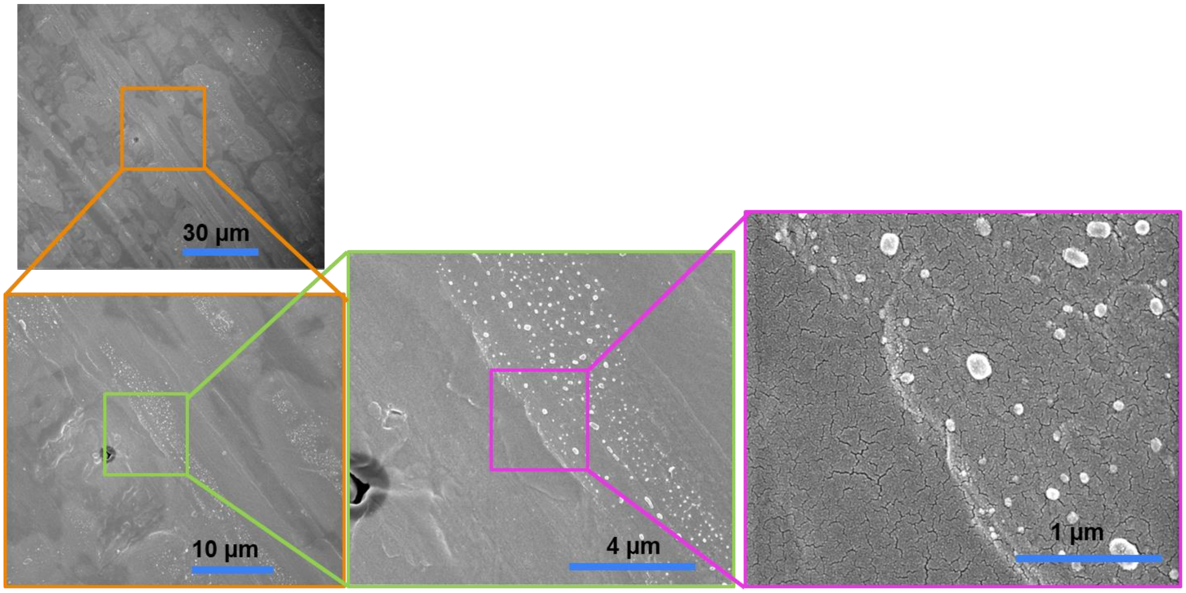

Figure 6-5. Pan #1 (SPNPs with collection). The appearance of SPNPs is shown not evenly distributed on the surface, but rather appear in these streaks.

In effort to mitigate the use of scraping, create an even surface, and expediate the collection process, coating the pans prior to EHD was tested. Dilute sucrose solutions were prepared (0.2, 0.6, 1 g/mL) and sprayed onto the pans using a TLC coater. For each concentration, the pan was sprayed for 2-4 seconds or until coated at the following distances: 30, 50, 70 cm. The coatings are shown below.

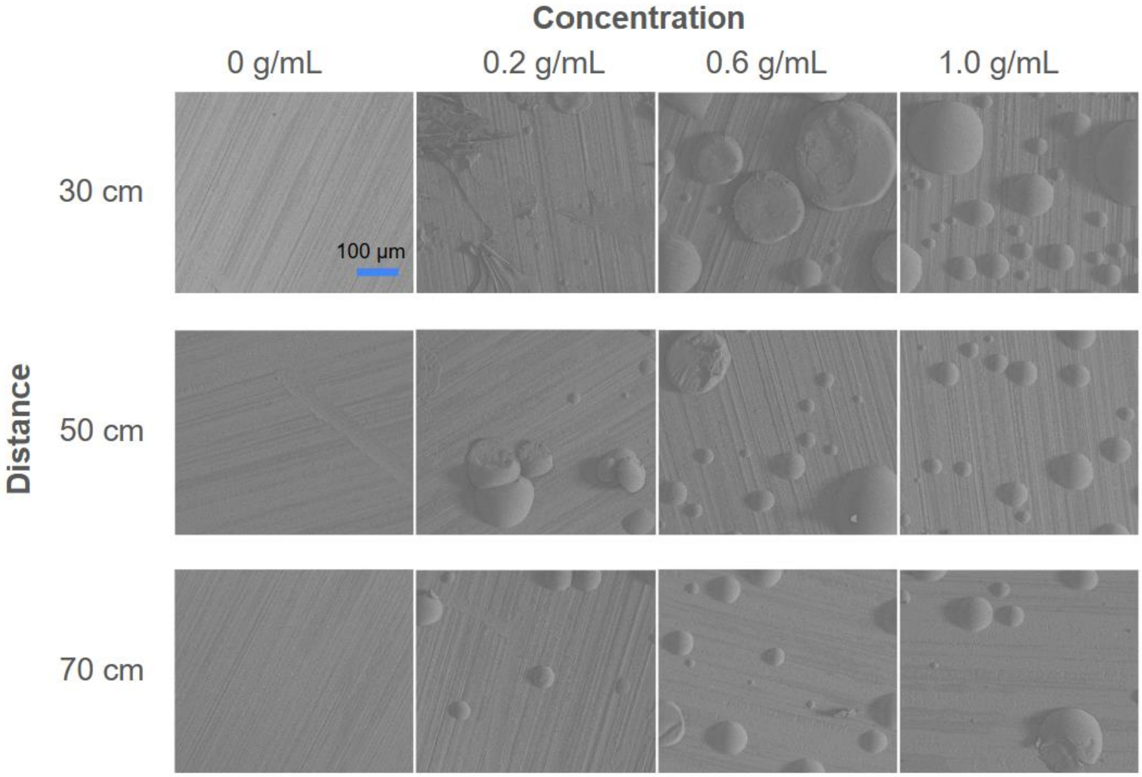

Figure 6-6. Sucrose coating at varying concentrations and spray distance. Scale bar = 100 µm.

From the above images, the 0.2 g/mL solution at 70 cm was used to jet SPNPs. The jetting was HSA SPNPs (7.5 wt/v% HSA, 20% v/v ethylene glycol, 80% v/v ultrapure water, 10% wt/wt crosslinker (2 kDa, relative to HSA). The jetting was at 0.2 mL/hour with each jetting lasting 30 minutes per pan. The SPNPs were jetted on the 2x coat (meaning it was coated twice with sucrose at the 0.2 g/mL concentration) and is shown below after incubation at 37 ˚C for 7 days.

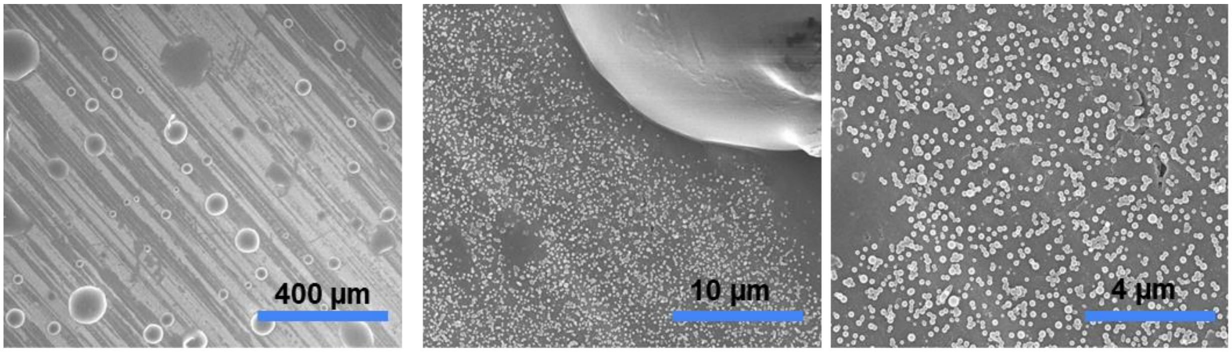

Figure 6-7. Jetted HSA SPNPs on a sucrose-coated pan. The pan was coated twice with a 0.2 g/mL sucrose solution in water and sprayed at 70 cm.

From **Figure 6-7,** bigger droplets of sucrose are seen across the surface. In addition, the streak appearance is also seen with the SPNPs in the streak features. Sucrose was sprayed on the pans, but it would be needed for the spray to fill the indentations on the pans to create an even surface. The coating was likely distrubuted relatively evenly thus providing the same amount of coating throughout the pan. The SPNP jetted on the surface have good morphological features despite the coating. Next, the SPNPs were collected using PBS by pipetting 2 mL on the surface. Unfortunately, moving the PBS around the suface with the guide of the micropipette tip, it was not sufficient to remove the layer of SPNPs on the surface. Ideally, the layer of sucrose would be dissolved and release the SPNPs above the coating. Because of this, mechanical scraping was used once per pan. These pans were imaged and shown below in **Figure 6-8.**

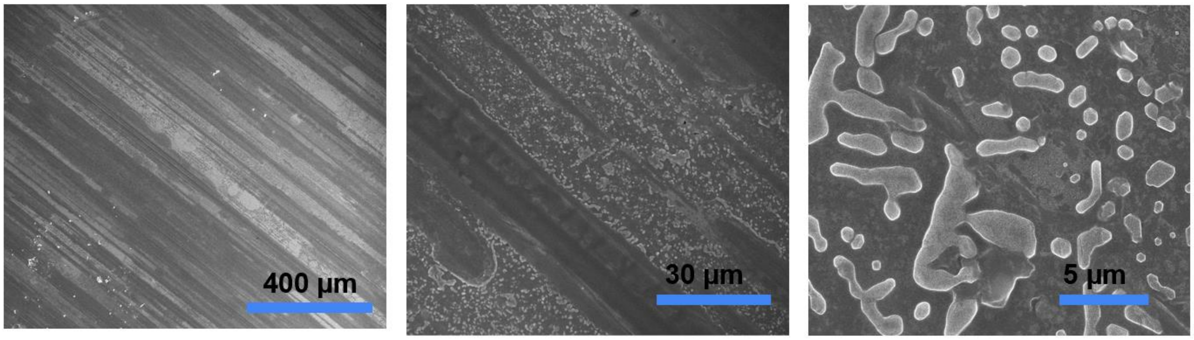

Figure 6-8. SEM image of collection pan after collection with PBS. The pan had been previously coated twice with 0.2 g/mL sucrose at 70 cm then was used as the surface for HSA SPNPs to be jetted atop of.

The purpose of coating was 2 fold: (1) Eliminate mechanical scraping, which would reduce the time it takes to collect and (2) provide an even surface for EHD jetting. With an even surface, the SPNPs would not land within the crevaces of the collector's surface thus reducing aggregation and improving the yield by not allowing the SPNPs to get stuck. Unfortunately, eliminating mechanical scraping was not achieved. While the results have shown that the SPNPs are still not evenly distributed, an investagion of the yield was conducted in a follow-up study.

In this follow-up study, it was investigated whether coating of sugar or starch prior to EHD jetting would impact the yield. The coating followed the prior experiment (sucrose and starch coated at 0.2 g/mL in water and sprayed 2 times 70 cm away). HSA SPNPs were produced at 7.5 wt/v% HSA, 20% v/v ethylene glycol, 80% v/v ultrapure water, 10% wt/wt crosslinker (2 kDa, relative to HSA). The jetting was at 0.2 mL/hour with each jetting lasting 30 minutes per pan. A control group (no coating) was also included. After incubation at 37 ˚C for a week, the SPNPs were collected with 5 mL of DPBS with 0.01% tween20. The SPNPs were processed (filtered and serial centrifuged) and the concentration was tested using the P660 assay. The theoretical mass for 4 pans of jetted SPNPs was 0.03 g. The percentage yield was calculated by dividing the mass of the SPNPs by the total protein multiplied by 100%. The control group resulted in a yield of 0.658% whereas the sucrose and starch coated groups had a yield of 0.546% and 0.480% respectively. While this shows there was not an improvement in the yield, it should be noted that perhaps the coating was not sufficient. It is possible that the coating was not even and therefore not sufficient to create a layer underneath the SPNPs. Instead of spraying the pans, a coating solution can be poured into the pan then evaporated to create an even surface without ridges.

Further investigations on coating pans prior to jetting can be performed, however, it must reduce the time to collect and not introduce further purification steps. If the coating works and eliminates the need to scrape the pans, but simultaneously introduces the need to purify the nanoparticles, there may not be any benefit in terms of saving time. However, if the coating can improve the yield, this may warrant the use of this method.

6.1.3 Modification of the serial centrifugation method

The serial centrifugation method in processing SPNPs was established to obtain sizes of SPNPs ranging from 100-300 nm. It was hypothesized that this process causes a loss in SPNPs, particularly at the 5 minute 3200 rcf centrifugation step. This step is in place to remove large particles and isolate the smaller particles. However, it is possible that the small particles are also getting pulled down into the pellet and being discarded as shown in **Figure 6-9**.

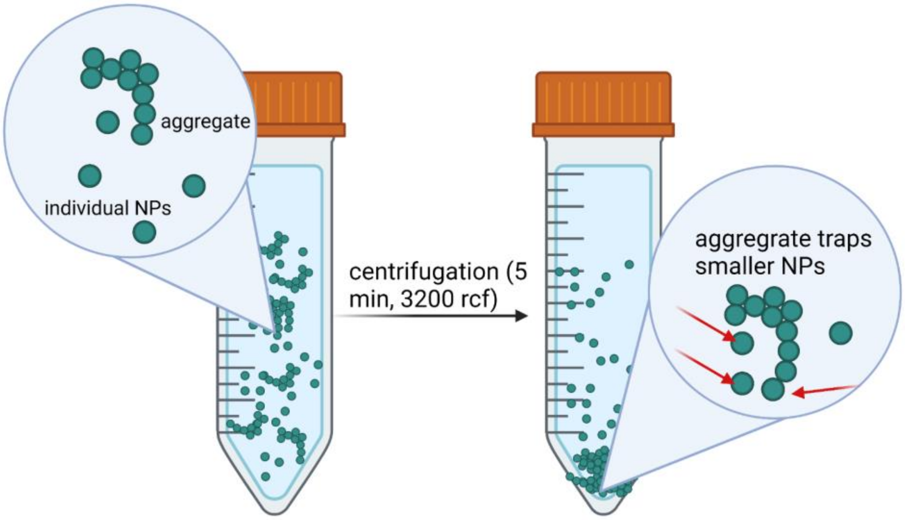

Figure 6-9. Hypothesized method of SPNP entrapment in the 5-minute centrifugation processing step.

To investigate this, the traditional method for processing SPNPs was modified to reprocess the 5-minute pellet as shown in **Figure 6-10**. The black font shows the traditional processing and follows steps 1 through 5. In attempts to retrieve more of the SPNPs, the 5-minute pellet was reprocessed by repeating steps 2 through 5 instead of discarding it (step 4.2). This is shown in the red font. Although this 5-minute pellet is reprocessed, it can be reprocessed again (shown in blue font).

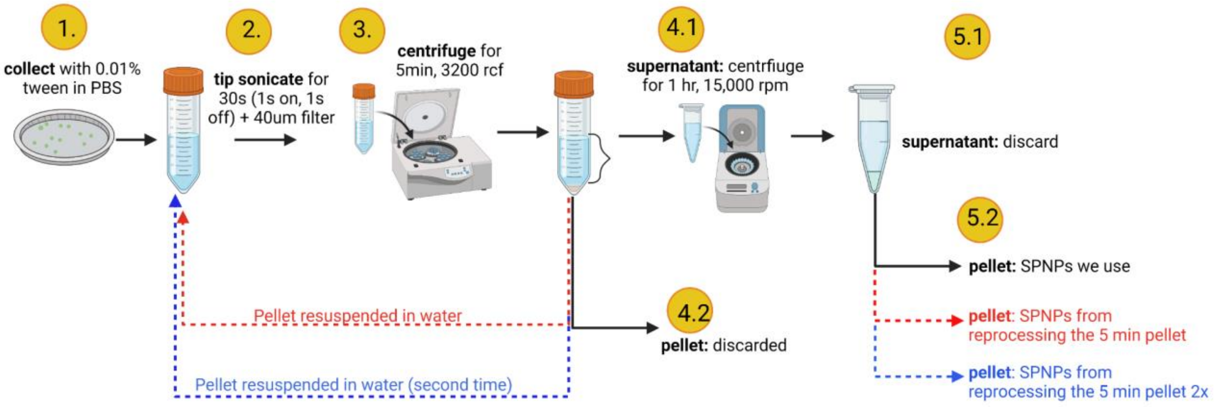

Figure 6-10. SPNP collection and processing steps. The black arrows indicate the traditional method for processing SPNPs. The red arrows and font show the first 5-minute processing step that can be added to the traditional processing. The blue arrows and font indicate a second iteration of the reprocessing. In step 1, collection with 0.01% Tween20 in PBS is conducted. Thereafter, it is tip sonicated for 30 seconds (one second on and 1-3 seconds off) on ice (step 2). The sonicated solution is filtered through a 40-micron filter (step 2) then centrifuged for 5 minutes at 3200 rcf (step 3). The supernatant is centrifuged at 15,000 rpm (21130 rcf) for 1 hour (step 4.1). The pellet is traditionally discarded (step 4.2). After step 4.1, the supernatant from the resulting spin is discarded (step 5.1) and the pellet is kept (step 5.2), which contains the SPNPs used. For the 5-minute reprocessing, instead of proceeding with step 4.2, the pellet is

resuspended in solvent (water or PBS) and steps 2, 3, 4, and 5 are performed. In a second 5-minute reprocessing, the 5-minute pellet is reprocessed again.

The three groups (SPNPs from traditionally processed method, SPNPs from 5-minute pellet and SPNPs from the second 5-minute pellet) were measured via DLS and is shown below in **Figure 6-11**. **Figure 6-11**A shows the intensity-based DLS of each group and **Figure 6-11**B shows the number-based LDS. There is good overlap between these groups showing that the reprocessing of the 5-minute pellet can retrieve SPNPs in the desired size range. This further proves that there are viable SPNPs getting discarded in the traditional method, but the next question is, how much and how many times is the reprocessing necessary?

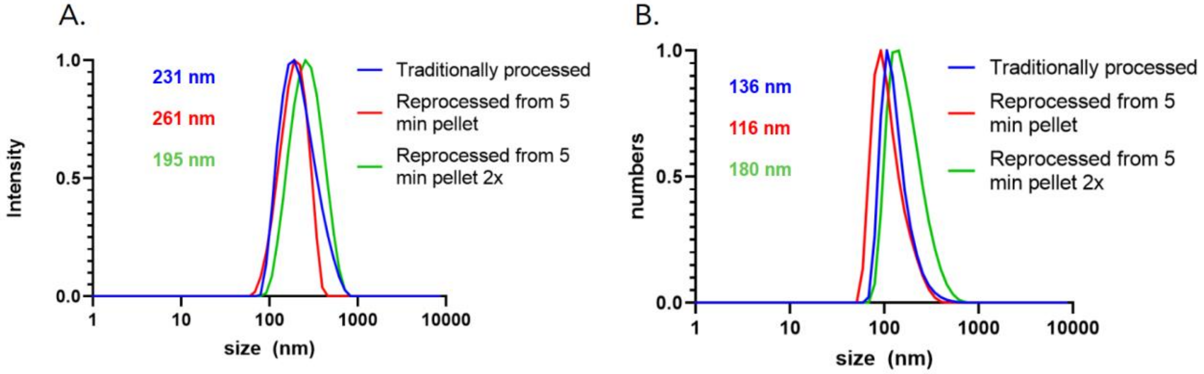

Figure 6-11. DLS spectra of SPNPs that were traditionally processed, reprocessed from the 5-minte pellet, and reprocessed from the second 5-minute pellet. A. Intensity-based DLS. Traditionally processed SPNPs, SPNPs reprocessed from the 5-minute pellet, and SPNPs reprocessed from the 5-minute pellet the second time had peak diameter of 231 nm, 261 nm, and 195 nm, respectively. B. The number based DLS. Traditionally processed SPNPs, SPNPs reprocessed from the 5-minute pellet, and SPNPs reprocessed from the 5-minute pellet the second time had peak diameter of 136 nm, 116 nm, and 180 nm, respectively.

A P660 assay was performed on each of these groups to answer those questions. The results are shown below in **Figure 6-12**. Here, we see that the 5-minute reprocessing could improve the yield by 34%. If considering the second 5-minute reprocessing step, it increases it to 46%. While these values may not be of value if not many SPNPs are needed, this is extremely important when producing SPNPs that are expensive to produce, or if large quantities are needed. Future users should incorporate this method to improve their yields if needed. However, it is recommended that the SPNPs from the 5-minute reprocessing steps are separated from the traditionally processed SPNPs until DLS is performed to confirm they are the same size.

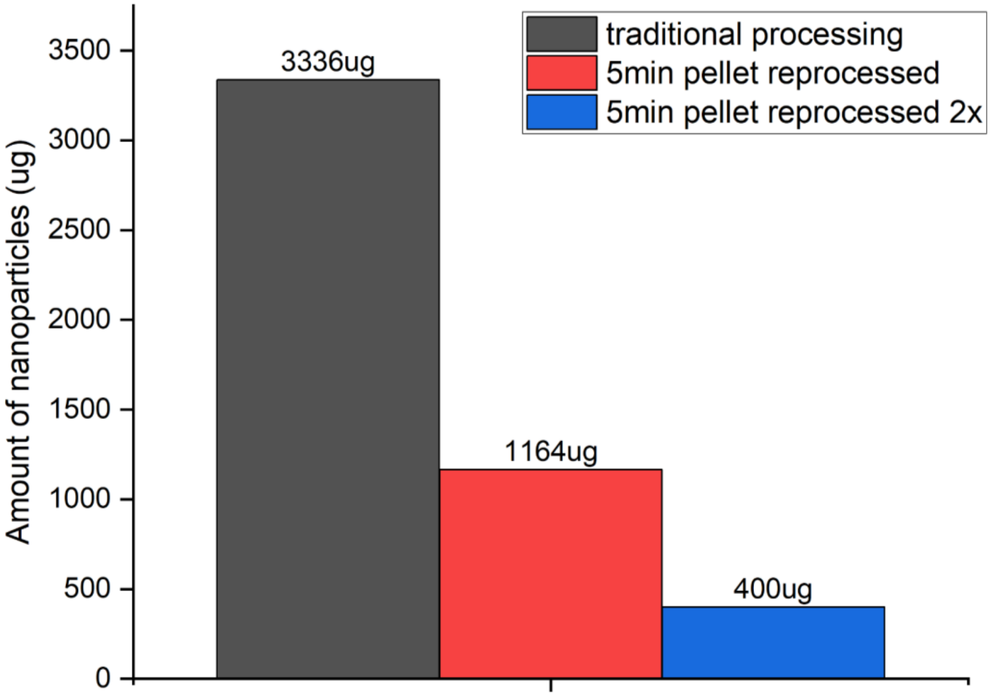

Figure 6-12. Mass of nanoparticles from three processing methods: (1) traditional processing, (2) Reprocessed 5-minute pellet, and (3) reprocessed 5-minute pellet conducted twice.

It should also be noted that the amount of solvent added to the 5-minute pellet is important and could impact the final size results. If the pellet is not diluted enough, the large particles can still be present in the supernatant and will not be filtered out. Therefore, further work on investigating the amount of solvent to add to the 5-minute pellet can be conducted. Alternatively, users can seek to modify the 5-minute step and whether that is necessary for processing a type of SPNP. An example of this is shown in the next section.

6.1.4 Jetting density of SPNPs impact on yield

During EHD jetting, the collection pans are exchanged every so often (usually 30 minutes). This was used even if changing the rate of the pump during jetting, the formulation, and other parameters. However, the exchange rate should be altered to fit the SPNP produced and the conditions it's being produced because it could cause layers of SPNPs on the collection pan leading to aggregation. To explore whether changing the pans more frequently impacted the yield, pans changed at 10 minutes versus 30 minutes were compared. A 7.5 wt/v% HSA solution in a cosolvent system of 80%(v/v) ultrapure water and 20% (v/v) ethylene glycol with a 10% wt/wt bifunctional crosslinker (2 kDa, relative to HSA) was jetted at 0.1 mL/hour. Nine centimeters between the tip of the needle and collection plate was maintained. Every 10 minutes, the plate was exchanged for one group. In the other group, the plate was exchanged every 30 minutes. Thereafter, the plate was incubated at 37 ˚C for 7 days, collected and processed according to **Figure 6-13**.

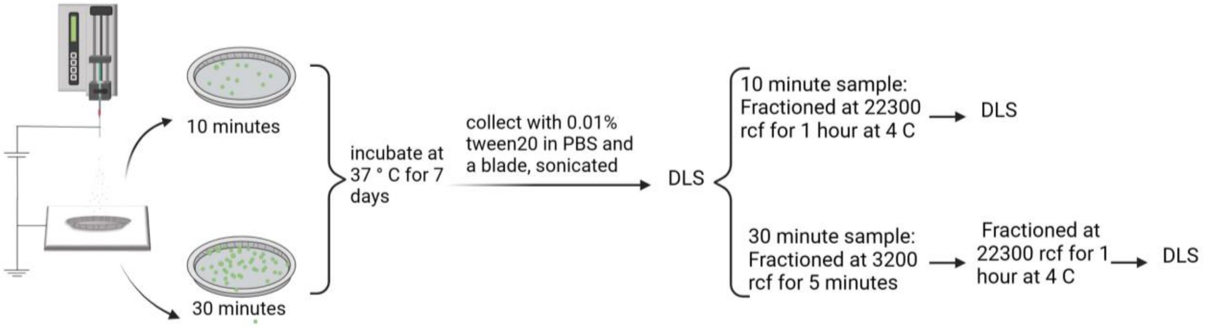

Figure 6-13. Experimental flow of SPNPs jetted on the collection pan for 10 minutes versus 30 minutes. After EHD jetting, the pans were incubated for 7 days at 37 ˚C. Thereafter, they were collected with 0.01% tween20 in PBS with a plastic blade and tip sonicated at an amplitude of 5 for 30 seconds (1 second on, 2 seconds off) on ice. Each group was measured via DLS to inform the next processing steps. For the 10-minute sample, it was fractioned at 22300 rcf for 1 hour at 4 ˚C. The supernatant was discarded, and the pellet was resuspended and measured via DLS. For the 30-minute sample, it was first fractioned at 3200 rcf for 5 minutes. The pellet was discarded, and the supernatant was further processed at 22300 rcf for 1 hour at 4 ˚C. The supernatant was discarded, the pellet was resuspended and measured via DLS.

After the SPNPs were collected with Tween20 (0.01%v/v) in PBS and sonicated, the DLS measurements were made to see the initial sizes prior to any centrifugation processing (**Figure 6-14**).

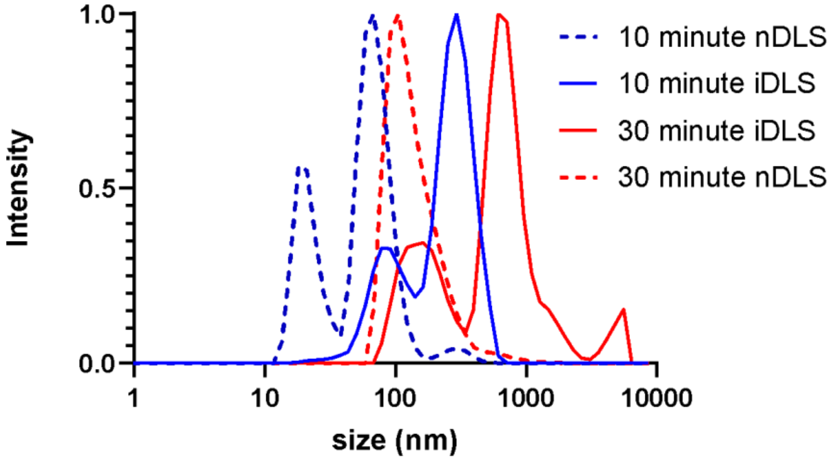

Figure 6-14. Intensity DLS (solid line) and number DLS (dashed line) of the 10-minute EHD jetted SPNPs (blue) and the 30-minute EHD jetted SPNPs (red). Spectra represent SPNPs after collection and tip sonication.

According to **Figure 6-14**, the 30-minute DLS has a larger population than is not seen for the 10-minute DLS. Using this information, it led to the decision to process each differently as shown in **Figure 6-15** For the 10-minute group, the SPNPs would be high speed centrifuged to remove smaller SPNPs. On the other hand, the 30-minute group would require the use of the traditionally employed method, which is low speed centrifuging (to remove the large aggregates/particles) followed by high-speed centrifugation (to isolate the smaller nanoparticles). After these processing steps, the following DLS spectra was obtained.

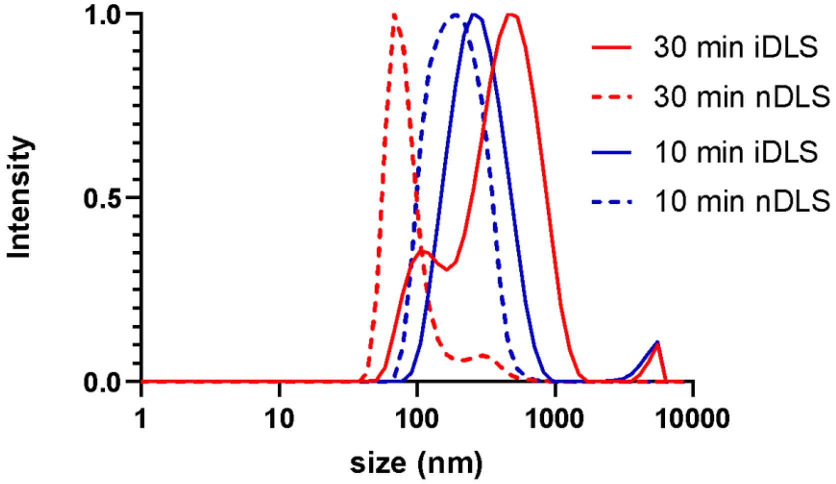

Figure 6-15. Intensity DLS (solid line) and number DLS (dashed line) of SPNPs EHD jetted for 10 minutes (blue lines) and 30 minutes (red lines). Spectra represent the final SPNPs produced from each group after processing.

Figure 6-15 indicates a larger size for the 30-minute group and the presence of a smaller peak. Data extracted from the DLS is shown in **Table 6-2**, which shows the 10-minute group was smaller and less polydisperse with a PDI of 0.272 compared to the 0.392 from the 30-minute group. Next, the yield was calculated by running a P660 assay. The yield was calculated by quotient of the P660 determined mass of SPNPs and the mass of protein in the jetting solution. This was multiplied by 100%. The 10-minute sample had a yield of 2.6% whereas the 30-minute sample had a yield of 1.9% (**Table 6-2**).

Table 6-2. Intensity DLS (iDLS), number DLS (nDLS), PDI, and percent yield of the EHD jetted SPNPs from the 10-minute group and the 30-minute group.

	10-minute sample	30-minute sample
iDLS (nm)	296± 131	505 ± 242,
nDLS (nm)	205 ± 88	84 ± 30
PDI	0.272	0.392
Yield (%)	2.6%	1.9%

These results indicate that the deposition time for SPNPs is important not only for determining processing steps, but also for assessing the yield. A comparison of the SEMs from each of the groups is shown in **Figure 6-16**.

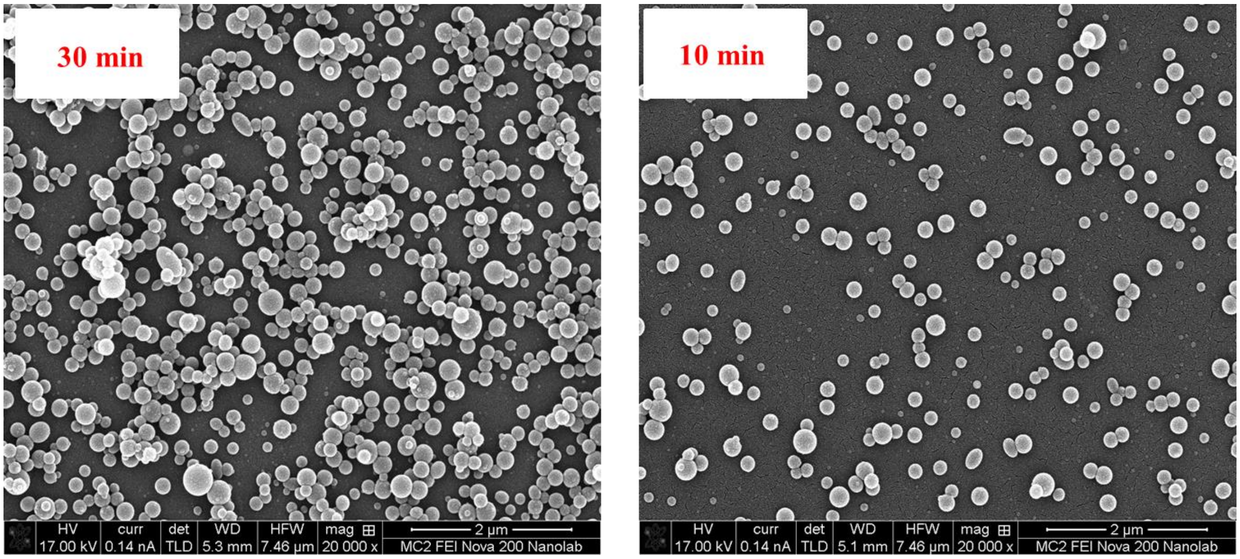

Figure 6-16. SEM micrographs of SPNPs that were jetted for 30 minutes (left image) and 10 minutes (right image).

For the 30-minute group, there is SPNP-SPNP stacking, which could form aggregates during the 7-day incubation period. Future users should perform an SEM study on their samples to assess an appropriate exchange rate to minimize such aggregation. It is understood that an exchange rate of 10 minutes can be cumbersome, so other parameters could be changed (i.e. lowering the flow rate of the pump) to decrease deposition rate without having to exchange so frequently.

6.1.5 4-arm PEG crosslinker versus 2-arm PEG crosslinker influence on SPNP yield

Low yield of SPNPs could be attributed to the type of crosslinker and the amount used. In the current formulation, 10% (wt/wt) of *O*,*O′*-Bis[2-(*N*-Succinimidyl-succinylamino)ethyl]polyethylene glycol is used relative to the protein. This can be described as a two-arm crosslinker. Here, it was investigated whether a 4-arm crosslinker would have a better yield than a 2-arm crosslinker. It was hypothesized that the addition of more arms in the crosslinker would lead to a higher SPNP yield. To test this, HSA SPNPs were produced with two different crosslinkers: (1) 4-arm-PEG-SS (2kDa, Nanosoft Materials, #4178-2k) (**Figure 6-17**A) and (2) SS-PEG2000-SS (2 kDa, Nanosoft Polymers #2574-2000) (**Figure 6-17**C). The formulation consisted of 7.5% (w/v) HSA in a cosolvent system of 20% (v/v) ethylene glycol and 80% (v/v) ultrapure water. The crosslinker was added at 10% (w/w) relative to the HSA. The SPNPs were jetted at a flow rate of 0.2 mL/hour and pans were changed every 30 minutes. Protein 660 was used to quantify the SPNP yield and supernatant (from the final spin down). The as-jetted SPNPs are shown in **Figure 6-17**.

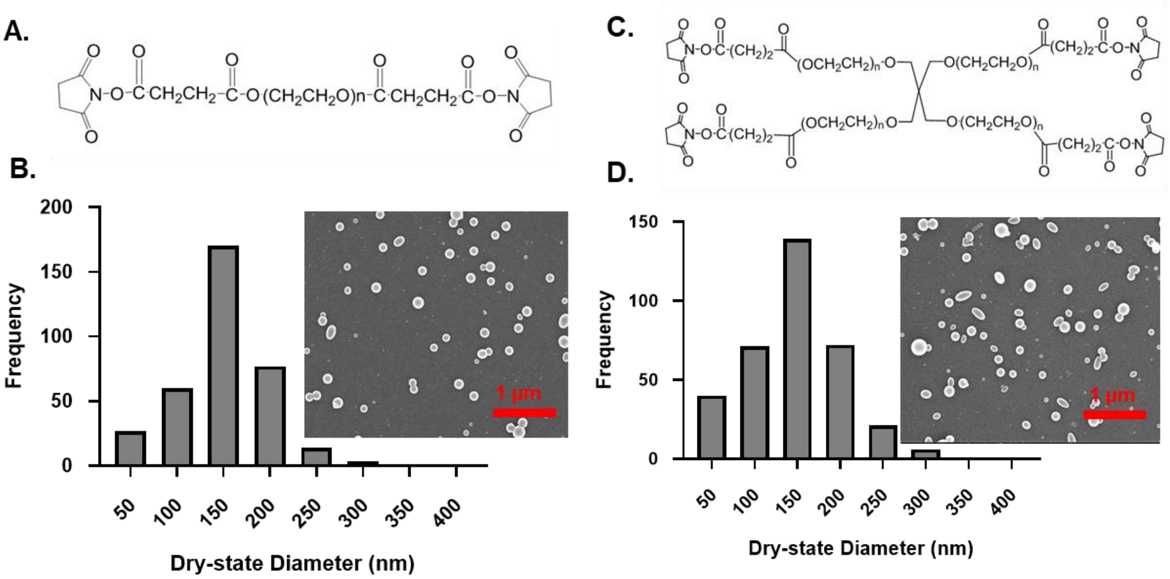

Figure 6-17. A. SS-PEG2000-SS crosslinker structure. B. SEM image (scale bar = 1 micron) and histogram showing size distribution of HSA SPNPs jetted with crosslinker shown in (A). C. 4-arm-PEG-SS crosslinker structure. D. SEM image (scale bar = 1 micron) and histogram of size distribution of HSA SPNPs jetted with crosslinker shown in (B).

The jetting of each were very similar with most of the size being around 100 nm. Further, the morphology of the SPNPs were similar as indicated by the SEM micrographs. After collection and processing of the SPNPs, the SPNPs hydrodynamic size were measured via DLS.

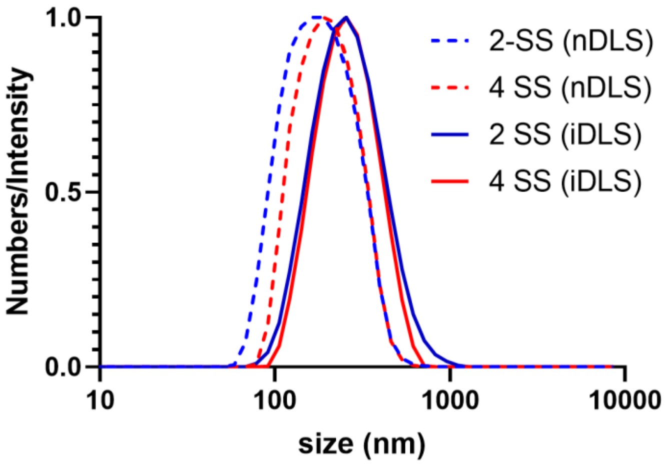

Figure 6-18. Hydrodynamic diameter of 2-arm (2-SS) and 4-arm (4-SS) crosslinked SPNPs. Number DLS (nDLS) is shown as dotted lines. Intensity DLS is shown as solid lines.

The extracted peak diameter and PDI from DLS is listed in **Table 6-3** and compared with the SEM analysis values. The SEM and nDLS values are comparable regarding size.

Table 6-3. Summary of SPNP properties crosslinked from the 2-arm crosslinker (2-SS) and the 4-arm crosslinker (4-SS). The SEM analysis is data from ImageJ analysis and represents the SPNPs in their dry-state, or "as-jetted" state. The DLS values represent SPNPs in their hydrated state in PBS after collection and processing.

	SEM analysis		nDLS measurements	
SPNP	2 SS	4 SS	2 SS	4 SS
Diameter (nm)	150 ± 45	147 ± 54	211 ± 82	194 ± 86
Circularity	0.94 ± 0.05	0.93 ± 0.08	-----	-----
PDI	0.191	0.228	0.263	0.260

After characterization of the structure, the quantification of the concentration was performed. The yield for the 2-arm crosslinked SPNPs was 0.58%, whereas the yield for the 4-arm crosslinked SPNPs was slightly higher at 0.78%. The supernatant was also measured to quantify uncrosslinked protein. The supernatant for the 2-arm crosslinked SPNPs and 4-arm crosslinked SPNPs was 5.8% and 2.8%, respectively. These results are depicted in **Figure 6-19** below.

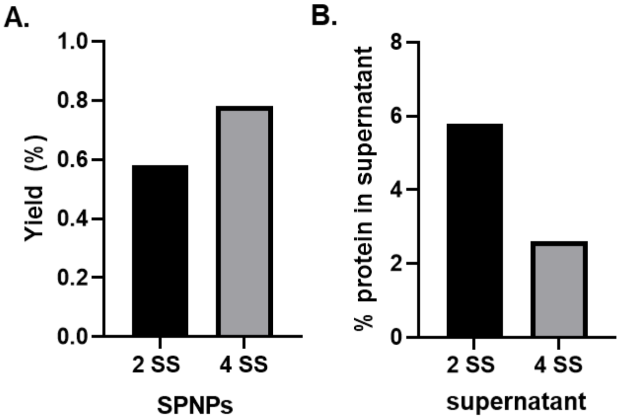

Figure 6-19. A. Yield of SPNPs produced with the 2-arm crosslinker (2-SS) and the 4-arm crosslinker (4-SS). B. The percentage of protein detected in the supernatant in the final spin down of SPNP processing (after high-speed centrifugation for 1 hour).

Therefore, the yield of the 4-arm crosslinker was higher and showed less protein was in the supernatant, which could mean that more of the protein was crosslinked and thus more SPNPs were formed. Thus, changing the crosslinker may be an effective strategy to improve the yield. Future work can explore the use of other crosslinkers to improve the yield, but great care must be taken to fully characterize such SPNPs as adjusting the crosslinker can impact the SPNP properties.

6.1.6 Influence of increasing crosslinker concentration on SPNP yield

Prior work has investigated how the concentration of the crosslinker influences the physical properties of the nanoparticle such as the size, swelling ratio, and elasticity. [113] However, it was not studied if it would impact the yield. Here, HSA SPNPs were produced varying the amount of crosslinker. Each formulation contained a 7.5% w/v HSA in a cosolvent system of 80%v/v water and 20% ethylene glycol. Crosslinker (NHS-PEG-NHS, 2kDa) was added to obtain 10%, 20% and 30%, by weight relative to HSA. The molar ratio between crosslinker and the HSA (crosslinker: HSA) would therefore be 3.3 for the 10% group, 6.6 for the 20% group, and 9.9 for the 30% group. The 10% group represented the control as that followed the traditional method for producing SPNPs. In **Figure 6-20**A-C, the SEM images for the 10%, 20% and 30% wt/wt_{HSA} is shown. The morphology between SPNPs is similar, suggesting that the EHD spraying process was not affected by the increasing concentration of crosslinker. **Figure 6-20**D shows the DLS spectra of each SPNP. As the amount of crosslinker increased, the SPNPs were smaller in their hydrated state as expected because the mesh size decreased, which was also the finding by Habibi et al.[113] Lastly, the yield was calculated to determine whether the yield would be improved. From **Figure 6-20**E, the yield does slightly increase with a higher percentage of crosslinker relative to the HSA. The supernatant from the spin down at 21130 rcf had less protein quantified via P660 assay with the higher concentration of crosslinker. While the 30% wt/wt$_{HSA}$ crosslinked SPNPs had less protein that was not crosslinked compared to the other groups, it is important to consider that these SPNPs would need to be validated further.

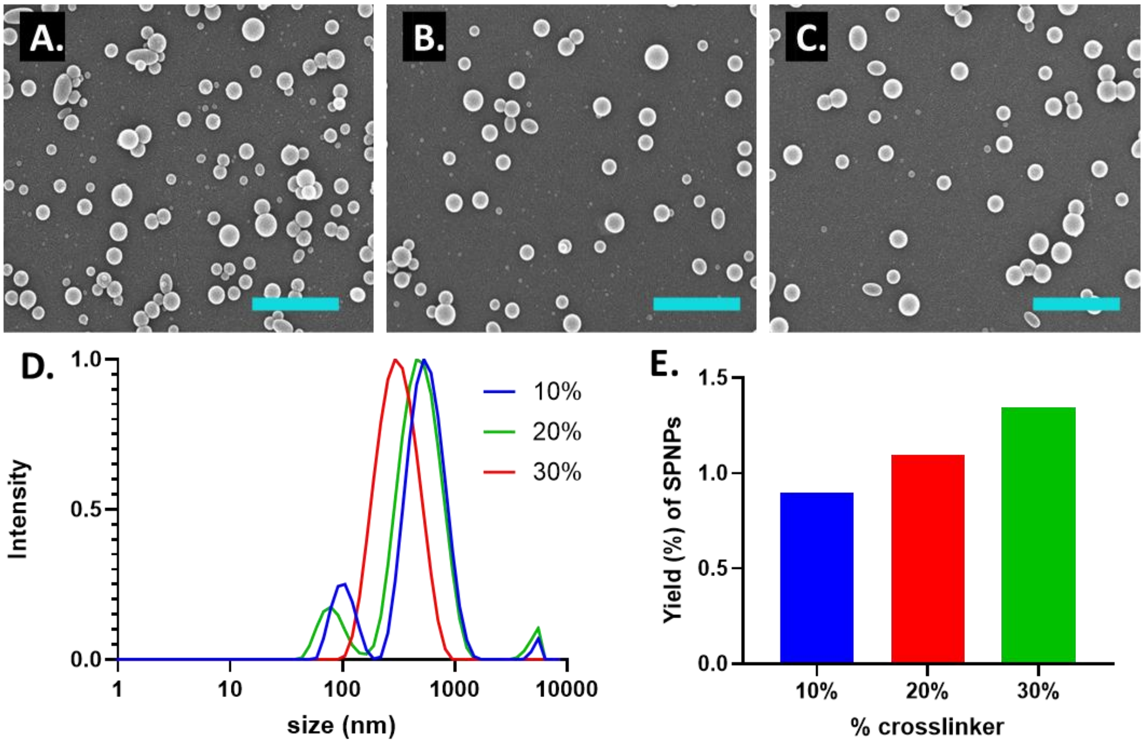

Figure 6-20. Characterization of SPNPs produced with 10%, 20% and 30% w/w NHS-PEG-NHS (2 kDa) crosslinker. A-C. SEM images of SPNPs formulated with 10% (A), 20% (B) and 30% (C) wt/wt crosslinker (scale bar = 1 micron). D. DLS spectra of SPNPs after collection and processing. E. Yield of SPNPs graphed as an average of three replicates.

6.2 Toward altering SPNP size through operational and formulation parameters

Knowing how to change the size of SPNPs is beneficial because nanoparticles size can affect pharmacokinetics and biodistribution.[306] In electrospraying, parameters like the formulation (type of polymer, concentration of polymer, solvent system properties), and instrumental settings (flow rate, distance, needle dimensions) can impact the size.[98,201,307,308] In the following studies, EHD jetting parameters and EHD jetting formulations were changed to study the impact on size of HSA SPNPs through SEM analysis.

6.2.1 Influence of jetting distance and flow rate on SPNP size

Jetting parameters (distance between collector and the needle, needle size, flow rate, etc.) and jetting formulation (concentration, solvent system, etc.) can affect nanoparticle size. Here, the distance between the collector and the needle was investigated using three distances: 5 cm, 9 cm and 15 cm. In addition, two solvent systems were used: (1) methanol (10%v/v) with water (90%v/v) and (2) ethylene glycol (20%v/v) with water (80%v/v). Both were formulated to have an HSA concentration of 7.5% wt/v. No crosslinker was used since the SPNPs were only studied via SEM in their dry state and not collected. **Figure 6-21**A shows that the distance between the tip of the needle and the plate was varied. **Figure 6-21**B shows the SEM images of the SPNPs produced according to their solvent system and the distance. From the SEM images, ImageJ analysis was performed,[114] and the diameter, circularity, and PDI were obtained (**Figure 6-21**C).

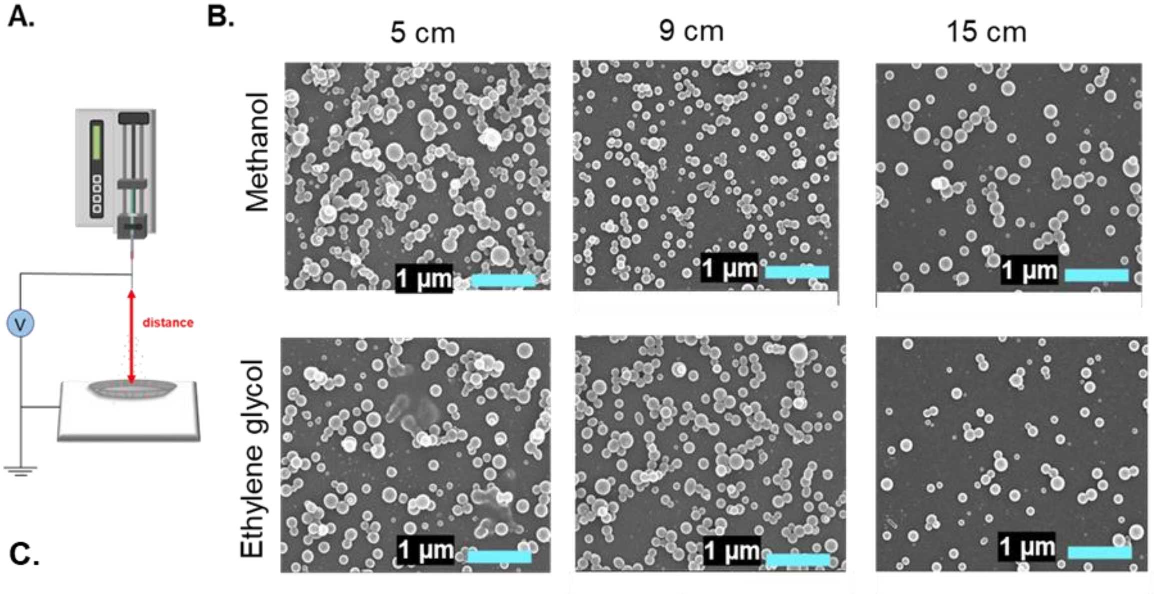

	Methanol 10% (v/v)			Ethylene glycol 20% (v/v)		
Distance (cm)	Diameter	Circularity	PDI	Diameter	Circularity	PDI
5	168 ± 52	0.87 ± 0.08	0.23	185 ± 43	0.89 ± 0.05	0.18
9	137 ± 39	0.91 ± 0.08	0.17	180 ± 46	0.92 ± 0.07	0.20
15	146 ± 45	0.94 ± 0.04	0.19	166 ± 44	0.93 ± 0.05	0.19

Figure 6-21. A. EHD jetting station depicting the distance that was varied. B. Grid of SEM micrographs showing HSA SPNPs jetted at distances 5cm, 9cm, and 15 cm with two solvent systems (methanol and ethylene glycol). Scale bar = 1 micron. Jetting was performed using a syringe pump flow rate of 0.1 mL/hour. C. Table summarizing the diameter, circularity and PDI of the SPNPs analyzed using ImageJ (n=300). Error is reported as the standard deviation.

The circularity was relatively high for all groups (>0.87). The PDI was also low (<0.20) except for the methanol solvent system at 5 cm, which had a PDI of 0.23. The diameter of SPNP produced with ethylene glycol showed a decreasing trend as the distance increased (from diameter of 185 nm to 166 nm). The SPNPs produced with methanol also decreased when the distance increased from 5 to 9 cm, but it increased again from 9 to 15 cm. This is shown in **Figure 6-22**.

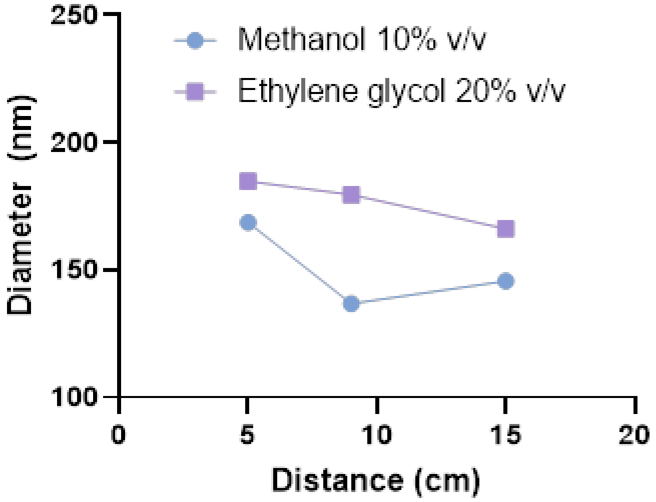

Figure 6-22. Effect of EHD jetting distance on the diameter of 7.5%w/v HSA SPNPs formulated with a cosolvent system of (1) methanol (10%v/v) + water (90% v/v) or (2) ethylene glycol (20% v/v) with water (80% v/v). Points are reported as averages of diameters from n=300 analyzed SPNPs from SEM images.

Overall, the SPNPs produced with 10% methanol exhibited a smaller diameter than the 20% ethylene glycol SPNPs. While the distance can impact the diameter of the SPNPs, the spray size on the collection plate should be considered. At larger distances, the SPNPs are sprayed over a larger area, which can be larger than the collection plate. If this occurs, it can decrease the yield. Conversely, if the particles are sprayed over a smaller area (i.e. a closer distance) then the area covered on the collection plate will be smaller; however, the SPNPs will be more crowded and could cause aggregation. In addition, if too close, it will not allow for sufficient evaporation of the solvent that is needed to form solid SPNPs at the surface of the plate. If a smaller SPNPs is desired, it is recommended that the distance is maximized without causing the SPNPs to jet outside of the bounds of the collection plate. Alternatively, changing the solvent systems can alter the size.

Next, the flow rate was varied while keeping the distance constant at 9 cm (**Figure 6-23**A) and using the same SPNP formulation as the distance study. The SEM images of the SPNP produced at rates of 0.01, 0.05, and 0.10 mL/hour with the two solvent systems is shown in **Figure 6-23**B. The summary of the analysis of the SEMs is shown in **Figure 6-23**C. The circularity was high for all groups and no apparent trend is noted. The PDI was relatively low except for the SPNPs produced with ethylene glycol at a flow rate of 0.01 mL/hour. Again, no trend in terms of polydispersity is observed.

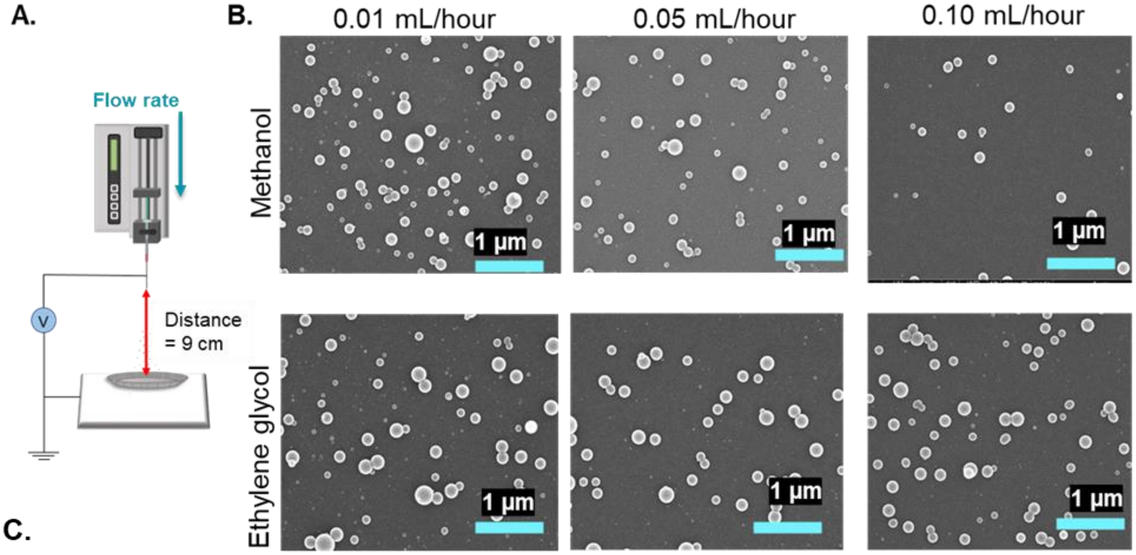

C.

	Methanol 10% (v/v)			Ethylene glycol 20% (v/v)		
Flow rate (mL/hour)	Diameter	Circularity	PDI	Diameter	Circularity	PDI
0.01	147 ± 45	0.93 ± 0.07	0.19	174 ± 65	0.92 ± 0.05	0.27
0.05	149 ± 43	0.94 ± 0.07	0.18	179 ± 45	0.93 ± 0.06	0.19
0.10	137 ± 39	0.91 ± 0.08	0.17	180 ± 46	0.92 ± 0.07	0.20

Figure 6-23. A. EHD jetting station depicting the distance was constant at 9 cm and the flow rate was varied. B. Grid of SEM micrographs showing HSA SPNPs jetted at flow rates of 0.01, 0.05, and 0.10 mL/hour with two solvent systems (methanol and ethylene glycol). Scale bar = 1 micron. C. Table summarizing the diameter, circularity and PDI of the SPNPs analyzed using ImageJ (n=300). Error is reported as the standard deviation.

The diameter for the SPNPs appears to not have a trend with the flow rates for either solvent system. However, the SPNPs produced with the methanol solvent system exhibited smaller diameters than the ethylene glycol SPNPs by about 40 nm (**Figure 6-24**). From this study, flow rate should not be adjusted to change the size of the SPNPs. Instead, using a different solvent system would be more effective at changing the size. While the flow rate does not have a significant effect on the size, this does not mean that users should instantly choose a faster flow rate to expediate EHD jetting. Other factors must be considered. For example, if the faster flow rate causes the reduction in the stability of the jet, this can lead to less SPNP formation and cause the formation of a puddle of jetting solution to form at the collection plate. Consequently, the yield will be lower since not the entire jetting solution is being used to produce SPNPs.

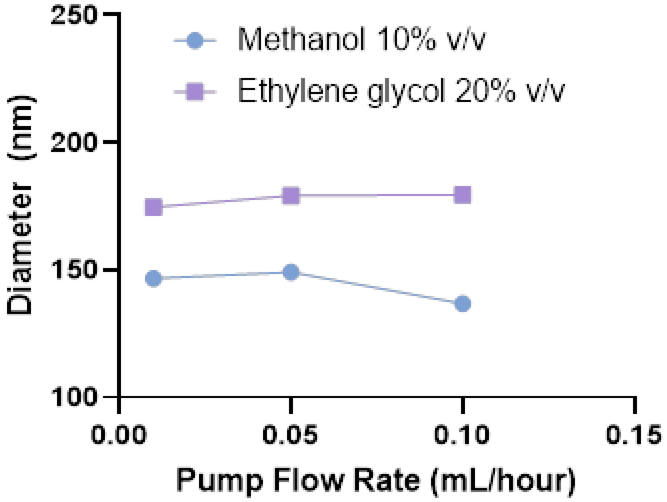

Figure 6-24. Effect of EHD jetting distance on the diameter of 7.5%w/v HSA SPNPs formulated with a cosolvent system of (1) methanol (10%v/v) + water (90% v/v) or (2) ethylene glycol (20% v/v) with water (80% v/v). Points are reported as averages of diameters from n=300 analyzed SPNPs from SEM images.

6.2.2 Interplay between solvent system and HSA concentration on SPNP size

From the prior studies, it was shown that the solvent system impacts the size of the SPNPs more than the distance or flow rate. It is also known that the concentration of polymers can influence the size of nanoparticles produced through electrospraying.[191,201] In this study, the interplay between the solvent system and HSA concentration on SPNP size was studied. HSA concentrations were 1% wt/v, 2.5% wt/v and 7.5% wt/v. The solvent systems were all 80% v/v water and 20% a secondary solvent (ethylene glycol, methanol, or acetone). No crosslinker was used in the formulation. The flow rate and distance were maintained at 0.06 mL/hour and 7 cm, respectively. The SEM images of these SPNPs are shown below (**Figure 6-25**).

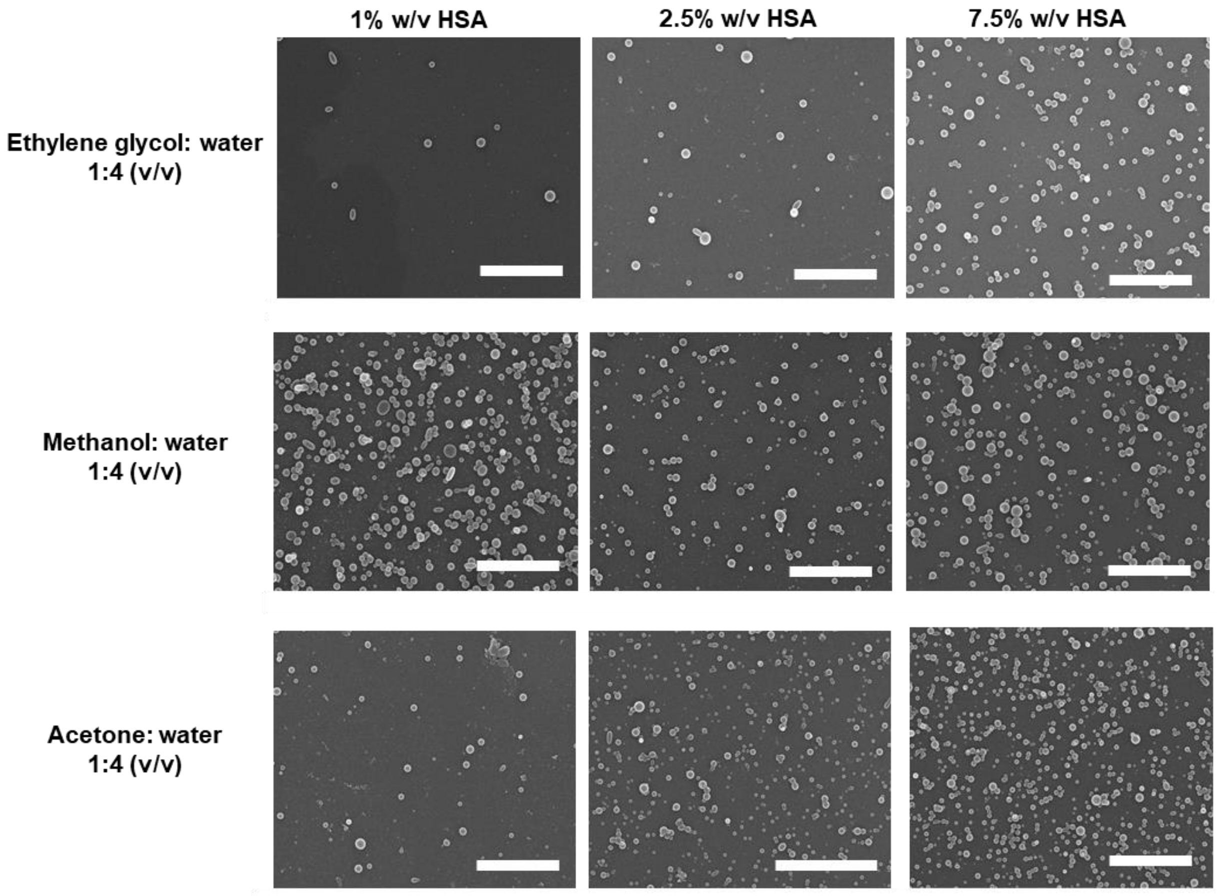

Figure 6-25. SEM images showing the interplay between HSA concentration and solvent system on SPNP morphology. Scale bar = 2 micron. All SEM images are at a magnification of 25,000 except for the acetone: water at 2.5% w/v HSA, which is at 25,000 magnification.

ImageJ analysis was performed on n=100 SPNPs per group except for 1%wt/v HSA produced with 1:4 ethylene glycol: water, which had n=58. **Figure 6-26** shows the influence of the solvent system and the HSA concentration in the resulting SPNPs produced via EHD jetting. Overall, the solvent system had the biggest impact on the diameter of the HSA SPNPs. SPNPs produced with ethylene glycol had SPNPs in the range of 165 nm to 203 nm while the methanol solvent system made smaller SPNPs in the range of 121 nm to 143 nm. SPNPs from 85 nm to 148 nm were produced with the acetone solvent system. The largest SPNPs at an average diameter of 203 nm were formulated with 1%w/v HSA and with 1:4 ethylene glycol: water. The smallest SPNPs at an average diameter of 85 nm was formulated with 2.5%w/v and with 1:4 acetone: water.

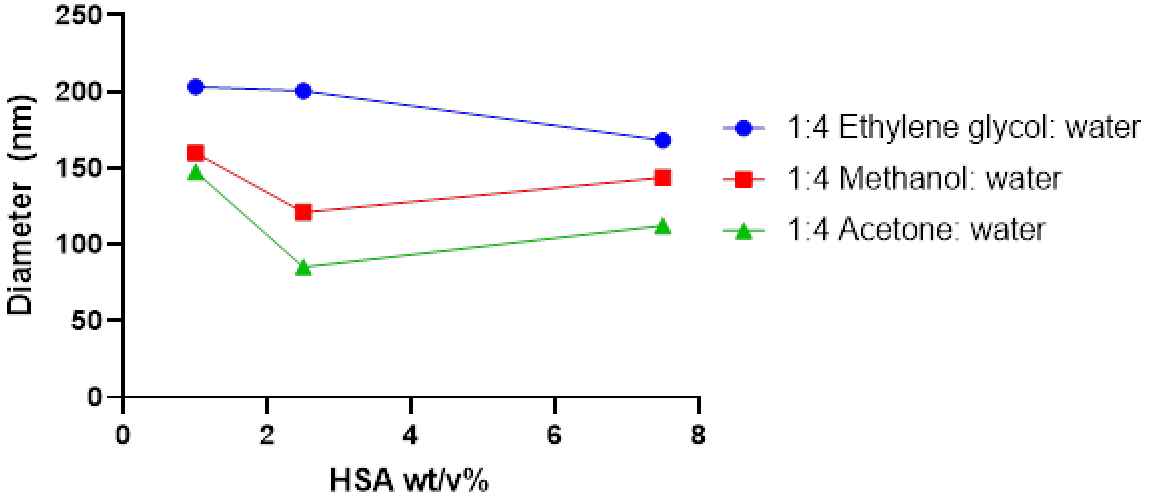

Figure 6-26. Influence of HSA concentration and solvent system on SPNP diameter. HSA concentration was 1% wt/v, 2.5% wt/v and 7.5% wt/v. The solvent systems were 1:4 solvent: water, where solvent was either ethylene glycol, methanol, or acetone.

The remainder of the diameters are reported in **Table 6-4** along with the corresponding circularity and PDI. The average circularity of the SPNPs was at least 0.91, indicating that the formulations did not have a great impact on the shape. The PDI ranged from 0.14 to 0.37 with the most polydisperse SPNPs coming from the 2.5%w/v HSA in the ethylene glycol solvent system. The least polydisperse SPNPs were from the SPNP formulated with the acetone solvent system.

Table 6-4. Solvent and HSA concentration effect on diameter, circularity and PDI of HSA SPNPs produced via EHD jetting. The flow rate was constant at 0.06 mL/hour and the distance between the plate and the needle was 7 cm.

Solvent system	**HSA (wt/v) %**	**Diameter ± SD (nm)**	**Circularity ± SD**	**PDI**
Ethylene glycol (1:4 v/v)	1	203 ± 66	0.92 ± 0.06	0.28
	2.5	197 ± 87	0.92 ± 0.06	0.37
	7.5	165 ± 48	0.91 ± 0.07	0.21
Methanol: water (1:4 v/v)	1	137 ± 50	0.91± 0.08	0.21
	2.5	121 ± 50	0.94 ± 0.07	0.21
	7.5	143 ± 62	0.91 ± 0.05	0.26
Acetone: water (1:4 v/v)	1	148 ± 48	0.94 ± 0.05	0.20
	2.5	85 ± 33	0.93 ± 0.07	0.14
	7.5	112 ± 34	0.92 ± 0.05	0.14

6.3 Toward computation-informed synergistic drug combinations for bi-compartmental nanoparticle glioma combination therapy

As shown in **Chapter 3**, bicompartmental nanoparticles are advantageous to deliver two different therapeutics (i.e. hydrophobic small molecule and siRNA) in the same nanoparticle for combination therapy. The combination of STAT3i siRNA and PTX in b was chosen because of the results in a prior publication, and the recent demonstration of encapsulating hydrophobic small molecules (i.e PTX) in the EHD jetting system for SPNPs (**Chapter 2**). However, deciding on the combination is typically biased, which limits the scope towards these biases. In addition, deciding between several combinations would be best determined through experiments, but this approach is cumbersome and costly. Therefore, leveraging machine learning, or computational programs to screen combinations according to the biological landscape of interest, can eliminate this bias, broaden the scope of possible therapeutics, and provide a data-driven decision. One such computational platform is SynergySeq, which identifies synergistic combinations of FDA approved drugs by integrating information from The Cancer Genome Atlas (TCGA) and the Library of Integrated Network-Based Cellular Signatures (LINCS).[309] A benefit of this platform is it allows the user to create a specific disease signature by uploading the RNA-seq data that describes the differentially expressed genes in a control versus the disease. Thereafter, the user can choose the reference drug, or the drug in which the program will compute synergistic combinations with. It then ranks hundreds of combinations according to the ability of the combination to reverse the disease signature and the secondary drug's orthogonality to the user's reference drug. Such programs can drive patient-specific combinations, which is valuable considering the inter- and intra- heterogeneity of gliomas. Here, SynergySeq was used to identify combinations by uploading RNA-seq data from a model for diffuse astrocytoma, provided by the Maria Castro Lab.

Diffuse astrocytoma is resistant to ionizing radiation as described in **Chapter 4** and a prior publication.[196] We sought to use this program to identify drug combinations for this model. More specifically, we used an RNA-seq file that described the differentially expressed genes in mutant IDH1 tumors versus their wild-type counterpart, with and without ionizing radiation. The purpose was to find secondary drugs that synergize with STAT3 siRNA because of the recent demonstration of its anti-glioma activity in SPNPs. However, because the program only includes FDA approved drugs and STAT3 siRNA is not FDA approved, surrogate STAT3 inhibitors were screened from SynergySeq's reference drug options. The following drugs were identified, which were found to be implicated in the inhibition of STAT3/JAK pathways: AZD1480, cepharanthine, crizotinib, CYT387, diacerin. Each of these were tested in the program with the RNA-seq file to find potential synergistic secondary compounds, which are ranked according to orthogonality and disease discordance as shown below. The top left quadrant represents where the idea secondary candidates would be located (low similarity to the reference molecule, but high disease signature reversal potential). Orthogonality describes how different the secondary drug is from the reference drug. Disease signature reversal refers to the ability of the drug combination to reverse the RNA-seq profile to the control. From this information, CYT387 was found to be synergistic with SNS-032, a cell cycle checkpoint inhibitor.

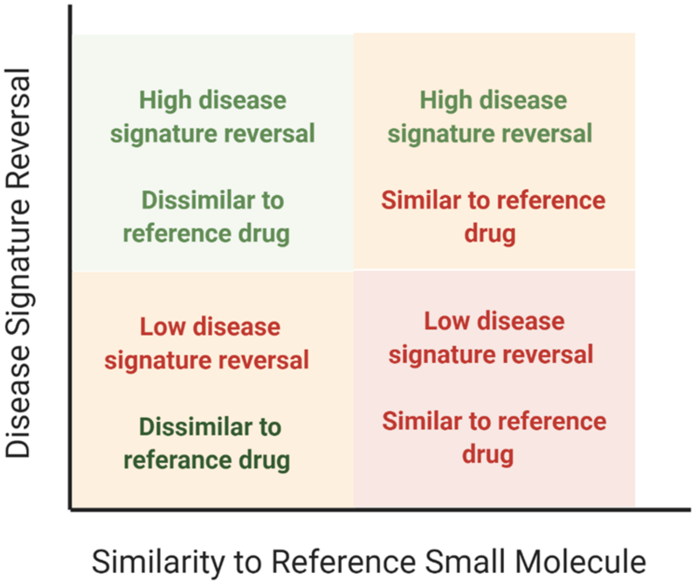

Figure 6-27. Output plot from SynergySeq ranks the secondary drug according to its similarity to the reference small molecule and the ability to reverse the disease signature. Ideal synergistic combinations would be found in the top left quadrant, with the highest disease signature reversal potential. It also is the least similar to the reference molecule.

Bi-compartmental synthetic protein nanoparticles (biSPNPs) were produced using EHD co-jetting (**Figure 6-28A)** as previously described.[99,102,110,310] The right compartment was formulated using the same procedure described in **Chapter 3** and by Gregory, J et al.[218] Briefly, mouse or human STAT3 siRNA (0.75 nmol) was complexed with branched PEI (60 kDa, 5% wt/v, 25 µL) for 30 minutes. The HSA (29.5 mg) was dissolved in ultrapure water (750 µL) then BSA 647 Alexa Fluor conjugate (29.5 µL, 5 mg/mL) was incorporated. Next, IRGD (0.1 mg/mL, 2.4 µL) was added followed by ethylene glycol (236 µL) then the complex of siRNA/PEI. Lastly, the crosslinker dissolved in water was added (2.95 mg, 62 µL).

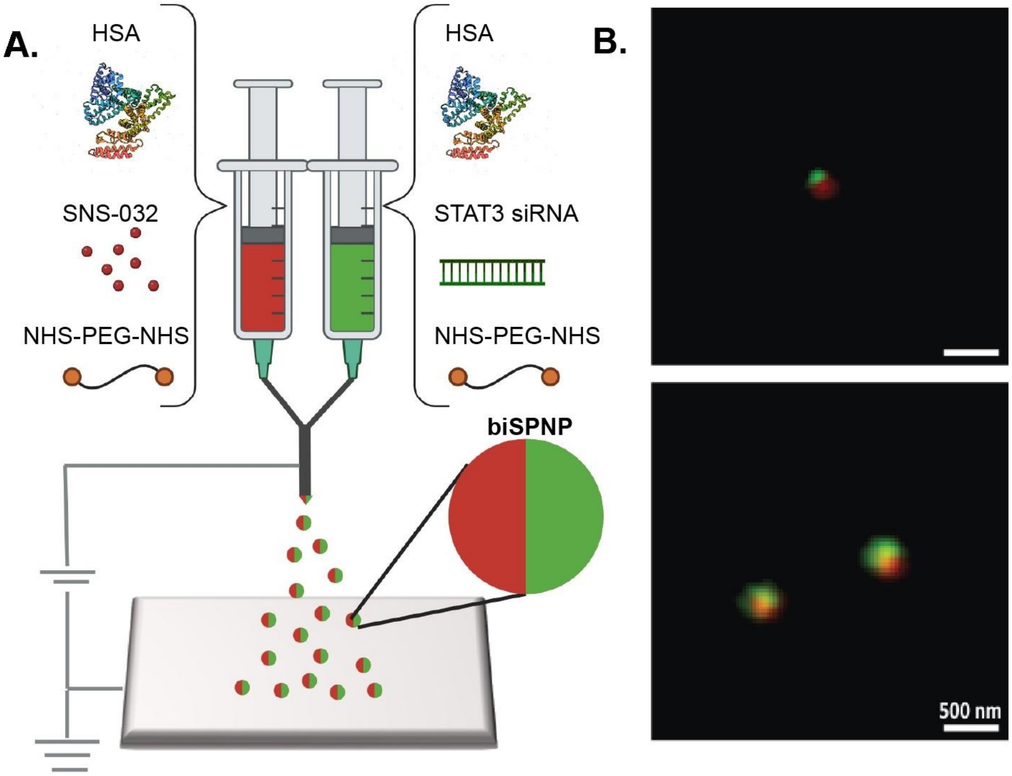

Figure 6-28. Fabrication of STAT3i/SNS-032 biSPNPs via electrohydrodynamic co-jetting. The left compartment contains SNS-032 (red) and the right contains STAT3 siRNA (green). Both compartments contain the tumor penetrating peptide, iRGD, HSA, and crosslinker (NHS-PEG-NHS).

The SNS-032 compartment was formulated like the STAT3i compartment, but instead of STAT3i/PEI, SNS-032 was used. HSA (29.5 mg) was first dissolved in 850 µL of ultrapure water. The fluorescent tag, Alexa Fluor 647 conjugate (29.5 µL, 5 mg/mL) was added, then 2.4 µL of iRGD (0.1 mg/mL). SNS-032 (50 mg) was dissolved in 3336 µL of ethanol and 750 µL of DMSO to have a concentration of 12.23 mg/mL. From that stock, 236 µL was added to the jetting solution for a theoretical loading of 9.8%, relative to HSA. The formulations were loaded separately into 1 mL syringes with a 25-guage stainless steel needle. The needles were bent to enable a side-by-side configuration and the solutions were pumped at a rate of 0.1 mL per hour. The needles were held together using plastic tubing. A positive voltage source was attached to the joined needles and grounded at the plate underneath the collection plate (approximately 9 cm distance from the needle tip to the plate). Solid STAT3i/SNS-032 biSPNPs were formed on the collection plate (**Figure 6-28**A). To visualize the two compartments, Structured Illumination Microscopy (SIM) was used

(**Figure 6-28**B). The characterization of the mouse-specific STAT3i/SNS-032 biSPNPs is shown in **Figure 6-29**. The morphology of the as-jetted dry biSPNPs is shown in the micrograph. Using these micrographs, ImageJ analysis was performed to measure the sizes, and shape. The distribution of sizes is shown as an inset of the SEM (n=300 analyzed biSPNPs). The mSTAT3/SNS-032 biSPNPs had an average dry diameter of 122 ± 36 nm. The circularity was 0.92 ± 0.05 and a PDI of 0.155. This shows that the as jetted biSPNPs were in a good size range, highly circular, and had a low polydispersity index. After collection and processing (following procedures described in **Chapter 4**), the hydrated biSPNPs were measured through DLS (**Figure 6-29**B, Z_{avg} diameter = 221 nm)

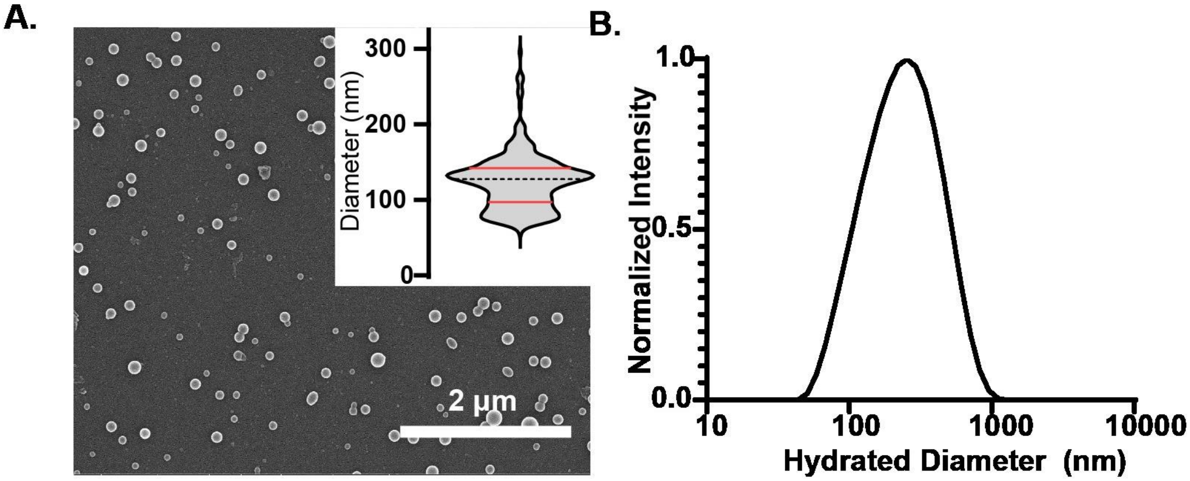

Figure 6-29. Mouse STAT3i/SNS-032 biSPNP characterization. A. SEM micrograph (scale bar = 2 microns) with the corresponding diameter distribution. Pink indicates the mean diameter (122 ± 36 nm), and the black lines show the interquartile range. B. Hydrated diameter of biSPNPs measured through DLS (Z_{avg} =221 nm).

The same characterization was performed for the human-specific STAT3i/SNS-032 biSPNPs (**Figure 6-30**). The average diameter was found to be 125 ± 30 nm with a circularity of 0.94 ± 0.04, and a PDI of 0.129. After collection and processing, the DLS spectra was recorded (Z_{avg}= 214 nm)

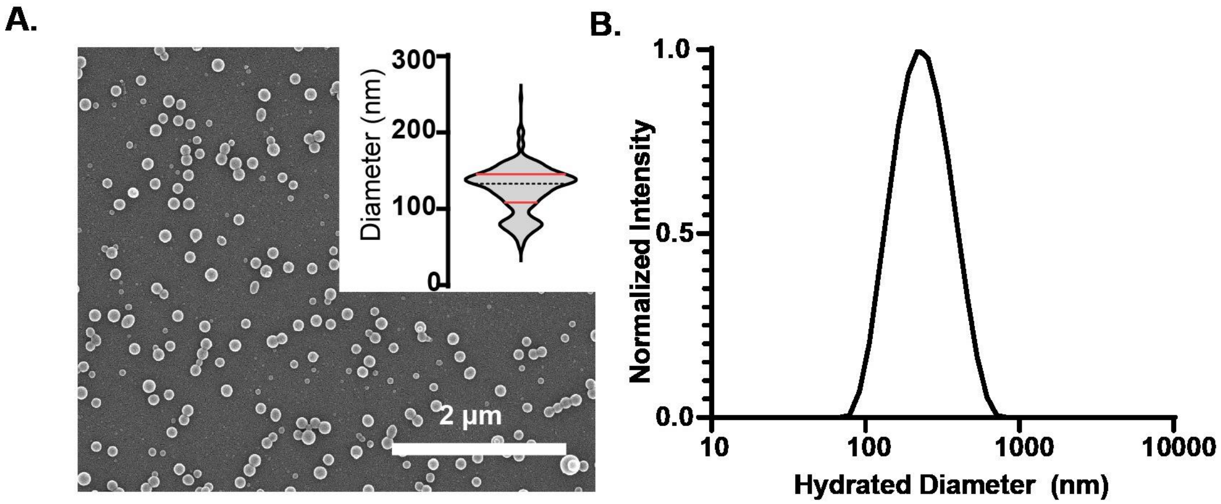

Figure 6-30. Human STAT3i/SNS-032 biSPNP characterization. A. SEM micrograph (scale bar = 2 microns) with the corresponding diameter distribution. Pink indicates the mean diameter (125 ± 30 nm), and the black lines indicate the interquartile range. B. Hydrated diameter of the biSPNPs measured via DLS (Z_{avg} = 214 nm)

The in vitro cytotoxicity of these biSPNPs is currently being studied in six glioma cell lines: mouse neurospheres (NPA wtIDH1 versus NPA mIDH1), human glioma cells (SJ-GBM2 versus SJ-GBM2 mIDH1), and human patient-derived glioblastoma cells (SF10602+AGI5198 versus SF10602). The treatment was at the IC50 of SNS-032, which was established for the six cells. Experimental groups included: untreated, empty biSPNPs (without siRNA and SNS-032), scrambeled siRNA, free STAT3i, free SNS-032, free STAT3i and free SNS-032, and the STAT3i/SNS-032 biSPNPs. Each of these was tested with and without ionizing radiation (3 Gy for mouse, 5 Gy for human cells). After 24 hours of cell seeding (1000 cells per well, 96 well plate, 200 µL per well), the therapeutic treatment was given. Two hours later, ionizing radiation was performed on the cells. At 72 hours, cell viability was determined through the Cell Titer Glo assay. Since the loading of the SNS-032 was not established prior to this, they were assumed to have the same loading efficiency as the PTX (**Chapter 2**) within the PTX SPNPs (94% loading efficiency). With a theoretical loading of 9.8% relative to HSA with a theoretical loading efficiency of 94%, the dosing was established using an assumed 9.2% loading.

The computationally informed drug combinations for biSPNP represent a new era of SPNPs. Here, SynergySeq, an open-source computational platform, was used to determine drug combinations for diffuse astrocytoma using the unique RNA-seq profile. Some benefits of SynergySeq may also speak to the limitations. For example, only FDA approved drugs are available for the combinations, which can make the approval of combinations easier. However, this also limits the scope. Outside of SynergySeq, many other computational platforms are available as described by the cited reviews.[311–313] Despite the exciting advent of these platforms, the jump from using these for nanoparticle combination therapy must be acknowledged. Encapsulating drugs inside a nanoparticle can complicate the understanding of synergism. In other words, certain ratios of the drugs must be maintained to obtain the synergistic effect. If this is not maintained, it could weaken the effect, or even produce an antagonistic effect. Therefore, it would be advisable to first test the combinations using methods outlined by Chou T.C.[314,315] After establishing the effective dose to impact 50% of the population (i.e. ED50), the drugs should be tested in a matrix in multiples of the ED50. Leveraging platforms like DECREASE platform can fill out the remaining matrix. [316] This result will be useful to understand how many possible ratios will elicit a synergistic effect. If there is only one ratio that can provide this synergistic effect, it may not be the most suitable for nanoparticle combination therapy as that ratio must be retained. Therefore, while this area is exciting, we must realize that extending this into nanoparticle combination therapy will take additional work.

6.4 Outlook

Electrohydrodynamic (co) jetting is a versatile technique to produce synthetic protein nanoparticles for glioma therapy, but there is still room for development in several areas. As described in this chapter, the electrohydrodynamic (co) jetting process needs to be better understood. More specifically, understanding how to tune the formulation and operational parameters to yield a nanoparticle of desired properties, is not completely elucidated. This could be achieved through design of experiments coupled with computational methods, but it would first be required that controlled environment is achieved (humidity, temperature, precise and accurate operational parameters). Yield is another critical aspect when considering large-scale experiments like in vivo testing, especially when using costly materials. Alternative crosslinking strategies could hold promise when increasing yields and even minimizing processing time.

Another area for future work would be elucidating the mechanism of delivery of the SPNPs. Most of the work shown here focused on therapeutic efficacy and toxicity, which are necessary components for the development of therapeutic agents. However, if pharmacokinetics and pharmacodynamics were better understood, this could lead to improvements upon the nanoparticle design. For example, if the SPNPs get transported to the brain via cellular hitchhiking, there may be more effective methods to leverage this. As of now, we know that the incorporation of iRGD, the tumor penetrating peptide, impacts the accumulation of SPNPs in a glioma model,[218] but that result does not reveal how the SPNPs are transported to the tumor. In addition, dose escalation studies could be utilized to identify the ideal dosage. Without this, it is likely that the maximum therapeutic effect will not be used. Therefore, rational design and thorough testing are needed to create SPNPs that can realize their full potential as therapeutics.

Bibliography

1. Berger, T. R., Wen, P. Y., Lang-Orsini, M. & Chukwueke, U. N. World Health Organization 2021 classification of central nervous system tumors and implications for therapy for adult-type gliomas: a review. *JAMA Oncol.* (2022).
2. Louis, D. N., Holland, E. C. & Cairncross, J. G. Glioma classification: a molecular reappraisal. *Am. J. Pathol.* **159**, 779–786 (2001).
3. Louis, D. N. *et al.* The 2021 WHO Classification of Tumors of the Central Nervous System: a summary. *Neuro. Oncol.* **23**, 1231–1251 (2021).
4. Whitfield, B. T. & Huse, J. T. Classification of adult-type diffuse gliomas: Impact of the World Health Organization 2021 update. *Brain Pathol.* **32**, e13062 (2022).
5. Park, Y. W. *et al.* The 2021 WHO Classification for Gliomas and Implications on Imaging Diagnosis: Part 1—Key Points of the Fifth Edition and Summary of Imaging Findings on Adult-Type Diffuse Gliomas. *J. Magn. Reson. Imaging* **58**, 677–689 (2023).
6. Internò, V. *et al.* Molecular Aberrations Stratify Grade 2 Astrocytomas Into Several Rare Entities: Prognostic and Therapeutic Implications. *Front. Oncol.* **12**, 866623 (2022).
7. Kessler, T., Ito, J., Wick, W. & Wick, A. Conventional and emerging treatments of astrocytomas and oligodendrogliomas. *J. Neurooncol.* **162**, 471–478 (2023).
8. Weller, J. *et al.* Limited efficacy of temozolomide alone for astrocytoma, IDH-mutant, CNS WHO grades 2 or 3. *J. Neurooncol.* **160**, 149–158 (2022).
9. Yang, K. *et al.* Glioma targeted therapy: insight into future of molecular approaches. *Mol. Cancer* **21**, 39 (2022).
10. Alshiekh Nasany, R. & de la Fuente, M. I. Therapies for IDH-Mutant Gliomas. *Curr. Neurol. Neurosci. Rep.* **23**, 225–233 (2023).
11. Deacu, M. *et al.* Aggressiveness of Grade 4 Gliomas of Adults. *Clin. Pract.* **12**, 701–713 (2022).
12. Melhem, J. M., Detsky, J., Lim-Fat, M. J. & Perry, J. R. Updates in IDH-Wildtype

Glioblastoma. *Neurother. J. Am. Soc. Exp. Neurother.* **19**, 1705–1723 (2022).

13. Stupp, R. *et al.* Radiotherapy plus concomitant and adjuvant temozolomide for glioblastoma. *N. Engl. J. Med.* **352**, 987–996 (2005).
14. Kalaydina, R.-V., Bajwa, K., Qorri, B., Decarlo, A. & Szewczuk, M. R. Recent advances in 'smart' delivery systems for extended drug release in cancer therapy. *Int. J. Nanomedicine* **13**, 4727–4745 (2018).
15. Abbott, N. J., Patabendige, A. A. K., Dolman, D. E. M., Yusof, S. R. & Begley, D. J. Structure and function of the blood-brain barrier. *Neurobiol. Dis.* **37**, 13–25 (2010).
16. Furtado, D. *et al.* Overcoming the Blood–Brain Barrier: The Role of Nanomaterials in Treating Neurological Diseases. *Adv. Mater.* **30**, (2018).
17. Arvanitis, C. D., Ferraro, G. B. & Jain, R. K. The blood–brain barrier and blood–tumour barrier in brain tumours and metastases. *Nat. Rev. Cancer* **20**, 26–41 (2020).
18. Belykh, E. *et al.* Blood-brain barrier, blood-brain tumor barrier, and fluorescence-guided neurosurgical oncology: delivering optical labels to brain tumors. *Front. Oncol.* **10**, 739 (2020).
19. Goldstein, M. J., Peters, M., Weber, B. L. & Davis, C. B. Optimizing the Therapeutic Window of Targeted Drugs in Oncology: Potency-Guided First-in-Human Studies. *Clin. Transl. Sci.* **14**, 536–543 (2021).
20. Pineda, E., Domenech, M., Hernández, A., Comas, S. & Balaña, C. Recurrent Glioblastoma: Ongoing Clinical Challenges and Future Prospects. *Onco. Targets. Ther.* **16**, 71–86 (2023).
21. Smita, P., Narayan, P. A., J, K. & Gaurav, P. Therapeutic drug monitoring for cytotoxic anticancer drugs: Principles and evidence-based practices. *Front. Oncol.* **12**, 1015200 (2022).
22. Stage, T. B., Bergmann, T. K. & Kroetz, D. L. Clinical Pharmacokinetics of Paclitaxel Monotherapy: An Updated Literature Review. *Clinical Pharmacokinetics* **57**, 7–19 (2018).
23. Gelderblom, H., Verweij, J., Nooter, K. & Sparreboom, A. Cremophor EL: The drawbacks and advantages of vehicle selection for drug formulation. *Eur. J. Cancer* **37**, 1590–1598 (2001).
24. Ioele, G. *et al.* Anticancer Drugs: Recent Strategies to Improve Stability Profile, Pharmacokinetic and Pharmacodynamic Properties. *Molecules* **27**, (2022).
25. Souza, C., Pellosi, D. S. & Tedesco, A. C. Prodrugs for targeted cancer therapy. *Expert Rev.*

Anticancer Ther. **19**, 483–502 (2019).

26. Smith, D. A., Beaumont, K., Maurer, T. S. & Di, L. Relevance of Half-Life in Drug Design. *J. Med. Chem.* **61**, 4273–4282 (2018).
27. AlQahtani, A. D., O'Connor, D., Domling, A. & Goda, S. K. Strategies for the production of long-acting therapeutics and efficient drug delivery for cancer treatment. *Biomed. Pharmacother.* **113**, 108750 (2019).
28. Hauert, S. & Bhatia, S. N. Mechanisms of cooperation in cancer nanomedicine: towards systems nanotechnology. *Trends Biotechnol.* **32**, 448–455 (2014).
29. Wilhelm, S. *et al.* Analysis of nanoparticle delivery to tumours. *Nat. Rev. Mater.* **1**, 16014 (2016).
30. Jain, A., Singh, S. K., Arya, S. K., Kundu, S. C. & Kapoor, S. Protein Nanoparticles: Promising Platforms for Drug Delivery Applications. *ACS Biomater. Sci. Eng.* **4**, 3939–3961 (2018).
31. Verma, D., Gulati, N., Kaul, S., Mukherjee, S. & Nagaich, U. Protein based nanostructures for drug delivery. *J. Pharm.* **2018**, (2018).
32. Habibi, N., Mauser, A., Ko, Y. & Lahann, J. Protein Nanoparticles: Uniting the Power of Proteins with Engineering Design Approaches. *Adv. Sci.* **9**, 2104012 (2022).
33. Leader, B., Baca, Q. J. & Golan, D. E. Protein therapeutics: A summary and pharmacological classification. *Nat. Rev. Drug Discov.* **7**, 21–39 (2008).
34. Mitchell, M. J. *et al.* Engineering precision nanoparticles for drug delivery. *Nat. Rev. Drug Discov.* **20**, 101–124 (2021).
35. Dietzen, D. J. *Amino acids, peptides, and proteins*. *Principles and Applications of Molecular Diagnostics* (Elsevier Inc., 2018). doi:10.1016/B978-0-12-816061-9.00013-8
36. Marengo-Rowe, A. J. Structure-function relations of human hemoglobins. *Proc. Baylor Univ. Med. Cent.* **19**, 239–245 (2006).
37. RCSB PDB: Homepage. Available at: https://www.rcsb.org/. (Accessed: 21st July 2021)
38. Tripathi, N. K. & Shrivastava, A. Recent Developments in Bioprocessing of Recombinant Proteins: Expression Hosts and Process Development. *Front. Bioeng. Biotechnol.* **7**, (2019).
39. Kratz, F. & Elsadek, B. Clinical impact of serum proteins on drug delivery. *J. Control. Release* **161**, 429–445 (2012).
40. Maslanka Figueroa, S., Fleischmann, D. & Goepferich, A. Biomedical nanoparticle design:

What we can learn from viruses. *J. Control. Release* **329**, 552–569 (2021).

41. Parodi, A. *et al.* Bio-inspired engineering of cell- and virus-like nanoparticles for drug delivery. *Biomaterials* **147**, 155–168 (2017).
42. Bulcha, J. T., Wang, Y., Ma, H., Tai, P. W. L. & Gao, G. Viral vector platforms within the gene therapy landscape. *Signal Transduct. Target. Ther.* **6**, (2021).
43. Chung, Y. H., Cai, H. & Steinmetz, N. F. Viral nanoparticles for drug delivery, imaging, immunotherapy, and theranostic applications. *Adv. Drug Deliv. Rev.* **156**, 214–235 (2020).
44. Kratz, F. Albumin as a drug carrier: Design of prodrugs, drug conjugates and nanoparticles. *J. Control. Release* **132**, 171–183 (2008).
45. Hawkins, M. J., Soon-Shiong, P. & Desai, N. Protein nanoparticles as drug carriers in clinical medicine. *Adv. Drug Deliv. Rev.* **60**, 876–885 (2008).
46. Chang, T. Z., Diambou, I., Kim, J. R., Wang, B. & Champion, J. A. Host- and pathogen-derived adjuvant coatings on protein nanoparticle vaccines. *Bioeng. Transl. Med.* **2**, 120–130 (2017).
47. Tang, C. H. Nanostructured soy proteins: Fabrication and applications as delivery systems for bioactives (a review). *Food Hydrocoll.* **91**, 92–116 (2019).
48. Cohen, Y. *et al.* The bioavailability of vitamin D3, a model hydrophobic nutraceutical, in casein micelles, as model protein nanoparticles: Human clinical trial results. *J. Funct. Foods* **30**, 321–325 (2017).
49. Jin, B. *et al.* Elucidation of stabilizing pickering emulsion with jackfruit filum pectin-soy protein nanoparticles obtained by photocatalysis. *J. Dispers. Sci. Technol.* **40**, 909–917 (2019).
50. Li, C. *et al.* Current multifunctional albumin-based nanoplatforms for cancer multi-mode therapy. *Asian J. Pharm. Sci.* **15**, 1–12 (2020).
51. Zhu, X. J. *et al.* A Novel Self-Assembled Mitochondria-Targeting Protein Nanoparticle Acting as Theranostic Platform for Cancer. *Small* **15**, 1–7 (2019).
52. Huang, P.-S., Boyken, S. E. & Baker, D. The coming of age of de novo protein design. *Nature* **537**, 320–327 (2016).
53. Sripriyalakshmi, S., Jose, P., Ravindran, A. & Anjali, C. H. Recent Trends in Drug Delivery System Using Protein Nanoparticles. *Cell Biochem. Biophys.* **70**, 17–26 (2014).
54. Lohcharoenkal, W., Wang, L., Chen, Y. C. & Rojanasakul, Y. Protein Nanoparticles as

Drug Delivery Carriers for Cancer Therapy. *Biomed Res. Int.* **2014**, 1–12 (2014).

55. Tarhini, M., Greige-Gerges, H. & Elaissari, A. Protein-based nanoparticles: From preparation to encapsulation of active molecules. *International Journal of Pharmaceutics* **522**, 172–197 (2017).
56. Stromer, B. S. *et al.* Multicolored Protein Nanoparticles: Synthesis, Characterization, and Cell Uptake. *Bioconjug. Chem.* **29**, 2576–2585 (2018).
57. Yu, X. *et al.* Activatable Protein Nanoparticles for Targeted Delivery of Therapeutic Peptides. *Adv. Mater.* **30**, 1–7 (2018).
58. Morozova, O. V. *et al.* Protein nanoparticles with ligand-binding and enzymatic activities. *Int. J. Nanomedicine* **13**, 6637–6646 (2018).
59. Swartz, A. R., Sun, Q. & Chen, W. Ligand-Induced Cross-Linking of Z-Elastin-like Polypeptide-Functionalized E2 Protein Nanoparticles for Enhanced Affinity Precipitation of Antibodies. *Biomacromolecules* **18**, 1654–1659 (2017).
60. Madan, B., Chaudhary, G., Cramer, S. M. & Chen, W. ELP-z and ELP-zz capturing scaffolds for the purification of immunoglobulins by affinity precipitation. *J. Biotechnol.* **163**, 10–16 (2013).
61. Langer, K. *et al.* Human serum albumin (HSA) nanoparticles: Reproducibility of preparation process and kinetics of enzymatic degradation. *Int. J. Pharm.* **347**, 109–117 (2008).
62. Davidov-Pardo, G., Joye, I. J. & Mcclements, D. J. *Food-Grade Protein-Based Nanoparticles and Microparticles for Bioactive Delivery: Fabrication, Characterization, and Utilization*. *Advances in Protein Chemistry and Structural Biology* **98**, (Elsevier Inc., 2015).
63. Teng, Z., Luo, Y. & Wang, Q. Nanoparticles synthesized from soy protein: Preparation, characterization, and application for nutraceutical encapsulation. *J. Agric. Food Chem.* **60**, 2712–2720 (2012).
64. De Frates, K. *et al.* Protein polymer-based nanoparticles: Fabrication and medical applications. *Int. J. Mol. Sci.* **19**, 1–20 (2018).
65. Joye, I. J. & McClements, D. J. Biopolymer-based nanoparticles and microparticles: Fabrication, characterization, and application. *Curr. Opin. Colloid Interface Sci.* **19**, 417–427 (2014).

66. Sengupta, S., Bhattacharyya, D. K., Goswami, R. & Bhowal, J. Emulsions stabilized by soy protein nanoparticles as potential functional non-dairy yogurts. *J. Sci. Food Agric.* **99**, 5808–5818 (2019).
67. Wouters, A. G. & Delcour, J. A. Cereal protein-based nanoparticles as agents stabilizing air–water and oil–water interfaces in food systems. *Curr. Opin. Food Sci.* **25**, 19–27 (2019).
68. Hong, S., Choi, D. W., Kim, H. N. & Park, C. G. Protein-Based Nanoparticles as Drug Delivery Systems. 1–29 (2020).
69. Johnson, R. & Jiskoot, W. Models for evaluation of relative immunogenic potential of protein particles in biopharmaceutical protein formulations. *J. Pharm. Sci.* **101**, 3586–3592 (2012).
70. Bee, J. S., Goletz, T. J. & Ragheb, J. A. The future of protein particle characterization and understanding its potential to diminish the immunogenicity of biopharmaceuticals: A shared perspective. *J. Pharm. Sci.* **101**, 3580–3585 (2012).
71. Carpenter, J. *et al.* Meeting report on protein particles and immunogenicity of therapeutic proteins: Filling in the gaps in risk evaluation and mitigation. *Biologicals* **38**, 602–611 (2010).
72. Nakashima, F. *et al.* Structural and functional insights into S-thiolation of human serum albumins. *Sci. Rep.* **8**, 1–12 (2018).
73. Weiss, B. R. B. *et al.* Hypersensitivity Reactions From Taxol. *J. Clin. Oncol.* **8**, 1263–1268 (1990).
74. Foote, M. A. Using nanotechnology to improve the characteristics of antineoplastic drugs: Improved characteristics of nab-paclitaxel compared with solvent-based paclitaxel. *Biotechnol. Annu. Rev.* **13**, 345–357 (2007).
75. Van Zuylen, L. *et al.* Pharmacokinetic modeling of paclitaxel encapsulation in Cremophor EL micelles. *Cancer Chemother. Pharmacol.* **47**, 309–318 (2001).
76. Desai, N. P., Tao, C., Louie, L. & Shoon-Shiong, P. Formulations of Pharmacological agents, methods for the preparation thereof and methods for the use thereof. (2012).
77. Lee, H. *et al.* Efficacy and safety of nanoparticle-albumin-bound paclitaxel compared with solvent-based taxanes for metastatic breast cancer: A meta-analysis. *Sci. Rep.* **10**, 1–9 (2020).
78. Adrianzen Herrera, D., Ashai, N., Perez-Soler, R. & Cheng, H. Nanoparticle albumin

bound-paclitaxel for treatment of advanced non-small cell lung cancer: an evaluation of the clinical evidence. *Expert Opin. Pharmacother.* **20**, 95–102 (2019).

79. Adkins, D. *et al.* Nanoparticle albumin-bound paclitaxel with cetuximab and carboplatin as first-line therapy for recurrent or metastatic head and neck cancer: A single-arm, multicenter, phase 2 trial. *Oral Oncol.* **115**, 105173 (2021).
80. Yoneshima, Y. *et al.* Phase 3 Trial Comparing Nanoparticle Albumin-Bound Paclitaxel With Docetaxel for Previously Treated Advanced NSCLC. *J. Thorac. Oncol.* (2021). doi:10.1016/j.jtho.2021.03.027
81. Yadav, K. S. & Kale, K. High Pressure Homogenizer in Pharmaceuticals: Understanding Its Critical Processing Parameters and Applications. *J. Pharm. Innov.* **582**, (2020).
82. Füredi, P., Kovács, K., Ludányi, K., Antal, I. & Klebovich, I. Development and characterization of voriconazole loaded nanoparticles for parenteral delivery. *Int. J. Pharm.* **510**, 159–163 (2016).
83. Seo, J. *et al.* Therapeutic advantage of inhaled tacrolimus-bound albumin nanoparticles in a bleomycin-induced pulmonary fibrosis mouse model. *Pulm. Pharmacol. Ther.* **36**, 53–61 (2016).
84. Yu, X. *et al.* An in vitro and in vivo study of gemcitabine-loaded albumin nanoparticles in a pancreatic cancer cell line. *Int. J. Nanomedicine* **10**, 6825–6834 (2015).
85. Kim, T. H. *et al.* Preparation and characterization of water-soluble albumin-bound curcumin nanoparticles with improved antitumor activity. *Int. J. Pharm.* **403**, 285–291 (2011).
86. Kim, B. *et al.* Albumin nanoparticles with synergistic antitumor efficacy against metastatic lung cancers. *Colloids Surfaces B Biointerfaces* **158**, 157–166 (2017).
87. Stein, N. C., Mulac, D., Fabian, J., Herrmann, F. C. & Langer, K. Nanoparticle albumin-bound mTHPC for photodynamic therapy: Preparation and comprehensive characterization of a promising drug delivery system. *Int. J. Pharm.* **582**, 119347 (2020).
88. Joshi, M., Nagarsenkar, M. & Prabhakar, B. Albumin nanocarriers for pulmonary drug delivery : An attractive approach. *J. Drug Deliv. Sci. Technol.* **56**, (2020).
89. Cloupeau, M. & Prunet-Foch, B. Electrostatic spraying of liquids in cone-jet mode. *J. Electrostat.* **22**, 135–159 (1989).
90. Peltonen, L., Valo, H., Kolakovic, R., Laaksonen, T. & Hirvonen, J. Electrospraying, spray drying and related techniques for production and formulation of drug nanoparticles. *Expert*

Opinion on Drug Delivery **7**, 705–719 (2010).

91. Collins, R. T., Jones, J. J., Harris, M. T. & Basaran, O. A. Electrohydrodynamic tip streaming and emission of charged drops from liquidcones. *Nat. Phys.* **4**, 149–154 (2008).
92. Gaskell, S. J. SPECIAL FEATURE : Electrospray : Principles and Practice. *Practice* **32**, 677–688 (1997).
93. Roh, K.-H., Martin, D. C. & Lahann, J. Biphasic Janus particles with nanoscale anisotropy. *Nat. Mater.* **4**, 759–763 (2005).
94. Gregory, J. V *et al.* Programmable Delivery of Synergistic Cancer Drug Combinations Using Bicompartmental Nanoparticles. *Adv. Healthc. Mater.* **9**, 1–11 (2020).
95. Misra, A. C. & Lahann, J. Progress of Multicompartmental Particles for Medical Applications. *Adv. Healthc. Mater.* **7**, 1–9 (2018).
96. Fernández-rodríguez, M. Á. *et al.* Colloids and Surfaces A : Physicochemical and Engineering Aspects Synthesis and interfacial activity of PMMA / PtBMA Janus and homogeneous nanoparticles at water / oil interfaces. *Colloids Surfaces A Physicochem. Eng. Asp.* **536**, 259–265 (2018).
97. Ross, A. M. *et al.* Persistence, distribution, and impact of distinctly segmented microparticles on cochlear health following *in vivo* infusion. *J. Biomed. Mater. Res. Part A* **104**, 1510–1522 (2016).
98. Rahmani, S. *et al.* Engineering of nanoparticle size via electrohydrodynamic jetting. *Bioeng. Transl. Med.* **1**, 82–93 (2016).
99. Rahmani, S. *et al.* Dual Release Carriers for Cochlear Delivery. *Adv. Healthc. Mater.* **5**, 94–100 (2016).
100. Rahmani, S. *et al.* Long-circulating Janus nanoparticles made by electrohydrodynamic co-jetting for systemic drug delivery applications. *J. Drug Target.* **23**, 750–758 (2015).
101. Misra, A. C., Luker, K. E., Durmaz, H., Luker, G. D. & Lahann, J. CXCR4-Targeted Nanocarriers for Triple Negative Breast Cancers. *Biomacromolecules* **16**, 2412–2417 (2015).
102. Sokolovskaya, E., Rahmani, S., Misra, A. C., Brase, S. & Lahann, J. Dual-stimuli-responsive microparticles. *ACS Appl. Mater. Interfaces* **7**, 9744–9751 (2015).
103. Rahmani, S. *et al.* Chemically orthogonal three-patch microparticles. *Angew. Chemie - Int. Ed.* **53**, 2332–2338 (2014).

104. Derived, H. B. E. T. Macromolecular Chemistry and Physics Preparation and Characterization of Highly Bio-Based Epoxy-Amine Thermosets Preparation and Characterization of Highly Bio-Based Epoxy-Amine Thermosets Derived from Lignocellulosics. 1554–1559 (2013). doi:10.1002/marc

105. Park, T. H. *et al.* Photoswitchable particles for on-demand degradation and triggered release. *Small* **9**, 3051–3057 (2013).

106. Misra, A. C., Bhaskar, S., Clay, N. & Lahann, J. Multicompartmental particles for combined imaging and siRNA delivery. *Adv. Mater.* **24**, 3850–3856 (2012).

107. Lahann, J. Recent Progress in Nano-biotechnology: Compartmentalized Micro- and Nanoparticles via Electrohydrodynamic Co-jetting. *Small* **7**, 1149–1156 (2011).

108. Quevedo, D. F. *et al.* Electrokinetic characterization of synthetic protein nanoparticles. *Beilstein J. Nanotechnol.* **11**, 1556–1567 (2020).

109. Brown, T. D., Habibi, N., Wu, D., Lahann, J. & Mitragotri, S. Effect of Nanoparticle Composition, Size, Shape, and Stiffness on Penetration across the Blood-Brain Barrier. *ACS Biomater. Sci. Eng.* **6**, 4916–4928 (2020).

110. Myerson, J. *et al.* Supramolecular Organization Predicts Protein Nanoparticle Delivery to Neutrophils for Acute Lung Inflammation Diagnosis and Treatment. *bioRxiv* 1–44 (2020). doi:10.1101/2020.04.15.037564

111. Gregory, J. V. *et al.* Systemic brain tumor delivery of synthetic protein nanoparticles for glioblastoma therapy. *Nat. Commun.* **11**, 1–15 (2020).

112. Quevedo, D. F. *et al.* Multifunctional Synthetic Protein Nanoparticles via Reactive Electrojetting. *Macromol. Rapid Commun.* **41**, (2020).

113. Habibi, N. *et al.* Engineered Ovalbumin Nanoparticles for Cancer Immunotherapy. *Adv. Ther.* **3**, 2000100 (2020).

114. Habibi, N., Mauser, A., Raymond, J. E. & Lahann, J. Systematic studies into uniform synthetic protein nanoparticles. *Beilstein J. Nanotechnol.* **13**, 274–283 (2022).

115. Jordahl, J. H., Ramcharan, S., Gregory, J. V. & Lahann, J. Needleless Electrohydrodynamic Cojetting of Bicompartmental Particles and Fibers from an Extended Fluid Interface. *Macromol. Rapid Commun.* **38**, 1–7 (2017).

116. Hong, S. *et al.* Protein-Based Nanoparticles as Drug Delivery Systems. *Pharmaceutics* **12**, (2020).

117. Shi, A., Feng, X., Wang, Q. & Adhikari, B. Pickering and high internal phase Pickering emulsions stabilized by protein-based particles: A review of synthesis, application and prospective. *Food Hydrocoll.* **109**, 106117 (2020).
118. Yang, Y. *et al.* An overview of pickering emulsions: Solid-particle materials, classification, morphology, and applications. *Front. Pharmacol.* **8**, 1–20 (2017).
119. Zhang, T. *et al.* Trends in Food Science & Technology Protein nanoparticles for Pickering emulsions : A comprehensive review on their shapes , preparation methods , and modification methods. *Trends Food Sci. Technol.* **113**, 26–41 (2021).
120. Elzoghby, A. O., Samy, W. M. & Elgindy, N. A. Albumin-based nanoparticles as potential controlled release drug delivery systems. *J. Control. Release* **157**, 168–182 (2012).
121. Elzoghby, A. O., Samy, W. M. & Elgindy, N. A. Protein-based nanocarriers as promising drug and gene delivery systems. *J. Control. Release* **161**, 38–49 (2012).
122. Herrera Estrada, L. P. & Champion, J. A. Protein nanoparticles for therapeutic protein delivery. *Biomater. Sci.* **3**, 787–799 (2015).
123. Estrada, L. H., Chu, S. & Champion, J. A. Protein nanoparticles for intracellular delivery of therapeutic enzymes. *J. Pharm. Sci.* **103**, 1863–1871 (2014).
124. Broadhead, J., Edmond Rouan, S. K. & Rhodes, C. T. The spray drying of pharmaceuticals. *Drug Dev. Ind. Pharm.* **18**, 1169–1206 (1992).
125. Lee, S. H., Heng, D., Ng, W. K., Chan, H. K. & Tan, R. B. H. Nano spray drying: A novel method for preparing protein nanoparticles for protein therapy. *Int. J. Pharm.* **403**, 192–200 (2011).
126. Zlotnick, A. Theoretical aspects of virus capsid assembly. *J. Mol. Recognit.* **18**, 479–490 (2005).
127. Hagan, M. F. & Elrad, O. M. Understanding the Concentration Dependence of Viral Capsid Assembly Kinetics-the Origin of the Lag Time and Identifying the Critical Nucleus Size. *Biophys. J.* **98**, 1065–1074 (2010).
128. Crisante, F. *et al.* Antibiotic delivery polyurethanes containing albumin and polyallylamine nanoparticles. *Eur. J. Pharm. Sci.* **36**, 555–564 (2009).
129. Yang, L. *et al.* Preparation , characterization and biodistribution of the lactone form of 10-hydroxycamptothecin (HCPT) -loaded bovine serum albumin (BSA) nanoparticles. *Pharm. Nanotechnol.* **340**, 163–172 (2007).

130. Füredi, P., Kovács, K., Ludányi, K., Antal, I. & Klebovich, I. Development and characterization of voriconazole loaded nanoparticles for parenteral delivery. *Int. J. Pharm.* **510**, 159–163 (2016).

131. Weber, C., Coester, C., Kreuter, J. & Langer, K. Desolvation process and surface characterisation of protein nanoparticles. *Int. J. Pharm.* **194**, 91–102 (2000).

132. Langer, K. *et al.* Optimization of the preparation process for human serum albumin (HSA) nanoparticles. *Int. J. Pharm.* **257**, 169–180 (2003).

133. Von Storp, B., Engel, A., Boeker, A., Ploeger, M. & Langer, K. Albumin nanoparticles with predictable size by desolvation procedure. *J. Microencapsul.* **29**, 138–146 (2012).

134. Bale, J. B. *et al.* Accurate design of megadalton-scale two-component icosahedral protein complexes. *Science (80-.).* **353**, 389–394 (2016).

135. Lu, P. *et al.* Accurate computational design of multipass transmembrane proteins. *Science (80-.).* **359**, 1042–1046 (2018).

136. Divine, R. *et al.* Designed proteins assemble antibodies into modular nanocages. *Science (80-.).* **372**, eabd9994 (2021).

137. King, N. P. *et al.* Accurate design of co-assembling multi-component protein nanomaterials. *Nature* **510**, 103–108 (2014).

138. Butterfield, G. L. *et al.* Evolution of a designed protein assembly encapsulating its own RNA genome. *Nature* **552**, 415–420 (2017).

139. Gradišar, H. *et al.* Design of a single-chain polypeptide tetrahedron assembled from coiled-coil segments. *Nat. Chem. Biol.* **9**, 362–366 (2013).

140. Matsuura, K., Watanabe, K., Matsuzaki, T., Sakurai, K. & Kimizuka, N. Self-Assembled Synthetic Viral Capsids from a 24-mer Viral Peptide Fragment. *Angew. Chemie Int. Ed.* **49**, 9662–9665 (2010).

141. De Santis, E. *et al.* Antimicrobial peptide capsids of de novo design. *Nat. Commun.* **8**, 2263 (2017).

142. Noble, J. E. *et al.* A De Novo Virus-Like Topology for Synthetic Virions. *J. Am. Chem. Soc.* **138**, 12202–12210 (2016).

143. Patra, J. K. *et al.* Nano based drug delivery systems: recent developments and future prospects. *J. Nanobiotechnology* **16**, 71 (2018).

144. Peer, D. *et al.* Nanocarriers as an emerging platform for cancer therapy. *Nature*

Nanotechnology **2**, 751–760 (2007).

145. Ragelle, H., Danhier, F., Préat, V., Langer, R. & Anderson, D. G. Nanoparticle-based drug delivery systems: a commercial and regulatory outlook as the field matures. *Expert Opin. Drug Deliv.* **14**, 851–864 (2017).
146. Wang, A. Z., Langer, R. & Farokhzad, O. C. Nanoparticle delivery of cancer drugs. *Annu. Rev. Med.* **63**, 185–198 (2012).
147. Hrkach, J. & Langer, R. From micro to nano: evolution and impact of drug delivery in treating disease. *Drug Deliv. Transl. Res.* **10**, 567–570 (2020).
148. Moghimi, S. M., Hunter, A. C. & Murray, J. C. Long-Circulating and Target-Specific Nanoparticles: Theory to Practice. *Pharmacol. Rev.* **53**, 283–318 (2001).
149. Kamaly, N., Yameen, B., Wu, J. & Farokhzad, O. C. Degradable controlled-release polymers and polymeric nanoparticles: Mechanisms of controlling drug release. *Chemical Reviews* **116**, 2602–2663 (2016).
150. Anselmo, A. C. & Mitragotri, S. Nanoparticles in the clinic: An update. *Bioeng. Transl. Med.* **4**, 1–16 (2019).
151. Habibi, N., Quevedo, D. F., Gregory, J. V. & Lahann, J. Emerging methods in therapeutics using multifunctional nanoparticles. *Wiley Interdisciplinary Reviews: Nanomedicine and Nanobiotechnology* **12**, (2020).
152. Barua, S. & Mitragotri, S. Challenges associated with penetration of nanoparticles across cell and tissue barriers : A review of current status and future prospects. *Nano Today* **9**, 223–243 (2014).
153. Gomme, P. T. & McCann, K. B. Transferrin: Structure, function and potential therapeutic actions. *Drug Discov. Today* **10**, 267–273 (2005).
154. Ponka, P. & Lok, C. N. The transferrin receptor: Role in health and disease. *Int. J. Biochem. Cell Biol.* **31**, 1111–1137 (1999).
155. Eckenroth, B. E., Steere, A. N., Chasteen, N. D., Everse, S. J. & Mason, A. B. How the binding of human transferrin primes the transferrin receptor potentiating iron release at endosomal pH. *Proc. Natl. Acad. Sci. U. S. A.* **108**, 13089–13094 (2011).
156. Ulbrich, K., Hekmatara, T., Herbert, E. & Kreuter, J. Transferrin- and transferrin-receptor-antibody-modified nanoparticles enable drug delivery across the blood-brain barrier (BBB). *Eur. J. Pharm. Biopharm.* **71**, 251–256 (2009).

157. Chen, X. *et al.* Transferrin gated mesoporous silica nanoparticles for redox-responsive and targeted drug delivery. *Colloids Surfaces B Biointerfaces* **152**, 77–84 (2017).

158. Kawamoto, M., Horibe, T., Kohno, M. & Kawakami, K. A novel transferrin receptor-targeted hybrid peptide disintegrates cancer cell membrane to induce rapid killing of cancer cells. *BMC Cancer* **11**, (2011).

159. Calzolari, A. *et al.* Transferrin receptor 2 is frequently and highly expressed in glioblastomas. *Transl. Oncol.* **3**, 123–134 (2010).

160. Wang, K. *et al.* Self-assembled IR780-loaded transferrin nanoparticles as an imaging, targeting and PDT/PTT agent for cancer therapy. *Sci. Rep.* **6**, 1–11 (2016).

161. Cui, Y., Xu, Q., Chow, P. K.-H., Wang, D. & Wang, C.-H. Transferrin-conjugated magnetic silica PLGA nanoparticles loaded with doxorubicin and paclitaxel for brain glioma treatment. *Biomaterials* **34**, 8511–8520 (2013).

162. Koneru, T. *et al.* Transferrin: biology and use in receptor-targeted nanotherapy of gliomas. *ACS omega* **6**, 8727–8733 (2021).

163. Ramalho, M. J., Loureiro, J. A., Coelho, M. A. N. & Pereira, M. C. Transferrin receptor-targeted nanocarriers: overcoming barriers to treat glioblastoma. *Pharmaceutics* **14**, 279 (2022).

164. Luo, M. *et al.* Systematic evaluation of transferrin-modified porous silicon nanoparticles for targeted delivery of doxorubicin to glioblastoma. *ACS Appl. Mater. Interfaces* **11**, 33637–33649 (2019).

165. Liu, G. *et al.* Transferrin-modified Doxorubicin-loaded biodegradable nanoparticles exhibit enhanced efficacy in treating brain glioma-bearing rats. *Cancer Biother. Radiopharm.* **28**, 691–696 (2013).

166. Xiao, W. *et al.* The protein corona hampers the transcytosis of transferrin-modified nanoparticles through blood–brain barrier and attenuates their targeting ability to brain tumor. *Biomaterials* **274**, 120888 (2021).

167. Sepand, M. R. *et al.* Impact of plasma concentration of transferrin on targeting capacity of nanoparticles. *Nanoscale* **12**, 4935–4944 (2020).

168. Salvati, A. *et al.* Transferrin-functionalized nanoparticles lose their targeting capabilities when a biomolecule corona adsorbs on the surface. *Nat. Nanotechnol.* **8**, 137–143 (2013).

169. Spada, A., Emami, J., Tuszynski, J. A. & Lavasanifar, A. The Uniqueness of Albumin as a

Carrier in Nanodrug Delivery. *Mol. Pharm.* **18**, 1862–1894 (2021).

170. Elzoghby, A. O., Samy, W. M. & Elgindy, N. A. Albumin-based nanoparticles as potential controlled release drug delivery systems. *J. Control. Release* **157**, 168–182 (2012).
171. Schnitzer, J. E. gp60 is an albumin-binding glycoprotein expressed by continuous endothelium involved in albumin transcytosis. *Am. J. Physiol. - Hear. Circ. Physiol.* **262**, (1992).
172. Malin, B. *et al.* An engineered human albumin enhances half-life and transmucosal delivery when fused to protein-based biologics. *Sci. Transl. Med.* **12**, eabb0580 (2020).
173. Hoogenboezem, E. N. & Duvall, C. L. Harnessing albumin as a carrier for cancer therapies ☆. *Adv. Drug Deliv. Rev.* **130**, 73–89 (2018).
174. Alghamri, M. S. *et al.* Systemic Delivery of an Adjuvant CXCR4–CXCL12 Signaling Inhibitor Encapsulated in Synthetic Protein Nanoparticles for Glioma Immunotherapy. *ACS Nano* **16**, 8729–8750 (2022).
175. Kamali, M. *et al.* Preparation of imatinib base loaded human serum albumin for application in the treatment of glioblastoma. *RSC Adv.* **5**, 62214–62219 (2015).
176. Lin, T. *et al.* Blood-Brain-Barrier-Penetrating Albumin Nanoparticles for Biomimetic Drug Delivery via Albumin-Binding Protein Pathways for Antiglioma Therapy. *ACS Nano* **10**, 9999–10012 (2016).
177. Yang, Z. *et al.* Co-delivery of ibrutinib and hydroxychloroquine by albumin nanoparticles for enhanced chemotherapy of glioma. *Int. J. Pharm.* **630**, 122436 (2023).
178. Lu, W., Wan, J., Zhang, Q., She, Z. & Jiang, X. Aclarubicin-loaded cationic albumin-conjugated pegylated nanoparticle for glioma chemotherapy in rats. *Int. J. cancer* **120**, 420–431 (2007).
179. Housman, G. *et al.* Drug resistance in cancer: An overview. *Cancers (Basel).* **6**, 1769–1792 (2014).
180. Leary, M., Heerboth, S., Lapinska, K. & Sarkar, S. Sensitization of drug resistant cancer cells: A matter of combination therapy. *Cancers (Basel).* **10**, 1–18 (2018).
181. Rawal, S. & Patel, M. M. Threatening cancer with nanoparticle aided combination oncotherapy. *Journal of Controlled Release* (2019). doi:10.1016/j.jconrel.2019.03.015
182. Dai, W. *et al.* Combination antitumor therapy with targeted dual-nanomedicines. *Adv. Drug Deliv. Rev.* **115**, 23–45 (2017).

183. Zanders, E. D., Svensson, F. & Bailey, D. S. Therapy for glioblastoma: is it working? *Drug Discov. Today* **24**, 1193–1201 (2019).

184. Ganipineni, L. P., Danhier, F. & Préat, V. Drug delivery challenges and future of chemotherapeutic nanomedicine for glioblastoma treatment. *J. Control. release Off. J. Control. Release Soc.* **281**, 42–57 (2018).

185. Awosika, A. O., Farrar, M. C. & Jacobs, T. F. Paclitaxel. in (2023).

186. Band Horwitz, S. Mechanism of action of taxol. *Trends Pharmacol. Sci.* **13**, 134–136 (1992).

187. Ma, P. & Mumper, R. J. Paclitaxel Nano-Delivery Systems: A Comprehensive Review. *J. Nanomed. Nanotechnol.* **4**, 1000164 (2013).

188. Yardley, D. A. Nab-Paclitaxel mechanisms of action and delivery. *J. Control. Release* **170**, 365–372 (2013).

189. Sofias, A. M., Dunne, M., Storm, G. & Allen, C. The battle of "nano" paclitaxel. *Adv. Drug Deliv. Rev.* **122**, 20–30 (2017).

190. Zhang, D. Y. *et al.* Ultrasound-mediated Delivery of Paclitaxel for Glioma: A Comparative Study of Distribution, Toxicity, and Efficacy of Albumin-bound Versus Cremophor Formulations. *Clin. cancer Res. an Off. J. Am. Assoc. Cancer Res.* **26**, 477–486 (2020).

191. Pawar, A., Thakkar, S. & Misra, M. A bird's eye view of nanoparticles prepared by electrospraying: advancements in drug delivery field. *J. Control. Release* **286**, 179–200 (2018).

192. Calinescu, A.-A. *et al.* Transposon mediated integration of plasmid DNA into the subventricular zone of neonatal mice to generate novel models of glioblastoma. *J. Vis. Exp.* (2015). doi:10.3791/52443

193. Calinescu, A.-A. *et al.* Survival and Proliferation of Neural Progenitor–Derived Glioblastomas Under Hypoxic Stress is Controlled by a CXCL12/CXCR4 Autocrine-Positive Feedback Mechanism. *Clin. Cancer Res.* **23**, (2017).

194. Comba, A. *et al.* Fyn tyrosine kinase, a downstream target of receptor tyrosine kinases, modulates antiglioma immune responses. *Neuro. Oncol.* **22**, 806–818 (2020).

195. Koschmann, C. *et al.* ATRX loss promotes tumor growth and impairs nonhomologous end joining DNA repair in glioma. *Sci. Transl. Med.* **8**, 328ra28 (2016).

196. Núñez, F. J. *et al.* IDH1-R132H acts as a tumor suppressor in glioma via epigenetic up-

regulation of the DNA damage response. *Sci. Transl. Med.* **11**, eaaq1427 (2019).

197. Mauser, A. *et al.* Enzyme-Based Synthetic Protein Nanoparticles as Colloidal Antioxidants. *Adv. Ther.* **n/a**, 2300007 (2023).

198. Miles, A. J., Ramalli, S. G. & Wallace, B. A. DichroWeb, a website for calculating protein secondary structure from circular dichroism spectroscopic data. *Protein Sci.* **31**, 37–46 (2022).

199. Whitmore, L. & Wallace, B. A. DICHROWEB, an online server for protein secondary structure analyses from circular dichroism spectroscopic data. *Nucleic Acids Res.* **32**, W668-73 (2004).

200. Whitmore, L. & Wallace, B. A. Protein secondary structure analyses from circular dichroism spectroscopy: methods and reference databases. *Biopolymers* **89**, 392–400 (2008).

201. Boda, S. K., Li, X. & Xie, J. Electrospraying an enabling technology for pharmaceutical and biomedical applications: A review. *J. Aerosol Sci.* **125**, 164–181 (2018).

202. Richheimer, S. L., Tinnermeier, D. M. & Timmons, D. W. High-performance liquid chromatographic assay of taxol. *Anal. Chem.* **64**, 2323–2326 (1992).

203. Abbassi, R. H. *et al.* Lower Tubulin Expression in Glioblastoma Stem Cells Attenuates Efficacy of Microtubule-Targeting Agents. *ACS Pharmacol. Transl. Sci.* **2**, 402–413 (2019).

204. Masoumi, S. *et al.* Understanding cytoskeleton regulators in glioblastoma multiforme for therapy design. *Drug Des. Devel. Ther.* **10**, 2881–2897 (2016).

205. Risinger, A. L., Giles, F. J. & Mooberry, S. L. Microtubule dynamics as a target in oncology. *Cancer Treat. Rev.* **35**, 255–261 (2009).

206. Lim, P. T., Goh, B. H. & Lee, W.-L. 3 - Taxol: Mechanisms of action against cancer, an update with current research. in (eds. Swamy, M. K., Pullaiah, T. & Chen, Z.-S. B. T.-P.) 47–71 (Academic Press, 2022). doi:https://doi.org/10.1016/B978-0-323-90951-8.00007-2

207. Serpico, A. F., Visconti, R. & Grieco, D. Exploiting immune-dependent effects of microtubule-targeting agents to improve efficacy and tolerability of cancer treatment. *Cell Death Dis.* **11**, 361 (2020).

208. Škubník, J., Pavlíčková, V., Ruml, T. & Rimpelová, S. Current Perspectives on Taxanes: Focus on Their Bioactivity, Delivery and Combination Therapy. *Plants (Basel, Switzerland)* **10**, (2021).

209. Kampan, N. C., Madondo, M. T., McNally, O. M., Quinn, M. & Plebanski, M. Paclitaxel and Its Evolving Role in the Management of Ovarian Cancer. *Biomed Res. Int.* **2015**, 413076 (2015).

210. Wang, T. H., Wang, H. S. & Soong, Y. K. Paclitaxel-induced cell death: where the cell cycle and apoptosis come together. *Cancer* **88**, 2619–2628 (2000).

211. Li, R. *et al.* Novel Paclitaxel-Loaded Nanoparticles Based on Human H Chain Ferritin for Tumor-Targeted Delivery. *ACS Biomater. Sci. Eng.* **5**, 6645–6654 (2019).

212. Goenka, A. *et al.* The Many Facets of Therapy Resistance and Tumor Recurrence in Glioblastoma. *Cells* **10**, (2021).

213. Kalepu, S. & Nekkanti, V. Improved delivery of poorly soluble compounds using nanoparticle technology: a review. *Drug Deliv. Transl. Res.* **6**, 319–332 (2016).

214. Piperi, C., Papavassiliou, K. A. & Papavassiliou, A. G. Pivotal Role of STAT3 in Shaping Glioblastoma Immune Microenvironment. *Cells* **8**, (2019).

215. Fu, W., Hou, X., Dong, L. & Hou, W. Roles of STAT3 in the pathogenesis and treatment of glioblastoma. *Front. cell Dev. Biol.* **11**, 1098482 (2023).

216. Gu, Y., Mohammad, I. S. & Liu, Z. Overview of the STAT-3 signaling pathway in cancer and the development of specific inhibitors. *Oncol. Lett.* **19**, 2585–2594 (2020).

217. Zou, S. *et al.* Targeting STAT3 in Cancer Immunotherapy. *Mol. Cancer* **19**, 145 (2020).

218. Gregory, J. V *et al.* Systemic brain tumor delivery of synthetic protein nanoparticles for glioblastoma therapy. *Nat. Commun.* **11**, 5687 (2020).

219. Alqahtani, F. Y., Aleanizy, F. S., El Tahir, E., Alkahtani, H. M. & AlQuadeib, B. T. Paclitaxel. in *Profiles of Drug Substances, Excipients and Related Methodology* **44**, 205–238 (Academic Press Inc., 2019).

220. Cho, S. K., Dang, C., Wang, X., Ragan, R. & Kwon, Y. J. Mixing-sequence-dependent nucleic acid complexation and gene transfer efficiency by polyethylenimine. *Biomater. Sci.* **3**, 1124–1133 (2015).

221. Krieg, B. *et al.* New Techniques to Assess In Vitro Release of siRNA from Nanoscale Polyplexes. *Pharm. Res.* **32**, 1957–1974 (2015).

222. Fliervoet, L. A. L. *et al.* Local release of siRNA using polyplex-loaded thermosensitive hydrogels. *Nanoscale* **12**, 10347–10360 (2020).

223. Zou, L. *et al.* Targeted delivery of nano-PTX to the brain tumor-associated macrophages.

Oncotarget **8**, 6564–6578 (2017).

224. Lim, J. *et al.* Harnessing type I interferon-mediated immunity to target malignant brain tumors. *Front. Immunol.* **14**, 1203929 (2023).

225. Blomberg, E., Silginer, M., Roth, P. & Weller, M. Differential roles of type I interferon signaling in tumor versus host cells in experimental glioma models. *Transl. Oncol.* **28**, 101607 (2023).

226. Bready, D. & Placantonakis, D. G. Molecular Pathogenesis of Low-Grade Glioma. *Neurosurg. Clin. NA* **30**, 17–25 (2019).

227. Duffau, H. Repeated Awake Surgical Resection(s) for Recurrent Diffuse Low-Grade Gliomas: Why, When, and How to Reoperate? *Front. Oncol.* **12**, 947933 (2022).

228. Ed, T. A. G., Vidence, H. E. & Reatment, B. T. Evidence-Based Treatment for Low-Grade Glioma. *Semin. Oncol. Nurs.* **34**, 465–471 (2018).

229. Gilbert, M. R. *et al.* Autophagy and oxidative stress in gliomas with IDH1 mutations. *Acta Neuropathol.* **127**, 221–233 (2014).

230. Núñez, F. J. *et al.* IDH1-R132H acts as a tumor suppressor in glioma via epigenetic up-regulation of the DNA damage response. *Sci. Transl. Med.* **11**, (2019).

231. Buckner, J. C. *et al.* Radiation plus Procarbazine, CCNU, and Vincristine in Low-Grade Glioma. *N. Engl. J. Med.* **374**, 1344–1355 (2016).

232. Keogh, R. J. *et al.* One year of procarbazine lomustine and vincristine is poorly tolerated in low grade glioma: a real world experience in a national neuro-oncology centre. *BMC Cancer* **21**, 140 (2021).

233. Rabinowitz, J. D. & White, E. Autophagy and metabolism. *Science* **330**, 1344–1348 (2010).

234. Matthew, R., Karantza-Wadsworth, V. & White, E. Role of Autophagy in Cancer. *Nat. Rev. Cancer* **7**, 961–967 (2007).

235. Chaachouay, H. *et al.* Autophagy contributes to resistance of tumor cells to ionizing radiation. *Radiother. Oncol. J. Eur. Soc. Ther. Radiol. Oncol.* **99**, 287–292 (2011).

236. Jones, L. E. *et al.* Patient-derived cells from recurrent tumors that model the evolution of IDH-mutant glioma. *Neuro-oncology Adv.* **2**, vdaa088 (2020).

237. Curtin, J. F. *et al.* HMGB1 mediates endogenous TLR2 activation and brain tumor regression. *PLoS Med* **6**, e10 (2009).

238. Gewirtz, D. A. Cytoprotective and nonprotective autophagy in cancer therapy. *Autophagy*

9, 1263–1265 (2013).

239. White, E. Deconvoluting the context-dependent role for autophagy in cancer. *Nat. Rev. Cancer* **12**, 401–410 (2012).
240. Levy, J. M. M., Towers, C. G. & Thorburn, A. Targeting autophagy in cancer. *Nat. Rev. Cancer* **17**, 528–542 (2017).
241. Choi, K. S. Autophagy and cancer. *Exp. Mol. Med.* **44**, 109–120 (2012).
242. Nunez, F. *et al.* RDNA-03. AUTOPHAGY AS A NOVEL THERAPEUTIC TARGET IN MUTANT IDH1 GLIOMAS. *Neuro-Oncology* **21**, vi207 (2019).
243. Ali Zaidi, S. S. *et al.* Engineering siRNA therapeutics: challenges and strategies. *J. Nanobiotechnology* **21**, 381 (2023).
244. Tatiparti, K., Sau, S., Kashaw, S. K. & Iyer, A. K. siRNA Delivery Strategies: A Comprehensive Review of Recent Developments. *Nanomaterials* **7**, (2017).
245. Gao, H., Cheng, R. & A. Santos, H. Nanoparticle-mediated siRNA delivery systems for cancer therapy. *VIEW* **2**, 20200111 (2021).
246. Swanson, W. B. *et al.* A library of Rhodamine6G-based pH-sensitive fluorescent probes with versatile in vivo and in vitro applications. *RSC Chem. Biol.* **3**, 748–764 (2022).
247. Ramirez, Y. P., Weatherbee, J. L., Wheelhouse, R. T. & Ross, A. H. Glioblastoma Multiforme Therapy and Mechanisms of Resistance. *Pharmaceuticals* **6**, 1475–1506 (2013).
248. Himes, B. T. *et al.* Immunosuppression in Glioblastoma: Current Understanding and Therapeutic Implications . *Frontiers in Oncology* **11**, (2021).
249. Parrish, K. E., Sarkaria, J. N. & Elmquist, W. F. Improving drug delivery to primary and metastatic brain tumors: Strategies to overcome the blood–brain barrier. *Clin. Pharmacol. Ther.* **97**, 336–346 (2015).
250. Ma, Q. *et al.* Impaired B-lymphopoiesis, myelopoiesis, and derailed cerebellar neuron migration in CXCR4- and SDF-1-deficient mice. *Proc. Natl. Acad. Sci.* **95**, 9448–9453 (1998).
251. Teicher, B. A. & Fricker, S. P. CXCL12 (SDF-1)/CXCR4 Pathway in Cancer. *Clin. Cancer Res.* **16**, 2927–2931 (2010).
252. Zou, Y.-R., Kottmann, A. H., Kuroda, M., Taniuchi, I. & Littman, D. R. Function of the chemokine receptor CXCR4 in haematopoiesis and in cerebellar development. *Nature* **393**,

595–599 (1998).

253. Lombardi, L. *et al.* Chemokine receptor CXCR4: Role in gastrointestinal cancer. *Crit. Rev. Oncol. Hematol.* **88**, 696–705 (2013).

254. Rubin, J. B. *et al.* A small-molecule antagonist of CXCR4 inhibits intracranial growth of primary brain tumors. *Proc. Natl. Acad. Sci.* **100**, 13513–13518 (2003).

255. Kioi, M. *et al.* Inhibition of vasculogenesis, but not angiogenesis, prevents the recurrence of glioblastoma after irradiation in mice. *J. Clin. Invest.* **120**, 694–705 (2010).

256. Goffart, N. *et al.* Adult mouse subventricular zones stimulate glioblastoma stem cells specific invasion through CXCL12/CXCR4 signaling. *Neuro. Oncol.* **17**, 81–94 (2015).

257. Eckert, F. *et al.* Potential role of CXCR4 targeting in the context of radiotherapy and immunotherapy of cancer. *Front. Immunol.* **9**, 3018 (2018).

258. Tabouret, E. *et al.* Recurrence of glioblastoma after radio-chemotherapy is associated with an angiogenic switch to the CXCL12-CXCR4 pathway. *Oncotarget; Vol 6, No 13* (2015).

259. Mullard, A. 2021 FDA approvals. *Nature reviews. Drug discovery* **21**, 83–88 (2022).

260. Desnick, R. J. & Schuchman, E. H. Enzyme replacement therapy for lysosomal diseases: lessons from 20 years of experience and remaining challenges. *Annu. Rev. Genomics Hum. Genet.* **13**, 307–335 (2012).

261. de la Fuente, M. *et al.* Enzyme Therapy: Current Challenges and Future Perspectives. *Int. J. Mol. Sci.* **22**, (2021).

262. Stepankova, V. *et al.* Strategies for stabilization of enzymes in organic solvents. *ACS Catalysis* **3**, 2823–2836 (2013).

263. Sheldon, R. A. & van Pelt, S. Enzyme immobilisation in biocatalysis: why, what and how. *Chem. Soc. Rev.* **42**, 6223–6235 (2013).

264. Torchilin, V. Intracellular delivery of protein and peptide therapeutics. *Drug Discovery Today: Technologies* **5**, e95–e103 (2008).

265. Torchilin, V. P. *Immobilized Enzymes in Medicine*. (Springer Berlin Heidelberg, 1991). doi:10.1007/978-3-642-75821-8

266. Chapman, R. & Stenzel, M. H. All Wrapped up: Stabilization of Enzymes within Single Enzyme Nanoparticles. *J. Am. Chem. Soc.* **141**, 2754–2769 (2019).

267. Gu, Z., Biswas, A., Zhao, M. & Tang, Y. Tailoring nanocarriers for intracellular protein delivery. *Chemical Society Reviews* **40**, 3638–3655 (2011).

268. Yamaguchi, H., Kiyota, Y. & Miyazaki, M. Techniques for preparation of cross-linked enzyme aggregates and their applications in bioconversions. *Catalysts* **8**, 174 (2018).

269. Elsadek, B. & Kratz, F. Impact of albumin on drug delivery - New applications on the horizon. *J. Control. Release* **157**, 4–28 (2012).

270. Sleep, D. Albumin and its application in drug delivery. *Expert Opin. Drug Deliv.* **12**, 793–812 (2015).

271. Bhushan, B., Khanadeev, V., Khlebtsov, B., Khlebtsov, N. & Gopinath, P. Impact of albumin based approaches in nanomedicine: Imaging, targeting and drug delivery. *Adv. Colloid Interface Sci.* **246**, 13–39 (2017).

272. Quevedo, D. F. *et al.* Multifunctional Synthetic Protein Nanoparticles. *TBA* (2020).

273. Lobley, A., Whitmore, L. & Wallace, B. A. DICHROWEB: an interactive website for the analysis of protein secondary structure from circular dichroism spectra. *Bioinformatics* **18**, 211–212 (2002).

274. Compton, L. A. & Johnson, W. C. J. Analysis of protein circular dichroism spectra for secondary structure using a simple matrix multiplication. *Anal. Biochem.* **155**, 155–167 (1986).

275. Manavalan, P. & Johnson, W. C. J. Variable selection method improves the prediction of protein secondary structure from circular dichroism spectra. *Anal. Biochem.* **167**, 76–85 (1987).

276. Sreerama, N., Venyaminov, S. Y. & Woody, R. W. Estimation of protein secondary structure from circular dichroism spectra: inclusion of denatured proteins with native proteins in the analysis. *Anal. Biochem.* **287**, 243–251 (2000).

277. Sreerama, N. & Woody, R. W. Estimation of protein secondary structure from circular dichroism spectra: comparison of CONTIN, SELCON, and CDSSTR methods with an expanded reference set. *Anal. Biochem.* **287**, 252–260 (2000).

278. Quevedo, D. F. *et al.* Multifunctional Synthetic Protein Nanoparticles via Reactive Electrojetting. *Macromol. Rapid Commun.* **41**, 1–7 (2020).

279. Quevedo, D. F. *et al.* Multifunctional Synthetic Protein Nanoparticles via Reactive Electrojetting. *Macromol. Rapid Commun.* **2000425**, 1–7 (2020).

280. Gregory, J. V. *et al.* Systemic brain tumor delivery of synthetic protein nanoparticles for glioblastoma therapy. *Nat. Commun.* **11**, 1–15 (2020).

281. Habibi, N. *et al.* Engineered Ovalbumin Nanoparticles for Cancer Immunotherapy. *Adv. Ther.* **3**, 2000100 (2020).

282. Smith, P. S., Zhao, W. & Robbins, M. Knocking down catalase leads to increased ROS production and proliferation in glioma cells. *Cancer Res.* **66**, 1037 (2006).

283. Flor, S. *et al.* Catalase Overexpression Drives an Aggressive Phenotype in Glioblastoma. *Antioxidants (Basel, Switzerland)* **10**, (2021).

284. Olivier, C., Oliver, L., Lalier, L. & Vallette, F. M. Drug Resistance in Glioblastoma: The Two Faces of Oxidative Stress . *Frontiers in Molecular Biosciences* **7**, (2021).

285. Smith, P. S., Zhao, W., Spitz, D. R. & Robbins, M. E. Inhibiting catalase activity sensitizes 36B10 rat glioma cells to oxidative stress. *Free Radic. Biol. Med.* **42**, 787–797 (2007).

286. Johnsen, K. B., Burkhart, A., Thomsen, L. B., Andresen, T. L. & Moos, T. Targeting the transferrin receptor for brain drug delivery. *Prog. Neurobiol.* **181**, 101665 (2019).

287. Calzolari, A. *et al.* Transferrin receptor 2 is frequently and highly expressed in glioblastomas. *Transl. Oncol.* **3**, 123–134 (2010).

288. David, A. Peptide ligand-modified nanomedicines for targeting cells at the tumor microenvironment. *Adv. Drug Deliv. Rev.* **119**, 120–142 (2017).

289. Gatter, K. C., Brown, G., Strowbridge, I., Woolston, R. E. & Mason, D. Y. Transferrin receptors in human tissues: Their distribution and possible clinical relevance. *J. Clin. Pathol.* **36**, 539–545 (1983).

290. Wang, K., Yuan, A., Yu, J., Wu, J. & Hu, Y. One-Step Self-Assembling Method to Prepare Dual-Functional Transferrin Nanoparticles for Antitumor Drug Delivery. *J. Pharm. Sci.* **105**, 1269–1276 (2016).

291. Weller, M. *et al.* Glioma. *Nat. Rev. Dis. Prim.* **1**, 15017 (2015).

292. Kan, L. K. *et al.* Potential biomarkers and challenges in glioma diagnosis, therapy and prognosis. *BMJ Neurol. open* **2**, e000069 (2020).

293. Jung, T.-Y. *et al.* Early prognostic factors related to progression and malignant transformation of low-grade gliomas. *Clin. Neurol. Neurosurg.* **113**, 752–757 (2011).

294. Abdalla, G., Hammam, A., Anjari, M., D'Arco, D. F. & Bisdas, D. S. Glioma surveillance imaging: current strategies, shortcomings, challenges and outlook. *BJR| Open* **2**, 20200009 (2020).

295. Watkins, S. & Sontheimer, H. Unique biology of gliomas: challenges and opportunities.

Trends Neurosci. **35**, 546–556 (2012).

296. Noch, E. K., Ramakrishna, R. & Magge, R. Challenges in the Treatment of Glioblastoma: Multisystem Mechanisms of Therapeutic Resistance. *World Neurosurg.* **116**, 505–517 (2018).

297. Luiz, M. T. *et al.* Highlights in targeted nanoparticles as a delivery strategy for glioma treatment. *Int. J. Pharm.* **604**, 120758 (2021).

298. Zhao, M., van Straten, D., Broekman, M. L. D., Préat, V. & Schiffelers, R. M. Nanocarrier-based drug combination therapy for glioblastoma. *Theranostics* **10**, 1355 (2020).

299. Ghosh, D., Nandi, S. & Bhattacharjee, S. Combination therapy to checkmate Glioblastoma: clinical challenges and advances. *Clin. Transl. Med.* **7**, 1–12 (2018).

300. Teng, C. *et al.* Recurrence-and malignant progression-associated biomarkers in low-grade gliomas and their roles in immunotherapy. *Front. Immunol.* **13**, 899710 (2022).

301. Blakstad, H. *et al.* Survival in a consecutive series of 467 glioblastoma patients: Association with prognostic factors and treatment at recurrence at two independent institutions. *PLoS One* **18**, e0281166 (2023).

302. Leary, M., Heerboth, S., Lapinska, K. & Sarkar, S. Sensitization of drug resistant cancer cells: a matter of combination therapy. *Cancers (Basel).* **10**, 483 (2018).

303. Mokhtari, R. B. *et al.* Combination therapy in combating cancer. *Oncotarget* **8**, 38022 (2017).

304. Shen, C.-H. Chapter 9 - Quantification and analysis of proteins. in (ed. Shen, C.-H. B. T.-D. M. B. (Second E.) 231–257 (Academic Press, 2023). doi:https://doi.org/10.1016/B978-0-323-91788-9.00002-8

305. Khramtsov, P. *et al.* Measuring the concentration of protein nanoparticles synthesized by desolvation method: Comparison of Bradford assay, BCA assay, hydrolysis/UV spectroscopy and gravimetric analysis. *Int. J. Pharm.* **599**, 120422 (2021).

306. Hoshyar, N., Gray, S., Han, H. & Bao, G. The effect of nanoparticle size on in vivo pharmacokinetics and cellular interaction. *Nanomedicine (Lond).* **11**, 673–692 (2016).

307. Alberto, L., Kalluri, L., Qu, J., Zhao, Y. & Duan, Y. Influence of Polycaprolactone Concentration and Solvent Type on the Dimensions and Morphology of Electrosprayed Particles. *Mater. (Basel, Switzerland)* **16**, (2023).

308. Zhang, S., Campagne, C. & Salaün, F. Influence of Solvent Selection in the Electrospraying

Process of Polycaprolactone. *Applied Sciences* **9**, (2019).

309. Stathias, V. *et al.* Drug and disease signature integration identifies synergistic combinations in glioblastoma. *Nat. Commun.* **9**, 5315 (2018).
310. Hwang, S. & Lahann, J. Differentially degradable janus particles for controlled release applications. *Macromol. Rapid Commun.* **33**, 1178–83 (2012).
311. Kong, W. *et al.* Systematic review of computational methods for drug combination prediction. *Comput. Struct. Biotechnol. J.* **20**, 2807–2814 (2022).
312. Sheng, Z., Sun, Y., Yin, Z., Tang, K. & Cao, Z. Advances in computational approaches in identifying synergistic drug combinations. *Brief. Bioinform.* **19**, 1172–1182 (2018).
313. Flanary, V. L., Fisher, J. L., Wilk, E. J., Howton, T. C. & Lasseigne, B. N. Computational Advancements in Cancer Combination Therapy Prediction. *JCO Precis. Oncol.* e2300261 (2023). doi:10.1200/PO.23.00261
314. Chou, T.-C. Theoretical Basis, Experimental Design, and Computerized Simulation of Synergism and Antagonism in Drug Combination Studies. *Pharmacol. Rev.* **58**, 621–681 (2006).
315. Chou, T.-C. Drug combination studies and their synergy quantification using the Chou-Talalay method. *Cancer Res.* **70**, 440–446 (2010).
316. Ianevski, A. *et al.* Prediction of drug combination effects with a minimal set of experiments. *Nat. Mach. Intell.* **1**, 568–577 (2019).